EFFECT OF INTAKE PRIMARY RUNNER BLOCKAGES ON COMBUSTION CHARACTERISTICS AND EMISSIONS IN SPARK IGNITION ENGINES

DISSERTATION

Presented in Partial Fulfillment of the Requirements for
the Degree Doctor of Philosophy in the
Graduate School of The Ohio State University

By

Yuesheng He, M.S.

*****

The Ohio State University
2007

Dissertation Committee:
Prof. Ahmet Selamet, Adviser
Prof. Mohammad Samimy
Prof. Walter R. Lempert
Prof. Xiaodong Sun

Approved by

_____

Adviser
Graduate Program in Mechanical Engineering

ABSTRACT

In-cylinder charge motion is known to significantly increase turbulence intensity, accelerate combustion rate, and reduce cyclic variation. This, in turn, extends the tolerance to exhaust gas recirculation (EGR), while the introduction of EGR results in much lowered nitrogen oxide emissions and reduced fuel consumption. The present study investigates the effect of charge motion in a spark-ignition engine on fuel consumption, combustion, in-cylinder heat release, and engine-out emissions with stoichiometric and EGR-diluted mixtures under part-load operating conditions. Experiments have been performed with a Chrysler 2.4L 4-valve I4 engine under five operating conditions: 0.78 bar brake mean effective pressure (BMEP) at 1200 rpm, 2.41 bar BMEP at 1600 rpm, 2.95 bar BMEP at 1300 rpm, 2 bar BMEP at 2000 rpm, and 5 bar BMEP at 2000 rpm, with a spark range around maximum brake torque timing. The primary intake runners are partially blocked to create different levels of tumble, swirl, and cross-tumble (swumble) motion in the cylinder before ignition. Various parameters are measured, including crank-angle resolved intake and exhaust runner and in-cylinder pressures, intake manifold absolute pressure, exhaust runner gas temperature, and engine-out emissions. The impact of blockages on combustion is characterized by burn duration, in-cylinder heat release, coefficient of variation, and lowest normalized value.

A method has also been developed simultaneously to quantify the tumble characteristics of blockages under steady flow conditions in a flow laboratory, by using the same cylinder head, intake manifold, and tumble blockages from the engine experiments. A refined tumblemeter is installed under the cylinder head to measure the compressive load of the tumble vortex, allowing for the calculation of angular momentum of the incoming air at varying intake valve lifts, hence the tumble number and the tumble ratio. A correlation is then sought between the engine and flow experiments to help quantify the impact of tumble motion on combustion and cyclic variation. The air flow rate into the cylinder, discharge coefficient of the intake system, and flow loss coefficient across the blockage are also analyzed for different levels of tumble motion. The validity of this method under steady flow conditions is confirmed by comparison of the results with the engine experiments.

Charge motion has been observed to reduce the combustion cyclic variability and burn delay more effectively than unblocked runner, while also extending the EGR tolerance. With increasing EGR, the brake specific fuel consumption (BSFC) has been continuously reduced until an optimum dilution level, along with an associated NO_x reduction. With increasing intake runner restriction, the tumble number above low intake valve lifts and the tumble ratio have increased, reducing the combustion duration and cyclic variations. The flow laboratory results with tumblemeter have also been correlated with those from the firing engine.

Dedicated to my parents and wife

ACKNOWLEDGMENTS

I would like to express my gratitude to my adviser, Professor Ahmet Selamet, for his valuable guidance and support during my Ph.D. studies, as well as his patience in correcting this dissertation. His exceptional enthusiasm and integral view of research and his commitment to providing high-quality work have left a deep impression on me. He could not even realize how much I have learned from him. Besides of being an excellent adviser, Professor Selamet is as close as a relative and a good friend to me. I am really glad that I have come to know him in my life.

I would like to thank Chrysler for providing the financial support for this work. I am grateful to numerous members of Chrysler, including Mr. Ron A. Reese, Mr. Roger K. Vick, and Dr. Amer A. Amer, for many productive discussions and their gracious personalities. I am also thankful to Dr. Philip S. Keller for his support in the early stages of this work and Pat Baer for providing a version of the underhead tumblemeter which was modified in this study.

Thanks extend to my committee members, Professors Mohammad Samimy, Walter R. Lempert, and Xiaodong Sun, for their valuable feedback and suggestions on this dissertation.

I am grateful to the current and former members of the research group who helped me: Dr. Emel Selamet, Dr. Iljae Lee, Dr. Mubing Xu, Cam Giang, Sridevi Rupal, Bill Cloyes, Yale Jones, and Naqash Palathamveed.

Finally, this dissertation is dedicated to my parents and wife, Liying Yang. Thank you for your unconditional love, support, and understanding.

VITA

November 1, 1977	Born – Shanghai, P. R. China
2002	M.S.M.E., Shanghai Jiao Tong University
1999	B.S.M.E., Shanghai Jiao Tong University
2002-2003	Graduate Teaching Associate, The Ohio State University
2003-2007	Graduate Research Associate, The Ohio State University

FIELD OF STUDY

Major Field: Mechanical Engineering

Area of Emphasis: Internal Combustion Engines

TABLE OF CONTENTS

Page

LIST OF TABLES

Table **Page**

LIST OF FIGURES

Figure **Page**

CHAPTER 1

INTRODUCTION

1.1 Background

In-cylinder gas motion before ignition is an important factor controlling the combustion process and exhaust emissions in spark ignition (SI) engines. It governs the turbulence intensity (TI) u' before ignition, turbulent flame speed S_T, hence the burn rate. As u' decreases, for example, under part-load operating conditions, where the throttling reduces the air flow rate as well as the volumetric efficiency η_v, S_T is reduced and more cycle-by-cycle variations occur in the combustion chamber, which lead to unstable combustion and possibly increased unburned hydrocarbon (HC) and carbon monoxide (CO) emissions (Selamet *et al.*, 2004). Diluted mixtures [by air lean operation or exhaust gas recirculation (EGR)] in SI engines offer improvements in fuel economy and pollutant emissions. The presence of dilution reduces the heating value per unit mass of mixture and thus, reduces the adiabatic flame temperature and in-cylinder gas temperature. Decreasing peak in-cylinder temperatures then reduce the formation rate of nitric oxides (NO_x). The fuel economy improves because of the decreased pumping and heat loss as well as the increased specific heat ratio γ. However, the reduction in the peak flame temperature and increase in the in-cylinder dilution lead to a slow burn rate, significant

cyclic variations, and combustion instability. Hence, mechanisms are highly desirable to counter these adverse factors by increasing u' in fresh charge before ignition, which will accelerate the flame propagation and increase the thermal efficiency.

In-cylinder charge motion produces rotating flow inside the combustion chamber to increase u' and mean gas flow velocity before spark timing. In general, for rotating flow, there is an inclination angle between the principle axis of rotation of the in-cylinder charge and the cylinder axis. The magnitude of this angle depends on the intake runner or inlet port and intake valve geometry, bore/stroke ratio, and the shape of the combustion chamber (Hill and Zhang, 1994). Tumble and swirl are two types of charge motion that have been studied extensively. Tumble is defined as the organized rotation of the in-cylinder charge about the axis perpendicular to that of the cylinder bore, whereas swirl is the rotation about the cylinder axis, as shown in Fig. 1.1.

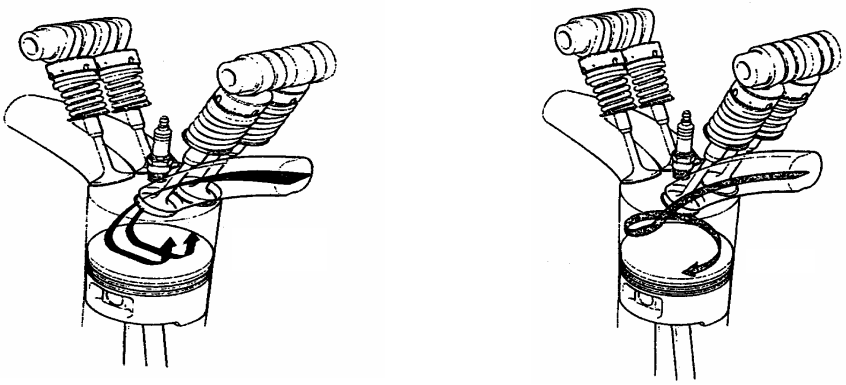

(a) Tumble motion (b) Swirl motion

Figure 1.1. In-cylinder charge motion (Lumley, 1999).

In a simplistic view, it is common to define an equivalent angular speed of swirl ω_s as that of a solid-body with conserved angular momentum (Dyer, 1979; Hill and Zhang, 1994):

$$\omega_s = \frac{M_s}{I_s} \tag{1.1}$$

where M_s is the constant angular momentum in the chamber and I_s is the angular inertia of momentum of the charge expressed as

$$I_s = \frac{1}{8} mB^2 \tag{1.2}$$

with m and B representing the in-cylinder mass and cylinder bore, respectively. Combining Eqs. (1.1) and (1.2) yields

$$\omega_s = \frac{8M_s}{mB^2}. \tag{1.3}$$

With the conserved angular momentum and given in-cylinder mass, Eq. (1.3) suggests that ω_s remains unchanged, hence the swirl motion can persist through the compression and combustion period. Then, it breaks down mainly by wall shear, releasing small scale turbulent eddies (Uzkan *et al.*, 1983; Miller *et al.*, 1998).

Similarly, the angular speed of tumble motion may be defined as

$$\omega_t = \frac{G_t}{I_t}, \tag{1.4}$$

where G_t is the angular momentum of the bulk in-cylinder fluid motion and

$$I_t = \int \vec{r} \times \vec{r} \; dm, \tag{1.5}$$

is the angular moment of inertia with r being the perpendicular distance from the reference axis of tumble vortex to the element with differential mass of dm. During compression, the upward movement of the piston decreases r which, in view of Eq. (1.5), reduces I_t. The angular speed ω_t will then increase for constant angular momentum G_t. Hence, piston motion plays an important role in compressing the tumble vortex and

increasing the magnitude of the rotating gas velocity (by conservation of G_t), resulting in increased shear stress and turbulence in the region near the wall (Hill and Zhang, 1994). During late compression [30° - 60° before Top Dead Center (TDC)], tumble starts breaking down into small scale eddies due to the change in the aspect ratio caused by the piston movement, thereby leading to increased turbulence u' before ignition (Witze *et al.*, 1983 and Kent *et al.*, 1989). Usually, swirl represents a higher mean kinetic energy and tumble a higher turbulence kinetic energy (TKE) at TDC of compression, particularly in 4-valve engines (Lord *et al.*, 1993 and Arcoumanis *et al.*, 1998).

Elevated u' through the introduction of foregoing rotating flows into the combustion chamber increases the flame front area as illustrated in Fig. 1.2 and S_T due to the wrinkling of the flame front by turbulent eddies. The increased flame front area raises heat transfer to nearby unburned gas. Since the temperature of the unburned gas increases more quickly due to the increased heat transfer, it can reach ignition temperature and initiate combustion much faster than without a wrinkled flame front. Guelder (1990) proposed an empirical relationship for the turbulent flame speed as

$$\frac{S_T}{S_L} = 1 + 0.62\left(\frac{u'}{S_L}\right)^{1/2} Re_\ell^{1/4}, \tag{1.6}$$

where S_L is the laminar flame speed, $Re_\ell = u'\ell/\nu$ with ℓ being the integral length scale and ν the kinematic viscosity. Under normal SI engine operating conditions, S_T may be 5 to 10 times as large as S_L, which illustrates the importance of increasing u' in promoting the burn rate.

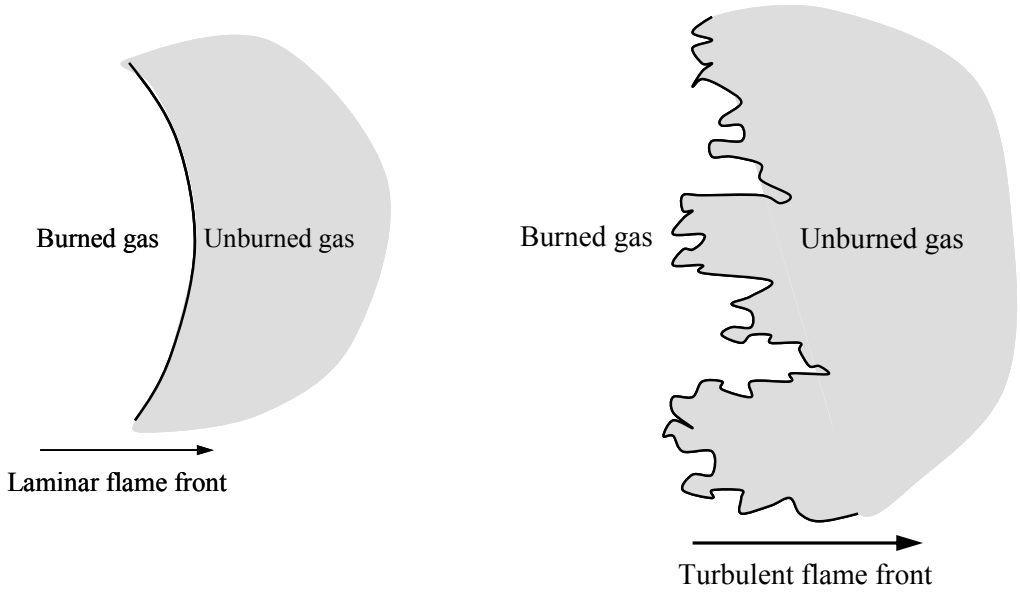

Figure 1.2. Comparison between laminar and turbulent flame fronts during combustion.

As a result, in-cylinder charge motion has increased the combustion rate and extended the flammability limit for diluted mixtures [such as lean misfire limit (LML) and EGR tolerance] (Selamet, *et al.*, 2004). This may lead to improved fuel economy due to three reasons. First, the conversion of thermal to mechanical energy is more efficient with a shorter combustion period. Second, the combustion stability can be improved with charge motion leading to a better engine performance particularly under part-load operating conditions. Third, flammability limits can be widened so that the engine may be operated with considerably leaner air or higher EGR than without charge motion. Along with the improved fuel consumption, fast burn may also reduce unburned hydrocarbon and carbon monoxide emissions due to the reduction in cyclic variations. The extended EGR tolerance or LML can reduce the cylinder peak temperature hence NO_x emissions.

1.2 Objective

The objective of the present study is to develop a comprehensive understanding of the effect of charge motion on fuel consumption, combustion characteristics, in-cylinder heat release, and exhaust emissions (such as HC, NO_x, and CO) with stoichiometric and EGR-diluted mixtures under part-load operating conditions. Dynamometer experiments are conducted with a Chrysler 2.4L 4-valve I4 engine for five operating conditions around maximum brake torque (MBT) timing:

(1) 35 psi (241 kPa) brake mean effective pressure (BMEP) at 1600 rpm, referred to hereafter as the "world wide point" (abbreviated as WP);

(2) 11 ft-lbf brake torque (78 kPa) BMEP at 1200 rpm, or "high speed idle point" (IP);

(3) 295 kPa BMEP at 1300 rpm (WP_GM);

(4) 200 kPa BMEP at 2000 rpm (WP_FEV); and

(5) 500 kPa BMEP at 2000 rpm, or "high load point" (HP).

The primary intake runners are partially blocked [20%, 40%, and 60% open cross-sectional area (80%, 60%, and 40% area blocked), to be elaborated in Chapter 3] to create different levels of tumble, swirl, and cross-tumble (swumble) motion in the cylinder before ignition. The impact of blockage is investigated by comparing the results with those of the unblocked runner. Next, a method has been developed to quantify the tumble characteristics of these blockages under steady flow conditions in a flow laboratory, by using the same cylinder head, intake manifold, and tumble blockages from the engine experiments. A refined tumble meter is installed under the cylinder head to measure the compressive load produced by the tumble vortex, allowing for the calculation of angular

momentum of the incoming air, tumble number, and tumble ratio at varying intake valve lifts. A correlation is then sought between the engine and flow experiments to help quantify the impact of tumble motion on combustion and cyclic variation.

For a comprehensive investigation of charge motion, different approaches of data analysis are developed to examine engine performance from both engine and flow experiments. In this study, the engine parameters include:

- Brake specific fuel consumption (BSFC), indicated specific fuel consumption (ISFC), and fuel conversion efficiency η_f;
- In-cylinder, intake and exhaust runner pressures;
- Coefficient of variation (COV) and lowest normalized value (LNV) on indicated mean effective pressure (IMEP), maximum cylinder pressure ($p_{\max}$), and location of maximum cylinder pressure ($\theta_{p\max}$) to determine cyclic variation;
- Pumping mean effective pressure (PMEP) and intake manifold absolute pressure (MAP) for pumping loss calculation;
- End of combustion (EOC) timing, burn delay, and burn duration (determined by using an improved combustion pressure rise method);
- In-cylinder heat release, heat transfer to combustion chamber walls, and heat loss due to crevice effects during combustion (analyzed by a heat release model);
- Exhaust gas temperature (EGT);
- Engine-out brake specific emissions.

Parameters that characterize the in-cylinder tumble motion from flow experiments include:

- Mass flow rate and runner velocity at varying intake valve lift;
- Flow loss coefficient K across blockage and discharge coefficient C_D;
- Angular momentum and torque produced by tumble vortex;
- Tumble number (TN) and tumble ratio (TR).

1.3 Outline

Following this introduction, Chapter 2 presents a review of pertinent works from the literature. Experimental setups for both engine and flow bench experiments are described in Chapter 3. The detailed methods for data analysis are illustrated in Chapter 4 for both setups. Engine results are presented in Chapter 5, including a comparison between blocked (charge motion) and unblocked runners in terms of fuel consumption, in-cylinder combustion, heat release, and exhaust emissions. Chapter 6 provides the corresponding flow bench experimental results in terms of air flow rate in the intake runner, discharge coefficient, flow loss coefficient across the blockage, tumble number, and tumble ratio. A correlation is also described in this chapter between the engine and flow bench experiments to quantify the impact of tumble motion on combustion. Finally, Chapter 7 presents a summary and concluding remarks along with suggestions for future work.

CHAPTER 2

LITERATURE REVIEW

This chapter gives an overview of existing literature on swirl and tumble in spark-ignition engine and their effects on turbulence generation, burn duration, and EGR diluted combustion. The effects of charge motion on combustion (such as burn duration, cyclic variation, and thermal efficiency) and turbulence enhancement are introduced first followed by a review of mechanisms to produce swirl and tumble. Next, the approaches to determine swirl/tumble intensity are presented. Finally, a review of literature on the EGR-diluted combustion with the impact of charge motion is also provided.

2.1 Combustion with swirl and tumble

Much experimental work (Tabaczynski , 1976; Hoult and Nguyen, 1985; Gouldin, 1989; Santavicca *et al.*, 1990; Guelder, 1990) has shown the strong effect of u' on flame propagation rate. Most of the experimental data have demonstrated the idea that S_T divided by S_L varies with the ratio of u' to S_L [i.e. Eq. (1.6)]. Swirl and tumble can increase u' significantly before ignition, thereby increasing S_T and reducing burn duration (Mayo, 1975; Kyriakides and Glover, 1988; Baritaud, 1989; Hadded and Denbratt, 1991).

In this section, the effects of swirl and tumble on combustion duration, cyclic variation, and thermal efficiency are reviewed.

2.1.1 Combustion duration

Fluid motion near spark plug can have a number of effects on ignition. One impact is the elongation of the arc which may reduce heat transfer to the electrodes. Pischinger and Heywood (1990) observed that a large flow velocity, produced by charge motion, convected the flame kernel away from the electrodes, thereby reducing the contact area and the heat loss to the electrodes. The large flow velocity usually resulted in higher u', which combined with reduced heat loss led to increased flame kernel growth rate, high turbulent flame speed, and hence the decreased burning period (Nagayama *et al.*, 1977; Baritaud, 1989; Hadded and Denbratt, 1991; Arcoumanis *et al.*, 1998; Selamet *et al.*, 2004).

In the results of a number of engine experiments (Kido *et al.*, 1980; Witze and Vilchis, 1981; Hamamoto *et al.*, 1985; Mikulec *et al.*, 1988; Kent *et al.*, 1989; Hadded and Denbratt, 1991; Urushihara *et al.*, 1996; Jeon *et al.*, 1998; Selamet *et al.*, 2004; Goldwitz and Heywood, 2005), there was a strong correlation between increased charge motion and decreased combustion duration. For example, in the experiment of Mikulec *et al.* (1988), the inlet kinetic energy flux was kept approximately constant while varying the swirl by shrouding the intake valve. The engine was operated at 1500 rpm and 400 kPa IMEP. Changing the average swirl speed from 0 – 2.8 times engine speed reduced the ignition delay [0 – 10% mass fraction burned (MFB)] by 25% and rapid burning period (10 – 90% MFB) by 10%, with significantly improved combustion stability. Jeon *et al.* (1998) investigated the effect of tumble on combustion duration (5 - 90% MFB) and

cyclic variation in a 4-valve SI engine with three inlet tumble ports. The generated tumble motion resulted in 15% reduction in combustion duration and 40% enhancement of cyclic variation. Selamet *et al.* (2004) examined the impact of tumble, swirl, and swumble through intake runner blockages on cyclic variation, burn duration, and emissions in an SI engine under part-load operating conditions. Burning period was considerably shortened by tumble compared to swirl and swumble. The similar results were reported by Goldwitz and Heywood (2005).

The burning rate, as Baritaud (1989) has shown, can be directly related to the turbulence intensity generated by swirl or tumble. It appears that increased turbulence during combustion corresponds to an increase in flame kernel growth rate and turbulent flame speed. The mechanism of turbulence generation by swirl or tumble will be reviewed in 2.2. Kyriakides and Glover (1988) conducted experiments in a conventional Mar 4 Hydra engine and concluded that tumble-generated turbulence at the time of ignition can reduce the burn delay (0 - 1% MFB) by about 50%. The authors also correlated u' at 10% MFB with rapid burning angle and revealed that the turbulence intensity before TDC had a substantial impact on 10 – 90% burned period.

2.1.2 Cyclic variations

Generally combustion in spark ignition engines varies appreciably from cycle to cycle, even with stoichiometric air fuel ratio and best ignition parameters (Young, 1981; Yamamoto and Misumi, 1987; Hill and Kapil, 1989; Sztenderowicz and Heywood, 1990). Measures are developed to quantify cyclic variability such as standard deviations of ignition delay (0 - 1% or 0 - 10% MFB), main combustion duration (10 - 90% MFB), IMEP, or peak in-cylinder pressure.

As shown by Young (1981), cyclic variations are strongly affected by combustion duration. The author concluded that changes in engine design or operating conditions, which resulted in increased burning speed, were associated with reduced cyclic variability. Further, experimental results indicated that variation in the ignition delay is much greater than the variation in the main combustion duration. Rauckis and Maclean (1979) observed much higher random variation in the period for burning 2% of the mixture than the standard deviation in the total burning time in an SI engine. Al-Alousi and Karim (1984) found that the variation in ignition delay appeared as almost twice the corresponding variation in the total combustion duration. Direct observations of kernel growth (Bates, 1989; Pischinger and Heywood, 1990; Gillespie *et al.*, 2000) demonstrated that cyclic variability was associated with variation of early flame kernels in size, shape and location.

Swirl and tumble accelerate the flame kernel growth rate and cyclic variation can then be substantially reduced (Witze *et al.*, 1988; Lord *et al.*, 1993; Aucoumanis *et al.*, 1998; Ancimer *et al.*, 1999; Selamet *et al.*, 2004). Mikulec *et al.* (1988) found the least standard deviation of peak cylinder pressure with the maximum rotating speed of swirl (2.8 times engine speed). Hadded and Denbratt (1991) reported the effects of tumble on cyclic variation in ignition delay, main combustion duration, and IMEP. They observed a significantly reduced cyclic variability with increased tumble intensity. Kang *et al.* (1997) and Jeon *et al.* (1998) studied the effect of tumble on lean burn characteristics in terms of combustion stability. The modified intake port corresponding to stronger tumble resulted in less cyclic combustion variation. Recently, Selamet *et al.* (2004) investigated

the effect of swirl, tumble, and swumble on a firing SI engine under part-load operating condition. They reported a reduction in COV of IMEP for charge motion at MBT timing.

2.1.3 Thermal efficiency

Swirl and tumble affect thermal efficiency of engines due to reduced ignition delay, increased heat transfer to the combustion chamber walls, and decreased volumetric efficiency (Davis and Borgnakke, 1982; Alkidas *et al.*, 1990; Zhang and Frankel, 1997). The potential to reduce specific fuel consumption is the net result of a number of effects.

Nagayama *et al.* (1977) observed a considerable improvement in BSFC using squish and swirl. Nagao and Tanaka (1983) pointed out an extended dilution limit with the introduction of intensified swirl which provided better BSFC. Yet, the benefit of increased fuel conversion efficiency did not increase in proportion to swirl intensity. They concluded that there existed an optimum swirl number at which maximum improvement of fuel economy could be obtained. The experimental results of Mikulec *et al.* (1988) in a propane-fuelled single-cylinder engine with disc chamber showed that, at a fixed air fuel ratio, swirl reduced indicated specific fuel consumption (ISFC) from 1 to 3% when the swirl ratio varied from 0 to 2.8. Jie *et al.* (1993) conducted experiments on single cylinder engines with tumble of different intensities and observed a reduction in BSFC for the engine with strong tumble. Recently, Selamet *et al.* (2004) found a moderate decrease of ISFC for tumble and swumble under two part-load operating conditions.

The net effect of swirl or tumble on the thermal efficiency depends on several effects including swirl or tumble intensity, mixture strength, ignition source, and

combustion chamber configuration (Hill and Zhang, 1994). Swirl and tumble can be an effective way to improve the thermal efficiency of SI engines.

2.2 Turbulence generation

Swirl and tumble are two forms of rotating flow inside engine combustion chamber, which can enhance the turbulence intensity during late compression, increase the turbulent flame speed, and hence accelerate the burning rate. This section briefly reviews the characteristics of turbulence generation for swirl and tumble, respectively.

2.2.1 Swirl motion

Swirl, considered as a two-dimensional solid body rotation, persists through the compression and combustion processes. Many researches have demonstrated that the decay of swirl in an engine cylinder during the compression process is relatively small so that the overall angular momentum of the swirl vortex is almost conserved (Dyer, 1979; Arcoumanis *et al.*, 1981; Hamamoto *et al.*, 1985; Hall and Bracco, 1987; Heywood, 1988). Since the flow pattern is strain-free, swirl is expected to have negligible effect on turbulence enhancement in the bulk of the flow. However, the turbulence generated in the wall boundary can be transported throughout the bulk of the flow by diffusion and swirl-driven secondary flow (Hill and Zhang, 1994). Protruding objects, such as the spark plug and valve head, also generated turbulence due to surface shear stress and vortex shedding with global swirl motion (Stephenson *et al.*, 1996). Thus, nearly solid body rotations could result in considerable enhancement of turbulence throughout the combustion chamber, particularly near TDC.

A number of engine results illustrated that turbulence was enhanced at TDC of combustion and tended to become homogeneous and isotropic for swirl motion (Liou and Santavicca, 1983; Ikegami *et al.*, 1985; Saxena and Rask, 1987; Heywood, 1988; Li *et al.*, 2001). For example, Liou and Santavicca (1983) found that turbulence was nearly homogeneous and isotropic near TDC in their engine experiments. They also showed that turbulence intensity near TDC at a given speed was 25-50% greater with swirl than without and then declined continuously with crank angle. As an indicator of u' at different engine speed, the ratio $u'/\overline{S}_p$ (turbulence intensity divided by mean piston speed) is often used. Arcoumanis and Whitelaw (1987) reported that $u'/\overline{S}_p$ was in an interval of 0.3-0.5 over a wide range of engine speed at TDC of combustion with little or no swirl. With intense swirl it appeared possible to appreciably increase the value of $u'/\overline{S}_p$ to 0.7 – 0.8 (Glover *et al.*, 1988; Urushihara *et al.*, 1995; Li *et al.*, 2000).

2.2.2 Tumble motion

Tumble, being a vertically oriented vortex with its axis transverse to the cylinder, compresses the flow vortex and increases the mean gas velocity during early compression due to piston motion, and then decays rapidly and breaks down into small scale turbulence near TDC (Naitoh *et al.*, 1990; Li *et al.*, 2000; Hascher *et al.*, 2000; Selamet *et al.*, 2004). The angular momentum of tumble motion decreases to almost zero at TDC according to the experimental measurement of Arcoumanis *et al*. (1990) and Yoo (1994), and the numerical simulation results of Haworth *et al.* (1990) and Hascher *et al.* (2000). Therefore, the tumble-generated turbulence near or at TDC is enhanced significantly,

leading to increased turbulent flame speed and accelerated burning rate, particularly during burn delay period.

In early experiments, Witze *et al.* (1983) created tumble in a side-valve research engine; the measured u' is higher than swirl, peaked at about 30˚ BTDC. The LDV measurements of Hadded and Denbratt (1991) in an SI engine with pent-roof chamber showed an obvious increase in the ensemble-averaged turbulence intensity about 20˚ BTDC. Floch *et al.* (1995) reported that the breakdown of the tumbling flow into turbulence occurred earlier in the compression stroke with higher turbulence intensity at ignition. Kang and Baek (1996, 1998) conducted engine experiments with various tumble, showing that u' near TDC for stronger tumble was almost twice as much as that for weaker tumble. Meanwhile, a number of numerical results also demonstrated the fact that tumble-generated turbulence tended to peak around 30˚ BTDC (Gosman *et al.*, 1985; Haworth *et al.*, 1990; Das and Dent, 1995; Bianchi *et al.*, 2002).

2.3 Generation of swirl and tumble

Tumble and swirl are two types of charge motion that have been studied extensively. The idea of generating swirl motion in the cylinder to enhance turbulence dates back to 1960s while tumble vortex has been investigated for over two decades. Different mechanisms have been employed in spark ignition engines to produce rotating flow during air induction process. Once created, the rotating gas motion can be intensified in the engine, depending on the piston and cylinder head geometry (Hill and Zhang, 1994).

2.3.1 Helical ports

Strong swirling flow can be generated upstream of the intake valve by helical ports (Tindal *et al.*, 1982, Partington, 1982, Kajiyama *et al.*, 1984, and Arcoumanis and Tanabe, 1989). Usually, with helical ports, a higher discharge coefficient at equivalent levels of swirl is obtained, resulting in a higher volumetric efficiency, since the whole periphery of the valve open area can be fully utilized (Heywood, 1988). During the intake stroke, the resulting in-cylinder fluid motion is three-dimensional (3D). However, and particularly for a flat piston and head, the swirl will tend, during the compression stroke, toward a two-dimensional rotation.

2.3.2 Directed ports

Directed port brings the flow toward the valve opening in a desired tangential direction. The resulting in-cylinder flow pattern will be determined by the orientation of the inlet port. The introduced charge motion usually intensifies the turbulence intensity and then increases the flame propagation rate. The use of directed port to produce swirl or tumble can be found from numerous references (Wigley and Hawkins, 1978; Pettiffer, 1982; Catania, 1982; Fansler, 1985; Mikulec *et al.*, 1988; Arcoumanis *et al.*, 1990; Gale, 1990; Hadded and Denbratt, 1991; Omori *et al.*, 1991; Kang *et al.*, 1997; Li *et al.*, 2000). Yet, with high tangential momentum to the cylinder, the flow across the valve is unlikely to be circumferentially uniform and volumetric efficiency can be significantly reduced (Catania, 1982; Omori *et al.*, 1991).

2.3.3 Variable swirl/tumble ports

The variable swirl/tumble ports usually include two separate intake ports, one of which has a control valve for changing the intensity of the resulting flow motion (Inoue

et al., 1988; Urushihara *et al.*, 1995; Urushihara *et al.*, 1996; Kawashima *et al.*, 1996; Kawashima *et al.*, 1997; Kawashima *et al.*, 1998; Yun and Lee, 2000). The benefit of engine performance with optimized charge motion was demonstrated by Nagao and Tanaka (1983) at various loads and speeds. Kawashima *et al.* (1998) examined the characteristics of swirl ratio and flow coefficient under a broad range of conditions with variable swirl ports. The results illustrated an effective port design by obtaining a wide range of swirl ratio from 3.5 to 10. Urushihara *et al.* (1995) generated swirl and tumble motion by 13 types of swirl control valves showing that tumble enhanced turbulence in combustion chamber more effectively than swirl.

2.3.4 Valve shrouding and masking

Both shrouds and masks partially block the flow through the intake valve; the shroud is part of the valve while the mask is attached rigidly to the valve seat. Intake valve shrouding and masking can bring about intense rotating flow in the cylinder but reduce volumetric efficiency substantially, leading to a limited application in production engines (Hill and Zhang, 1994). Strong charge motion has been generated by valve shrouding (Witze, 1982; Gosman *et al.*, 1985; Hadded and Denbratt, 1991; Khalighi *et al.*, 1995; Urushihara *et al.*, 1996; Udayakumar *et al.*, 2003) and valve masking (Wills *et al.*, 1966; Tabaczynski, 1976; Kyriakides and Glover, 1988; Blair and Drouin, 1996). For example, Tabaczynski (1976) and Urushihara *et al.* (1996) reported a significant turbulence enhancement during combustion by valve shrouding and masking. Kyriakides and Glover (1988) correlated turbulence intensity with 10%-90% burn angle by using masked valves. The authors also demonstrated that for this combustion chamber geometry, a tumbling air motion was a more effective means of generating turbulence at

TDC than swirl. Hadded and Denbratt (1991) considered the effect of tumble on burn duration and combustion stability with shrouded valves. Recently, Udayakumar *et al.* (2003) found a reduction of emissions achieved by shrouding valves.

2.3.5 Flow blockages and vanes

Another method of generating charge motion is to place flow blockages or vanes in the intake duct. Arcoumanis *et al.* (1987) employed vanes to create swirl in single transparent cylinder with the intake valve located coaxially with the cylinder. The swirl velocity fields were examined in the induction stroke. Arcoumanis *et al.* (1992) quantified in-cylinder tumble motion produced by partially blocked intake port in a steady flow setup. Floch *et al.* (1995) studied the effect of increased turbulence intensity, generated by swirl and tumble through flow blockages, on COV and burn duration using propane in a single-cylinder engine under a part-load operating condition. Arcoumanis *et al.* (1998) conducted experiments at MBT spark timing under idling and part-load operating conditions on an SI engine with a blocked intake port which generated tumble, to understand the effects on combustion and emissions. Recently, Selamet *et al.* (2004) reported the impact of different intake runner blockages, which created different kinds of tumble, swirl, and swumble in an SI engine, on combustion characteristics and engine-out emissions. In the present study, intake runner blockages will be used to produce various kinds of charge motion. The effects of tumble, swirl, and swumble will be investigated under different operating condition, EGR ratio, and spark timing.

2.4 Determination of flow intensity

To determine in-cylinder swirl/tumble intensity produced by intake ports and/or inlet valves, different approaches have been employed and reviewed in this section.

2.4.1 Steady flow testing

The steady flow testing of cylinder head is a widely adopted procedure in the development of engines (Stone and Ladommatos, 1992; Arcoumanis *et al.*, 1992; Challen and Baranescu, 1999). To evaluate charge motion generated by intake ports, a cylinder head may be used on a test bench with steady flow and experiments can then be performed at varying intake valve lift. The widely used instruments for measuring swirl are paddle wheel and flow torque meter (Xu, 2001). Paddle wheel is usually installed in the cylinder with the diameter close to cylinder bore. In flow experiment, the rotation rate of the paddle wheel is used as a measure of the swirl speed. With a number of derived parameters, for example, swirl coefficient, swirl number, and swirl ratio (Uzkan *et al.*, 1983; Stone and Ladommatos, 1992; Xu, 2001), swirl intensity could be quantified. Yet, the paddle wheel significantly underestimates the swirl ratio by up to 60% due to disturbance of the flow, friction of the wheel bearing and slip between the vanes and the flow (Heywood, 1988; Stone and Ladommatos, 1992). The swirl torque meter features a flow straightening element, on which the flow angular momentum about the straightener axis is turned into the restraining torque and then measured (Kent *et al.*, 1987; Heywood, 1987 and 1988; Arcoumanis and Tanabe, 1989). By this means, the measurement of swirl is sensitive to the position of the torque meter (Xu, 2001). For measuring tumble motion, a tumble adaptor is commonly used to convert in-cylinder tumble vortex into a swirling flow in a certain extended perpendicular pipe such as “T-pipe” or “L-pipe” (Arcoumanis

et al., 1992; Baker *et al.*, 1995; Arcoumanis *et al.*, 1997). Whereas, this conversion is subject to flow velocity head losses within the tumble adaptor, resulting in underestimated tumble ratio. Some literatures have reported a reduction of burn duration with increased swirl/tumble intensity (Kent *et al.*, 1987 and 1989; Trigui *et al.*, 1994; Jeon *et al.*, 1998). Yet, no consistent correlation is observed possibly due to more complicated transient flow characteristics in real engines.

2.4.2 Optical diagnostics

Optical diagnostic techniques have been used in engine experiments to measure in-cylinder velocity field. A number of studies are reported by using Laser Doppler Velocimetry (LDV) to establish the velocity field, determine the angular momentum flux with different intake valve lift, and then quantify the charge motion (Arcoumanis and Tanabe, 1989; Arcoumanis *et al.*, 1990; Hadded and Denbratt, 1991; Arcoumanis, 1992; Urushihara *et al.*, 1995; Floch *et al.*, 1995; Urushihara *et al.*, 1996; Kang *et al.*, 1997; Arcoumanis *et al.*, 1998; Hascher *et al.*, 2000; Hong and Tarng, 2001). Another effective means to measure instantaneous in-cylinder velocity distribution is Particle Tracking Velocimetry (PTV) and Particle Imaging Velocimetry (PIV) which have been increasingly applied to fluid flow measurements (Khalighi, 1990; Rönnbäck *et al.*, 1991; Neuber *et al.*, 1995; Reeves *et al.*, 1996; Marc *et al.*, 1997; Rouland *et al.*, 1997; Choi *et al.*, 1999; Fan and Reitz, 1999; Li *et al.*, 2001;). Pertinent literature on other diagnostic techniques, including Molecular Tagging Velocimetry (MTV) may be found in Schock *et al.* (2003). The flame growth images measured with high-speed CCD cameras have also been reported in Arcoumanis *et al.* (1998) and Gillespie *et al.* (2000).

2.4.3 Computational simulation

Even with the most advanced experimental technique, the difficulty of accessing in-cylinder processes in real engines, the uncertainty of measurements, and the high cost of engine test limit the experimental diagnostics of engine flow characteristics. Yet, mathematical models which simulate intake and cylinder flow can help to further realize the impact of swirl and tumble. Much effort has been devoted to numerical simulation of intake and in-cylinder flow to examine the effect of charge motion. Isshiki *et al.* (1985) used a numerical method to predict the effect of inlet port shape on swirl motion in a single cylinder engine. Nishiwaki (1985) simulated directed port, directed port with shroud, and helical port geometries. In each case he calculated 3D flow in the cylinder during intake process and demonstrated encouraging agreement with experimental data. Aita *et al.* (1990) applied the finite element method to calculate the port-valve-cylinder flow. Their numerical results appeared to be consistent with actual engine experimental observations.

Recently, the occurrence of computational tools, for example, computational fluid dynamics (CFD), has contributed to the engine development process significantly. Hascher *et al.* (2000) employed a 3D CFD to model the in-cylinder tumble motion throughout the displacement of a 4-valve SI engine. Ramadan (2001) conducted a computational study of swirl motion generated by shrouded intake valves in a direct-injection (DI) engine. Payri *et al.* (2004) developed a CFD model to calculate the in-cylinder flow field during intake and compression strokes of a four-valve DI Diesel engine and compared with experimental measurements. In spite of many achievements,

the simulation results highly depend on the accuracy of the mathematical model along with the discretization scheme.

2.5 EGR diluted combustion

EGR is a principal technique used for NO_x emission control. A fraction of the exhaust gases is recirculated through a control valve from the exhaust manifold to intake manifold. The recycled exhaust gas is usually mixed with the fresh fuel-air mixture downstream of the throttle valve. EGR acts as a diluent in the unburned gas mixture, thereby reducing the peak burned gas temperature and NO_x formation rates (Abd-Alla, 2002). Yet, EGR diluents reduce laminar flame speed, leading to lowered burn rate, substantial cyclic variation, and elevated hydrocarbon emissions, particularly when the in-cylinder mixtures approach the dilution limit. Charge motion can significantly enhance the turbulence intensity (discussed in Section 2.2) and increase the flame propagation rate, leading to stable combustion and extended flammability limit for EGR diluted engine operation (Hill and Zhang, 1994).

2.5.1 Effect of EGR on combustion and emissions

EGR-diluted combustion and emissions in IC engines have been extensively studied. The investigation of the effect of EGR on NO_x reduction in SI engine dates back to early 1970s (Glass *et al.*, 1970; Musser *et al.*, 1971; Quader, 1971; Benson and Stebar, 1971; Anderson *et al.*, 1973; Gumbleton *et al.*, 1974). For example, Gumbleton *et al.* (1974) observed a reduction in fuel consumption and NO_x emissions with EGR in a V-8 SI engine. They also found that increasing EGR rates can result in deteriorated HC emissions. The increasing EGR results in the improvement of fuel economy mainly due

to reduced pumping work and heat loss to the combustion chamber walls under part-load operating condition (Heywood, 1988). HC emissions increase with elevated EGR dilution because of reduced burn rate and increased cyclic combustion variation (Heywood, 1988). Baruah *et al.* (1978) simulated a four cylinder SI engine and compared in-cylinder pressures and emissions with experimental results under different EGR ratio. Their results showed that NO_x emissions can be reduced up to 50% at the cost of about 10% loss in engine power. Tabata *et al.* (1995) examined the effect of EGR on a 1.6L 4-valve SI engine under stoichiometric and lean operating conditions. The authors extended the EGR tolerance to about 48% by using a mixture injected SI engine system, leading to further BSFC and NO_x reduction. Meanwhile, they observed increased burn duration with EGR.

Recently, Przastek *et al.* (1999) studied the effects of EGR on fuel economy and exhaust emissions in an SI engine with both experimental and computational results. The authors reported a reduced BSFC and NO_x emissions with EGR, similar to the previous findings. Fons *et al.* (1999) used a mean value engine model (MVEM) to simulate an SI engine with EGR. Shayler *et al.* (1999, 2000) provided generic functions for combustion and emissions with the effects of EGR and residual gas fraction. Ivanic *et al.* (2005) inspected the effect of hydrogen enhancement on fuel economy and NO_x emissions of EGR diluted combustion in an SI engine. They also observed reduced burning rate and increased cyclic variation with EGR dilution. Ozkan *et al.* (2005) determined EGR ratio by using four different calculation methods and the deviation among them was less than 1%.

2.5.2 Effect of charge motion

Swirl and tumble significantly enhance turbulence intensity and then reduce the burning period, which can extend EGR dilution limit (or EGR tolerance) leading to better fuel economy and more reduction in NO_x emissions. A number of studies have demonstrated the benefit of charge motion on EGR diluted combustion (Nueber *et al.*, 1994; Stokes *et al.*, 1994; Jackson *et al.*, 1996; Cains *et al.*, 1997; Geiger *et al.*, 1999; Kapus and Poetscher, 2000). For example, Neuber *et al.* (1994) designed a variable intake system to produce a combination of swirl and tumble which was applied in a 4-valve SI engine. EGR tolerance was significantly extended compared to that with conventional intake system under a part-load operating condition at 2000 rpm, while fuel economy and NO_x emissions also improved. Similar results were reported by Caines *et al.* (1997). The authors generated strong swirl and tumble in an SI engine by valve shrouding, thus giving optimum air motion at the spark plug. BSFC improved from 3% to 7% with the extended EGR tolerance. Geiger *et al.* (1999) investigated engine combustion by using a continuous variable tumble system (CVTS) to produce tumble motion of different intensity. With an SI engine running part load at 2000 rpm, dilution limit was increased to 40% EGR ratio with a reduction of NO_x emissions by more than 70%.

CHAPTER 3

EXPERIMENTAL SETUPS

An engine dynamometer setup was used to investigate the engine performance under five operating conditions introduced earlier in Chapter 1 with blocked and unblocked intake runners. The measured engine data include cycle averaged brake torque, engine speed, fuel mass flow rate, air fuel ratio (AFR), intake manifold absolute pressure (MAP), exhaust gas temperature (EGT), engine-out emissions as well as the crank angle resolved intake, in-cylinder, and exhaust pressures. The engine cyclic variation, pumping loss, combustion characteristics (such as EOC and burn duration), and in-cylinder heat release could be specified based on the measured in-cylinder pressure. In order to quantify the tumble characteristics of blockages, a method has been developed under steady flow conditions in a flow laboratory, by using the same cylinder head, intake manifold, and tumble blockages from the engine experiments. A refined tumblemeter is installed under the cylinder head to measure the compressive load of the tumble vortex, allowing for the calculation of angular momentum of the incoming air, hence the tumble number and tumble ratio at varying intake valve lifts. A correlation is then sought

between the engine and flow experiments to help quantify the impact of tumble motion on combustion and cyclic variation. The present chapter describes both the engine dyno and flow lab setups along with the associated data acquisition and experimental procedures.

3.1 Dynamometer Experimental Setup

All dynamometer experiments are conducted on a Chrysler 2.4L 4-valve I4 spark ignition engine with a rated power of 150 HP at 5,500 rpm with the specifications given in Table 3.1 (Rupal, 2003). The engine has a double overhead cam (DOHC) and a sequential multi-port electronic fuel injection system. Figure 3.1 is a schematic of the engine dynamometer setup showing the type of measurements and the corresponding locations. The intake manifold and exhaust runner 4 are connected through an EGR flow valve so that a controlled fraction of the exhaust gas could be recycled into the intake plenum, and re-enter the combustion chamber mixed with fresh air and fuel. The intake system is equipped with a production air cleaner box (ACB). The exhaust system includes a 3-way catalytic converter, a production muffler, and a resonator. Figures 3.2 and 3.3 show the pictures of the overall engine setup and the EGR system, respectively.

Combustion chamber	Pent roof
Bore (mm)	87.5
Stroke (mm)	101
Connecting rod length (mm)	151
Compression ratio	9.47
Clearance volume (cm^3)	71.43
Firing order	1-3-4-2
Intake valve opening (IVO)	1˚ BTDC
Intake valve closing (IVC)	51˚ ABDC
Exhaust valve opening (EVO)	52˚ BBDC
Exhaust valve closing (EVC)	8˚ ATDC

Table 3.1. Chrysler 2.4L Engine Specifications.

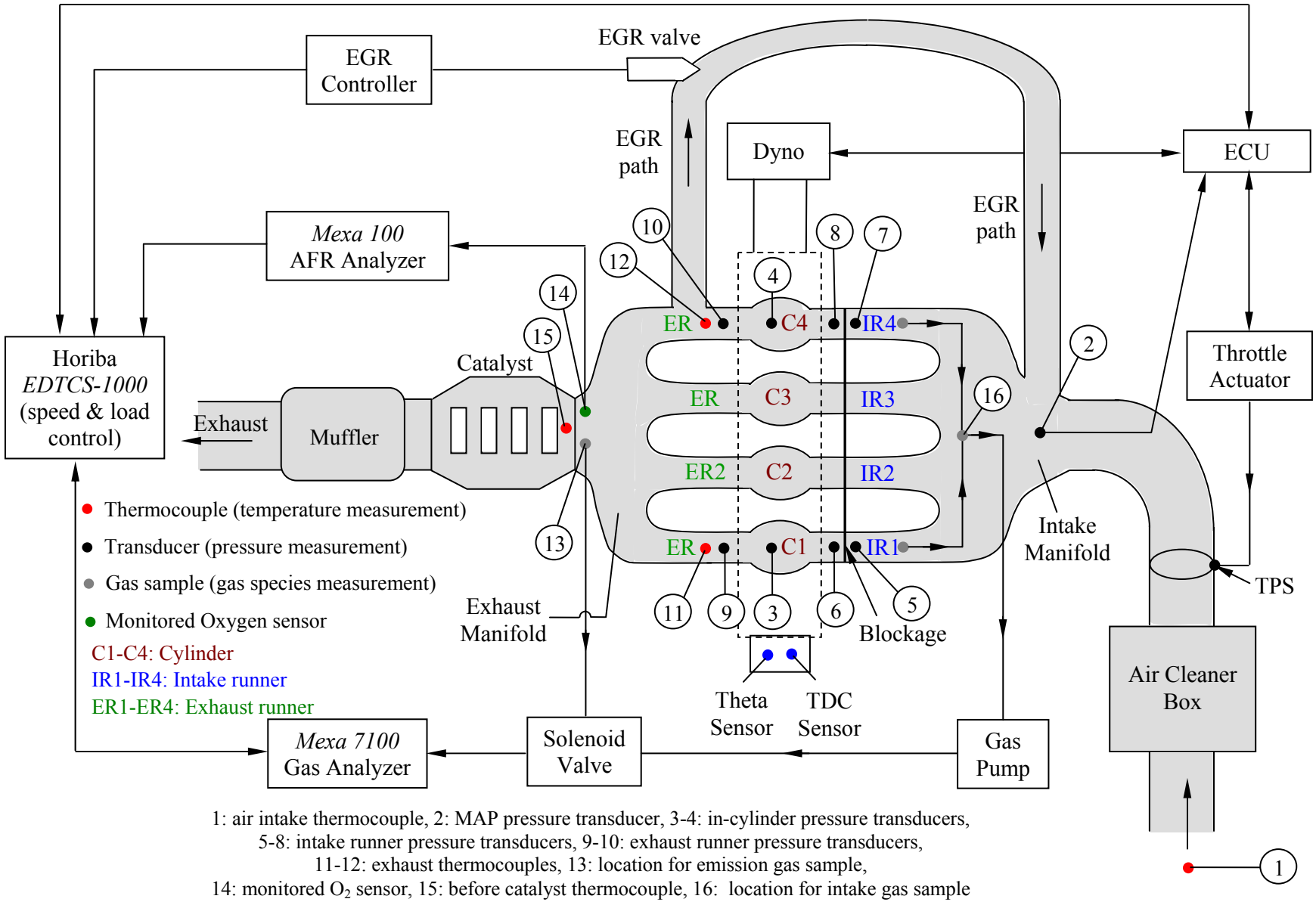

1: air intake thermocouple, 2: MAP pressure transducer, 3-4: in-cylinder pressure transducers,
5-8: intake runner pressure transducers, 9-10: exhaust runner pressure transducers,
11-12: exhaust thermocouples, 13: location for emission gas sample,
14: monitored O_2 sensor, 15: before catalyst thermocouple, 16: location for intake gas sample

Figure 3.1. Engine setup and measurement locations.

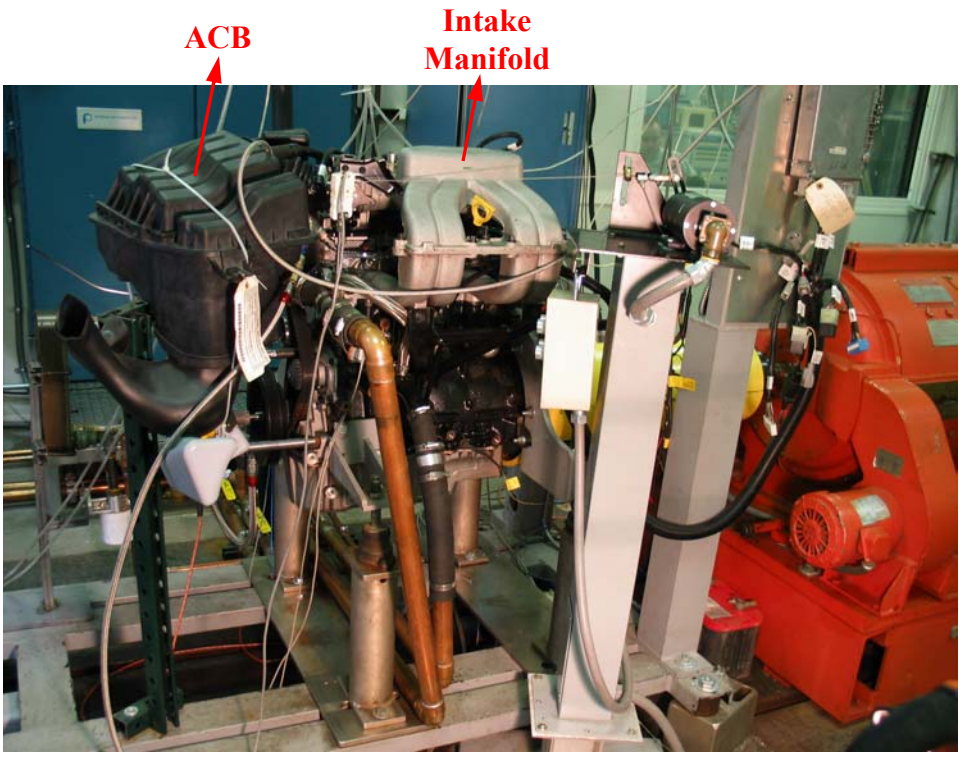

Figure 3.2. A view of the engine setup.

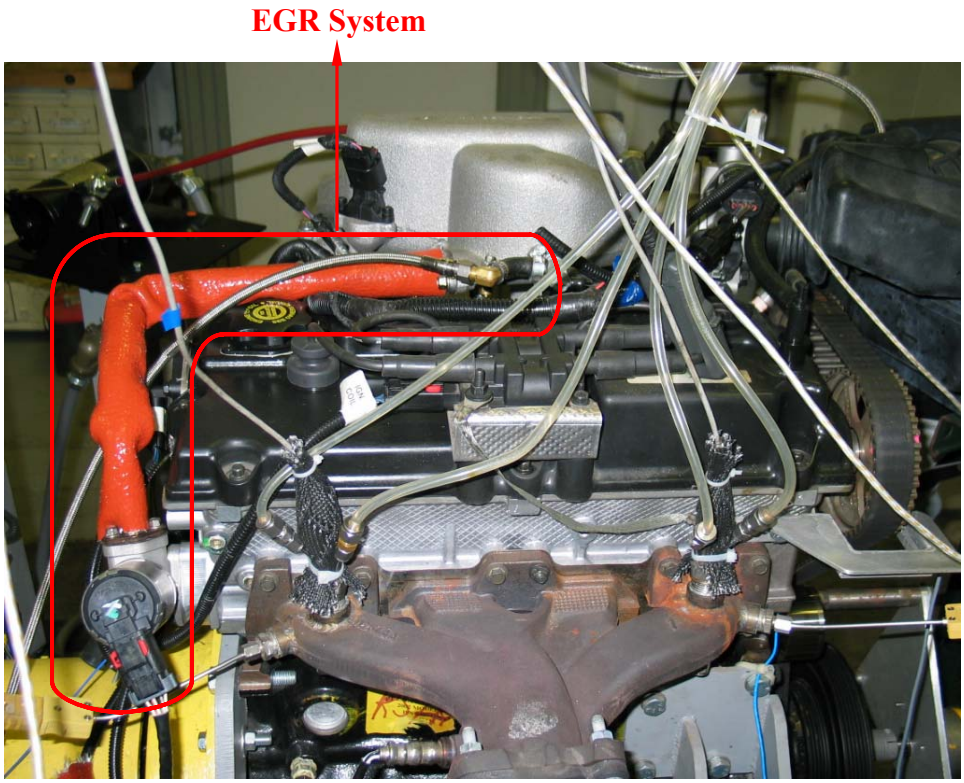

Figure 3.3. A view of the EGR system.

Through a drive shaft engine is coupled to a *General Electric Type TLC 3352F Direct Current Dynamometer* capable of providing 180 HP for motoring and 190 HP absorbing. The rotor of the dynamometer is coupled to a stator which is balanced with the rotor. The static force exerted on the stator with the rotor turning is measured by a *Revere Transducer load cell* for engine brake torque calculation. Engine cooling water and lubricant oil temperatures are controlled within ±2 ˚F by a *StanleyCarter closed loop cooling stand* using shell and tube type heat exchangers and Resistance Temperature Detectors (RTD).

The engine operating conditions are controlled and monitored by *Horiba EDTCS-1000*, a module that combines a *Dyne Systems Digital Dynamometer Controller DYN-LOC IV* with a *Digital Throttle Controller DTC-1* and communicates with the *Engine Control unit* (ECU) and *Dyne Systems throttle actuator*. The throttle can be controlled by the *throttle actuator* and the signal from the Throttle Position Sensor (TPS) is transmitted to ECU as shown in Fig. 3.1. *EDTCS-1000* is integrated with *HyperScript Tools*, a software for dyno data display and analysis which automatically saves the experimental reports in spreadsheets. The operating conditions are controlled by *EDTCS-1000* through a *LabView interface*.

Gasoline (93 Octane – $C_8H_{14.6}$ or with H/C = 1.825) is used as the fuel for dynamometer experiments. For this given H/C ratio, the corresponding stoichiometric Air/Fuel Ratio (AFR) is 14.50. Emission analysis is carried out by using Horiba's *Mexa 7100 Exhaust Gas Analyzer* which is capable of measuring species mole fractions of nitrogen oxide (NO_x), total unburned hydrocarbon (HC), carbon monoxide (CO), carbon dioxide (CO_2), and oxygen (O_2) while also allowing the calculation of AFR based on

chemical analysis. The *Exhaust Gas Analyzer* is interfaced with *EDTCS-1000* and operated with a touch screen. By using a solenoid valve switching mechanism, samples are collected from either the exhaust side (before catalyst; Location 13 in Fig. 3.1) or the intake side (combination of intake runners 1 and 4; Location 15 in Fig. 3.1).

The distributorless ignition system [or the Direct Ignition System (DIS)] includes the ignition coil and battery-operated resistor spark plugs. *Accurate Technologies IGTM-2000 Ignition timing meter* continuously measures spark advance with ±0.05 CAD accuracy. Chrysler Motors *Instrumentation's Interrogator Monitor* is used to manually control the spark discharge timing and fuel injection. Fuel mass flow rate is measured by *Pierburg Instruments FT22-34 fuel measurement system with a FT10E flow meter*. The average exhaust gas temperature is measured by *Omega Type K ungrounded* thermocouples in exhaust runners 1 and 4 located 1.5" away from the cylinder head (Locations 11 and 12 in Fig. 3.1). The same type of thermocouple is placed before the catalyst (Location 15 in Fig. 3.1). AFR is monitored by a *Mexa-110λ AFR analyzer* connected to an O_2 sensor. Intake manifold pressure is measured by a MAP pressure transducer (Location 2 in Fig. 3.1). All signals are fed into *EDTCS-1000* for real time display, monitoring, and recording. Further details of the experimental setup may be found in Rupal [2003].

3.1.1 Blockage setup

In the current study, intake runners are partially blocked with blockages (Fig. 3.4) to create different kinds of in-cylinder charge motion. 3mm-thick blockages with various shapes are introduced in the intake runner, 0.875" upstream of each cylinder head face. Figure 3.5 provides pictures of the tumble blockages and the location they are mounted on the intake system. Below are the details of the blockages used in the engine experiments:

(1) unblocked (or fully open) intake primary runner (Fig. 3.4b);

(2) 20% open (or, 80% blocked) cross-sectional area intake primary runner with tumble motion (Tumble 20%-open blockage, Fig. 3.4c);

(3) 40% open cross-sectional area intake primary runner with tumble motion (Tumble 40%-open blockage, Fig. 3.4d);

(4) 60% open cross-sectional area intake primary runner with tumble motion (Tumble 60%-open blockage, Fig. 3.4e);

(5) 20% open cross-sectional area intake primary runner with swirl motion (swirl blockage, Fig. 3.4f);

(6) 20% open cross-sectional area intake primary runner with cross-tumble motion (swumble blockage, Fig. 3.4g);

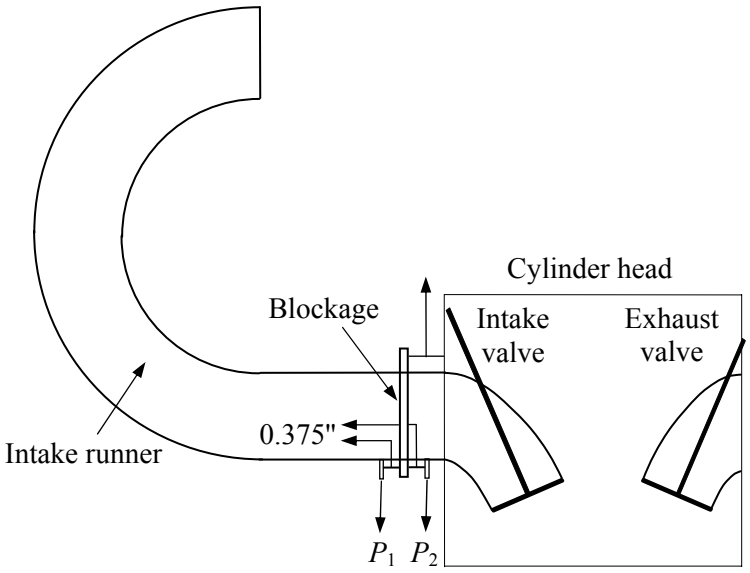

(a) Position of the intake runner blockage.

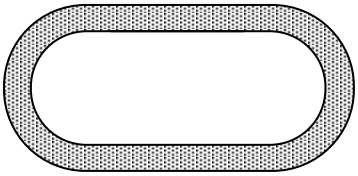

(b) fully open
(cross sectional area = 1.65 in^2)

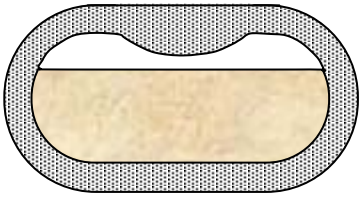

(c) tumble – 20% area open

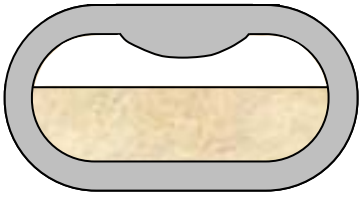

(d) tumble – 40% area open

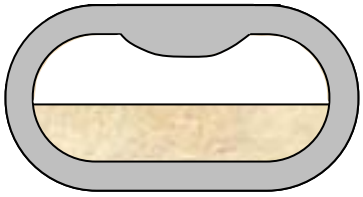

(e) tumble – 60% area open

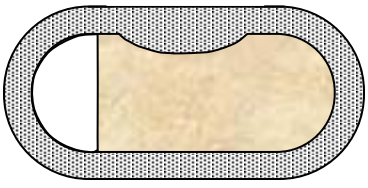

(f) swirl – 20% area open

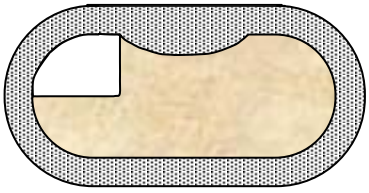

(g) swumble – 20% area open

Figure 3.4. Intake runner blockages.

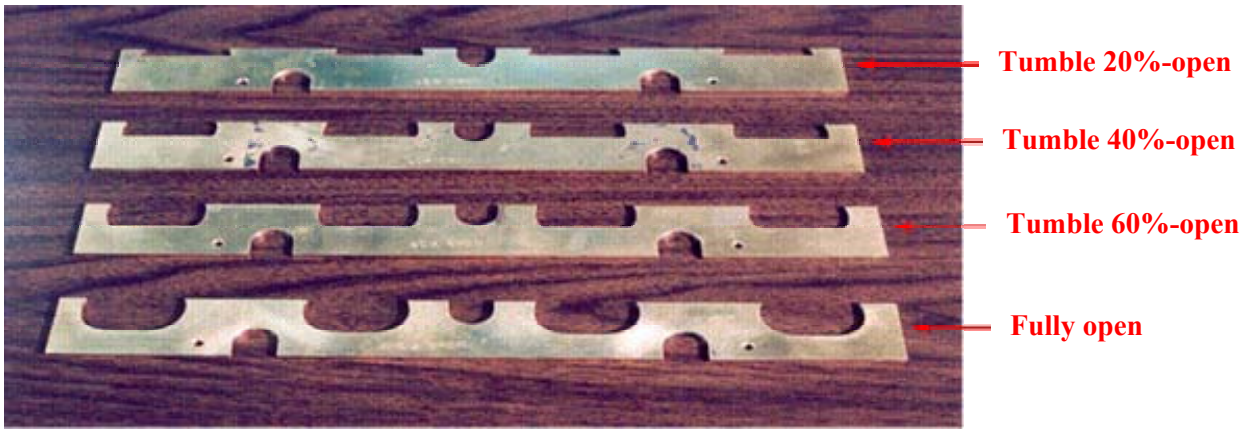

(a)

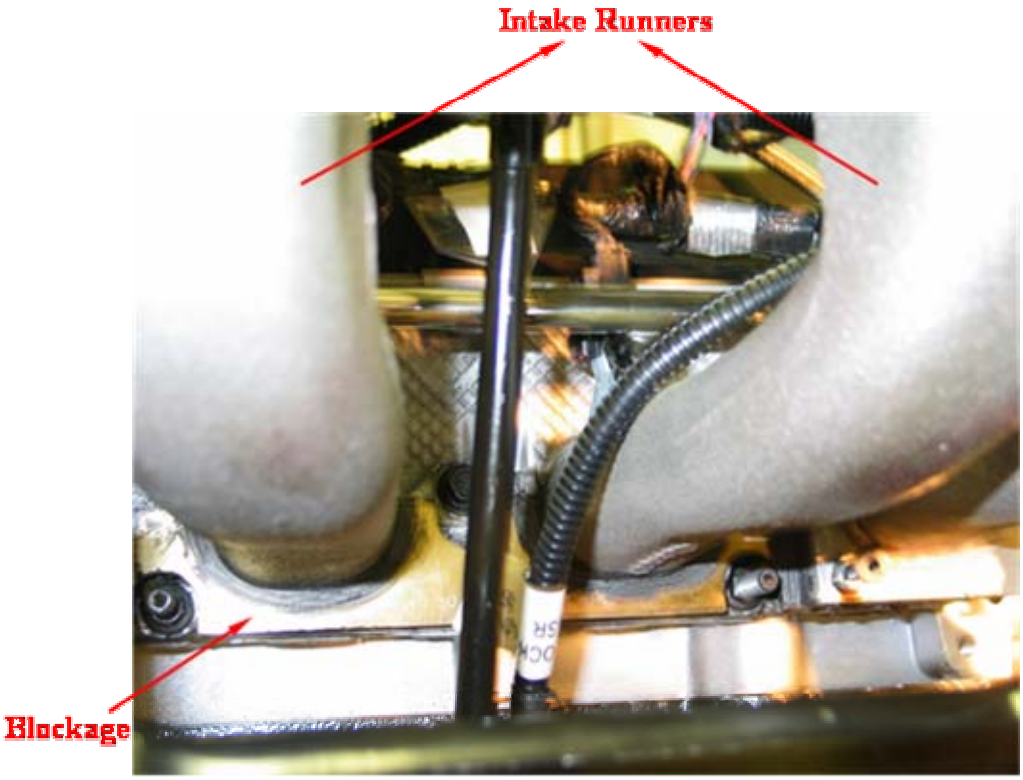

(b)

Figure 3.5. The tumble blockages and their placement on the engine intake.

3.1.2 High speed data acquisition

In the firing engine experiments, all pressures are measured and recorded on a crank angle degree (CAD) basis. Pressures in cylinders 1 and 4 (Locations 3 and 4 in Fig. 3.1) are measured by *Kistler 6125B Piezoelectric transducers*. The signals are then amplified by *Kistler 5010 dual mode amplifiers*. Intake pressures upstream and downstream of the blockage in runners 1 and 4 (Locations 5 - 8 in Fig. 3.1) are acquired by *Kistler 4045A2 (2 bar) Piezoresistive absolute pressure transducers* connected to *Kistler 4603A amplifiers*. The transducers in intake runners are located about 0.375" upstream and downstream the blockage. In the current study, P_1 and P_2 represent the upstream and downstream pressures, respectively, as shown in Fig. 3.4(a). Same type of transducers are placed in exhaust runners 1 and 4 (Locations 9 and 10 in Fig. 3.1), about 1" downstream of the cylinder head face to measure exhaust runner pressure. All exhaust pressure transducers are mounted within cooling jackets.

The crank-angle-resolved in-cylinder, intake and exhaust runner pressures are then recorded by *Concurrent Masscomp 7250-IC70 RTU high speed data acquisition system*. This unit is capable of acquiring data in 32 channels simultaneously at a sampling rate of 2 MHz and consists of a 12-bit Analog to Digital Converter (ADC), a Sample and Hold Circuit (SHC), and five internal synchronization clocks. A *Honeywell Microswitch model 982Rs0* magnetic proximity sensor is mounted on the camshaft (abbreviated as TDC sensor in Fig. 3.1) and a *Lucas Ledex model DG25D* rotary optical encoder is connected to the crankshaft (Theta sensor in Fig. 3.1). The TDC sensor provides a pulse every cycle at top-dead-center of combustion in cylinder 1 that triggers the ADC clock to start data acquisition. The Theta sensor sends a pulse for every CAD that acts as a control

signal for the SHC. All pressure data are recorded with a platform operated in UNIX. Further details of the *high speed data acquisition system* have been provided by Rupal, 2003.

In dynamometer experiments, dynamic in-cylinder pressure is acquired for 256 consecutive firing cycles. Similarly, intake and exhaust runner pressures are obtained and averaged over 64 consecutive cycles. The intake and exhaust runner pressures need a small correction for ambient conditions using the mean value of the atmospheric pressure measured before and after the experiments. The reference for in-cylinder piezoelectric transducer pegging is chosen as an average of 3 consecutive crank angle degrees of the intake runner pressure downstream of the blockage around the intake bottom dead center (IBDC). This approach assumes that the in-cylinder pressure at IBDC is same as the intake runner pressure (Randolph, 1990).

3.1.3 Experimental procedure

After an initial motoring warm-up stage, data recording starts once the engine reaches steady state operating conditions, determined by the stable engine coolant temperature. The parameters controlled are engine speed, load, and spark timing. The engine is locked at a given speed through the *Digital Dynamometer Controller DYN-LOC IV* and the required spark advance is selected on the *Interrogator Monitor*. The throttle position and fuel flow rate are then adjusted through the *Digital Throttle Controller DTC-1* and *Instrumentation's Interrogator Monitor*, respectively, until the desired brake torque (or brake power) is reached for a stochiometric AFR of 14.50 (displayed by the *Mexa-110λ AFR analyzer*).

In addition to the parameters controlled, *EDTCS-1000* also records data such as fuel flow rate, EGT, MAP, engine coolant and oil temperatures, fuel and oil pressures, and ambient conditions. At each spark timing, an averaged value over 3 minutes is recorded after the engine retains steady state conditions. Crank-angle-resolved in-cylinder, intake, and exhaust pressures are also recorded. Some other quantities such as air flow rate, BSFC, and volumetric efficiency are computed by the software through conventional relationships. *The exhaust gas analyzer* measures the steady state intake and exhaust gas species mole fractions. In the current study, engine experiments are conducted under five part-load operating conditions (see Chapter 1) with stoichiometric and EGR diluted mixtures. Comparisons are provided between blocked and unblocked intake runners with a detailed test matrix shown in Table 3.2.

Operating condition	Blockage	Expected EGR ratio (%)	Actual EGR ratio (%)	Spark sweep (˚BTDC)
WP (2.41 bar BMEP @ 1600 rpm)	Fully open	0	0	22 - 42
		4	4	28 - 44
		8	8	32 - 48
		12	11	36 - 52
		16	16	44 - 60
		20	19	50 - 62
		22	22	54 - 62
	Tumble - 20% open	0	0	6 - 22
		4	3	8 - 24
		8	7	10 - 26
		12	11	12 - 28
		16	15	16 - 32
		20	19	20 - 36
		24	24	26 - 42
		26	26	32 - 42
		28	28	34 - 44
	Tumble - 40% open	0	0	10 - 30
	Tumble - 60% open	0	0	26 - 46
	Swirl - 20% open	0	0	16 - 32
		4	3	18 - 34
		8	7	20 - 36
		12	11	22 - 38
		16	15	26 - 42
		20	20	32 - 48
		24	25	38 - 54
	Swumble - 20% open	0	0	14 - 30
		4	3	16 - 32
		8	7	22 – 38
		12	11	26 - 42
		16	15	30 - 46
		20	20	34 - 50
		24	25	46 - 62
		26	27	54 - 62

Table 3.2. Test matrix for engine experiments. (Continued)

Table 3.2: Continued.

Operating condition	Blockage	Expected EGR ratio (%)	Actual EGR ratio (%)	Spark sweep (˚BTDC)
IP (0.78 bar BMEP @ 1200 rpm)	Fully open	0	0	30 – 46
		3	3	36 – 52
		6	5	44 – 54
	Tumble – 20% open	0	0	12 – 34
		5	5	16 – 36
		10	10	20 – 40
		15	15	24 – 44
	Tumble – 40% open	0	0	18 – 38
	Tumble – 60% open	0	0	20 – 40

Operating condition	Blockage	Expected EGR ratio (%)	Actual EGR ratio (%)	Spark sweep (˚BTDC)
WP_GM (2.95 bar BMEP @ 1300 rpm)	Fully open	0	0	22 – 38
		4	4	24 – 40
		8	8	28 – 44
		12	12	34 – 50
		16	15	42 – 58
		20	20	46 – 62
	Tumble – 20% open	0	0	0 – 20
		4	3	6 – 26
		8	7	8 – 28
		12	11	10 – 30
		16	16	12 – 32
		20	20	16 – 36
		24	24	20 – 40
		28	28	32 – 42
		30	30	34 – 42

(Continued)

Table 3.2: Continued.

Operating condition	Blockage	Expected EGR ratio (%)	Actual EGR ratio (%)	Spark sweep (˚BTDC)
WP_FEV (2 bar BMEP @ 2000 rpm)	Fully open	0	0	34 - 50
		4	4	42 - 60
		8	8	50 - 62
		12	12	54 - 62
		14	14	56 - 62
		16	16	56 - 62
	Tumble - 20% open	0	0	10 - 30
		5	5	10 - 30
		10	10	12 - 32
		15	15	16 - 36
		20	20	22 - 42
		25	26	30 - 46

Operating condition	Blockage	Expected EGR ratio (%)	Actual EGR ratio (%)	Spark sweep (˚BTDC)
HP (5 bar BMEP @ 2000 rpm)	Fully open	0	0	20 - 36
		3	3	26 - 38
		6	6	30 - 38
		9	9	30 - 38
		12	12	32 - 38
		15	15	34 - 38
	Tumble - 20% open	0	0	0 - 12
		5	5	2 -14
		10	10	4 - 14
		15	15	6 - 16

3.2 Steady State Flow-bench Setup

The flow-bench experiments are performed to quantify the in-cylinder tumble motion and engine breathing capacity in a steady state flow facility by using the same cylinder head, intake manifold, and tumble blockages from the engine experiments. The schematic of the flow lab setup is shown in Fig. 3.6 including the instrumentation, along with a photograph in Fig. 3.7. In the flow experiments, only a combination of cylinder and intake runner 4 is studied while both intake and exhaust valves of the remaining three cylinders are sealed to ensure no flow through them. A cylindrical spacer is connected underneath the cylinder head with diameter and length equal to the cylinder bore B and piston stroke S. The spacer is then mounted on top of a tumblemeter which includes a perforated plate (screen) to capture the compressive load of the tumble vortex. Three *Honeywell Sensotec Precision miniature model 34* transducers (load cells) are placed 120˚ apart around the periphery of the screen as shown in Fig. 3.8. The screen is attached to a press plate. The combination of the two forms the preload on supporting load cells. Transducer 1 is closer to the intake port while the other two are placed on the exhaust side. Under WP in engine experiments, the maximum vertical load on the piston is estimated on the order of 10 grams for 20%-open tumble blockage and the load decreases with reduced runner restriction. Therefore, the current transducers are calibrated for a full range of 0 – 150 grams each by taking into account a total preload of about 220 grams. In an earlier flow setup by Rupal (2003), the range of the load cells was 0 – 1000 grams with a total preload of 350 grams. This earlier range was found, however, to be too large for an adequate sensitivity, resulting in measurement inaccuracies and poor repeatability,

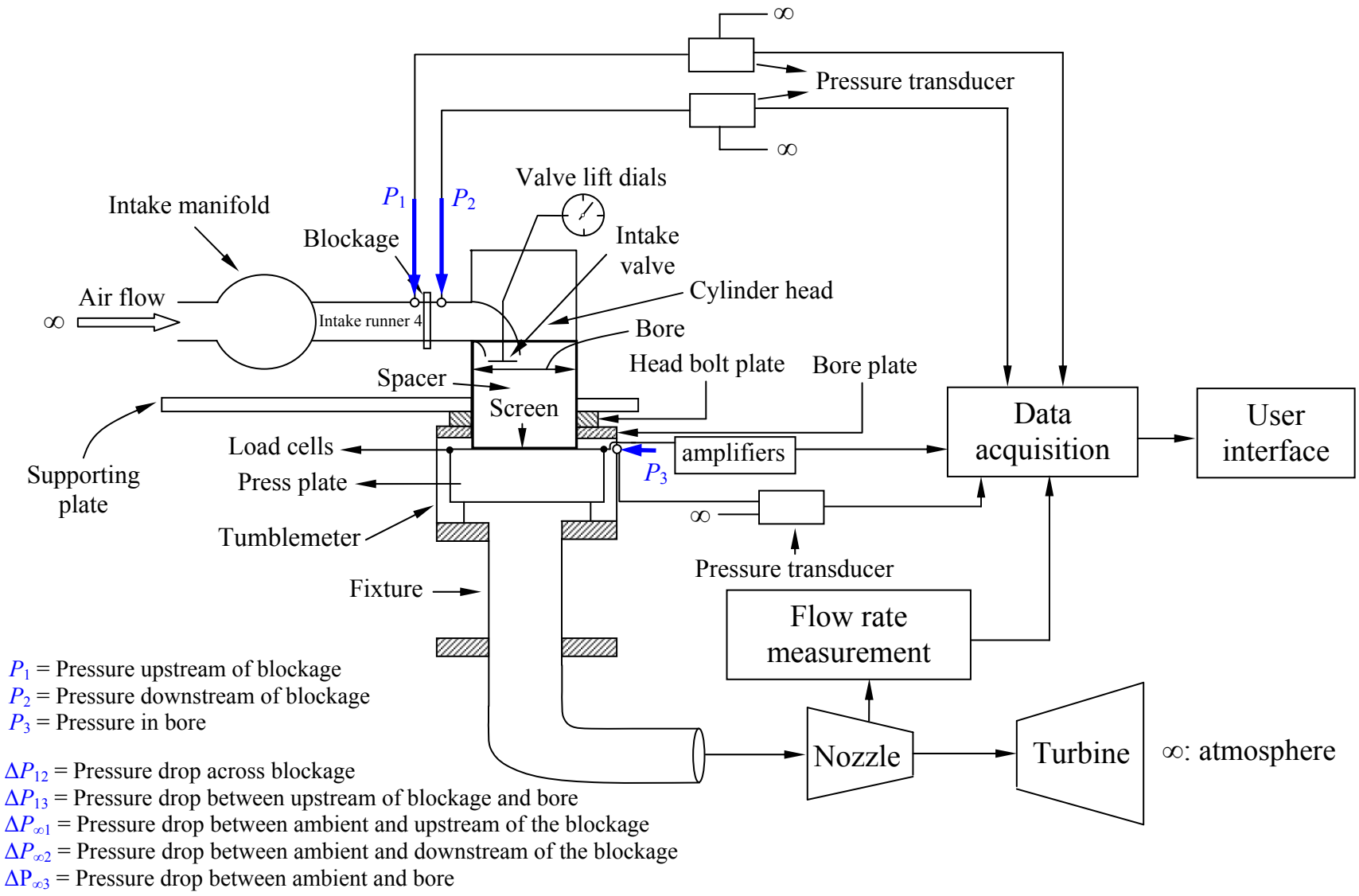

Figure 3.6. Schematic of the flow bench setup.

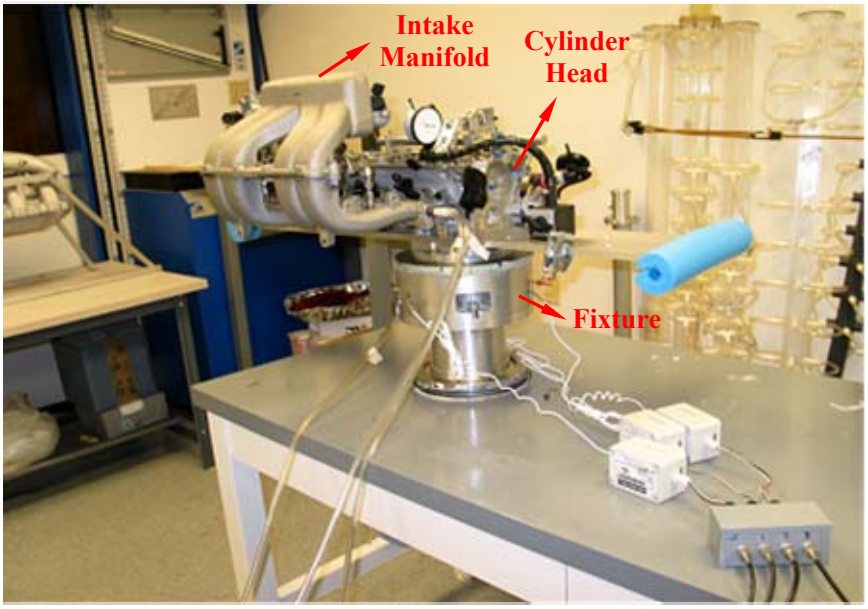

Figure 3.7. A view of the flow lab setup.

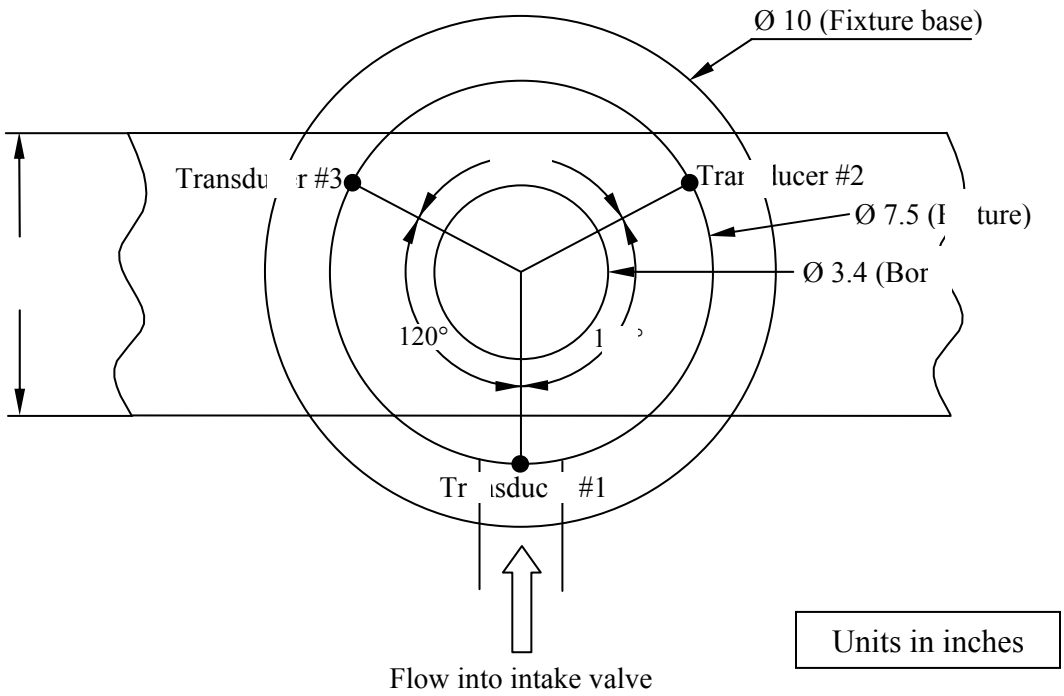

Figure 3.8. Location of load cells in flow bench setup.

particularly for the most restricted (20% open) configurations. Driven by a 40 HP turbine, air is inducted into the manifold under wide open throttle (WOT) condition and passes through the intake runner 4. The flow enters the cylinder through the intake valves, acts on the screen, and exerts a compressive load due to the vertical orientation of the tumble vortex. The volumetric flow rate $\dot{Q}$ is controlled and measured by means of calibrated nozzles of different sizes.

In flow bench experiments, three pressures (P_1, P_2, and P_3 in Fig. 3.6) are measured with *Validyne model P55D 1N630S4A1* differential pressure transducers and recorded at varying valve lifts. The intake valve movement is controlled by a spring and setscrew arrangement along with a calibrated dial indicator used to set the actual valve lift. A differential pressure is measured by the transducer to record the difference between the two input pressures. In the present work, one input is left open to the atmosphere and the other is connected to a measurement tap through *Tygon* tubes. Hence, the pressure drop is measured at each location relative to the atmosphere. The bore pressure drop $\Delta P_{\infty 3}$ is obtained at the edge of the inner cylinder on the same plane of the screen, shown in Fig. 3.9. The other two drops in intake runner 4, $\Delta P_{\infty 1}$ and $\Delta P_{\infty 2}$, are measured at the same locations as those used in the engine experiments [recall Fig. 3.4(a)], as shown in Fig. 3.10. Pressure drops could be adjusted by varying the calibrated nozzles. The ambient temperature and barometric pressure are also monitored.

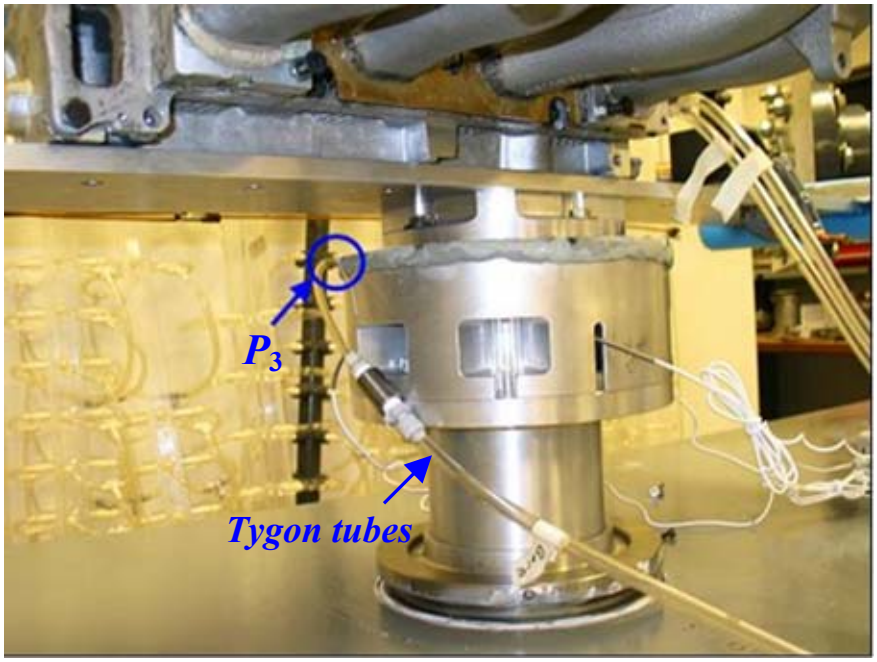

Figure 3.9. Location of bore pressure drop measurement.

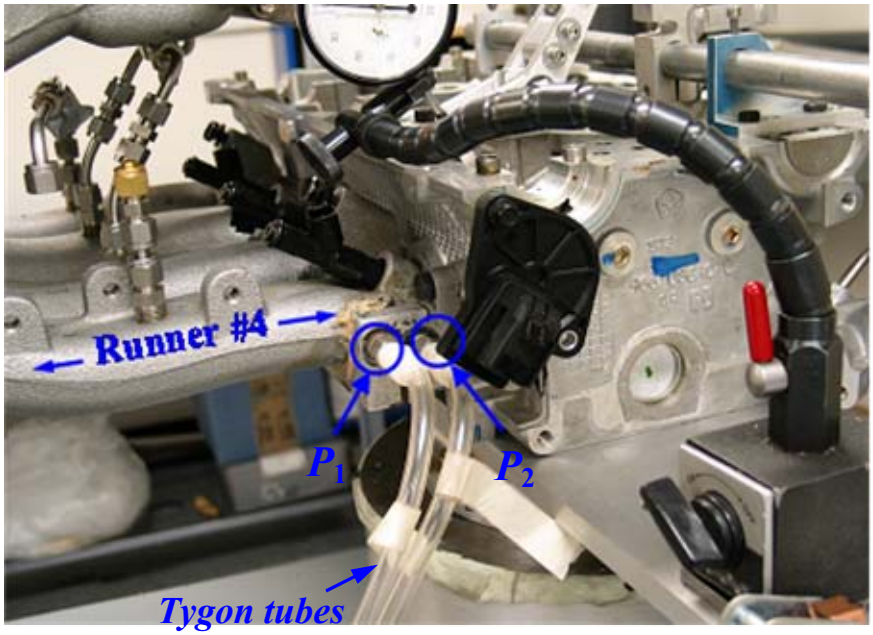

Figure 3.10. Locations of pressure measurements
at upstream and downstream of the blockage.

The signals from the load cells are fed into *Honeywell Sensotec Universal In-line model UV* amplifiers to give ±5 VDC output. The load cells are calibrated using calibration grade weights, and then the ratio of the output signal to the excitation voltage in mV/V is converted to the corresponding load scale through a first order linear curve fit. Both loading and unloading cycles are performed to check for hysteresis, and the zero-offset adjustments of the load cells are made by tuning the amplifiers to maintain 0 – 5 Volts output range. The *Validyne* differential pressure transducers are calibrated through a *Meriam Instrument 350 Series Smart Manometer* which generates a known pressure drop relative to the atmosphere. Similarly, the signals from the differential pressure transducer are transmitted into a *Simpson Digital Multimeter* with ±5 VDC output and the measured voltage is correlated with the pressure drop through a linear curve fit. All signals are fed into a *National Instruments AT-MIO-16L-9* data acquisition board through ADC. The parameters are monitored on a graphical user interface integrated with LabView data acquisition and measurement control module. When flow reaches the steady state condition, those parameters are recorded after they are averaged for about 1 minute.

3.2.1 Experimental procedure

Flow bench experiments are performed with 20%, 40%, and 60%-open tumble blockages. Fully open case is also included as the baseline for comparison. Two engine operating conditions: WP and IP are simulated in flow lab. The instantaneous air mass flow rate $\dot{m}_{air}$ in the intake runner 4 between IVO and IVC in engine experiments are calculated and the maximum mass flow rate $\dot{m}_{air,\max}$ is matched at the peak intake valve

lift ($L_{v,max}$ = 0.325") in flow experiments by using the same blockage. Under a given $\Delta P_{\infty 3}$ where $\dot{m}_{air,\max}$ is matched at $L_{v,max}$ = 0.325", flow experiment is performed at each valve lift (over 0 – 0.1" in increments of 0.01" and over 0.1 – 0.325" in 0.05") with measurements of $\dot{Q}$, $\Delta P_{\infty 1}$, $\Delta P_{\infty 2}$, and three vertical forces on the screen. The room temperature and barometric pressure are monitored to correct the flow rate into standard conditions. Eventually, the in-cylinder tumble motion is quantified from the measured data.

CHAPTER 4

DATA ANALYSIS

To develop a comprehensive understanding of the impact of charge motion, different approaches of data analysis are employed in order to quantify fuel consumption, combustion, in-cylinder heat release, emissions, engine breathing capacity, and in-cylinder tumble motion from both engine and flow experiments. A detailed data reduction approach is provided in this chapter with the key parameters listed below:

1. Fuel economy: BSFC, ISFC, and η_f;
2. In-cylinder, intake and exhaust runner pressures;
3. Cyclic variation: COV and LNV, $p_{\max}$ vs. $\theta_{p\max}$;
4. Pumping loss: Pumping work, pumping power, PMEP, and intake MAP;
5. Combustion: end of combustion (EOC) and mass fraction burned (MFB) determined by an improved combustion pressure rise method;
6. Heat release: in-cylinder heat transfer, piston work, and heat loss due to flow into and out of the crevice volume quantified by a one-zone heat release model;
7. Exhaust runner gas temperature;

8. Engine-out brake specific emissions;
9. EGR ratio;
10. Air mass flow rate at varying intake valve lifts;
11. Flow loss coefficient across the blockage K ;
12. Discharge coefficient C_D between the upstream of the blockage and the cylinder bore (recall Fig. 3.6);
13. Angular momentum and torque produced by tumble vortex; and
14. Tumble number and tumble ratio.

In this chapter, Sections 4.1 – 4.8 describe data analysis from engine experiments for the first nine of the foregoing variables, while Section 4.9 discusses the remaining parameters in flow experiments.

4.1 Fuel economy

In engine experiments, the fuel consumption is measured in terms of mass flow per unit time $\dot{m}_{fuel}$. A more useful parameter is the specific fuel consumption (sfc) – the fuel flow rate normalized with respect to power output. Depending on the power used for normalization, this parameter is defined as

$$\text{BSFC} = \frac{\dot{m}_{fuel}}{P_b}, \text{ NSFC} = \frac{\dot{m}_{fuel}}{P_n}, \text{ or } \text{ ISFC} = \frac{\dot{m}_{fuel}}{P_i}, \tag{4.1}$$

where BSFC, NSFC, and ISFC represent the brake, net indicated, and gross indicated specific fuel consumption, respectively; P_b, P_n, and P_i are the brake, net indicated, and gross indicated power, respectively. P_b is obtained through measured brake torque T_b and engine speed N_{eng} by

$$P_b = 2\pi N_{eng} T_b; \tag{4.2}$$

P_n and P_i can be calculated by

$$P_n = \frac{W_n N_{eng}}{2}, \quad P_i = \frac{W_i N_{eng}}{2}, \tag{4.3}$$

where

$$W_n = \int_{4\text{ strokes}} pdV, \quad W_i = \int_{\text{compression}}^{\text{expansion}} pdV,$$

with p and V being in-cylinder pressure and cylinder volume, respectively: p is recorded every CAD (θ) for 256 consecutive cycles, and V can be calculated using the geometric details of the engine shown in Fig. 4.1 (bore B, stroke S, crank radius $a = S/2$, connecting rod length L, displacement volume V_d, number of cylinders N_c, and compression ratio r_c) as

$$V = V_c + \frac{\pi}{4} B^2 \left(L + a - s\right), \tag{4.4}$$

where

$$V_c = \frac{V_d \left(r_c - 1\right)}{N_c} \tag{4.5}$$

is the clearance volume and

$$s = a\cos\theta + \left(L^2 - a^2 \sin^2\theta\right)^{1/2} \tag{4.6}$$

is the distance between the crank axis and piston pin.

Another important engine operating parameter is the fuel conversion efficiency η_f, defined as the ratio of the output work to the input (fuel chemical) energy during one engine cycle:

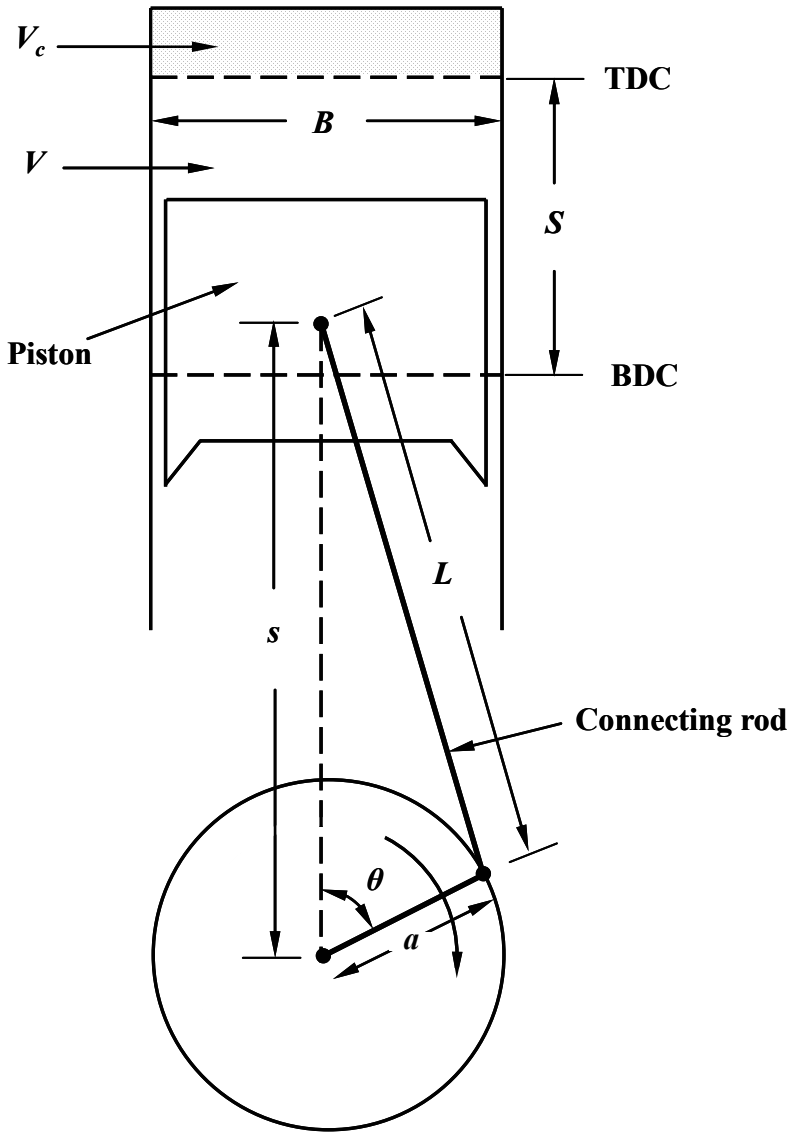

Figure 4.1. Geometry details of an internal combustion engine.

$$\eta_f = \frac{W}{m_{fuel} Q_{LHV}} = \frac{\left(2P_b / N_{eng}\right)}{\left(2\dot{m}_{fuel} / N_{eng}\right) Q_{LHV}} = \frac{P_b}{\dot{m}_{fuel}\ Q_{LHV}}, \tag{4.7}$$

with Q_{LHV} being the lower heating value of the fuel (44 MJ/kg). Combined with Eq. (4.1), η_f is expressed as

$$\eta_f = \frac{1}{\text{BSFC}\ Q_{LHV}}. \tag{4.8}$$

Hence, sfc is inversely proportional to the fuel conversion efficiency.

4.2 In-cylinder, intake and exhaust runner pressures

In-cylinder pressure for SI engines could change significantly under different operating conditions, spark timing, and charge motion, hence influencing the engine performance (such as fuel consumption, combustion, and emissions). In the present study, crank-angle-resolved cylinder pressure is analyzed for 256 consecutive cycles to characterize the combustion, pumping loss, and in-cylinder heat release. Intake and exhaust runner pressures are averaged over 64 cycles and compared between blocked and unblocked runners to examine the impact of blockage during the gas exchange process.

4.3 Cyclic combustion variation

Crank-angle-resolved in-cylinder pressure in SI engine exhibits substantial cyclic variation, particularly under part-load operating conditions. The cyclic variation is usually caused by variations in gas motion within the cylinder at the time of spark, the amounts of air and fuel fed to the cylinder each cycle, and the mixing of fresh mixture and residual gases within the cylinder for each cycle, particularly in the vicinity of the

spark plug (Heywood, 1988). Following parameters are used in the present study to quantify the cyclic combustion variation.

4.3.1 COV in IMEP

One important measure to quantify the cyclic variation is COV in IMEP, where the latter is calculated by dividing the indicated work per cycle by the displaced cylinder volume:

$$\mathrm{IMEP} = \frac{W_i N_c}{V_d}. \tag{4.9}$$

Then COV is determined by

$$\mathrm{COV} = \frac{\sigma_{IMEP}}{\overline{\mathrm{IMEP}}} \times 100\% \,, \tag{4.10}$$

where $\overline{\mathrm{IMEP}}$ is the mean value from all (N) recorded cycles [with N being the number of engine cycles (256 in the present work)] and

$$\sigma_{MEP} = \sqrt{\frac{1}{N-1}\sum_{i=1}^{N}\left(\mathrm{IMEP}_i - \overline{\mathrm{IMEP}}\right)^2} \tag{4.11}$$

represents the standard deviation. Higher COV means more cyclic variation in combustion. In the present study, intake runner blockages are introduced to accelerate the burn rate by increasing the turbulence intensity before the time of spark, which will improve combustion stability and reduce the cyclic variation.

4.3.2 LNV in IMEP

The lowest normalized value in IMEP defined as

$$\mathrm{LNV} = \frac{\mathrm{IMEP}_{\mathrm{lowest}}}{\overline{\mathrm{IMEP}}} \times 100\% \tag{4.12}$$

is an alternative parameter to quantify combustion stability, with $IMEP_{lowest}$ representing the lowest value from 256 engine cycles. Lower LNV would suggest a less stable combustion and therefore high LNV is desirable for engine operation.

4.3.3 Maximum cylinder pressure and the corresponding location

The peak in-cylinder pressure p_{max} is located slightly after combustion TDC depending on the operating condition, dilution level, spark timing, and charge motion. Combustion variation results in substantial fluctuation on both the magnitude of p_{max} and the corresponding location θ_{pmax} for successive engine cycles. Cycles of different p_{max} and θ_{pmax} may indicate varying burn rates, for example, fast or slow burning cycles (Heywood, 1988). Hence, the cyclic variation of p_{max} and θ_{pmax} can be used to characterize the combustion instability as well as the fast and slow burning cycles.

4.4 Pumping loss

In a four stroke SI engine, work is done on the piston over the intake stroke (positive work). During the exhaust stroke, however, work is done by the piston (negative work). The net work over these two strokes, or pumping work W_p, and the corresponding pumping power P_p are defined as

$$W_p = \int_{intake} pdV + \int_{exhaust} pdV, \qquad P_p = \frac{|W_p| N_{eng}}{2}. \tag{4.13}$$

Negative W_p characterizes the pumping loss. In a naturally aspirated SI engine, pumping loss is increased by throttling under part-load operating conditions, resulting in decreased mean cylinder pressure for intake stroke p_{int} compared to the mean cylinder pressure for exhaust stroke p_{exh}. Under the current part-load operating conditions (recall Section 1.2),

the pumping loss is generated because of $p_{int} < p_{exh}$. Hence, increasing p_{int} is desirable to reduce the pumping loss. Converting pumping work to an equivalent pressure produces the pumping mean effective pressure

$$\text{PMEP} = \frac{|W_p| N_c}{V_d}, \tag{4.14}$$

Intake MAP is closely related to p_{int} and may be another indirect indicator of the pumping loss. In general, higher MAP suggests higher p_{int} and lower pumping losses. For example, the introduction of EGR dilution increases MAP, hence reduces PMEP and the pumping loss.

4.5 Combustion characteristics

In a spark ignition engine, the fuel and air are mixed together in the intake system, inducted through the intake valve into the cylinder during intake process and then compressed over the compression stroke. Combustion is initiated near the end of compression stroke by an electric discharge at the spark plug. During the flame development (or burn delay) phase, a highly wrinkled turbulent flame front evolves from the spherical flame kernel established by the spark discharge. In the following flame propagation (or burn duration) phase, the developed turbulent flame propagates across the combustion chamber to the far wall, during which most of the mass is burned. During the final flame termination phase, the flame front reaches the wall and the flame propagation is no longer possible, when the remaining unburned mixture within the flame burns up (Heywood, 1988).

The total burn duration comprises of the flame development, rapid burning, and flame termination periods. Burn delay is a crank angle interval between the spark discharge and the time when a small but significant fraction of the cylinder mass has burned, when there is considerable pressure rise due to the burning of the fuel. In the present study, the interval of 0 – 10% cylinder mass fraction burned has been chosen for the burn delay period. The rapid burning phase is defined as an interval for 10 – 90% cylinder mass burned (Heywood, 1988) and the total burn duration is the period from the start of ignition to the end of combustion when all cylinder charge has been burned up.

In general, the burn rate is dictated by in-cylinder pressure rise due to combustion (Shayler *et al*., 1990; Rassweiler and Withrow, 1938). In the present study, in-cylinder pressure of 256 consecutive engine cycles has been used to determine the combustion characteristics for each cycle, with the results then being averaged. Another method to characterize the combustion is based on the average in-cylinder pressure for a number of engine cycles, which may lead to considerable scattering and noise, necessitating data smoothing and filtering, particularly under low load (Grimm *et al*., 1990). Another issue is that combustion parameters are not related to the average cylinder pressure. Therefore, analysis of the average pressure does not necessarily yield accurate values for combustion characteristics. In particular, the inaccuracy of the combustion parameters calculated by the average cylinder pressure becomes significant for the engine operated with partial burn or misfiring cycles under light load (Heywood, 1988; Stone, 1999).

4.5.1 Calculation of polytropic coefficient *n*

One of the key challenges in the determination of burn duration lies in the accuracy of the instantaneous polytropic coefficient *n* of the cylinder contents during combustion. One standard approach in calculating *n* is to use models based on the first law of thermodynamics, such as single- or two-zone models. Two-zone model assumes the cylinder contents consisting of burned and unburned zones with each zone being homogeneous in terms of composition and properties (Catania *et al*., 2001). Then, the energy conservation is applied to each zone with some reasonable assumptions. This approach does need details of the species and engine specifications in each zone, thermodynamic properties of both burned and unburned mixtures, and estimation of in-cylinder heat transfer in both zones. A single-zone model assumes a homogeneous mixture in the cylinder, hence calculates the state of the cylinder contents in terms of average properties (Brunt *et al*., 1998). The single-zone approach seems straightforward since the in-cylinder pressure and volume are the only details needed (Young, 1980) although the heat transfer during combustion still needs to be estimated.

An alternative method to determine *n*, used in the present analysis, is based on the idea of polytropic process for compression or expansion:

$$pV^n = C = \text{constant}, \tag{4.15}$$

which leads to

$$\log p + n \log V = \log C. \tag{4.16}$$

Hence, a linear regression fit to a specific period (*N* represents the number of total data points) on a log *p*-log *V* plot gives (Kothamasu, 1998)

$$n = \frac{N\sum_{j=1}^{N} \log V_j \log p_j - \sum_{j=1}^{N} \log V_j \sum_{j=1}^{N} \log p_j}{N\sum_{j=1}^{N} (\log V_j)^2 - (\sum_{j=1}^{N} \log V_j)^2}, \quad (4.17)$$

where j corresponds to a data point at a particular crank angle. The intervals for compression and expansion have to be selected in order to account for the deviation of the p-V diagram from a straight line due to combustion and flow through the valves.

4.5.2 Determination of EOC

In order to determine EOC, the compression and expansion polytropic coefficients n_c and n_e are calculated respectively, by using Eq. (4.17). The definition of n_c is based on a CAD range starting at 40˚ before spark, much later than intake valve closing timing (IVC at 129˚ BTDC) and ending at spark ignition point. To compute n_e, an iterative method of slope comparison is employed here to locate a reasonable interval for expansion (Selamet *et al.*, 2004). To begin with, polytropic coefficient n is calculated over a short interval, initially assumed to be between combustion TDC and 7˚ ATDC. This 7˚ interval is shifted by 1˚ ATDC (the start and end points of the interval are then incremented by 1˚) and the value of n is compared to the calculated n_c. This is repeated until the difference between n and n_c $\left(\left|n - n_c\right|\right)$ falls below 0.1. Meanwhile, the starting point of this 7˚ interval cannot exceed 90˚ ATDC which is close to the exhaust valve opening timing (EVO at 128˚ ATDC). Otherwise, the cycle is not included in the combustion calculation. When two slopes n and n_c become comparable, the starting point of the 7˚ interval is assumed as the approximate end of combustion (AEOC). Knowing AEOC, n_e is calculated over an interval extending from AEOC to 10˚ before EVO. For the period of combustion between ignition timing and AEOC, a weighted average of n_c

and n_e is calculated to yield n as a function of CAD:

$$n(\theta) = n_c + \Delta\theta(n_e - n_c), \tag{4.18}$$

where

$$\Delta\theta = \frac{\theta - \theta_{spark}}{\theta_{\text{AEOC}} - \theta_{spark}}. \tag{4.19}$$

For crank angles exceeding AEOC, n is identical to n_e.

The foregoing estimation of n_c and n_e is expected to be realistic because they are computed by means of a curve fit to the in-cylinder pressure. The objective of the iterative slope comparison of n is to make a realistic prediction of AEOC so that the heat transfer during expansion can be taken into account (Brunt *et al.*, 1997). In the present analysis, the polytropic coefficient n is varied as a function of CAD during combustion, leading to a smoother variation of mass fraction burned, while some other methods take an average of n_c and n_e over the entire combustion period. In addition, values between 1.2-1.4 for n_c and 1.1-1.4 for n_e are considered acceptable range for polytropic coefficients (Kothamasu, 1998). For example, a low n_e below 1.1 is indicative of incomplete combustion. Thus, cycles of n_e outside the normal range are not included in the combustion calculation (Brunt *et al.*, 1997).

Knowing n, EOC is determined from a combustion pressure rise method. The measured in-cylinder pressure rise consists of the increase due to volume change produced by the piston movement and the increment due to combustion at constant volume (Grimm *et al.*, 1990; Shayler *et al.*, 1990). The increase in pressure due to combustion is computed at every CAD (point j) starting from spark timing (Selamet *et al.*, 2004):

$$\Delta p_j = \left[p_j - \left(\frac{V_{j-1}}{V_j} \right)^n p_{j-1} \right] \frac{V_j}{V_{spark}} \ , \tag{4.20}$$

where Δp represents pressure rise due to combustion at constant volume. The polytropic coefficient n is calculated from Eqs. (4.17) and (4.18). In order to eliminate the effect of changes in cylinder volume on the combustion pressure rise, the volume at spark timing V_{spark} is chosen as the reference cylinder volume in Eq. (4.20). The ratio of the instantaneous (point j) to the total combustion pressure rise is defined as

$$\mathrm{RPR}_j = \frac{\Delta p_j}{\sum_{spark}^{j} \Delta p}. \tag{4.21}$$

Finally, combustion is assumed to end when the sum of RPR for three consecutive CAD is less than 0.005 with the first crank angle (for example, point j in Eq. 4.22) being considered as EOC, expressed as

$$\sum_{j}^{j+2} \mathrm{RPR} \le 0.005. \tag{4.22}$$

In order to minimize the combustion noise effects in the cylinder pressure, the sum of the three consecutive RPR is used to determine EOC for a particular engine cycle. The total burn duration (0 - 100% cylinder mass burned) is then given as the period between spark timing and EOC.

4.5.3 Mass fraction burned (MFB)

The progress of combustion is reflected by MFB curves from 0 to 1, representing the time of spark and EOC, respectively. The flame development (or, burn delay) θ_{0-10}, flame propagation θ_{10-90}, and the location of 50% mass burned θ_{50} can be determined

from MFB curves. A simple empirical expression often used to estimate MFB is the Wiebe function (Heywood, 1988). The major difficulty in applying the Wiebe function is to accurately determine the adjustable parameters *a* and *m* which may vary with different engine operating conditions.

Another well-established approach for estimating the mass fraction burned profile from the in-cylinder pressure and volume is developed by Rassweiler and Withrow (Rassweiler and Withrow, 1938). Assuming that the unburned gas filling the volume V_u ahead of the flame at any crank angle during combustion is polytropically compressed by the advancing flame front, the unburned gas volume at the time of spark $V_{u,\text{spark}}$ is

$$V_{u,\text{spark}} = V_u \left(\frac{p}{p_{\text{spark}}} \right)^{1/n}, \tag{4.23}$$

where the subscript *u* represents the unburned gas. Similarly, the burned gas behind the flame front filling the volume V_b is also polytropically compressed and the volume at the end of combustion $V_{b,\text{EOC}}$ is given by

$$V_{b,\text{EOC}} = V_b \left(\frac{p}{p_{\text{EOC}}} \right)^{1/n}, \tag{4.24}$$

with the subscript *b* designating the burned gas. The method assumes proportionality to the fractional pressure rise due to combustion from spark timing. MFB is then calculated by

$$\text{MFB}\ (j) = 1 - \frac{V_{u,\text{spark}}(j)}{V_{\text{spark}}} = \frac{V_{b,\text{EOC}}(j)}{V_{\text{EOC}}}. \tag{4.25}$$

Since the total cylinder volume $V = V_u + V_b$, Eq. (4.25) is rearranged as

$$\text{MFB}\ (j) = \frac{p_j^{1/n} V_j - p_{\text{spark}}^{1/n} V_{\text{spark}}}{p_{\text{EOC}}^{1/n} V_{\text{EOC}} - p_{\text{spark}}^{1/n} V_{\text{spark}}} . \tag{4.26}$$

Even though it contains several approximations, this approach to determine MFB is widely used and exhibits a good accuracy and consistency. As MFB is determined directly from in-cylinder pressure, the effect of in-cylinder heat transfer should be embedded in the calculation. However, the impact of heat transfer is reflected only by a constant *n* in Eqs. (4.23) and (4.24). In reality, the polytropic coefficient is a variable during combustion and different for compression and expansion, hence selecting an appropriate value for *n* is the major difficulty in applying this procedure.

In the present study, a modified expression similar to Rassweiler-Withrow (R-W) algorithm is applied, where MFB is determined by a normalized summation of the combustion pressure rise defined as (Rupal, 2003)

$$\text{MFB}\ (j) = \frac{\sum_{spark}^{j} \Delta p_j}{\sum_{spark}^{EOC} \Delta p} . \tag{4.27}$$

The combustion pressure rise is calculated based on the variable *n* from the time of spark to EOC, which exhibits more reasonable MFB curve than R-W algorithm. Therefore, the mass fraction burned calculation from Eq. (4.27) is reliable under a wide variety of operating conditions.

4.6 In-cylinder heat release analysis

The heat release analysis in terms of in-cylinder pressure has long been used to examine combustion and heat transfer in SI engines through a heat release approach

based on the first law of thermodynamics. The approach is divided into one-zone and two-zone models (Heywood, 1988 and Stone, 1999). One-zone model assumes a uniform and homogeneous mixture for cylinder contents during valve closed period (IVC – EVO). A major advantage of this model is that the pressure changes can be directly related to the amount of fuel chemical energy released by combustion, while retaining the simplicity of treating cylinder contents as a single zone. Two-zone model assumes that the cylinder contents consist of burned and unburned zones. Heat release is analyzed by applying the mass and energy conservation principles onto burned and unburned zones, respectively. Hence, MFB is determined and thermodynamic properties of each zone can be quantified. In the present study, one-zone model is applied for heat release analysis since MFB curve has already been determined (recall Section 4.5).

First law of thermodynamics may be written for the control volume (CV) consisting of the contents in a cylinder shown in Fig. 4.2 as

$$\frac{dE}{dt} = \dot{Q} - \dot{W} + \sum_i \dot{m}_i h_i, \tag{4.28}$$

where $\dot{Q}$ is the heat-transfer rate across the surface (CS) into the CV, $\dot{W}$ is the rate of work done by the CV, $\dot{m}_i$ is the mass flow rate into the CV at location *i* (flow out of the system is negative), h_i is the corresponding enthalpy of flux *i* entering or leaving the CV, and E is the energy of the contents inside the CV. For a closed valve period, Eq. (4.28) becomes

$$\frac{dU_S}{dt} = \dot{Q} - p\frac{dV}{dt} - \sum \dot{m}_{\text{crevice}} h \ , \tag{4.29}$$

where U_S and $\sum d\dot{m}_{\text{crevice}}\, h$ represent the internal energy of the cylinder contents and enthalpy loss due to flow of the in-cylinder mass into and out of the crevice volume (crevice effect). The heat transfer rate $\dot{Q}$ is equivalent to the difference between the rate of heat release from combustion $\dot{Q}_{hr}$ (into the CV) and heat transfer from the cylinder (out of the CV) $\dot{Q}_{ht}$, expressed as

$$\dot{Q} = \dot{Q}_{hr} - \dot{Q}_{ht} \ . \tag{4.30}$$

Combining Eqs. (4.29) and (4.30) yields

$$\dot{Q}_{hr} = \frac{dU_S}{dt} + p\frac{dV}{dt} + \dot{Q}_{ht} + \sum \dot{m}_{\text{crevice}}\, h^o \ . \tag{4.31}$$

Multiplying both sides of Eq. (4.31) by *dt* over IVC – IVO for a particular engine cycle, Eq. (4.31) becomes

$$dQ_{hr} = dU_S + p\,dV + dQ_{ht} + \sum dm_{\text{crevice}}\, h^o \ . \tag{4.32}$$

Regarding the cylinder contents as perfect gas, the differential change of the sensible internal energy dU_S could be expressed as

$$dU_S = m_c du(T) + u(T)\, dm_c, \quad u(T) = c_{\text{v}} dT = \frac{R}{\gamma - 1} dT, \tag{4.33}$$

with m_c, u, c_{v}, T, and R representing trapped mass in the cylinder, specific internal energy, specific heat at constant volume, in-cylinder temperature, and gas constant, respectively. In addition, γ is the specific heat ratio empirically given by (Brunt *et al*., 1998)

$$\gamma = 1.338 - 6.0\times10^{-5} T + 10^{-8} T^2 - 0.01, \tag{4.34}$$

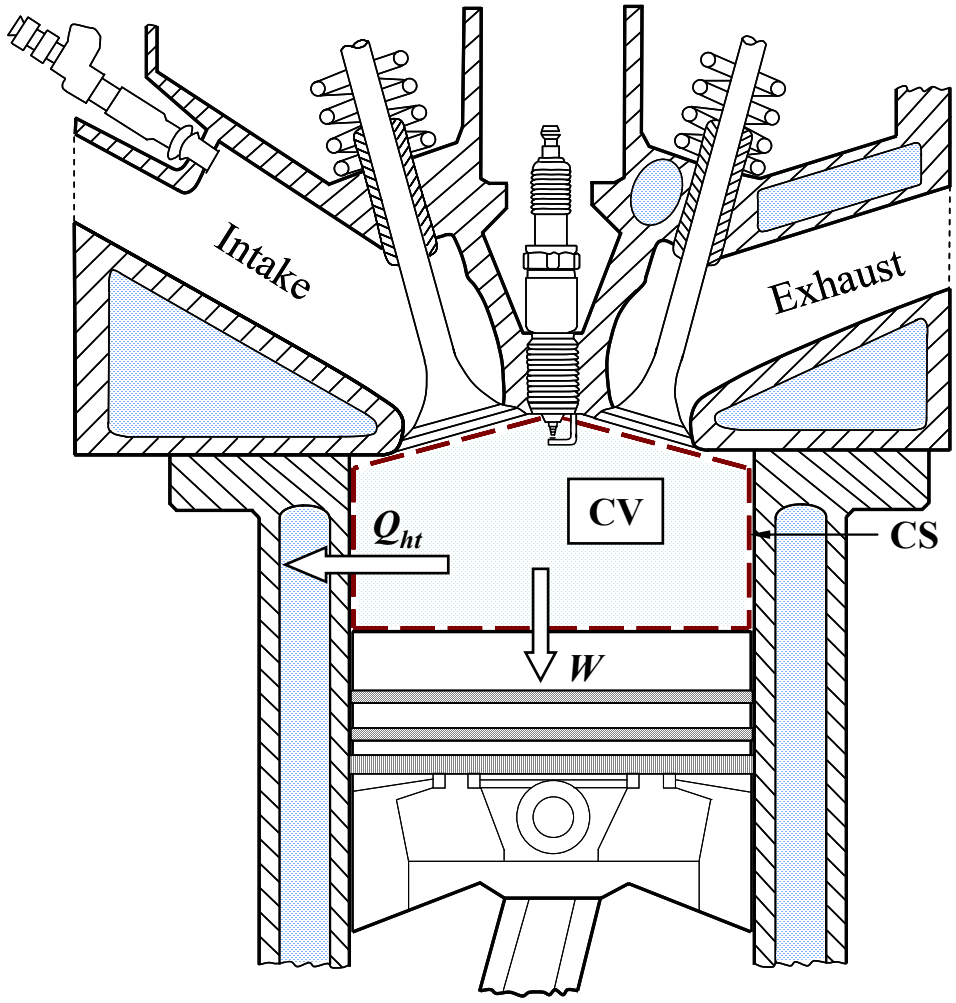

Figure 4.2. IC engine system used for thermodynamic analysis of combustion.
(CV is specified by dark red dash lines)

for stoichiometric air-fuel mixture. For EGR-diluted mixtures, Eq. (4.34) is still applied here to estimate γ because of the limited relevant literature.

In the present analysis, crevice volume is modeled as a single aggregate zone with a mass balance given as

$$dm_c = -dm_{\text{crevice}} \ , \tag{4.35}$$

with m_{crevice} being the mass in the crevice volume. Combined with Eqs. (4.33) - (4.35), Eq. (4.32) becomes

$$\begin{aligned} dQ_{hr} &= d\left(m_c u\right) + pdV + dQ_{ht} + h'dm_{\text{crevice}} \\ &= \frac{m_c R}{\gamma - 1} dT + pdV + dQ_{ht} + \left(h' - u\right) dm_{\text{crevice}}, \end{aligned} \tag{4.36}$$

where:

$dm_{\text{crevice}} > 0$ when flow is out of the cylinder into the crevice volume;
$dm_{\text{crevice}} < 0$ when flow is from crevice to cylinder;
primed quantities (') correspond to the condition in crevice volume.

In-cylinder temperature T could be calculated from ideal gas law during the valve closed period through

$$pV = m_c RT \ \Rightarrow \ dT = \frac{pdV}{m_c R} + \frac{Vdp}{m_c R} - \frac{pV}{m_c^2 R} dm_c \ . \tag{4.37}$$

Combining Eqs. (4.36) and Eq. (4.37) yields

$$dQ_{hr} = dQ_{app} + dQ_{ht} + dQ_{cr} \ , \tag{4.38}$$

where

$$dQ_{app} = \frac{\gamma}{\gamma - 1} pdV + \frac{1}{\gamma - 1} Vdp, \tag{4.39}$$

$$dQ_{cr} = \left(h' - u + c_{\text{v}} T\right) dm_{\text{crevice}}, \tag{4.40}$$

with Q_{app} and Q_{cr} representing the apparent heat release and heat loss due to crevice effect, respectively. The differential change of Q_{cr} can be further rearranged as

$$\begin{aligned} dQ_{cr} &= \left(h' - u + c_v T\right) dm_{\text{crevice}} = \left[u' + (pv)' - u + c_v T\right] dm_{\text{crevice}} \\ &= \left[u' - u + R\left(T' + \frac{T}{\gamma - 1}\right)\right] dm_{\text{crevice}}. \end{aligned} \tag{4.41}$$

The specific internal energy u may be written by

$$u = c_v T = \frac{R}{\gamma - 1} T.$$

Hence, the difference $u' - u$ may be expressed as

$$u' - u = \int_T^{T'} c_v dT = C_u R \ln \frac{\gamma' - 1}{\gamma - 1}, \tag{4.42}$$

where $C_u = 2$ is assumed in the current analysis (Gatowski, *et al.*, 1984). Substituting Eqs. (4.41) and (4.42) into (4.38) gives

$$\begin{aligned} dQ_{hr} &= dQ_{app} + dQ_{ht} + dQ_{cr} \\ &= \frac{\gamma}{\gamma - 1} p dV + \frac{1}{\gamma - 1} V dp + dQ_{ht} + R\left(T' + \frac{T}{\gamma - 1} + C_u \ln \frac{\gamma' - 1}{\gamma - 1}\right) dm_{\text{crevice}}. \end{aligned} \tag{4.43}$$

As indicated earlier, crevice volume is considered as a single aggregate zone where the gas pressure is assumed identical to the cylinder pressure. Crevice gas temperature, on the other hand, may simply be assumed identical to the combustion chamber wall temperature T_{wall}. A 50 K wall temperature change shows a 1% effect on the heat release (Gatowski, *et al.*, 1984). The ratio of the crevice volume V_{cr} to the clearance volume V_c usually ranges within 1-2% (Heywood, 1988) and use of 1% and 2% V_c as the crevice volume brings about 2% difference in the results. In the present analysis, V_{cr} and T_{wall} are

assumed to be 1.5% of V_c and 400 K, respectively (Gatowski, *et al.*, 1984). Hence, the mass in the crevice volume is determined by

$$m_{\text{crevice}} = pV_{cr} / RT_{wall}\,, \tag{4.44}$$

and

$$dm_{\text{crevice}} = \left(V_{cr} / RT_{wall}\right) dp. \tag{4.45}$$

Eventually, Eq. (4.43) becomes

$$\begin{aligned} dQ_{hr} &= dQ_{app} + dQ_{ht} + dQ_{cr} \\ &= \frac{\gamma}{\gamma - 1} pdV + \frac{1}{\gamma - 1} Vdp + dQ_{ht} + \left[\frac{V}{\gamma - 1} + \frac{V_{cr}}{T_{wall}} \left(T' + \frac{T}{\gamma - 1} + C_u \ln \frac{\gamma' - 1}{\gamma - 1} \right) \right] dp. \end{aligned} \tag{4.46}$$

Equation (4.46) represents energy conservation applied to the entire cylinder contents from IVC to EVO. The differential chemical energy release dQ_{hr} can be written as

$$dQ_{hr} = Q_{LHV}(-dm_{fuel}), \tag{4.47}$$

where m_{fuel} and Q_{LHV} represent trapped fuel in the cylinder and lower heating value of the fuel (44 MJ/kg). Since the trapped mass in the cylinder m_c is assumed fixed for the valve closed period,

$$m_c = m_u + m_b = \text{constant} \quad \Rightarrow \quad dm_c = dm_u + dm_b = 0\,, \tag{4.48}$$

where m_c, m_u, and m_b are total trapped mass, unburned and burned mass in the cylinder. With calculated mass fraction burned x_b (recall Section 4.5.3), the change of burned mass in the cylinder is

$$dm_b = m_c \; dx_b\,. \tag{4.49}$$

The unburned mass in the cylinder consists of air, fuel, and recirculated exhaust gas:

$$\begin{aligned} \mathrm{EGR}\% &= \frac{m_{EGR}}{m_{EGR}+m_{air}}, \\ m_u &= m_{fuel}+m_{air}+m_{EGR} = m_{fuel}\left(1+\frac{\mathrm{AFR}}{1-\mathrm{EGR}\%}\right), \end{aligned} \tag{4.50}$$

where m_{air} and m_{EGR} designate the mass of fresh air and recycled burned gas in the cylinder, respectively, with AFR being the air fuel ratio. Combining Eqs. (4.48) – (4.50) yields

$$\begin{aligned} dm_u &= \left(1+\frac{AFR}{1-EGR\%}\right)dm_{fuel} = -dm_b = -m_c\ dx_b\,, \\ dm_{fuel} &= -\frac{m_c\ dx_b}{1+\dfrac{AFR}{1-EGR\%}} = -\frac{m_c\left(1-EGR\%\right)dx_b}{1-EGR\%+AFR}. \end{aligned} \tag{4.51}$$

Substituting Eq. (4.51) into (4.47) gives

$$dQ_{hr} = \frac{m_c\left(1-EGR\%\right)Q_{LHV}}{1-EGR\%+AFR}dx_b. \tag{4.52}$$

Finally, the instantaneous and cumulative apparent heat release Q_{app}, in-cylinder heat transfer Q_{ht}, and heat loss due to crevice effect Q_{cr} can then be determined from Eqs. (4.39), (4.46), and (4.52).

4.7 Exhaust runner gas temperature

Exhaust runner gas temperature varies substantially during the exhaust process and plays an important role in exhaust gas oxidation and emissions. In the present study, time-averaged exhaust gas temperature (EGT) in runners 1 and 4 are measured under different operating conditions, EGR dilution levels, charge motion, and spark timing.

4.8 Engine-out emissions and EGR ratio

The pollutant emissions from the engine-out exhaust gas include NO_x, HC, and CO. NO_x mainly consists of nitric oxide (NO) which forms throughout the high-temperature burned gas behind the flame through chemical reactions involving nitrogen and oxygen molecules. The formation rate of NO is approximated by (Heywood, 1988)

$$\frac{d[\mathrm{NO}]}{dt} = \frac{6\times10^{16}}{T^{1/2}} \exp\left(-\frac{69090}{T}\right)[\mathrm{O_2}]_e^{1/2}[\mathrm{N_2}]_e \tag{4.53}$$

based on the extended Zeldovich mechanism. Hence, high flame temperature and oxygen mole fraction result in high NO formation rate. HC emission usually comes from the crevice volume, oil layers, deposits on the combustion chamber walls, and incomplete combustion. CO normally forms during the combustion process mainly within the local fuel rich zone. In the current analysis, mole fraction of five major exhaust gas species (NO_x, HC, CO, CO_2, and O_2) is measured in both exhaust manifold and a combination of intake runners 1 and 4 under different operating condition. The engine-out brake specific emissions for each species are determined by

$$\text{Brake specific emissions}_i\ [\mathrm{g/kW\cdot hr}] = \frac{3600 y_i \left(\dot{m}_{air}[\mathrm{g/s}] + \dot{m}_{fuel}[\mathrm{g/s}]\right)}{P_b[\mathrm{kW}]}, \tag{4.54}$$

where y_i and $\dot{m}_{air}$ designate mole fraction of the species i and air mass flow rate, respectively.

To determine the fraction of recirculated exhaust gas, EGR ratio is calculated based on the mole fraction of CO_2 $\left(y_{CO_2}\right)$ measured from both exhaust and intake gas samples (Desantes *et al.*, 2000 and Ozkan *et al.*, 2005) as

$$\text{EGR}\% = \frac{m_{EGR}}{m_{EGR} + m_{air}} \times 100 = \frac{y_{\text{CO}_2,\text{intake}} - y_{\text{CO}_2,\text{ambient}}}{y_{\text{CO}_2,\text{exhaust}}} \times 100 \ , \tag{4.55}$$

where the CO_2 mole fraction of the ambient air, $y_{CO_2,\text{ambient}}$, is measured to be a constant of 0.06%.

4.9 Data analysis in flow experiments

The objective of flow experiment is to characterize the in-cylinder tumble vortex during intake process and then correlate with engine experiments to assess the impact of such motion on combustion characteristics. A method has been developed to investigate the effect of in-cylinder tumble motion under steady conditions in a flow laboratory, by using the same cylinder head and intake manifold from the engine experiments. In order to make the in-cylinder flow characteristics comparable to the engine experiments, calculated peak air mass flow rate in the engine experiment is matched at the maximum intake valve lift in the flow laboratory, rather than imposing a fixed bore pressure drop. A refined tumblemeter is mounted under the cylinder head to measure the compressive load produced by the tumble vortex, allowing for the calculation of angular momentum of the incoming air, hence the tumble number and the tumble ratio. Eventually, a correlation between engine and flow experiments is observed to help quantify the impact of tumble motion on combustion and cyclic variation. In this section, a detailed flow experimental procedure is discussed first, followed by an introduction of the data reduction approach.

4.9.1 Flow experimental procedure

The introduction of blockage creates a significant flow loss during the intake process with the flow loss coefficient across the blockage given by

$$K_{12,f} = \frac{P_{1,f} - P_{2,f}}{\left(\frac{1}{2}\rho_{\infty} V_1^2\right)_f}, \tag{4.56}$$

where $V_1 = \dot{Q}_f \big/ A_{runner}$ is the runner velocity upstream of the blockage with A_{runner} being the cross-sectional area of the intake runner 4; and the air density ρ is estimated from the ideal gas law by using the ambient conditions. The subscript f implies parameters measured and calculated in the flow experiment, and the subscript e will represent those obtained in the engine experiments. This designation will be used in the following analysis and pertinent figures. In flow experiment, $K_{12,f}$ is determined from Eq. (4.56) with measured $\Delta P_{\infty 1}$, $\Delta P_{\infty 2}$, and $\dot{Q}_f$.

Crank-angle-resolved intake runner pressures upstream and downstream of the blockage are measured in engine experiments at MBT timing under two part-load conditions: WP and IP. Instantaneous air mass flow rate $\dot{m}_{air,e}$ in the intake runner 4 during the intake-valve-open period (IVOP, between IVO and IVC) can then be estimated with calculated $K_{12,f}$ as

$$\dot{m}_{air,e}(\theta) = \rho_{1,e}(\theta) V_{1,e}(\theta) A_{runner}, \tag{4.57}$$

where

$$V_{1,e}(\theta) = \pm \sqrt{\frac{2\left|P_{1,e}(\theta) - P_{2,e}(\theta)\right|}{K_{12,f}\rho_{1,e}(\theta)}}$$

and $\rho_{1,e}$ is the air density upstream of the blockage calculated by the ideal gas law using the measured $P_{1,e}$ and intake air temperature in engine lab. At the beginning and end of

the intake process, back flow usually occurs in the intake runner leading to $P_{1,e} < P_{2,e}$ which is captured by the minus sign in $V_{1,e}$.

For the runner without blockage, a different approach is used to estimate $\dot{m}_{air,e}$. In this case, another flow loss coefficient is calculated from

$$K_{\infty 1,e}(\theta) = \frac{P_{\infty,e} - P_{1,e}(\theta)}{\left[\frac{1}{2}\rho_{1,e}(\theta)V_{1,e}^2(\theta)\right]}, \tag{4.58}$$

with $P_{\infty,e}$ being the barometric pressure in engine lab. For blocked runner, the crank-angle-resolved $K_{\infty 1,e}$ can be calculated by Eq. (4.58) with measured $P_{\infty,e}$ and $P_{1,e}$ along with calculated $\rho_{1,e}$ and $V_{1,e}$. For unblocked runner, $V_{1,e}$ is obtained from Eq. (4.58) with the available $K_{\infty 1,e}$ for tumble and $\dot{m}_{air,e}$ is then computed from Eq. (4.57).

The enhanced in-cylinder turbulence for various intake ports is controlled by the intake flow characteristics during air induction process [Church and Farrell, 1998 and Justham *et al.*, 2006]. In the present work, the peak air mass flow rate $\dot{m}_{air,\max,e}$ is matched in flow experiments for each blockage-load combination instead of a constant bore pressure drop $\Delta P_{\infty 3}$ for all configurations. In the present approach, $\dot{m}_{air,\max,e}$ is first determined from estimated $\dot{m}_{air,e}$ in engine experiments and then matched at maximum intake valve lift, $L_{\mathrm{v,max}}$ = 0.325", in the flow laboratory by using the same blockage. At a given $\Delta P_{\infty 3}$ where $\dot{m}_{air,\max,e}$ is matched at $L_{\mathrm{v,max}}$ = 0.325", flow experiment is performed at each valve lift (over 0 – 0.1" in increments of 0.01" and over 0.1 – 0.325" in 0.05"), including measurements of $\dot{Q}$, $\Delta P_{\infty 1}$, $\Delta P_{\infty 2}$, and three vertical forces on the screen. Flow

parameters to quantify in-cylinder tumble vortex such as tumble number and tumble ratio are then calculated.

4.9.2 Discharge coefficient (C_D)

The impact of blockage on engine breathing is assessed through a discharge coefficient C_D that relates the actual mass flow rate $\dot{m}_{air,f}$ through the intake valve to the isentropic mass flow rate. In the present work, C_D is calculated between the upstream of the blockage and the cylinder bore (recall Fig. 3.6) defined as (Heywood, 1988 and Arcoumanis *et al.*, 1992):

$$C_D = \frac{\left(RT_0\right)^{1/2} \dot{m}_{air,f}}{A_{runner} P_{10}} \left(\frac{P_{10}}{P_3}\right)^{1/\gamma} \left\{ \frac{2\gamma}{\gamma - 1} \left[1 - \left(\frac{P_3}{P_{10}} \right)^{(\gamma-1)/\gamma} \right] \right\}^{-1/2}, \tag{4.59}$$

where P_3, T_0, and P_{10} represent bore pressure, ambient temperature, and stagnation (static + dynamic) pressure upstream of the blockage, respectively, and $\gamma = 1.4$ is the specific heat ratio for air.

4.9.3 Air mass flow per engine cycle

The air mass flow in an intake runner per engine cycle can be estimated from the engine experiment as

$$m_{air,e} = \frac{\dot{m}_{fuel} AFR \; T_e}{N_c}, \tag{4.60}$$

where $m_{air,e}$, $\dot{m}_{fuel}$, AFR, and T_e represent the air mass flow, fuel mass flow rate, air fuel ratio, and engine cycle period, respectively. Another means to determine the air mass

flow per cycle is to integrate the crank-angle-resolved $\dot{m}_{air,e}$, calculated by Eq. (4.57), over the IVOP as

$$m_{air,e,P} = \int_{\text{IVO}}^{\text{IVC}} \dot{m}_{air,e}\, dt, \tag{4.61}$$

with $m_{air,e,P}$ and dt being the air mass flow per engine cycle and differential time corresponding to a crank angle degree. In the present analysis, $m_{air,e}$ and $m_{air,e,P}$ are compared to evaluate the reliability of Eq. (4.57) in estimating $\dot{m}_{air,e}$.

4.9.4 Tumble number (TN)

To characterize tumble motion at each valve lift, the present work adopts a definition of tumble number (TN) similar to the AVL approach based on the ratio of angular speed (ω) of the in-cylinder tumble vortex to the corresponding engine speed (Xu, 2001)

$$\text{TN} = \frac{\omega_f}{\omega_e}. \tag{4.62}$$

In reality, the engine speed does not exist in flow experiment so that a correlation has to be sought to estimate ω_e. The mean piston speed

$$\overline{S}_p[\text{m/s}] = 2\omega_e\left[\text{rev/s}\right]\, S[\text{m}] \tag{4.63}$$

is used here. Assume mean axial velocity of the in-cylinder flow $\overline{U}_{ax}$ equal to $\overline{S}_p$ and then

$$\overline{U}_{ax} = \frac{\dot{m}_{air,f}}{\rho_{\infty,f} A} = \overline{S}_p = 2\omega_e S, \tag{4.64}$$

with $A = \pi B^2/4$ being the cylinder bore area. Therefore, the fictitious engine speed ω_e could be written as

$$\omega_e = \frac{2\ \dot{m}_{air,f}}{\pi\ \rho_{\infty,f} B^2 S}. \tag{4.65}$$

As introduced in Chapter 3, three vertical forces on the screen are measured in the flow experiment yielding the torque as

$$T = \frac{B}{2}\left[\left(F_2 + F_3\right)/2 - F_1\right], \tag{4.66}$$

with F_1, F_2, and F_3 designating the measured vertical loads at the corresponding locations (recall Fig. 3.8). Regarding tumble motion as a solid body rotation, the torque T is expressed as

$$\begin{aligned} T &= \frac{dG}{dt} = \frac{d\left(I_f \omega_f\right)}{dt} \\ &= \frac{d\left\{\frac{1}{2} m_{air,f}[\text{kg}]\left(B\ [\text{m}]/2\right)^2 2\pi\omega_f\left[\text{rev/s}\right]\right\}}{dt\ [\text{s}]} \\ &= \frac{1}{4}\dot{m}_{air,f}\pi B^2 \omega_f, \end{aligned} \tag{4.67}$$

where G and I_f denote the angular momentum and inertia of the tumble vortex, respectively. Equation (4.67) is then rearranged as

$$\omega_f = \frac{4\ T}{\pi\ \dot{m}_{air,f} B^2}. \tag{4.68}$$

Combining Eqs. (4.65) and (4.68), TN can then be calculated by

$$\mathrm{TN} = \frac{\omega_f}{\omega_e} = \frac{2\ T \rho_{\infty,f}\ S}{\dot{m}_{air,f}^2}. \tag{4.69}$$

4.9.5 Tumble ratio (TR)

The rate of angular momentum of the tumble vortex (or torque) can be written as

$$T = \frac{dG}{dt} \Rightarrow G = \int_{t_1}^{t_2} T\ dt = \int_{\theta_1}^{\theta_2} \frac{T\ [\mathrm{N \cdot m}]}{\omega_e\ [1/\mathrm{s}]} d\theta\,, \tag{4.70}$$

with θ_1 and θ_2 representing IVO and IVC timings, respectively. Combining Eqs. (4.69) and (4.70), the angular momentum at the end of induction G_0 becomes (Arcoumanis *et al.*, 1992)

$$G_0 = \int_{\theta_1}^{\theta_2} \frac{\mathrm{TN}\ \dot{m}_{air,f}^2}{2\ \rho_{\infty,f} S \omega_e}\ d\theta. \tag{4.71}$$

Since $\dot{m}_{air,f} = C_D \rho_{\infty,f} A_{runner} V_0$, with V_0 being the isentropic velocity, G_0 is rearranged as

$$G_0 = \int_{\theta 1}^{\theta 2} \frac{\mathrm{TN}\ {C_D}^2 \rho^2 A_{runner}^2 {V_0}^2}{2\rho S \omega_e}\ d\theta = \frac{\rho A_{runner}^2 {V_0}^2}{2 S \omega_e} \int_{\theta 1}^{\theta 2} \mathrm{TN}\ {C_D}^2 d\theta. \tag{4.72}$$

Substituting Eq. (4.67) into Eq. (4.70) for a solid body rotation, the angular momentum at the end of induction G_{0s} is written as

$$G_{0s} = \frac{m_{air}[\mathrm{kg}]\ B[m]^2 \omega_f\ [1/\mathrm{s}]}{8} = \eta_{\mathrm{v}} \frac{\pi B^2 S \rho}{4} \frac{B^2 \omega_f}{8}, \tag{4.73}$$

where η_{v} is the volumetric efficiency. For steady flow test, η_{v} = 1 is assumed (Arcoumanis *et al.*, 1992). Therefore,

$$G_{0s} = \frac{\pi\ \rho_{\infty,f} B^4 S \omega_f}{32} \tag{4.74}$$

and

$$\rho V_0 A_{runner} \int_{t_1}^{t_2} C_D dt = m_{air} \;\Rightarrow\; \rho V_0 A_{runner} \int_{\theta_1}^{\theta_2} \frac{C_D}{\omega_e} d\theta = \frac{\pi B^2 S \rho}{4}. \tag{4.75}$$

Hence, the isentropic velocity V_0 could be rearranged as

$$V_0 = \frac{\pi B^2 S \omega_e}{4 A_{runner} \int_{\theta_1}^{\theta_2} C_D d\theta} \tag{4.76}$$

Substituting Eq. (4.76) into Eq. (4.72), G_0 is rearranged to

$$G_0 = \frac{\pi^2 \rho B^4 S \omega_e}{32} \frac{\int_{\theta_1}^{\theta_2} \mathrm{TN}\, C_D^2 d\theta}{\left(\int_{\theta_1}^{\theta_2} C_D d\theta \right)^2}. \tag{4.77}$$

Let $G_0 = G_{0s}$, then

$$G_0 = G_{0s} \;\Rightarrow\; \frac{\pi^2 \rho_{\infty,f} B^4 S \omega_e}{32} \frac{\int_{\theta_1}^{\theta_2} \mathrm{TN}\, C_D^2 \, d\theta}{\left(\int_{\theta_1}^{\theta_2} C_D \, d\theta \right)^2} = \frac{\pi \, \rho_{\infty,f} B^4 S \omega_f}{32}. \tag{4.78}$$

Finally, Tumble Ratio is defined as the angular velocity of the cylinder charge motion divided by the crankshaft angular rotational speed over the IVOP:

$$TR = \frac{\omega_f}{\omega_e} = \pi \frac{\int_{\theta_1}^{\theta_2} \mathrm{TN}\, C_D^2 d\theta}{\left(\int_{\theta_1}^{\theta_2} C_D d\theta \right)^2} \approx \pi \frac{\sum_{i=1}^{N} \mathrm{TN}_i \, C_{D,i}^2}{\left(\sum_{i=1}^{N} C_{D,i} \right)^2}, \tag{4.79}$$

where N is the total measurement points from 0 – 0.325" intake valve lift in flow experiments.

CHAPTER 5

ENGINE RESULTS and DISCUSSION

Dynamometer experiments have been conducted under five part-load operating conditions (recall Section 1.2) with stoichiometric and EGR diluted mixtures. Comparisons are provided between blocked and unblocked intake runners. A detailed test matrix is given in Table 3.2. Each experiment has been conducted twice to illustrate the repeatability. For a specified operating condition, the MBT timing corresponding to the minimum BSFC is identified for each blockage-EGR% combination by spanning a spark range of about 16˚ with 9 spark timings. The air and fuel mixture is maintained at stoichiometric AFR of 14.50 for all experiments. The present chapter will first introduce the engine experimental procedure, then compare the engine results between unblocked and blocked runners, and examine the effect of blockages on fuel consumption, combustion, in-cylinder heat release, and engine-out emissions.

5.1 Experimental Procedure

For each configuration, experiments begin with no dilution and spark is swept starting from the most retarded point. Then, the recycled burned gas is introduced into the cylinder by opening the EGR control valve. With an expected increment of 3 - 5% EGR

ratio under different conditions (see Table 3.2), $y_{CO_2,intake}$ can be estimated in advance from Eq. (4.55) using the constant $y_{CO_2,ambient}$ and $y_{CO_2,exhaust}$ from the previous test. The solenoid valve is first switched for measurement of the intake gas samples. When the engine reaches steady state condition at the most retarded spark timing, the EGR valve is adjusted to match the estimated $y_{CO_2,intake}$ and the spark sweep is completed at the given position of the EGR valve. Next, the experiment is repeated starting from the most advanced ignition point with the solenoid valve now switched to measure the exhaust gas samples. Finally, the actual EGR ratio is determined from measured $y_{CO_2,intake}$ and $y_{CO_2,exhaust}$ at each spark point by Eq. (4.55). Compared to the expected increment, the exact EGR ratio varies by about ±1% (Table 3.2) due to slight variation of $y_{CO_2,exhaust}$. When the in-cylinder mixture approaches the dilution limit, the engine cannot be operated normally beyond a certain ignition timing. Hence a full spark range can not be retained and the expected increment of EGR is then reduced to about 2%.

5.2 EGR ratio and Fuel economy

Figures 5.1 – 5.5 depict the EGR ratio (from Eq. 4.55) as a function of spark timing for unblocked and blocked runners under WP, IP, WP_GM, WP_FEV, and HP, respectively. For WP, four configurations (fully open, tumble, swirl, and swumble) are compared. Whereas, only unblocked and tumble cases are included under the other four operating conditions. The MBT timings are indicated by circles with SA denoting the spark advance; the same designation will also be used in the following pertinent figures. At a given dilution level, the actual EGR ratio varies moderately over the spark range due

to slight variation of $y_{CO_2,intake}$ and $y_{CO_2,exhaust}$ at different ignition timing. Under a specific engine condition (except HP because of incomplete experiments due to knock), the maximum EGR rate for charge motion is higher than that of fully open runner. Figures 5.6 – 5.10 exhibit the corresponding variation of BSFC with spark timing. The MBT is advanced with dilution for all configurations because of reduced burn rate and increased burn duration (Heywood, 1988). The minimum in the BSFC variation is well established for both blocked and unblocked runners in Figs. 5.6, 5.8, and 5.9 for WP, WP_GM, and WP_FEV, respectively. Whereas, this trend doesn't hold explicitly for the lightest and highest engine loads of IP and HP (Figs. 5.7 and 5.10). Light load operating condition would suggest an unstable combustion and substantial cyclic variation, making the determination of MBT at IP difficult. The combustion deteriorates quickly with the introduction of EGR at IP, hence an increased BSFC shown in Fig. 5.7, particularly for unrestricted runner. As illustrated in Fig. 5.10, experiments can not be performed at further advanced spark timing under HP (beyond 38˚ and 16˚ BTDC for fully open and tumble 20% open, respectively) due to the occurrence of engine knock and therefore the MBT timing cannot be easily determined. For these reasons, the experimental results for IP and HP will not be discussed any further in this chapter. For the other three operating conditions WP, WP_GM, and WP_FEV, BSFC decreases with EGR mainly due to reduced pumping losses under part-load engine conditions which will be discussed in Section 5.4. As the mixture is diluted further at higher EGR ratios, the cyclic combustion variation increases. Eventually, partial burn and misfiring cycles increase substantially resulting in significantly deteriorated combustion, hence increasing BSFC. The experiment is terminated when BSFC starts to increase at MBT. The dramatic extension

of EGR dilution for 20% tumble blockage is clearly shown in Figs. 5.6, 5.8, and 5.9 with the maximum EGR ratio being 22%, 20%, and 16% for fully open and 28%, 30%, and 26% for tumble under WP, WP_GM, and WP_FEV, respectively. This chapter will compare and analyze the results between unblocked and blocked runners at WP only. The corresponding comparison between fully open and 20%-open tumble cases for WP_GM and WP_FEV are deferred to Appendix B.

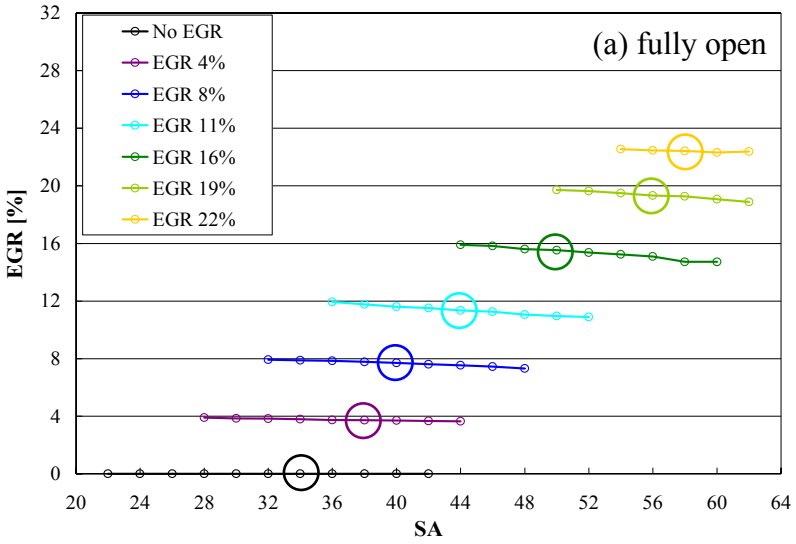

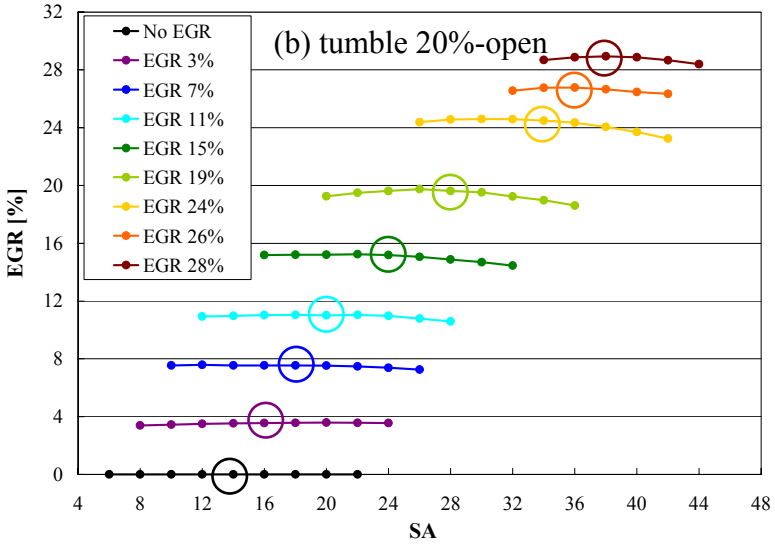

Figure 5.1. Variation of EGR ratio at WP. (Continued)

Figure 5.1: Continued.

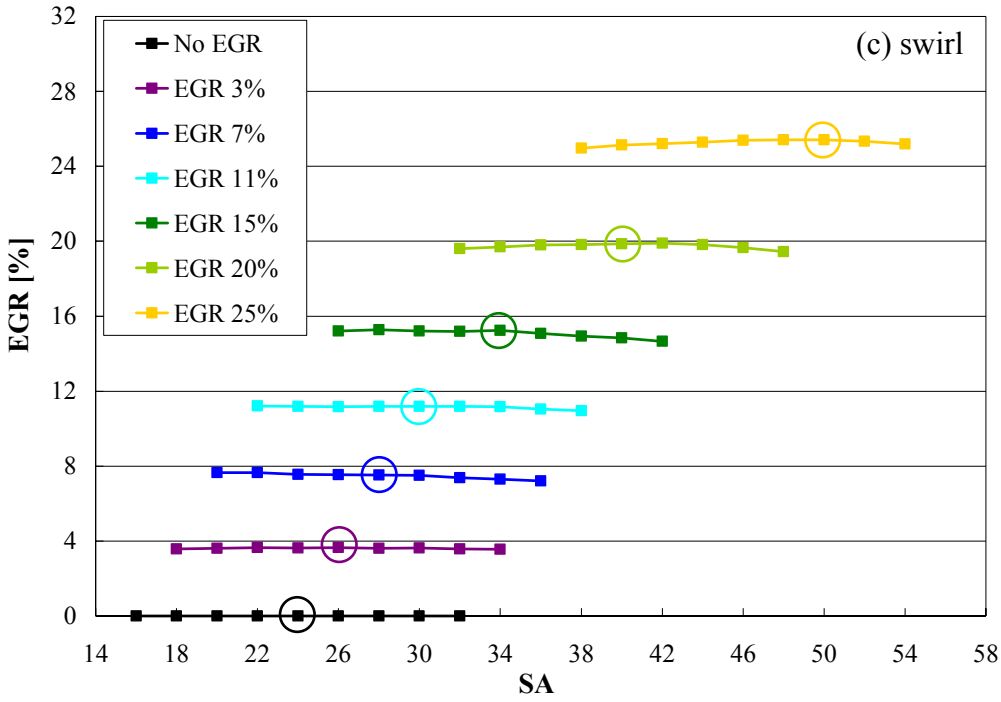

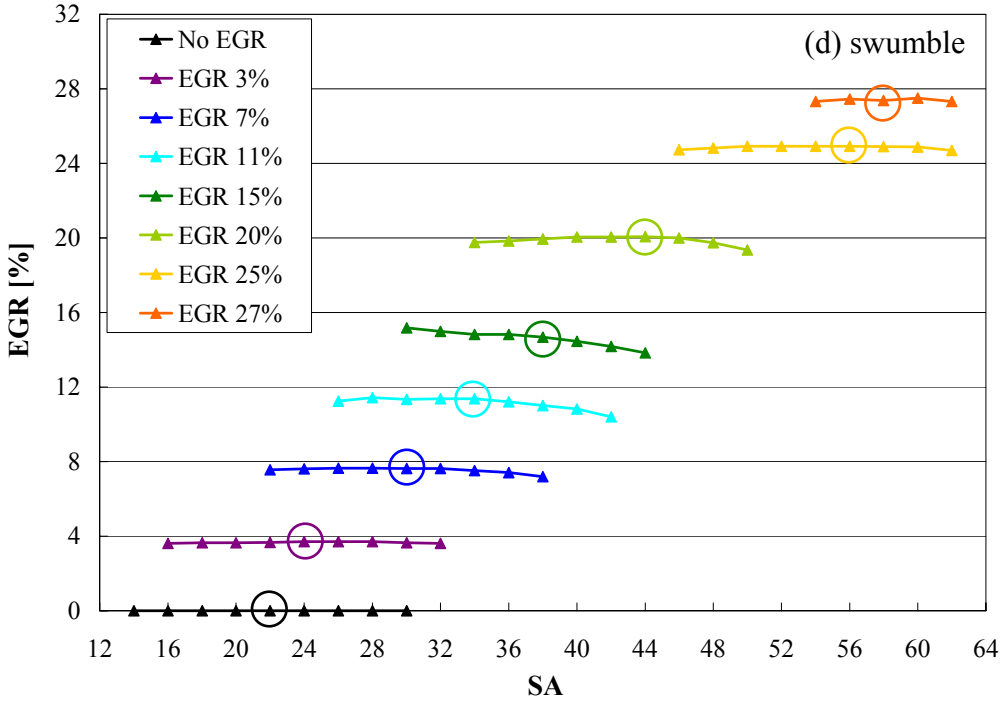

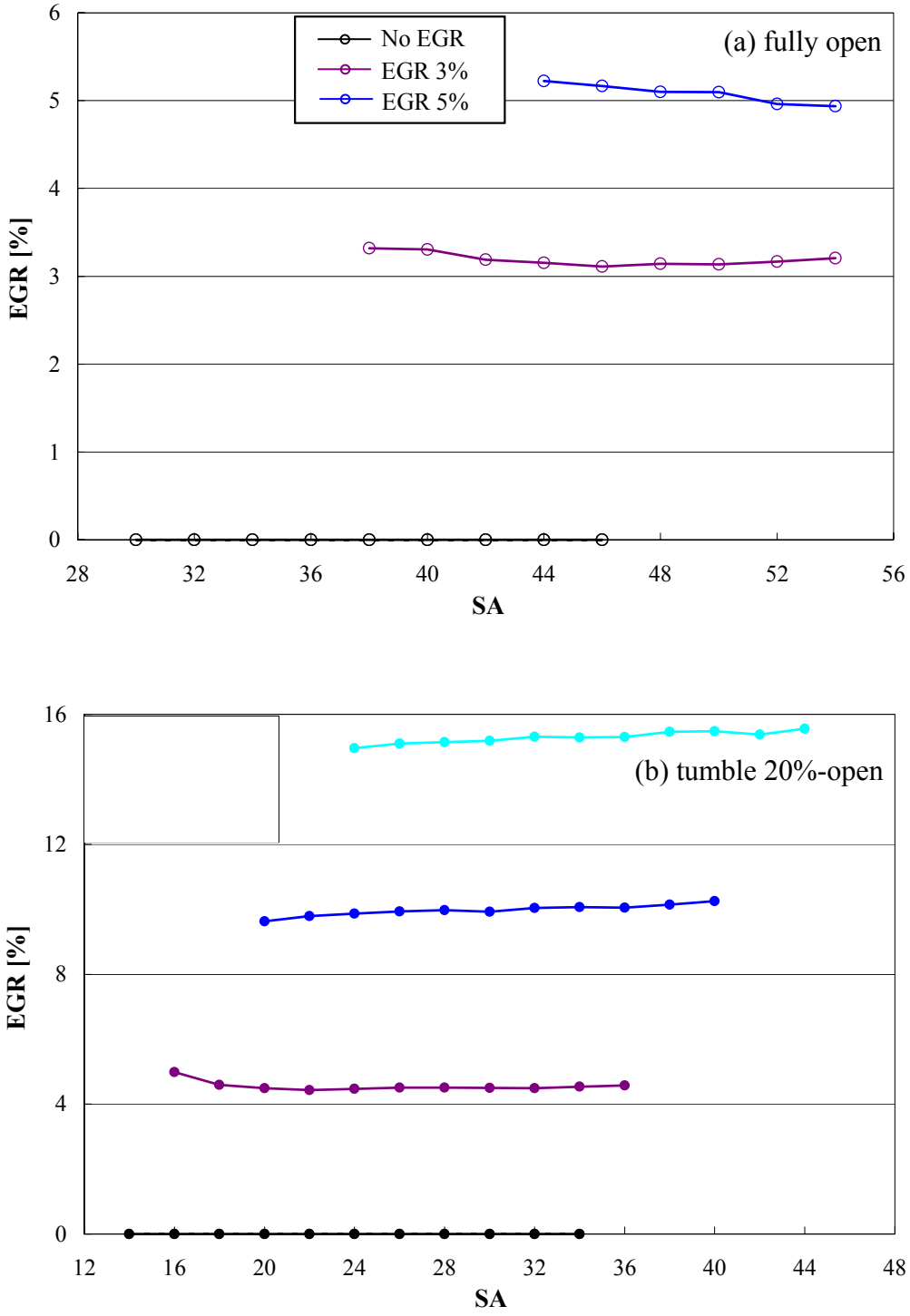

Figure 5.2. Variation of EGR ratio at IP.

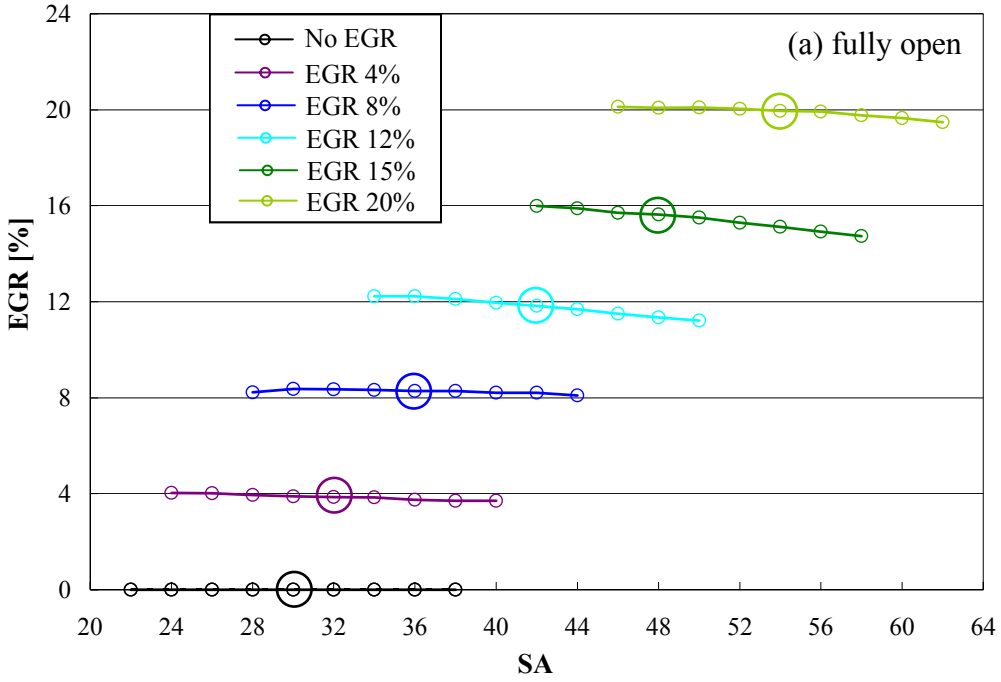

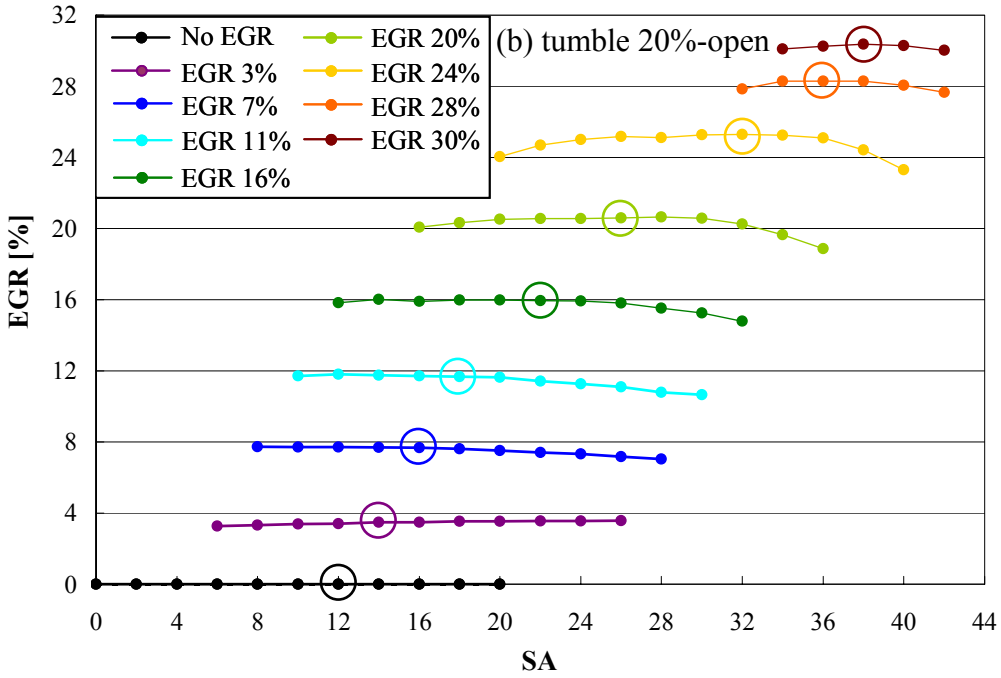

Figure 5.3. Variation of EGR ratio at WP_GM.

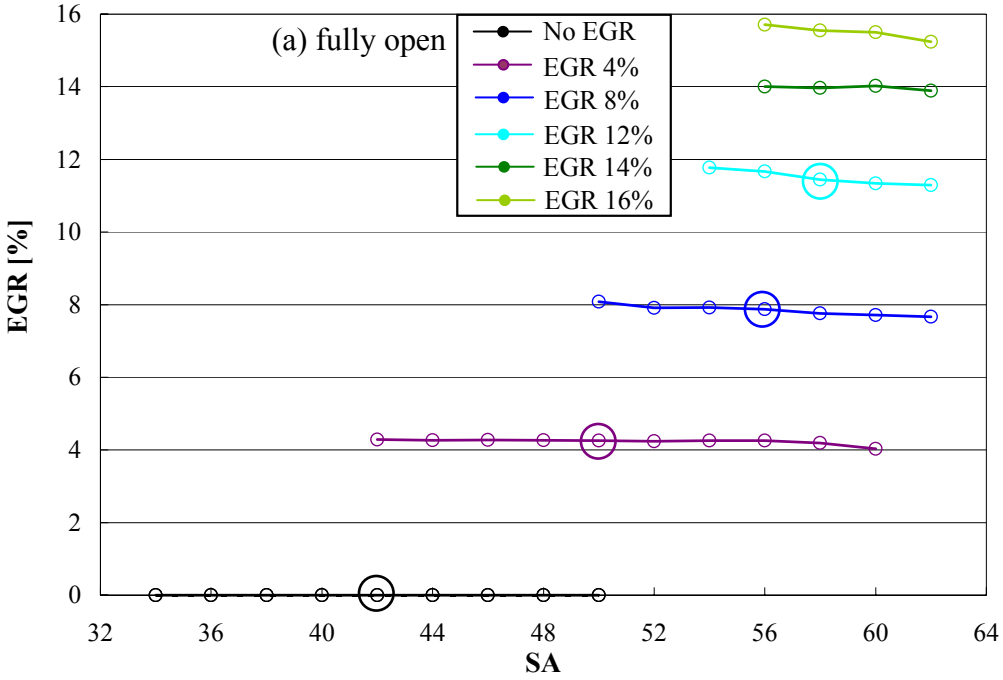

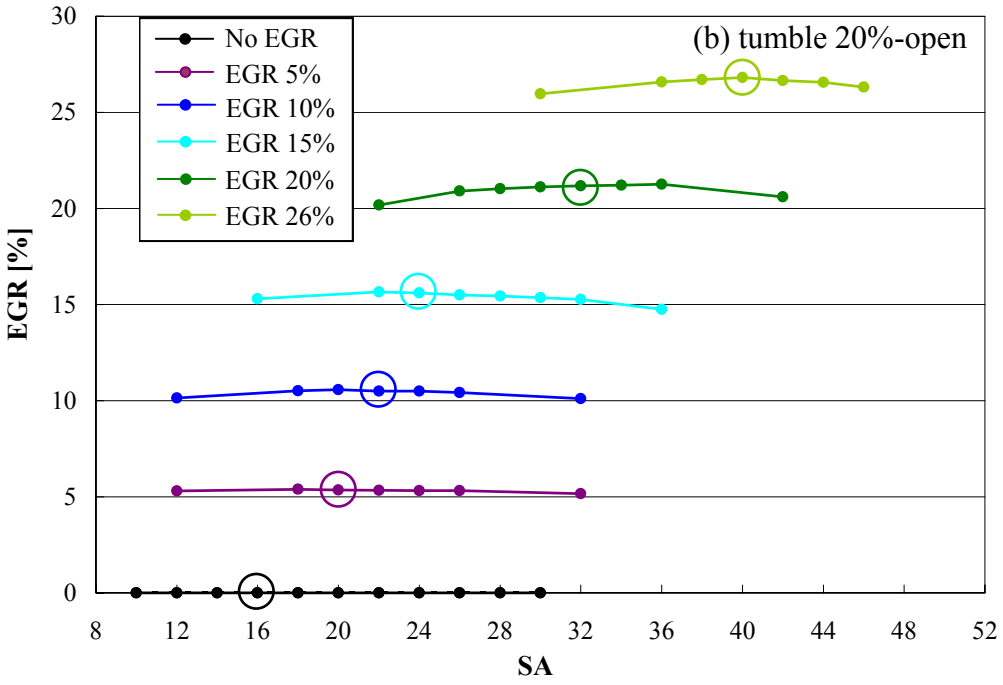

Figure 5.4. Variation of EGR ratio at WP_FEV.

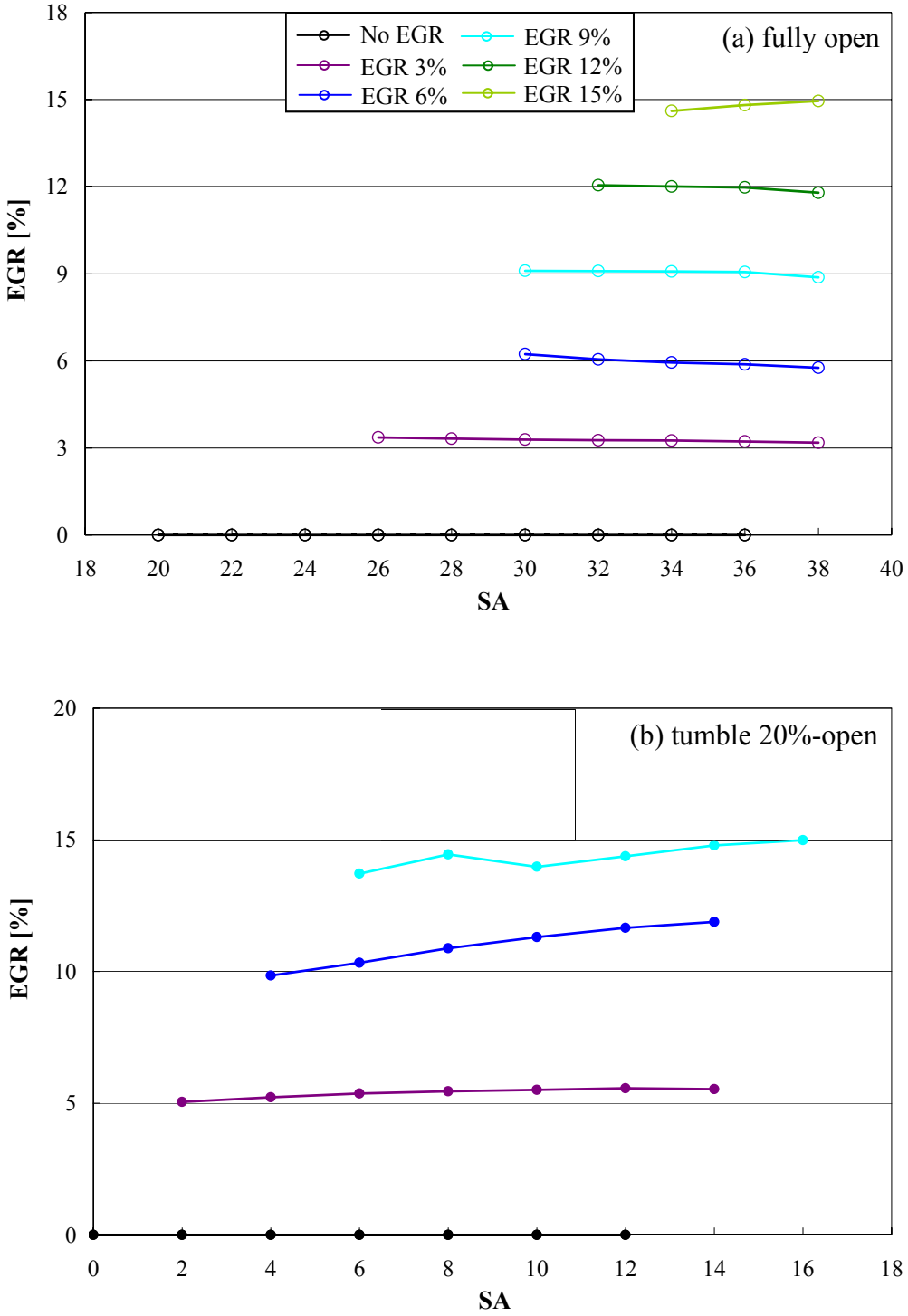

Figure 5.5. Variation of EGR ratio at HP.

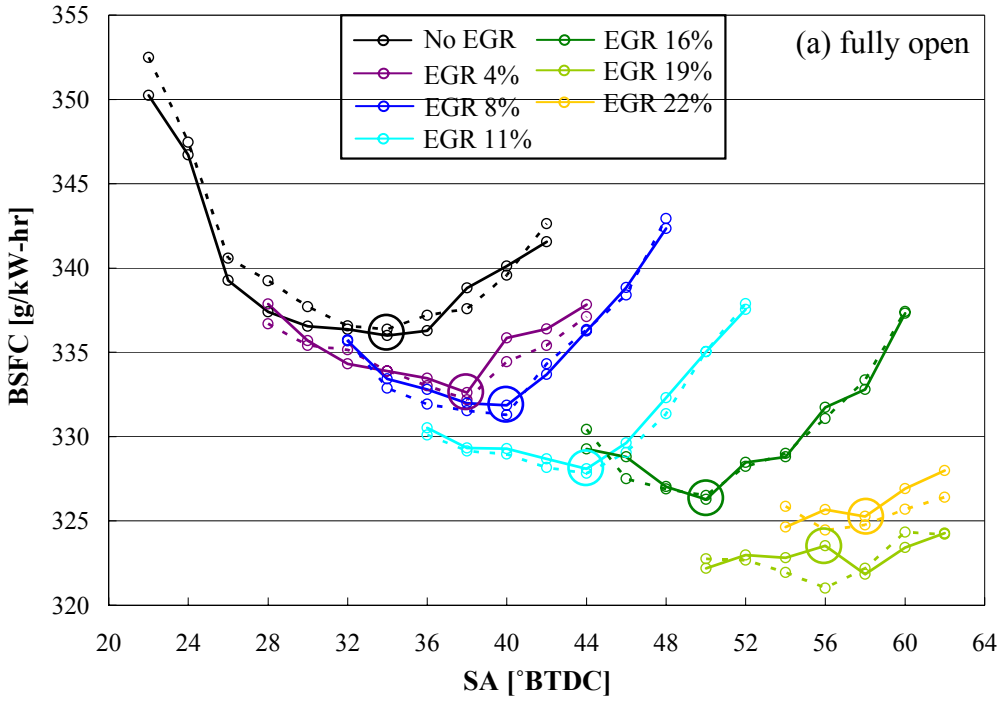

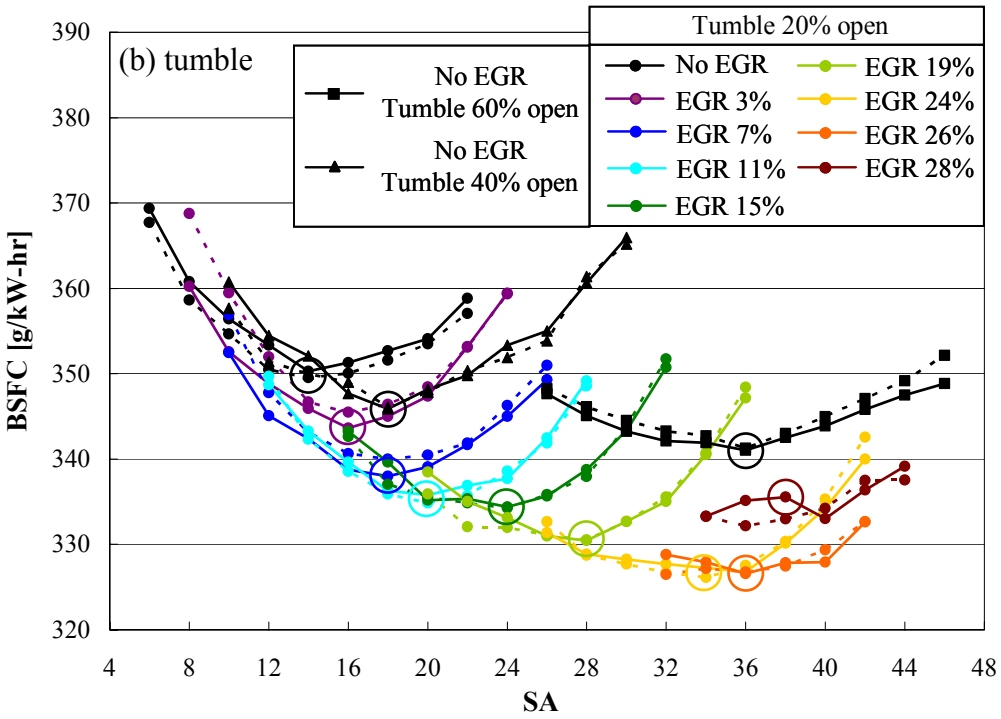

Figure 5.6. Effect of blockages on BSFC at WP. (Continued)

Figure 5.6: Continued.

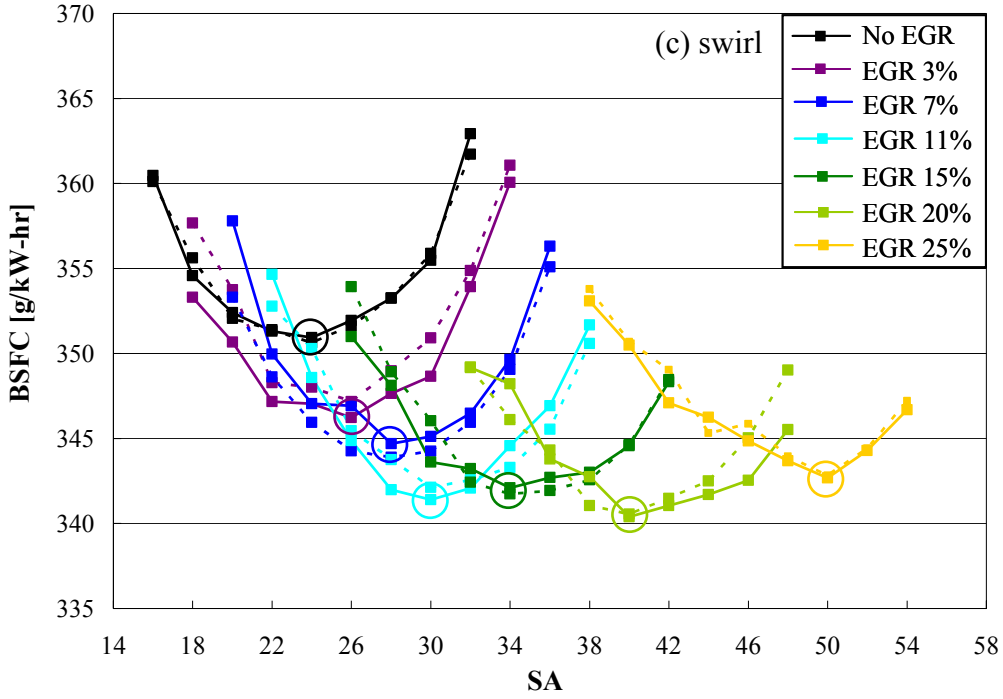

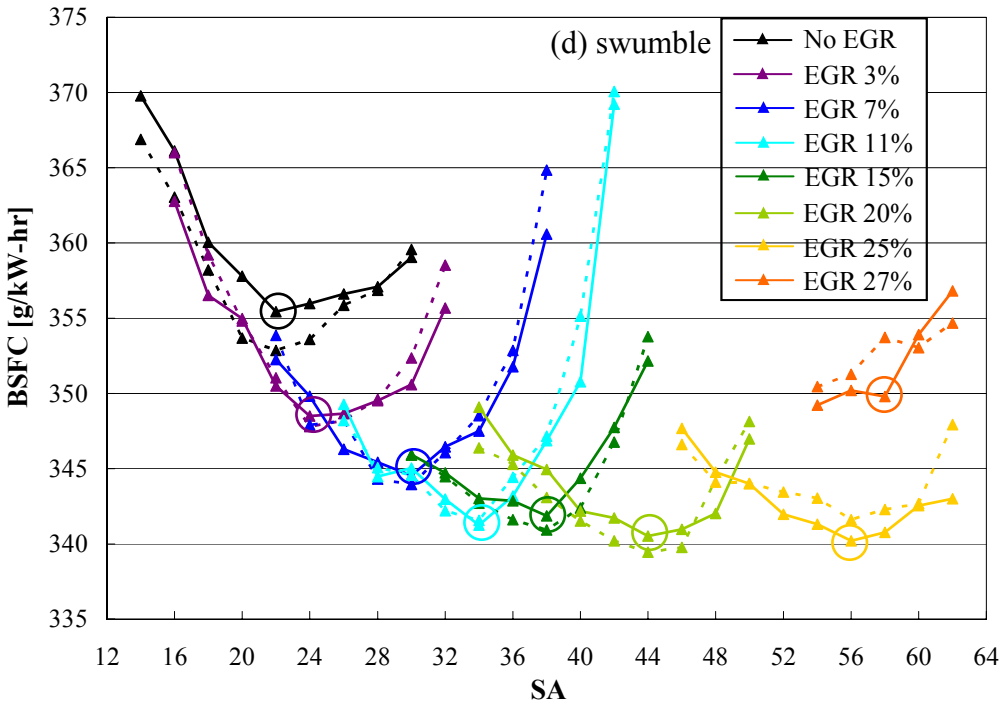

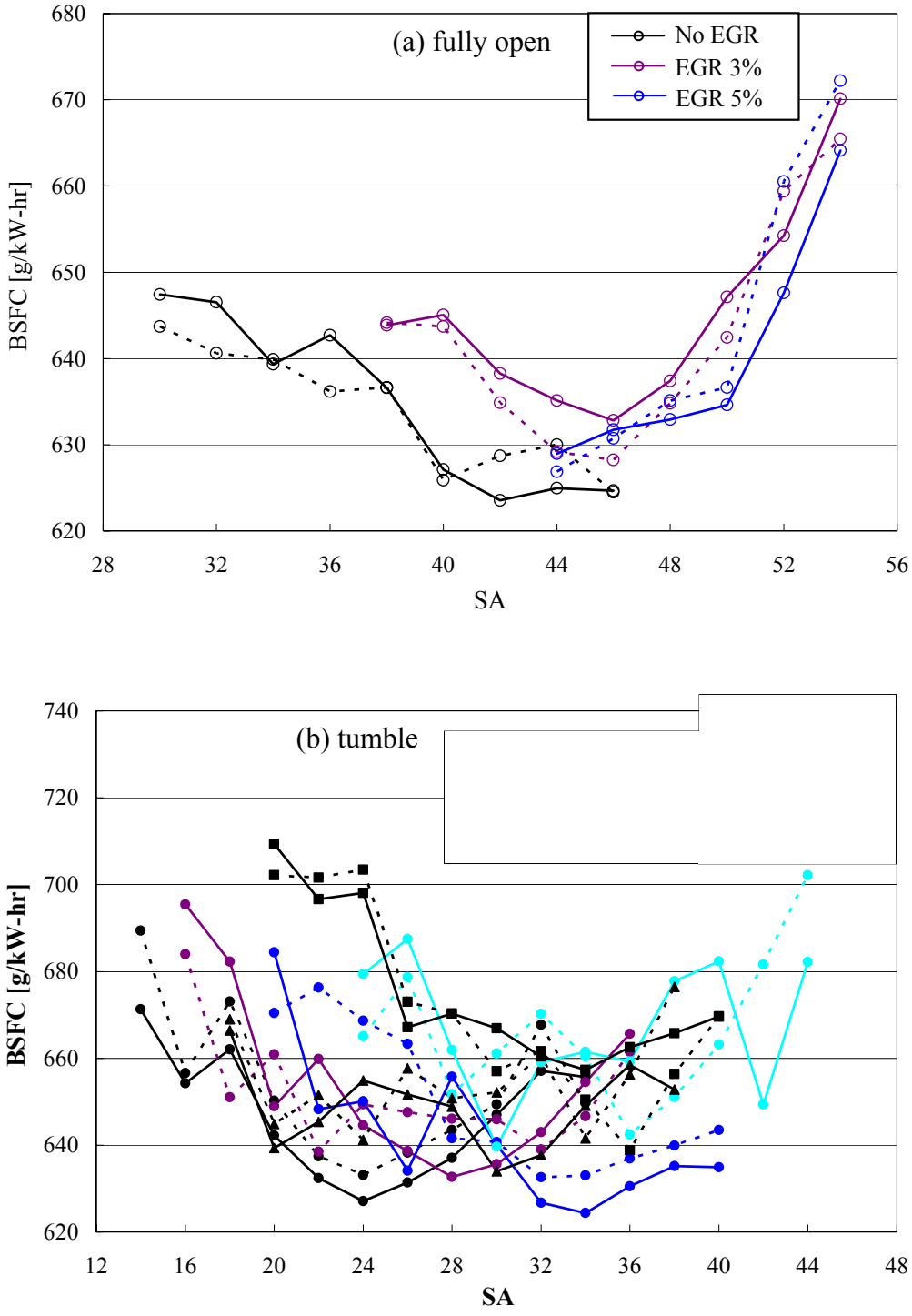

Figure 5.7. Effect of blockages on BSFC at IP.

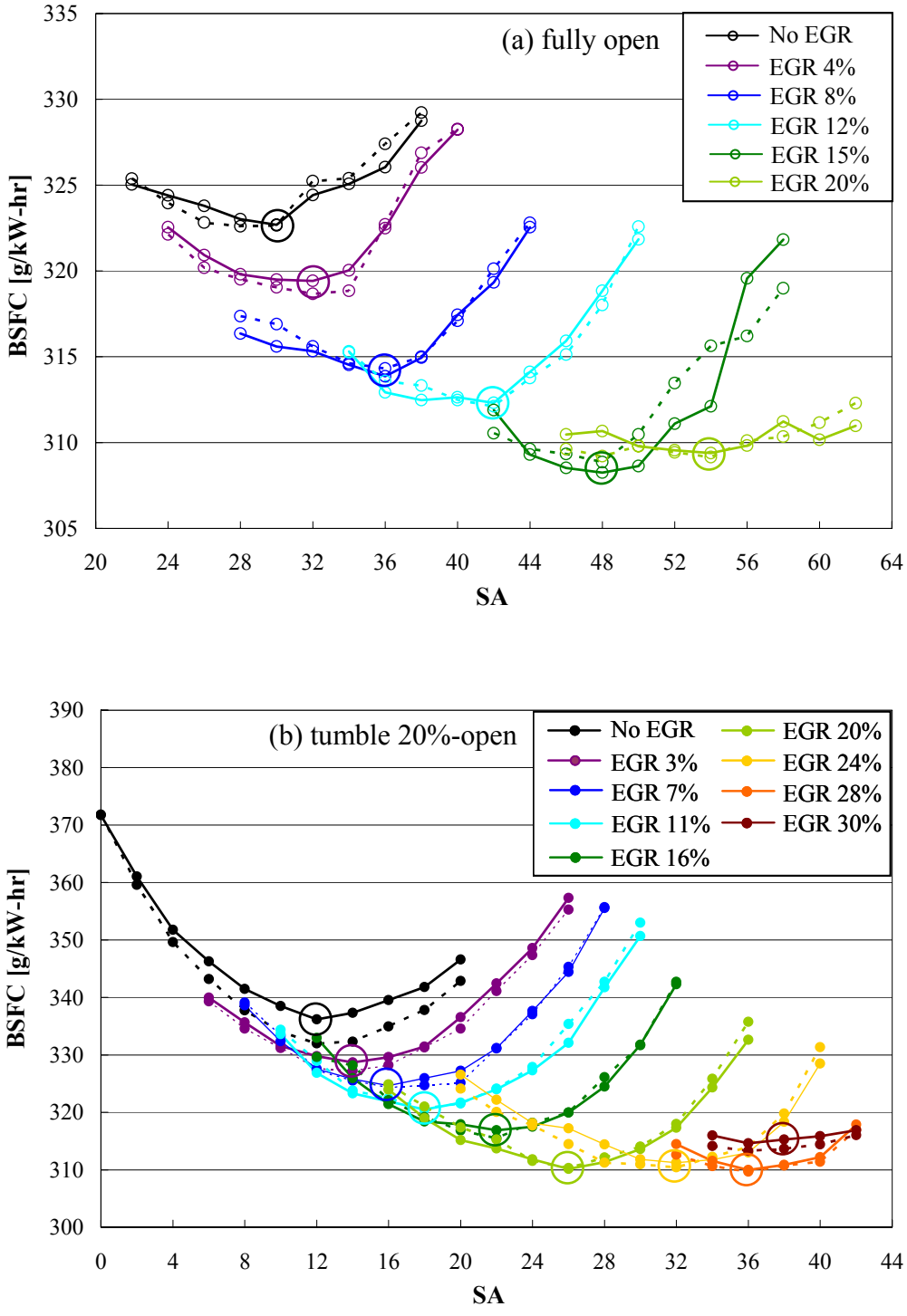

Figure 5.8. Effect of blockages on BSFC at WP_GM.

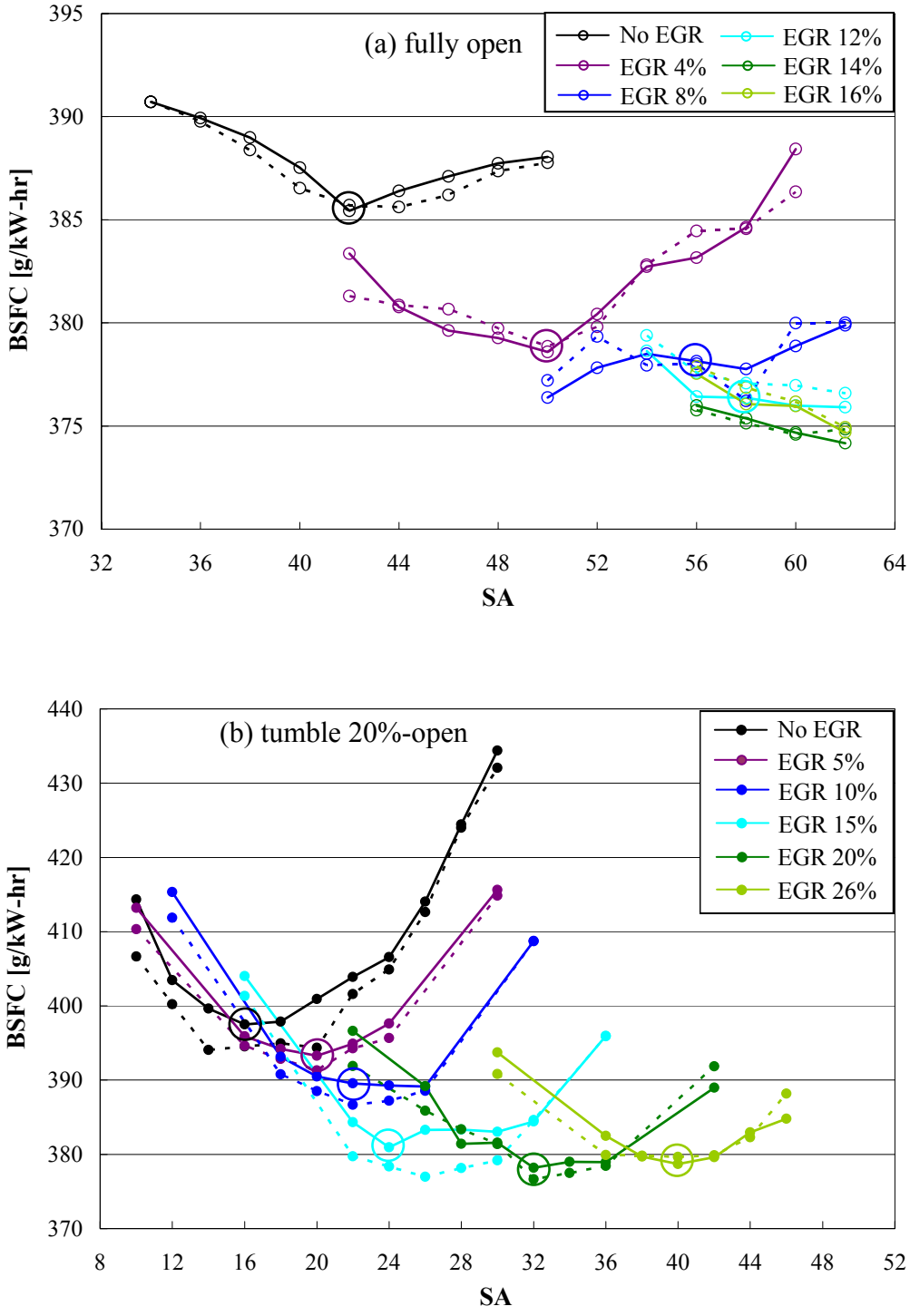

Figure 5.9. Effect of blockages on BSFC at WP_FEV.

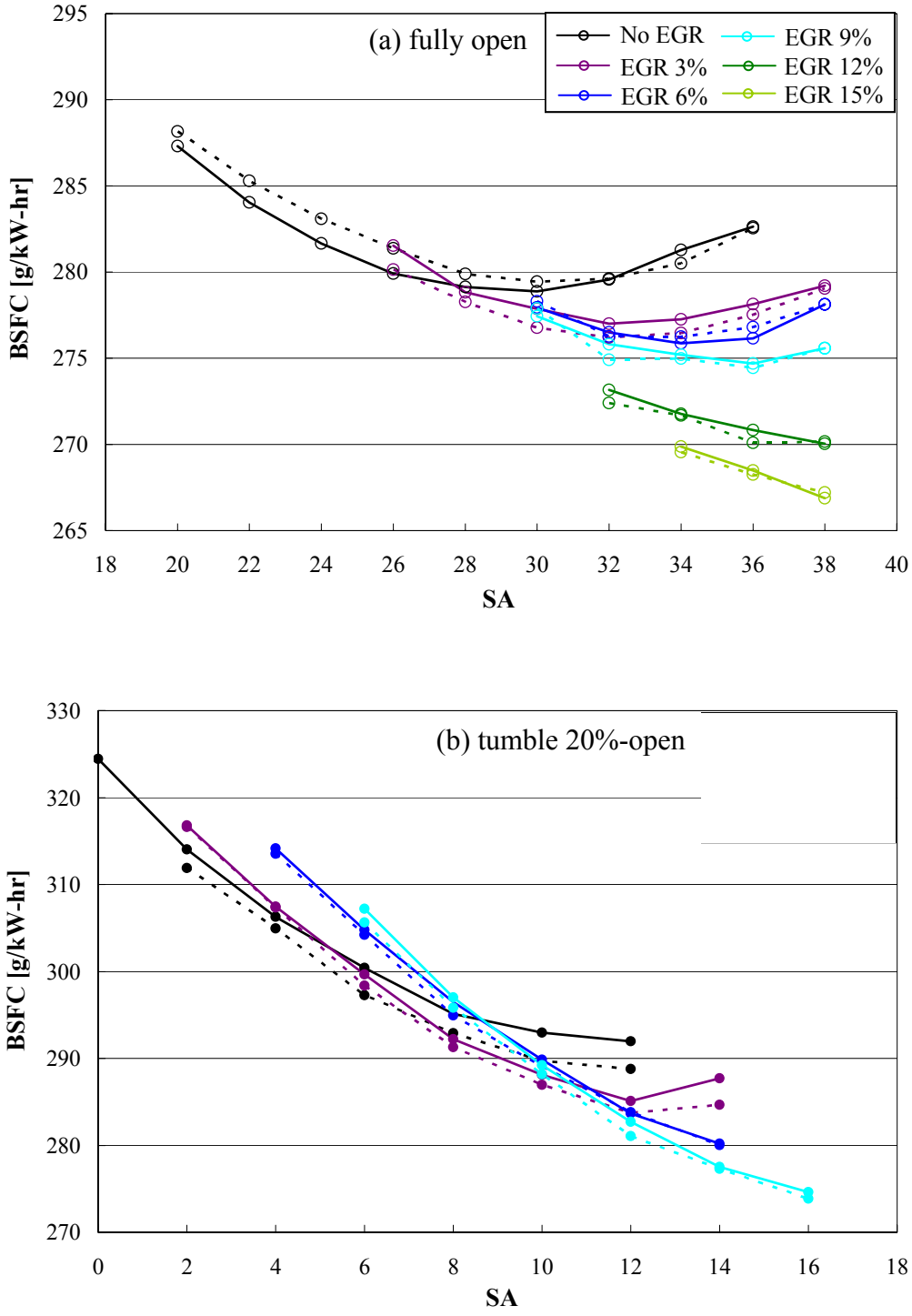

Figure 5.10. Effect of blockages on BSFC at HP.

In the present work, the optimum dilution level or, optimum EGR (of 19%, 26%, 20%, and 25% for fully open, tumble, swirl, and swumble, respectively, under WP) has been defined as the EGR ratio which yields the minimum BSFC at MBT, as shown in Fig. 5.6. Figure 5.11 depicts the BSFC comparison as a function of EGR at MBT timing only. BSFC decreases continuously with EGR until the optimum dilution level and improves by 3.7%, 6.7%, 3.0%, and 4.0% for fully open, tumble, swirl, and swumble, respectively, consistent with Tabata *et al.*, 1995. Tumble yields an optimum EGR higher than other types of charge motion, suggesting more stable combustion and less cyclic variation. On the other hand, the introduction of blockage has raised BSFC at a given EGR, primarily due to increased pumping loss. At the maximum EGR, the impact of partial burn and misfiring cycles overcomes the benefit from reduced pumping losses leading to significantly increased BSFC, particularly for tumble and swumble, which will be elaborated in Section 5.3. The fuel conversion efficiency η_f, determined from Eq. (4.8), is compared in Fig. 5.12 for all configurations at MBT timing, which is inversely proportional to BSFC, as expected.

The calculated EGR ratio and ISFC [recall Eqs. (4.1) and (4.55)] at MBT are illustrated in Table 5.1 for fully open, tumble, swirl, and swumble, respectively. Compared to the unrestricted runner, blockage has retarded MBT timing due to shortened combustion duration, while tumble showing the largest reduction in spark advance (20˚ BTDC without EGR) relative to swirl and swumble (10˚ and 12˚ BTDC, respectively, without EGR). Compared to the quoted EGR ratio (numbers in the first column for each configuration), the actual measured values exhibit a small deviation (third column). Without EGR dilution, blocked runners reduce ISFC by 2.87%, 2.26%, and 2.26% for

tumble, swirl, and swumble, respectively, suggesting an improved fuel conversion efficiency achieved by fast burn Selamet *et al.*, 2004. For all configurations, ISFC first decreases with dilution mainly due to improved fuel economy, followed by an increase to the maximum EGR since the reduced indicated work offsets the decreasing fuel flow rate.

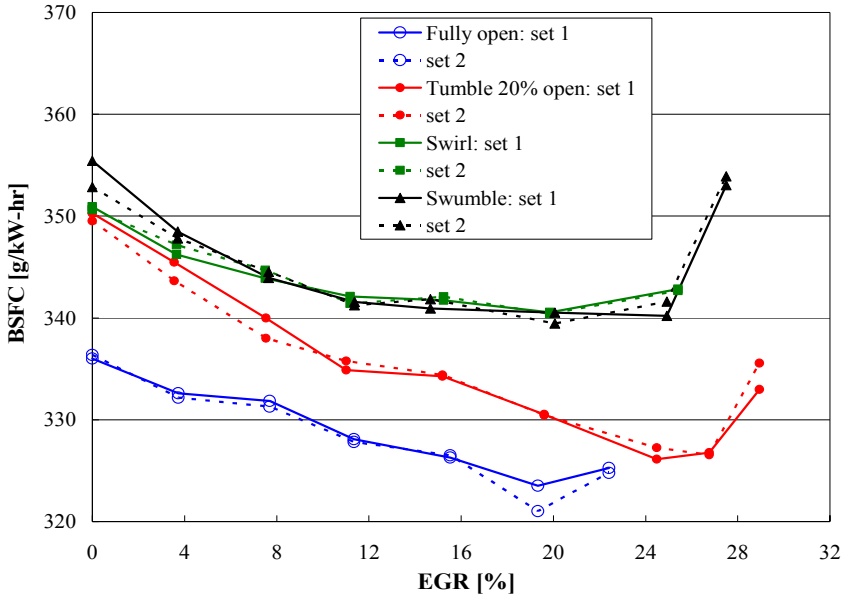

Figure 5.11. BSFC comparison with EGR under WP, at MBT.

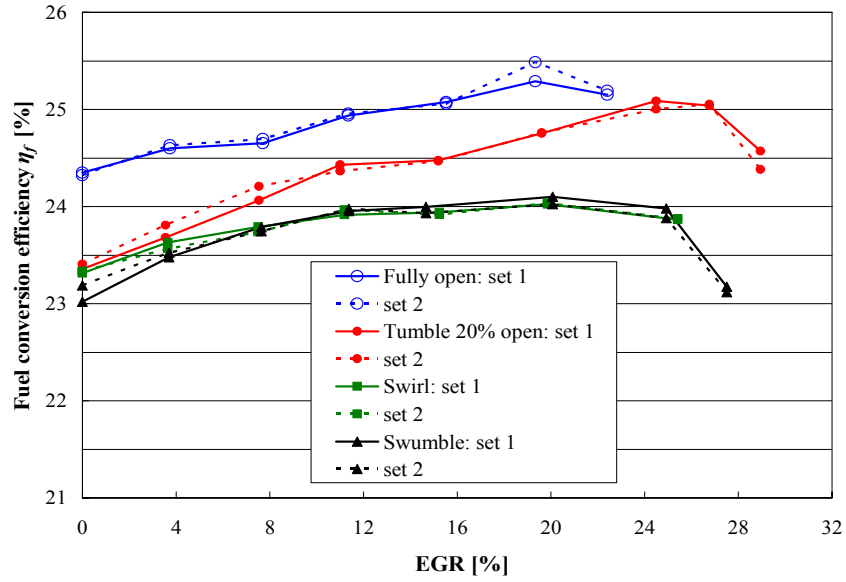

Figure 5.12. Fuel conversion efficiency comparison with EGR under WP, at MBT.

WP (2.41 bar BMEP @1600 rpm)							
IR fully open				IR 20% open - Tumble			
Estimated EGR	MBT (˚BTDC)	EGR at MBT (%)	ISFC (g/kW-hr)	Estimated EGR	MBT (˚BTDC)	EGR at MBT (%)	ISFC (g/kW-hr)
0	34	0	265.37	0	14	0	257.76
4%	38	3.73	264.66	3%	16	3.55	254.86
8%	40	7.70	262.08	7%	18	7.54	253.61
11%	44	11.35	263.12	11%	20	11.01	254.76
16%	50	15.53	263.91	15%	24	15.19	261.93
19%	56	19.33	266.88	19%	28	19.61	267.69
22%	58	22.41	268.66	24%	34	24.49	273.00
				26%	36	26.77	273.64
				28%	38	28.94	278.84

WP (2.41 bar BMEP @1600 rpm)							
IR 20% open - Swirl				IR 20% open - Swumble			
Estimated EGR	MBT (˚BTDC)	EGR at MBT (%)	ISFC (g/kW-hr)	Estimated EGR	MBT (˚BTDC)	EGR at MBT (%)	ISFC (g/kW-hr)
0	24	0	259.38	0	22	0	259.38
3%	26	3.65	258.90	3%	24	3.70	256.40
7%	28	7.51	258.42	7%	30	7.64	266.51
11%	30	11.19	263.40	11%	34	11.38	268.52
15%	34	15.24	267.01	15%	38	14.67	272.88
20%	40	19.85	275.48	20%	44	20.07	279.21
25%	50	25.41	285.76	25%	56	24.92	284.79
				27%	58	27.50	294.33

Table 5.1. Comparison of EGR and ISFC at MBT under WP
(IR = Intake Runner).

5.3 In-cylinder, intake and exhaust runner pressures

In-cylinder pressure varies with crank angle as a result of combustion, cylinder volume change, heat transfer to the combustion chamber walls, flow into and out of crevice regions, and leakage. The introduction of charge motion in an SI engine elevates u' at the time of spark, increases the burn rate, and shortens the combustion duration, which will substantially change the in-cylinder pressure. On the other hand, intake runner blockage is known to increase the flow loss, therefore reduce the volumetric efficiency η_v and increase the pumping loss during gas exchange process. In this section, the effect of blockage on cylinder, intake and exhaust runner pressures is discussed. In light of the similarity of results from cylinders 1 and 4, this chapter concentrates on cylinder and runner 1.

5.3.1 In-cylinder pressure

Charge motion can significantly change in-cylinder pressure leading to: (1) increased peak pressure and rate of pressure rise during combustion due to enhanced turbulence and accelerated flame propagation; and (2) decreased pressure during intake process because of reduction in volumetric efficiency which will be discussed in Section 5.4. The variation of in-cylinder pressure (averaged from 256 engine cycles) in a range of ±90˚ around TDC of combustion is compared in Fig. 5.13 at a fixed spark timing of 22˚ BTDC without EGR for unblocked and blocked runners. Charge motion does increase the peak cylinder pressure p_{max} with the corresponding location θ_{pmax} moving towards TDC, which is mainly due to the increased turbulent flame speed and reduced burn delay period (Hill and Zhang, 1994). Tumble displays a much higher p_{max} and more advanced θ_{pmax} than swirl and swumble, suggesting more rapid combustion.

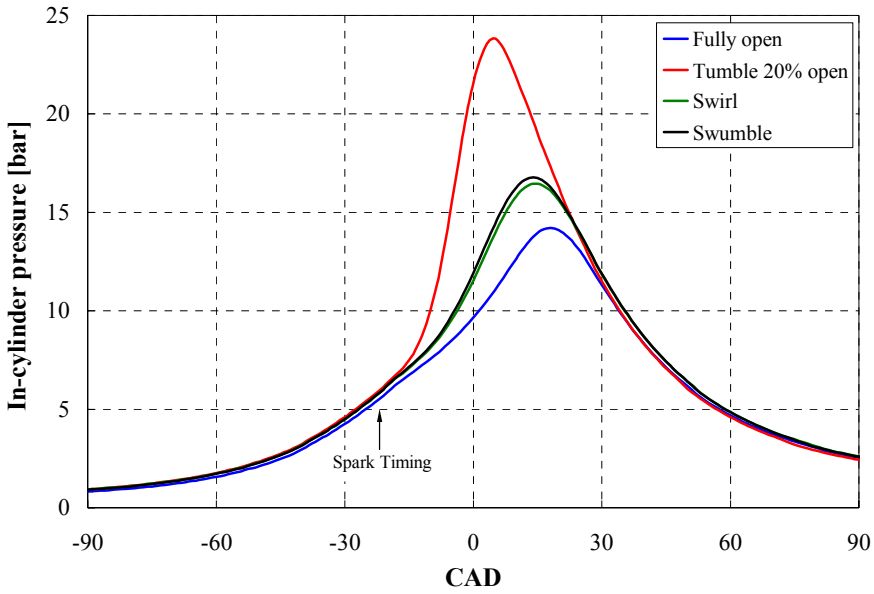

Figure 5.13. Variation of in-cylinder (#1) pressure at WP, SA = 22˚, no EGR.

Figure 5.14 depicts the variation of the averaged in-cylinder pressure with different dilution levels at a given spark timing for the unblocked runner. The peak cylinder pressure p_{max} decreases with EGR dilution with θ_{pmax} moving away from the combustion TDC, mainly due to reduced flame speed, hence increased burn duration.

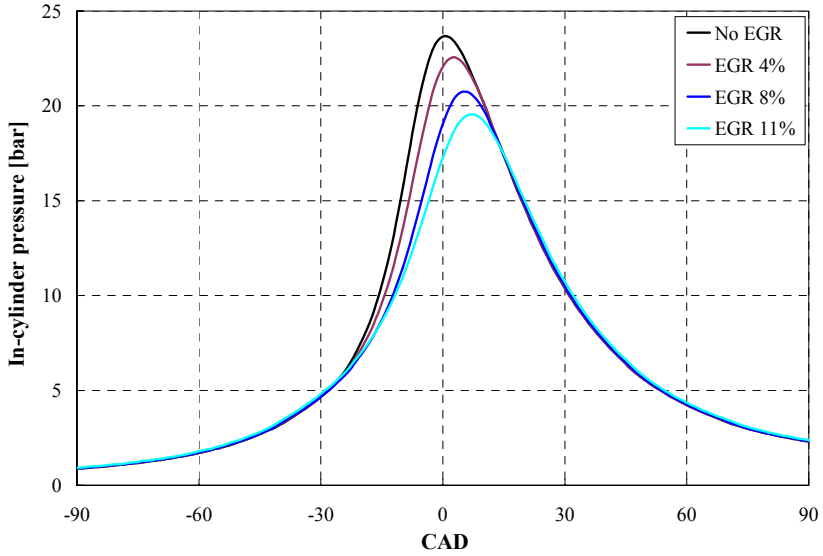

Figure 5.14. Variation of in-cylinder (#1) pressure at WP, SA = 42° BTDC, fully open runner.

The impact of spark advance on the averaged in-cylinder pressure is illustrated in Fig. 5.15 at 15% EGR for tumble 20%-open blockage under WP. The magnitude of p_{max} increases with advanced spark timing while θ_{pmax} moving toward TDC of combustion due to early combustion during compression. In-cylinder pressure following the combustion (approximately for $\theta > 40°$ ATDC during expansion stroke) decreases with advanced spark, leading to reduced in-cylinder and exhaust gas temperature.

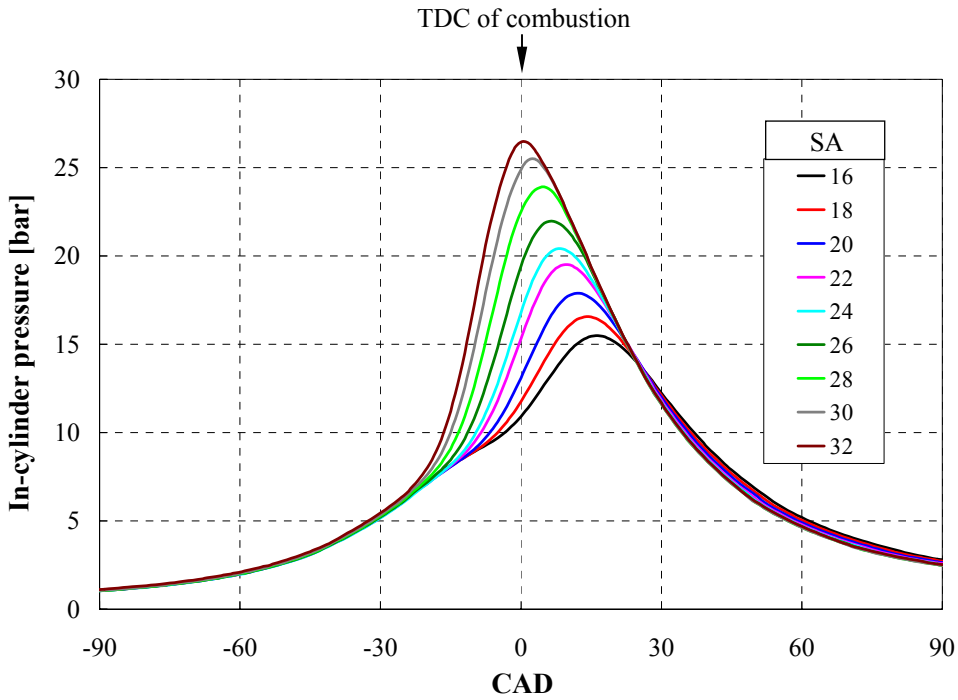

Figure 5.15. Variation of in-cylinder (#1) pressure at WP, 15% EGR, tumble 20%-open.

The variation of average in-cylinder pressure with different EGR rates is compared at MBT in Figs. 5.16(a) – 5.16(d) for fully open, tumble, swirl, and swumble, respectively. For unblocked case of Fig. 5.16(a), both phasing and magnitude of the peak cylinder pressure p_{max} are nearly comparable at different dilution levels. This is due to the effect of spark timing and EGR dilution. In general, under a fixed operating condition with a given EGR ratio, p_{max} increases gradually with advanced spark while the location of the peak cylinder pressure θ_{pmax} approaches TDC (Fig. 5.15). At a given spark timing, the peak cylinder pressure decreases with EGR for each blockage-load combination (Fig. 5.14), mainly due to the reduced flame speed. For unblocked runner, the introduction of EGR nearly offsets the effect of advanced MBT timing (Table 5.1) in terms of p_{max} and θ_{pmax}, where the latter remains around 8° ATDC. Charge motion, on the other hand, accelerates the flame propagation and increases the peak cylinder pressure as illustrated in Fig. 5.13, which more than compensates for the impact of EGR on p_{max}. Therefore, the variation of peak cylinder pressure strongly depends on the advanced MBT timing, leading to gradually increased p_{max} with EGR until the optimum dilution level (except tumble), as illustrated in Figs. 5.16(b) – 5.16(d).

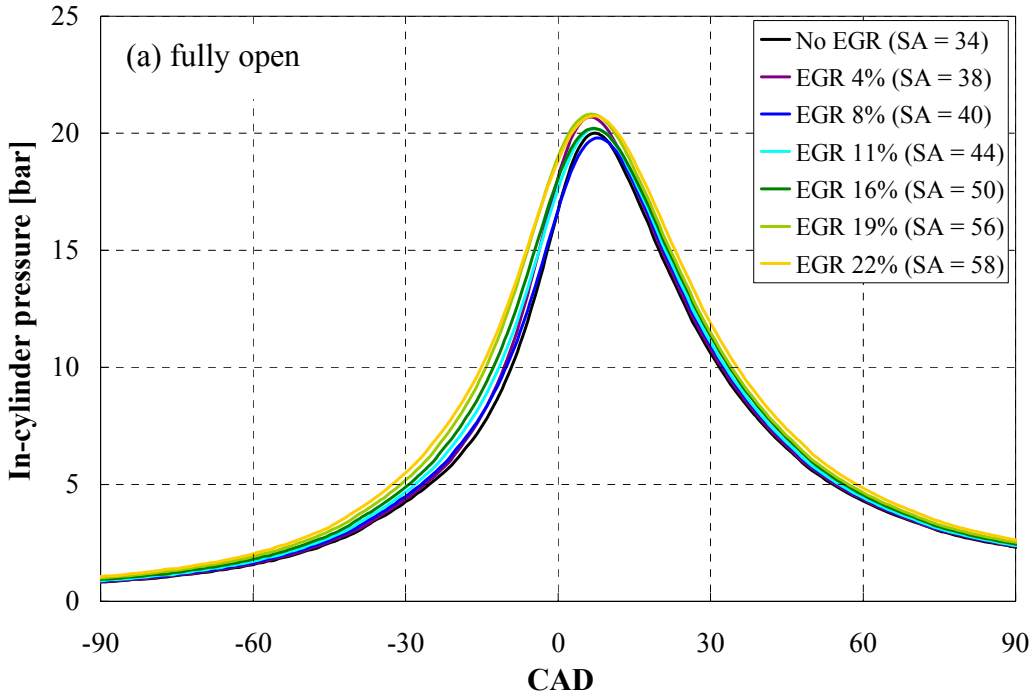

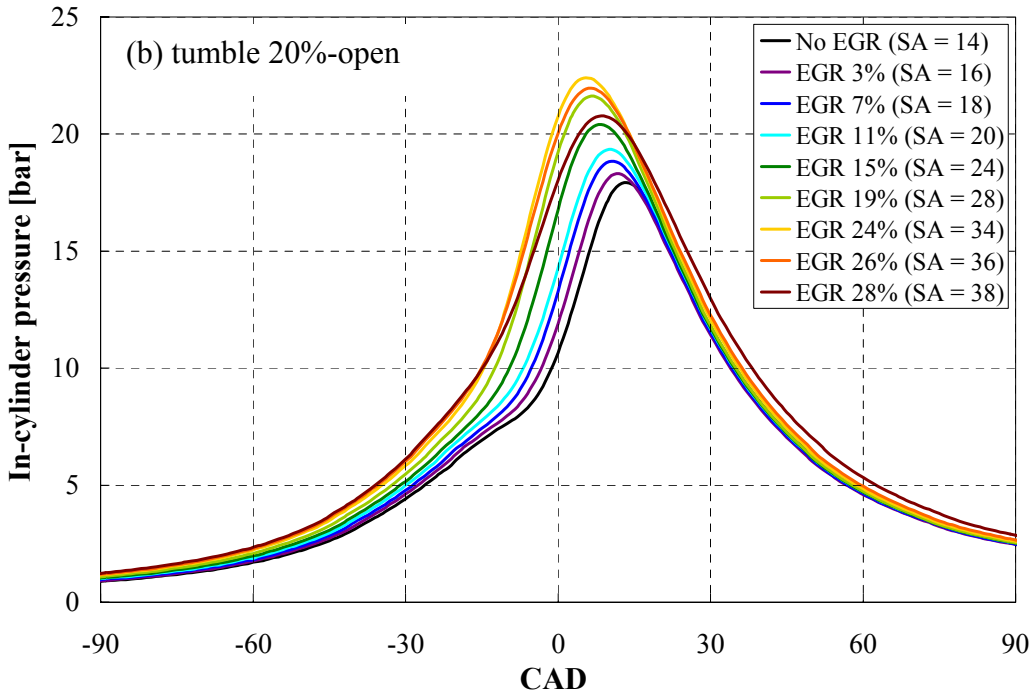

Figure 5.16. Effect of blockages on in-cylinder (#1) pressure at MBT under WP: (a) fully open, (b) tumble 20% open, (c) swirl, and (d) swumble.

(Continued)

Figure 5.16: Continued.

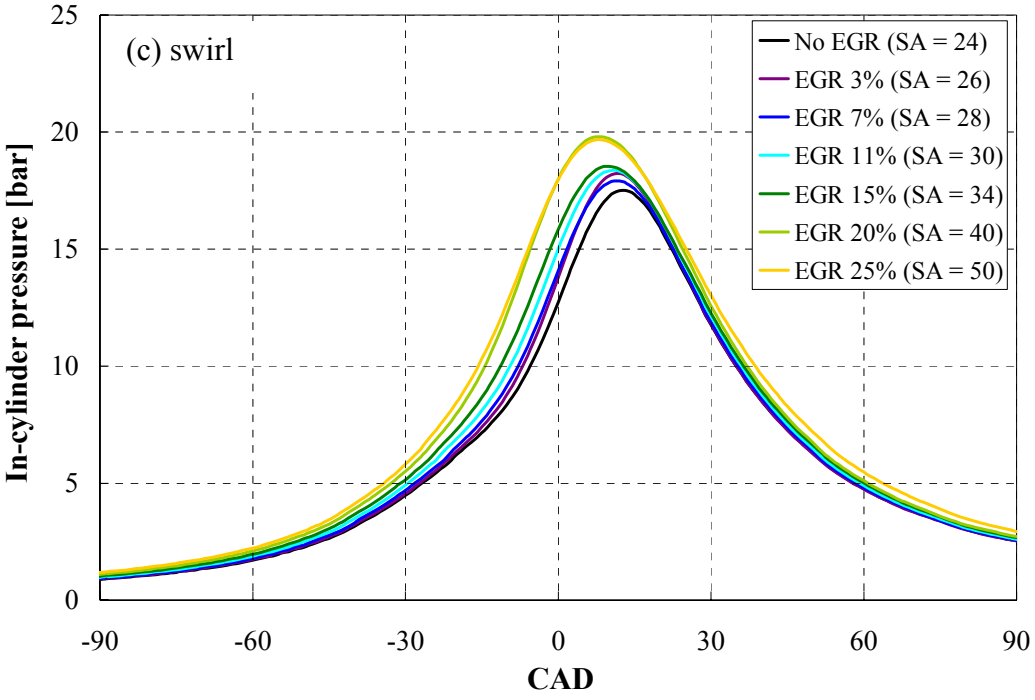

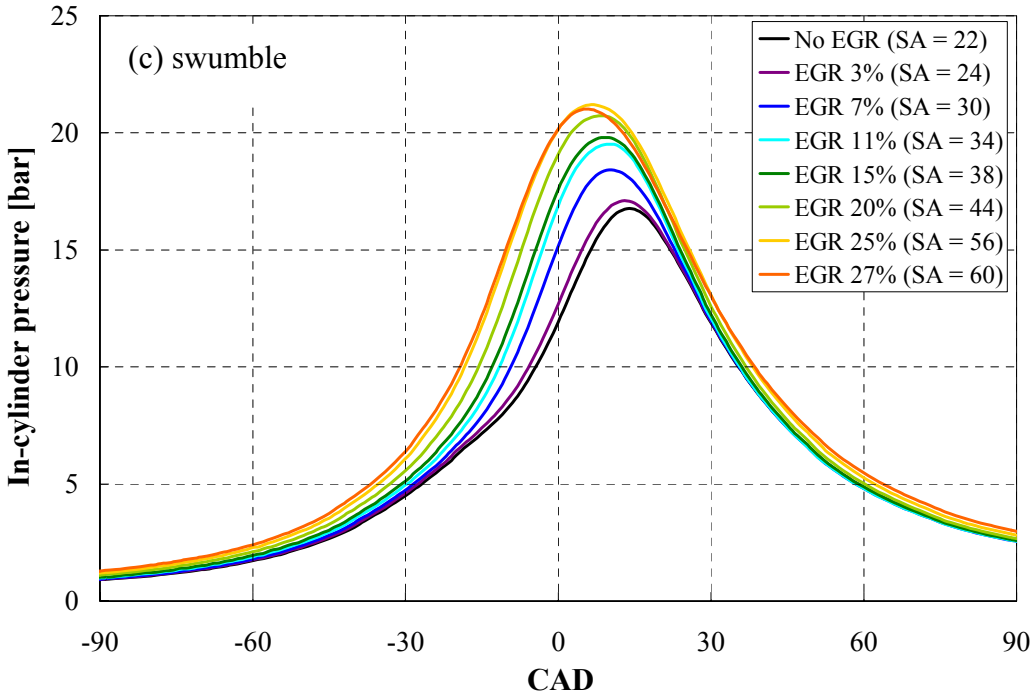

5.3.2 Intake runner pressure

Intake runner 1 pressures at upstream and downstream of blockages (Locations 5 and 6 in Fig. 3.1) are compared in Figs. 5.17(a) – 5.17(d) at MBT and three EGR ratios (0, 11%, and 15%) for fully open, tumble, swirl, and swumble, respectively. The overall magnitude of upstream and downstream pressures increases with EGR dilution due to additional exhaust gas being recirculated into the intake manifold, leading to increased MAP and reduced pumping loss. The phasing, on the other hand, is not influenced by EGR for all configurations. As expected, the variation between upstream and downstream pressures is essentially negligible for unrestricted runner at a given EGR. However, charge motion brings about changes in both magnitude and phasing of upstream and downstream runner pressures during the IVOP as illustrated in Figs. 5.17(b) – 5.17(d). This is due to increased flow losses because of the flow separation, along with the overlap and displacement back flows across the blockage. This results in a reduction of in-cylinder pressure for the intake stroke hence an increase in pumping losses (Selamet *et al.*, 2004).

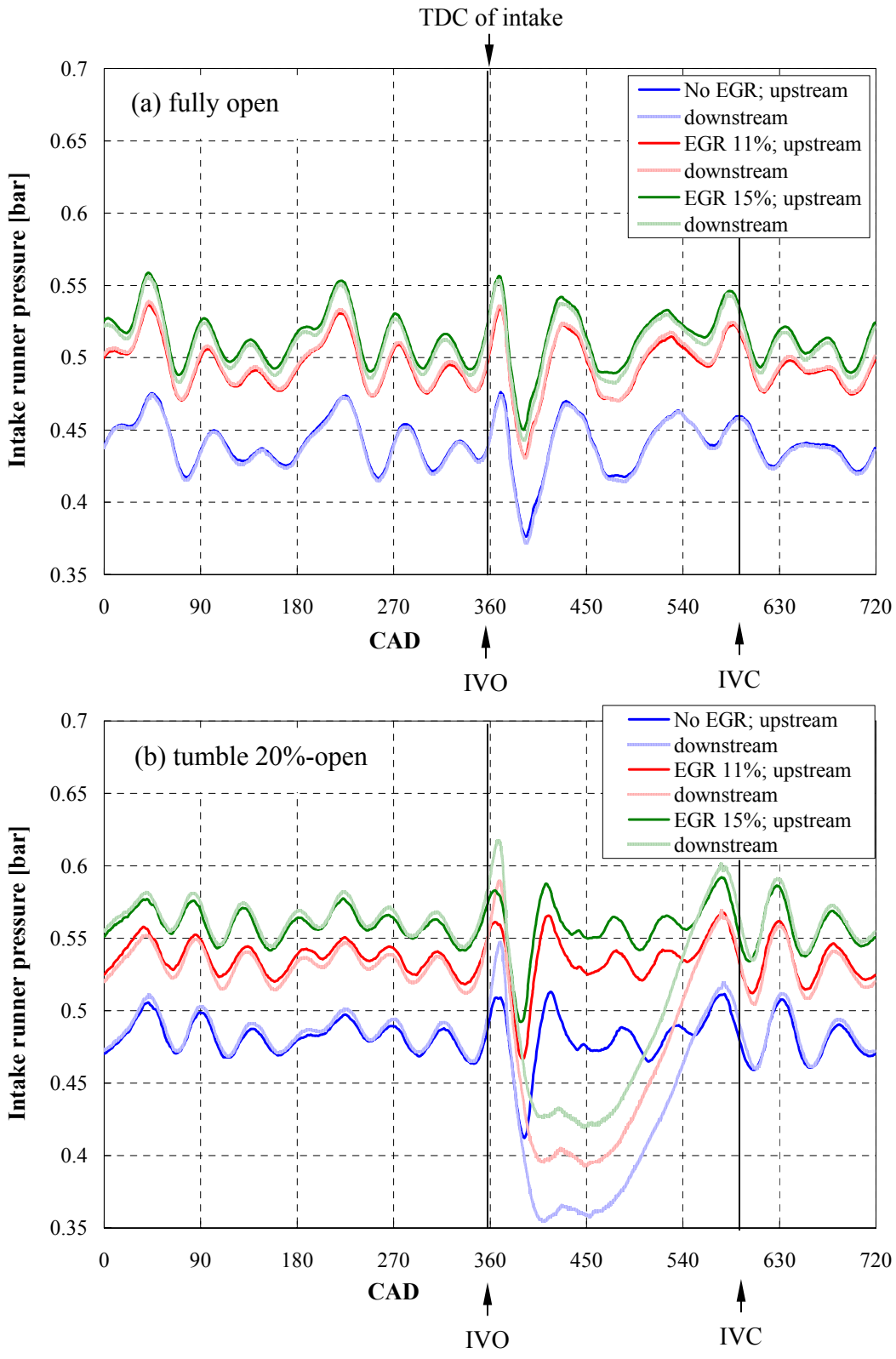

Figure 5.17. Comparison of intake runner pressure under WP, at MBT, runner 1: (a) fully open, (b) tumble 20% open, (c) swirl, and (d) swumble. (Continued)

Figure 5.17: Continued.

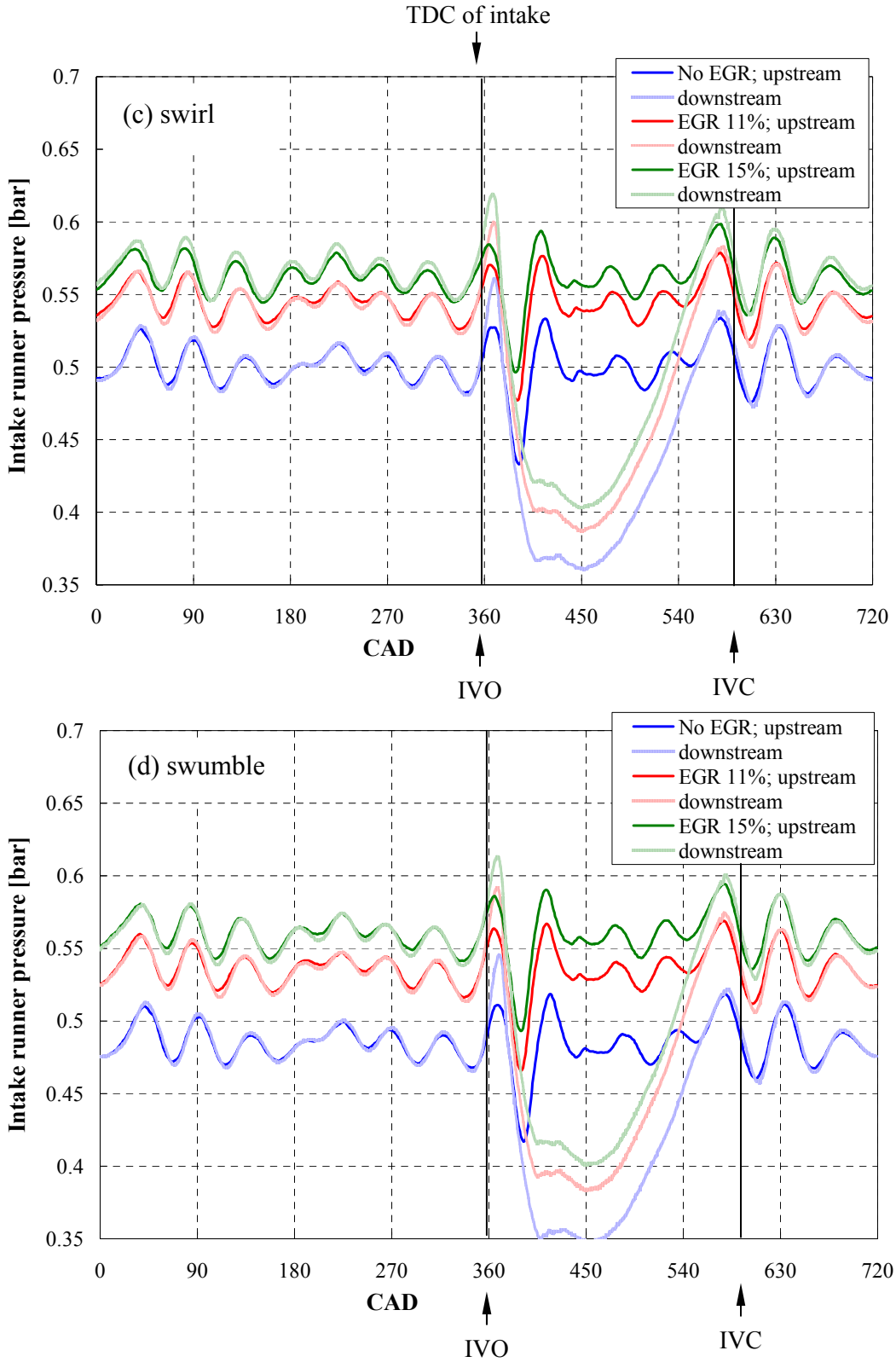

5.3.3 Exhaust runner pressure

The corresponding exhaust runner 1 pressures are illustrated in Figs. 5.18(a) – 5.18(d) for fully open, tumble, swirl, and swumble, respectively. Similar to the intake runner, the phasing of the exhaust pressure does not change with EGR. The magnitude is close to the barometric pressure and exhibits a small variation at different EGR rates possibly due to the fluctuation of ambient conditions.

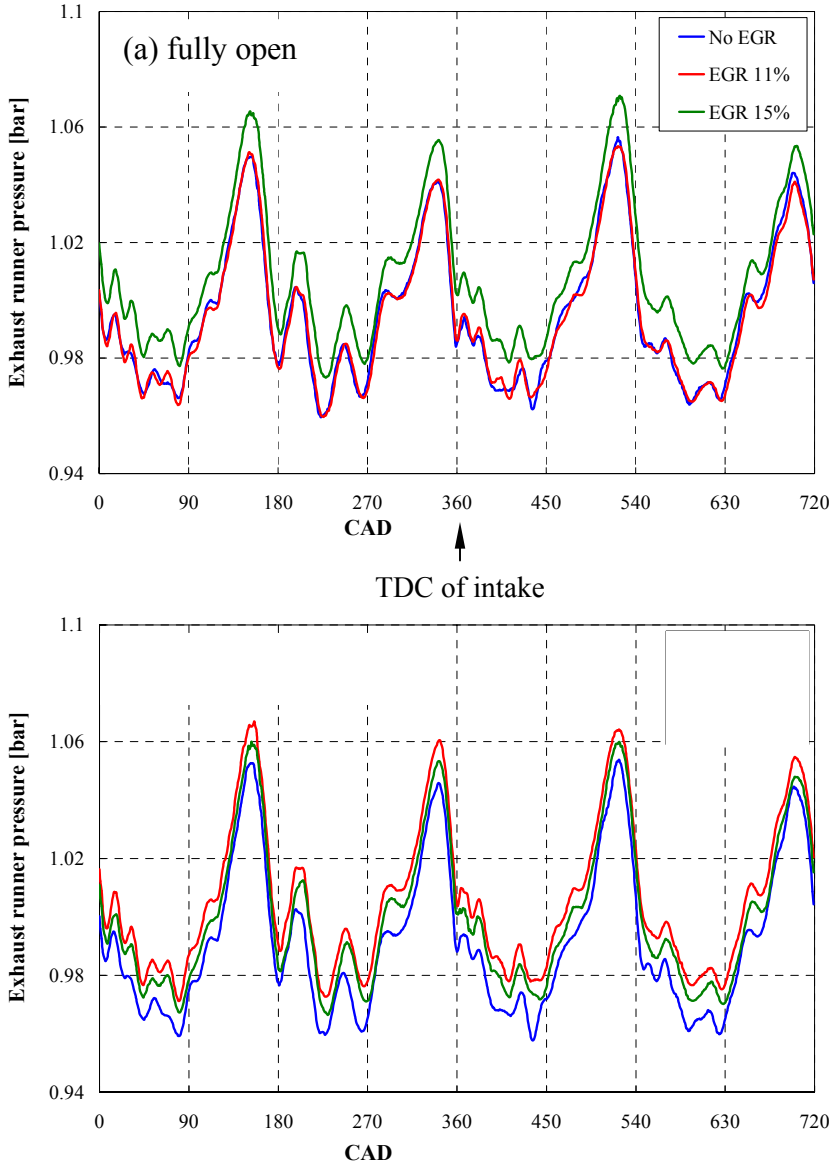

Figure 5.18. Comparison of exhaust runner pressure under WP, at MBT, runner 1. (Continued)

Figure 5.18: Continued.

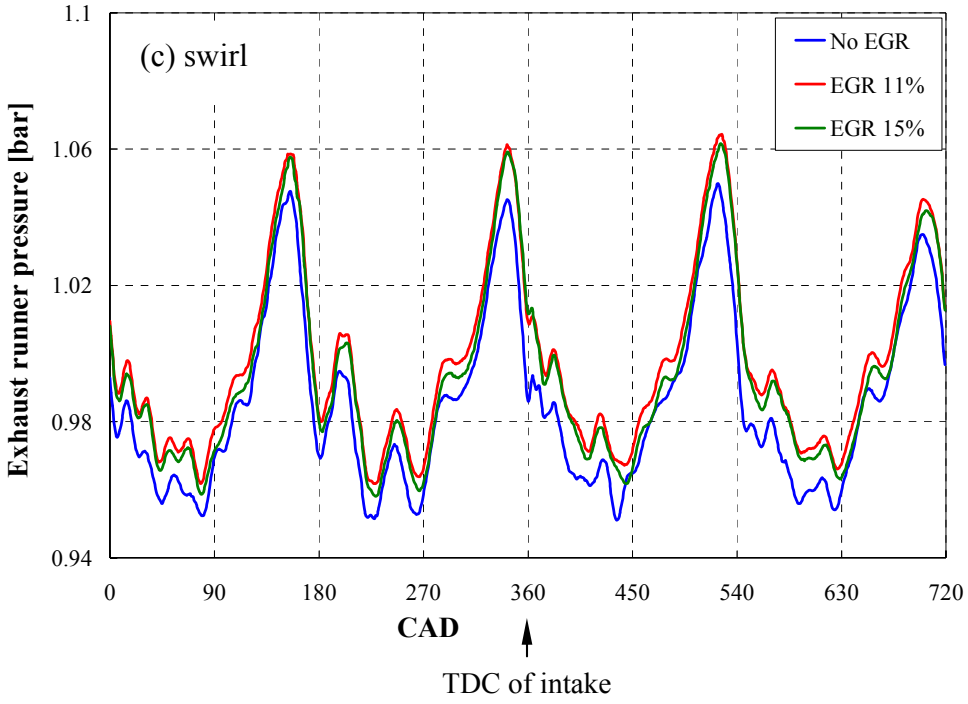

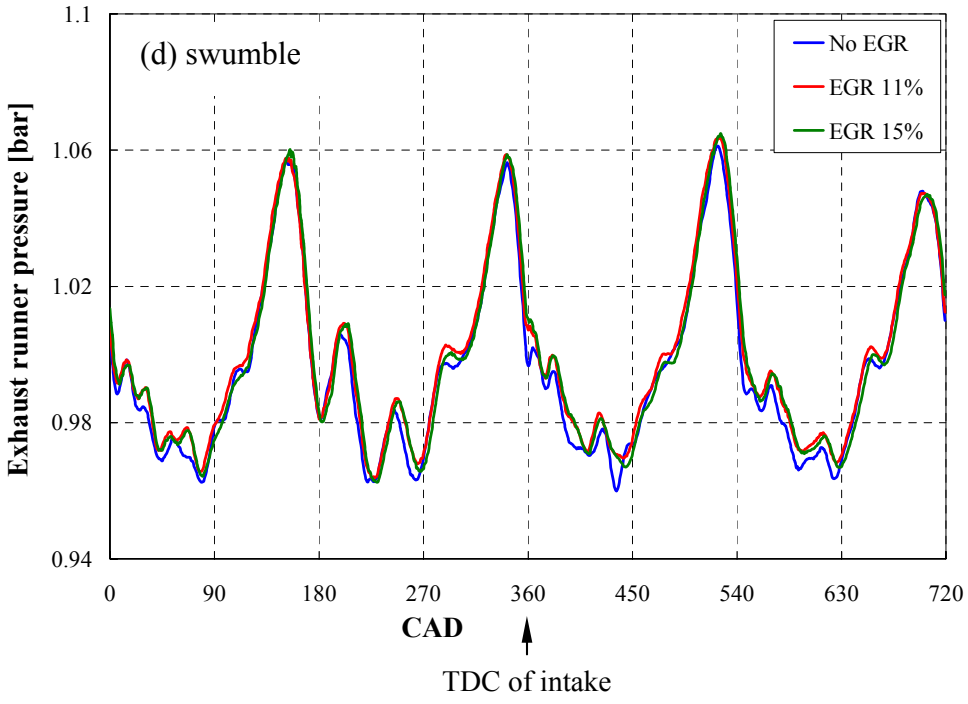

5.4 In-cylinder cyclic variation

Figures 5.19 and 5.20 compare COV and LNV, respectively, in IMEP as a function of spark advance between unblocked and blocked runners to examine the cyclic combustion variability. COV at MBT increases with EGR while LNV showing an expected opposite trend, indicating more cyclic combustion instability with increased dilution, consistent with Ivanic *et al.* (2005). At the maximum EGR, tumble and swumble display a significantly higher COV (Fig. 5.19) [or lower LNV (Fig. 5.20)] compared to that at the low dilution level, mainly due to the increase of partial burn and misfiring cycles. Cyclic variation is also observed to be more significant at the most advanced spark timing than the most retarded point over 0 to about 15% EGR, particularly for the unblocked runner.

Comparison of COV and LNV in IMEP at MBT timing is displayed in Figs. 5.21 and 5.22, respectively. The cyclic variation at MBT increases with EGR, as expected. Swirl and swumble reduce the cyclic variability from 0 to about 20% EGR compared to fully open runner. Tumble reveals a further reduction in COV compared to swirl and swumble, over a range from about 8% EGR to the optimum dilution level (for example, COV of 1.74%, 1.40%, 0.93%, and 0.78% for fully open, swumble, swirl, and tumble, respectively, at about 11% EGR). In general, organized gas motion such as tumble and swirl does stabilize the combustion and reduce the cyclic variation (Hill and Zhang, 1994). As in-cylinder dilution approaches the optimum EGR, COV is observed to be 2.33%, 1.82%, 1.69%, and 2.86 for fully open, tumble, swirl, and swumble respectively, a range that is consistent with other experimental observations (Ivanic *et al.*, 2005; Goldwitz and Heywood, 2005; which define the dilution limits as 3% and 2% COV,

respectively). Beyond the optimum dilution level, blocked runners exhibit substantial cyclic variation (highest COV and lowest LNV in Figs. 5.21 and 5.22, respectively) mainly due to the dramatic increase of partial burn and misfiring cycles. This results in increased BSFC at the highest EGR as illustrated in Fig. 5.11.

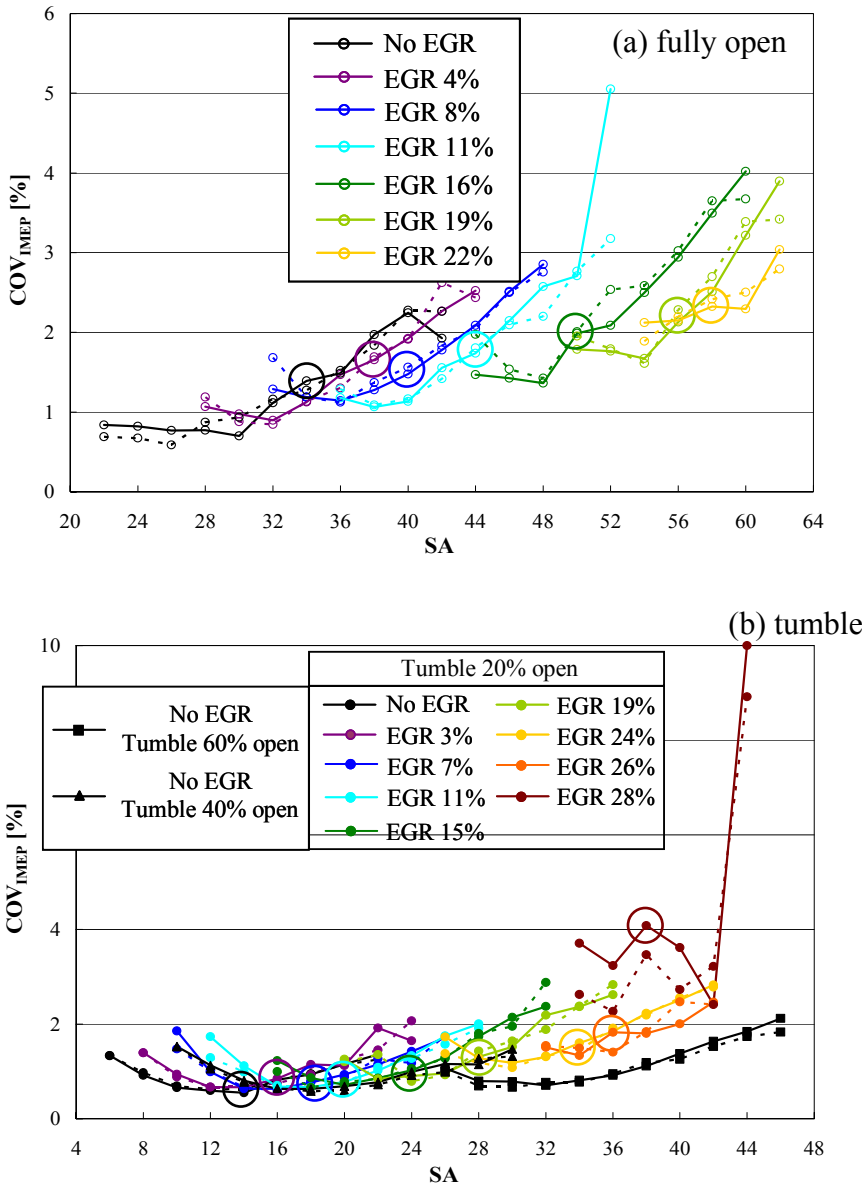

Figure 5.19. Effect of blockages on COV in IMEP at WP, Cylinder 1. (Continued)

Figure 5.19: Continued.

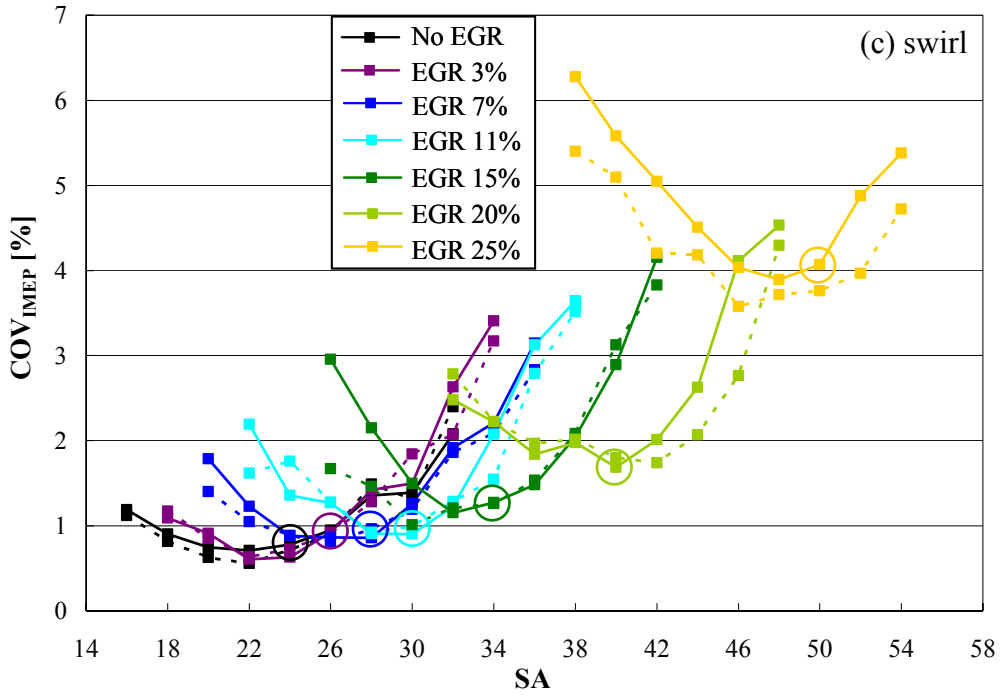

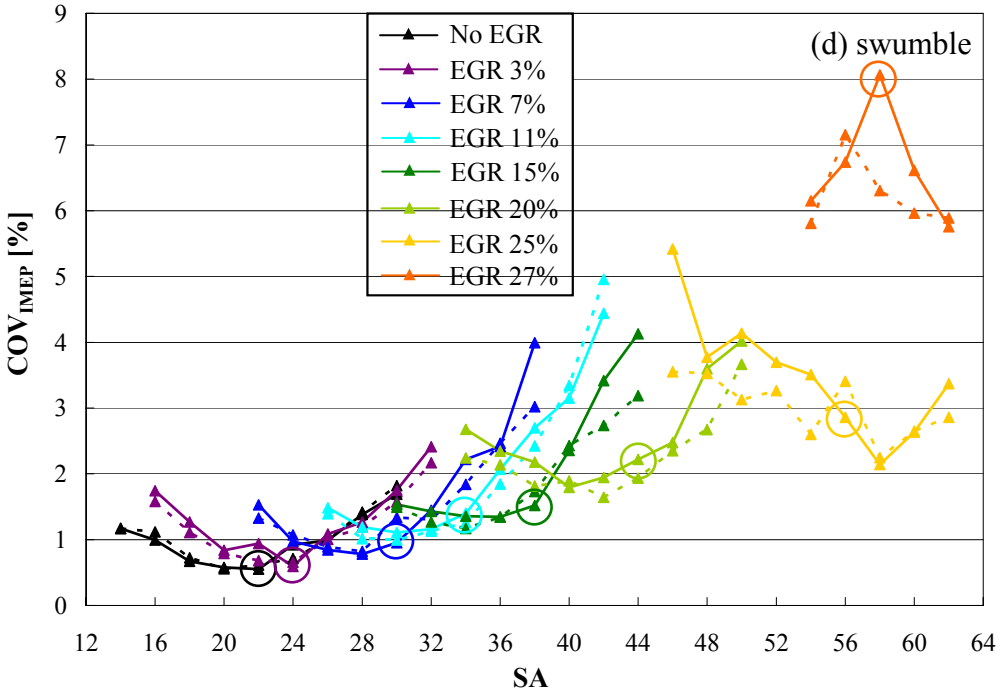

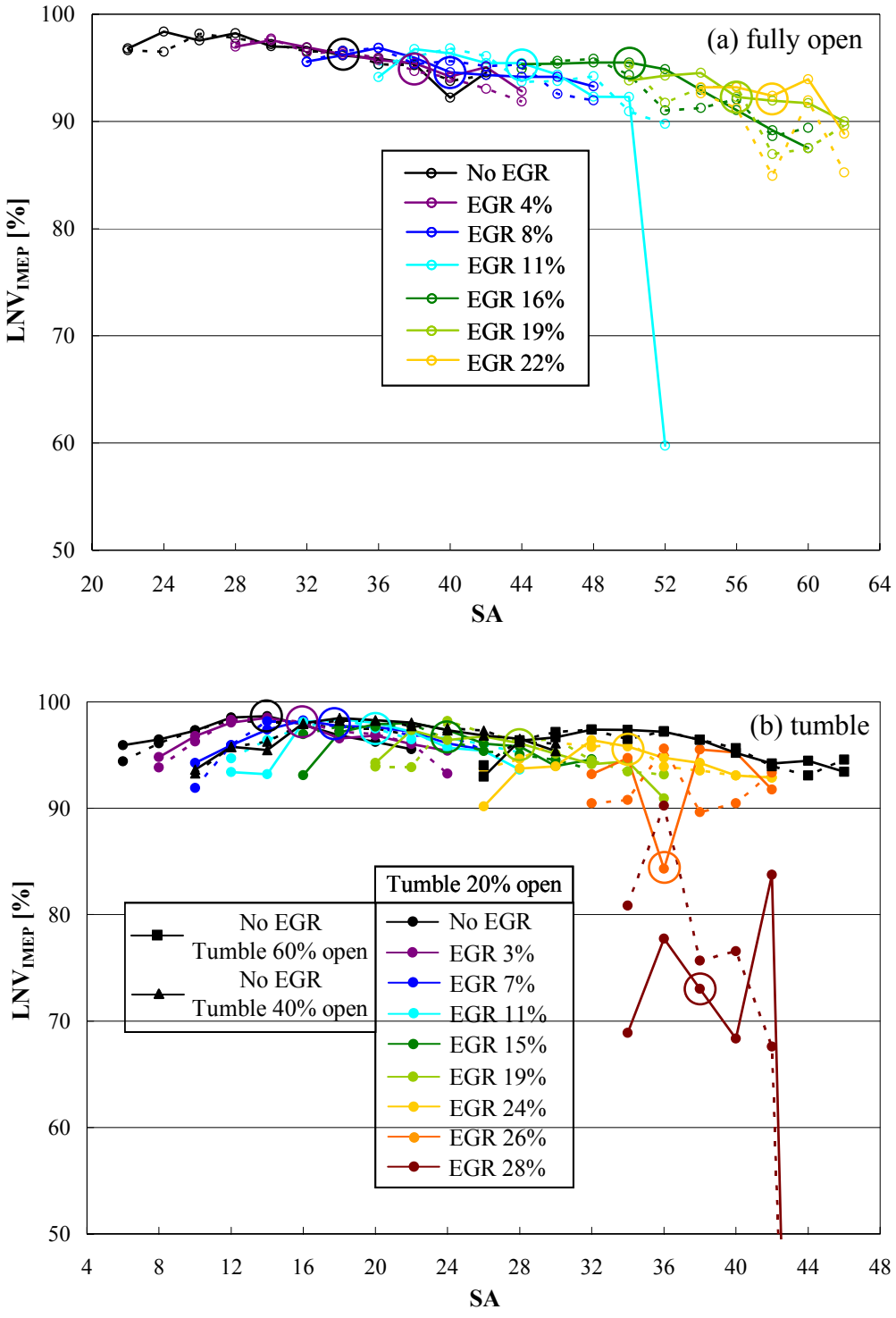

Figure 5.20. Effect of blockages on LNV in IMEP at WP, Cylinder 1. (Continued)

Figure 5.20: Continued.

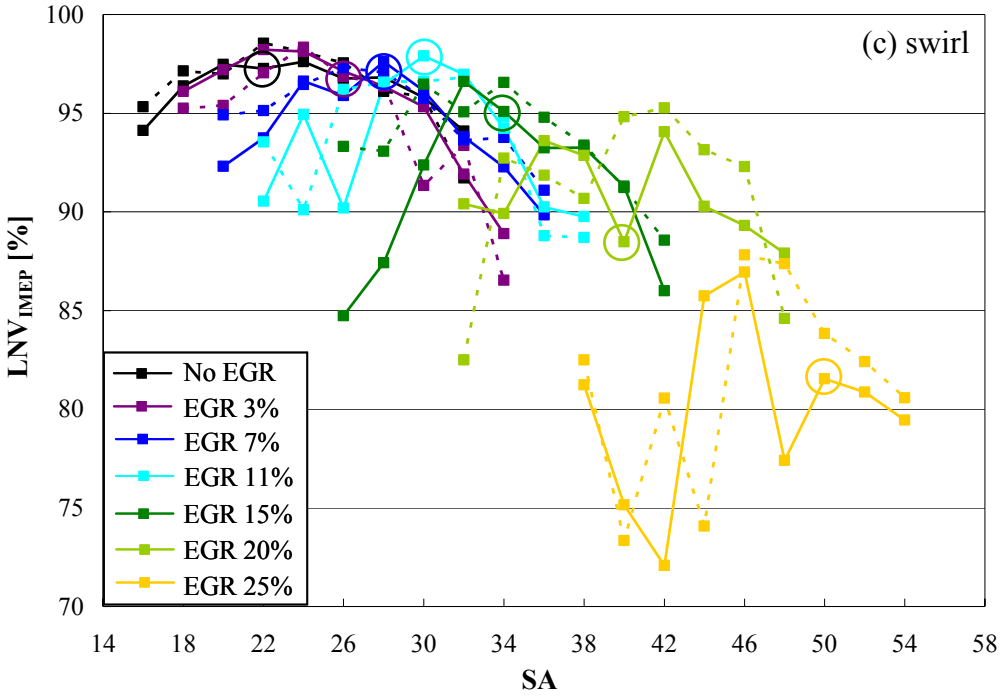

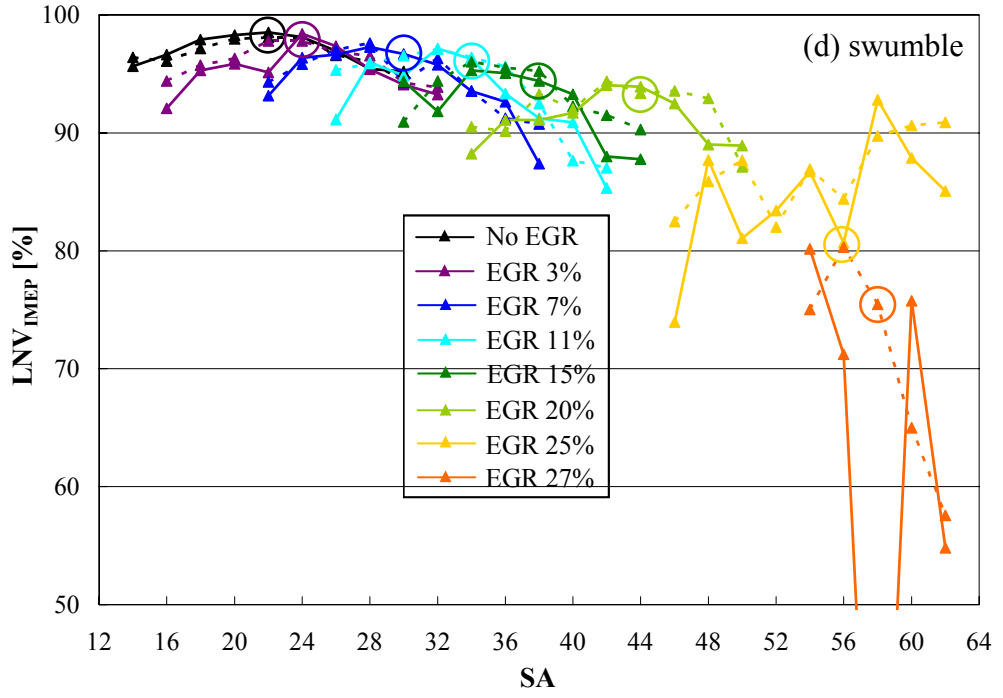

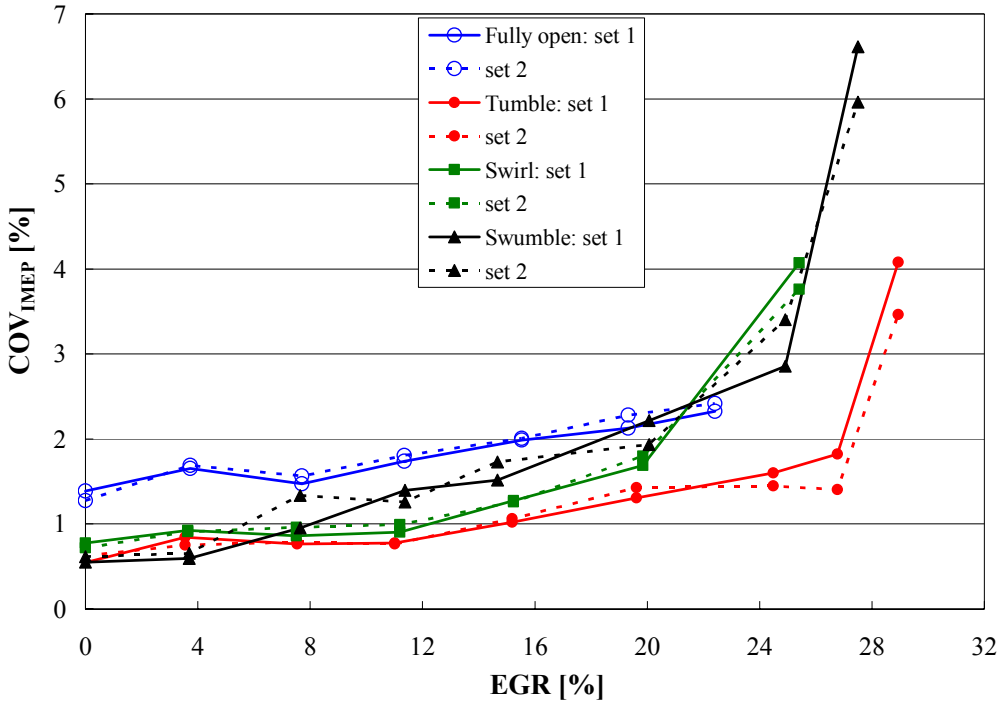

Figure 5.21. COV comparison with EGR under WP, at MBT, cylinder 1.

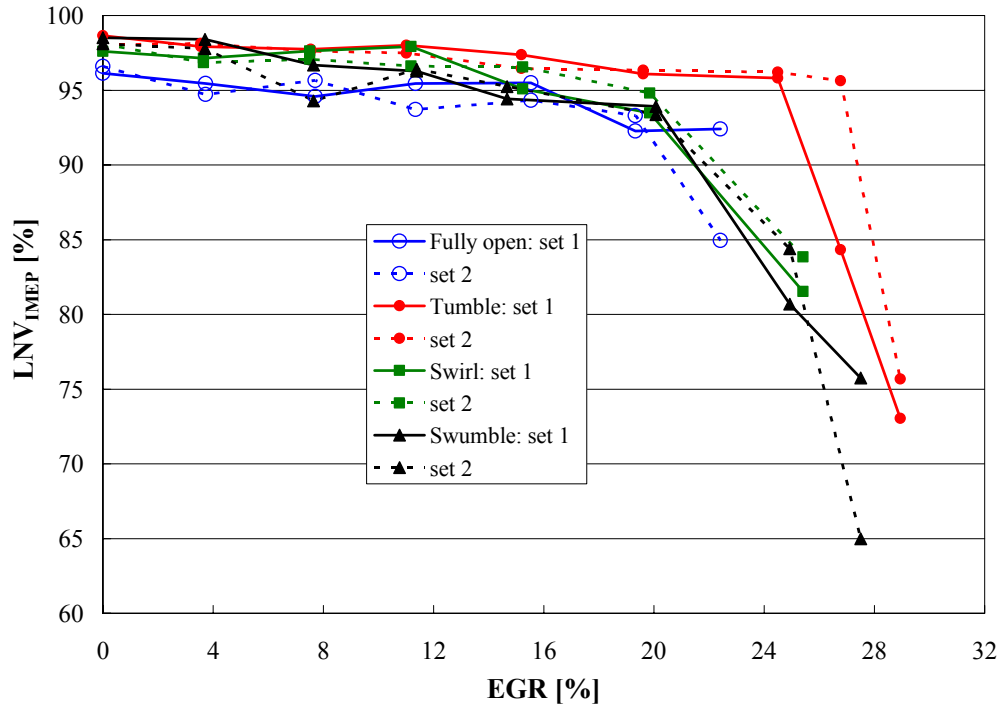

Figure 5.22. LNV comparison with EGR under WP, at MBT, cylinder 1.

Figure 5.23 exhibits IMEP variation for 256 cycles between two cases of no dilution at MBT and maximum EGR at the most advanced spark timing for all configurations. The cyclic variation of IMEP is insignificant for the engine operating without EGR (COV of 1.39%, 0.55%, 0.78%, and 0.56% for fully open, tumble, swirl, and swumble, respectively). However, a substantial number of partial burn and misfiring cycles are observed at the highest EGR with the corresponding COV being 3.04%, 10%, 5.38%, and 5.76% for fully open, tumble, swirl, and swumble, respectively.

Figure 5.24 displays the in-cylinder pressure of 256 cycles for all configurations at MBT timing of about 15% EGR. The reference (zero) for CAD is chosen as TDC of combustion. Relative to the fully open runner, note the reduction in the spread of peak pressure over 256 cycles due to the impact of blockages, particularly for the tumble case (COV of 1.02%, 1.28%, and 1.52% for tumble, swirl, and swumble, respectively, in contrast to 1.99% for fully open), which is consistent with Fig. 5.21. Therefore, the introduction of blockage does help reduce the cyclic combustion variation compared to the unblocked runner.

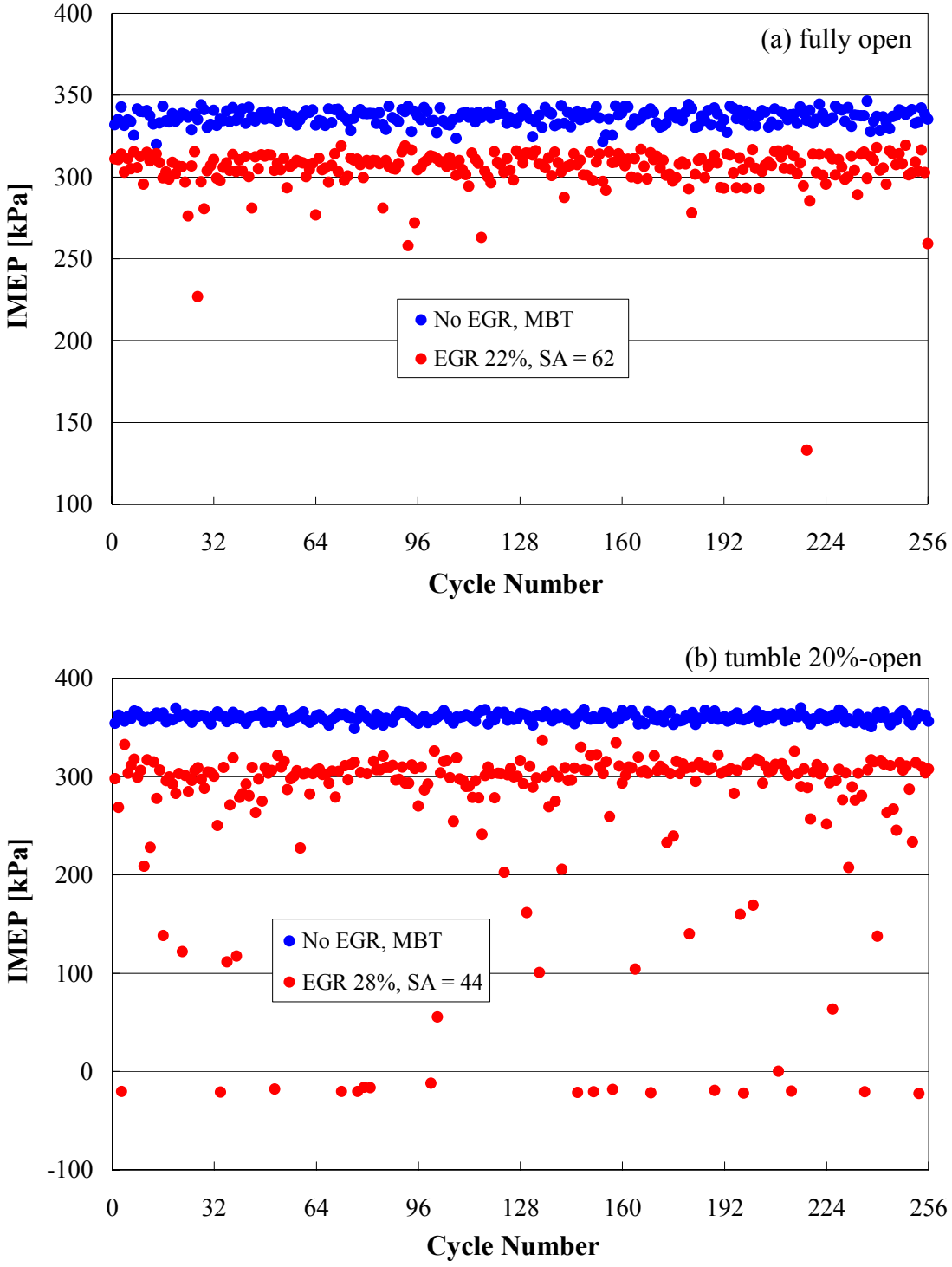

Figure 5.23. Effect of blockages on IMEP for 256 cycles at WP. (Continued)

Figure 5.23: Continued.

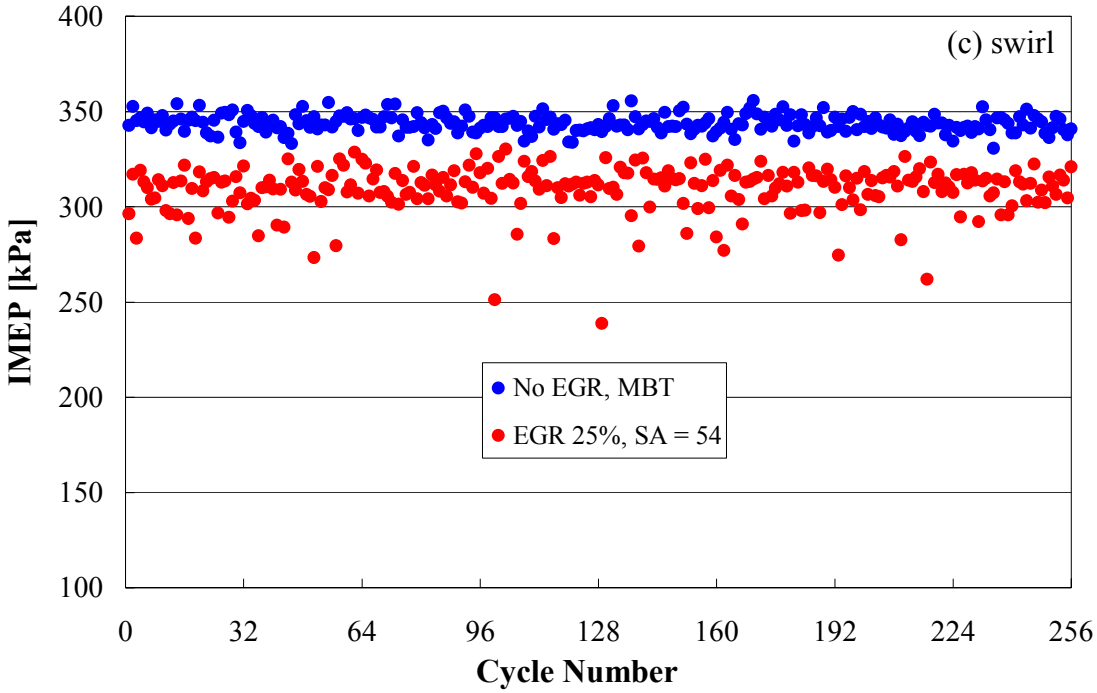

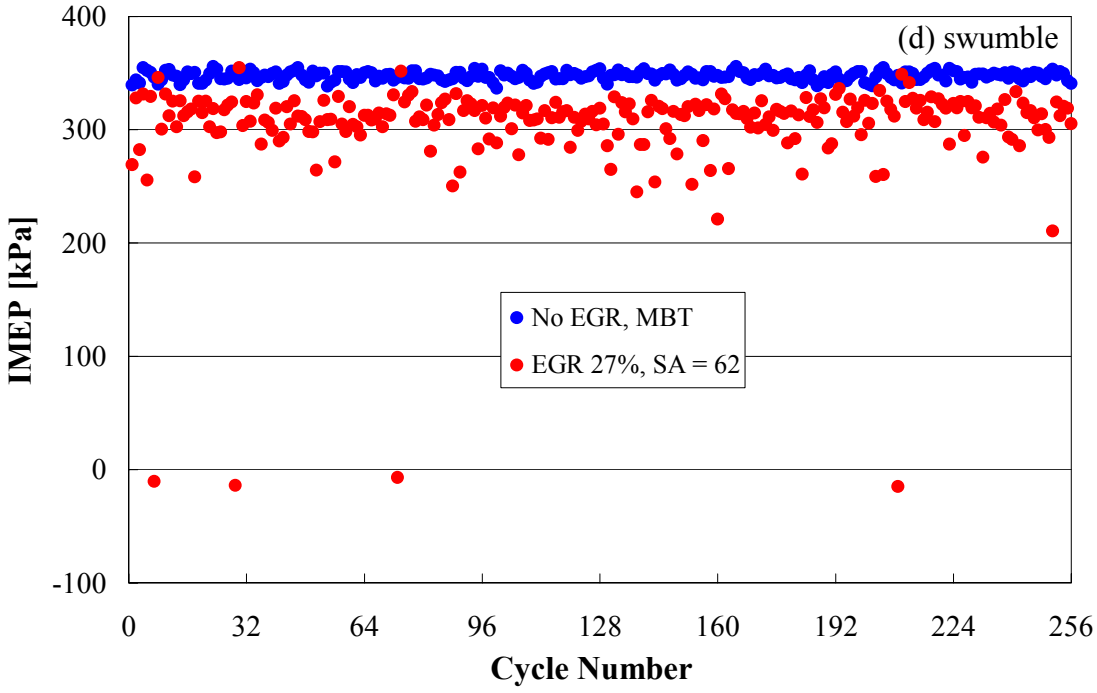

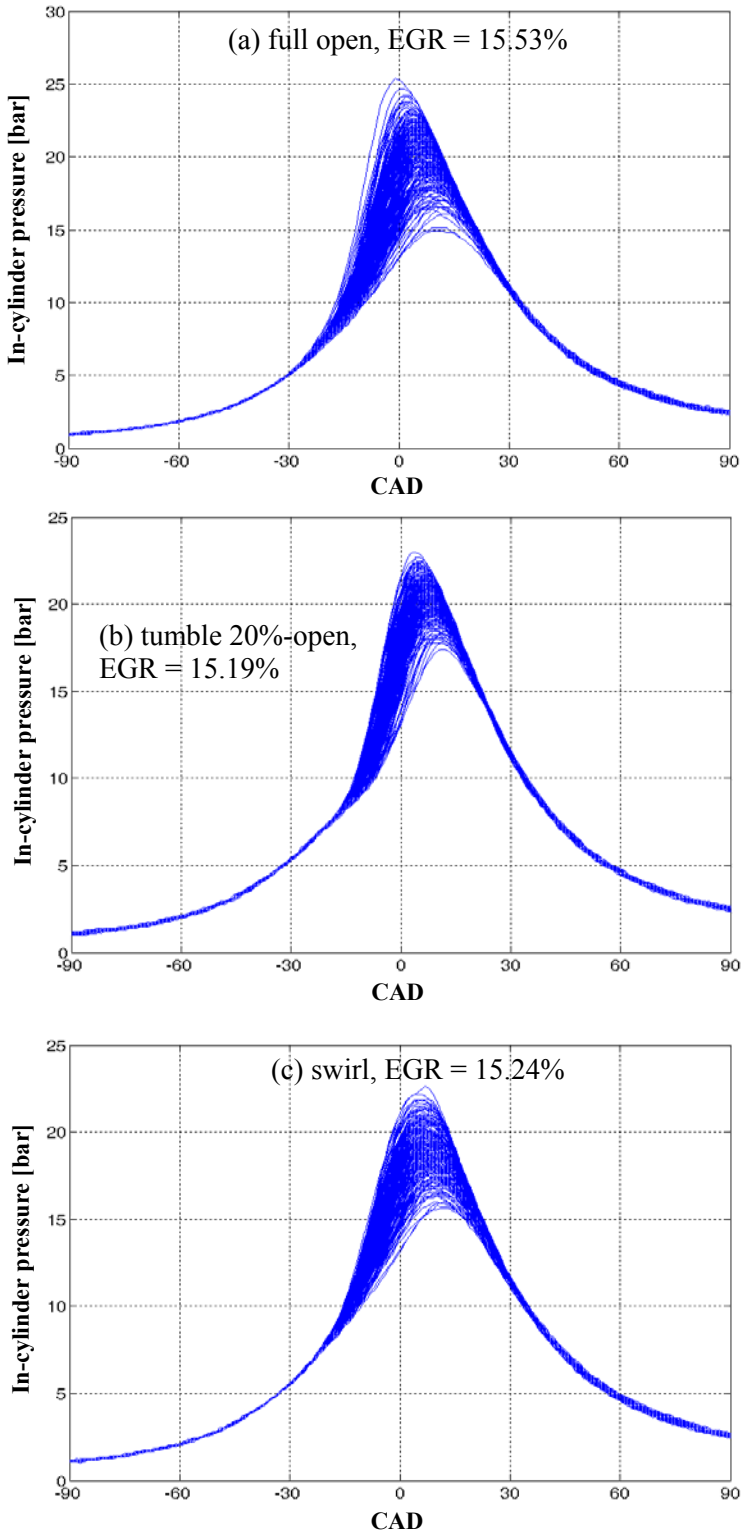

Figure 5.24. Variation of in-cylinder (#1) pressure for 256 cycles at WP, MBT: (a) fully open, (b) tumble, (c) swirl, and (d) swumble. (Continued)

Figure 5.24: Continued.

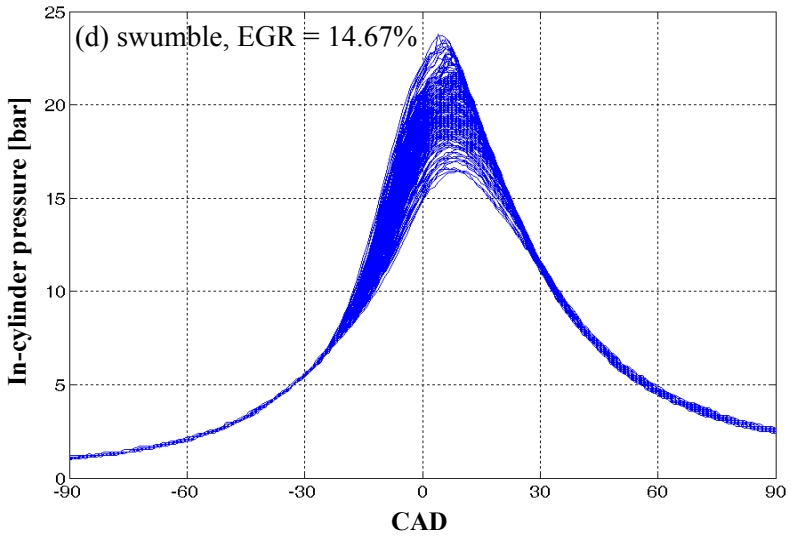

The relationship between the magnitude of the peak in-cylinder pressure p_{max} and the corresponding location θ_{pmax} is illustrated in Fig. 5.25 for 256 cycles at three spark timings under IP for unblocked runner with no dilution (including the most advanced and retarded points as well as the other point in the middle; recall Table 3.2). The right straight line and left curve represent how p_{max} and θ_{pmax} vary for fast and slow burning cycles, respectively (Heywood, 1988). For fast burn, the peak pressure decreases with retarded spark timing (from 46˚ to 30˚ BTDC) while θ_{pmax} moving away from the combustion TDC. Similar trends are observed for slow burning cycles at spark timings of 46˚ and 40˚ BTDC. On the other hand, θ_{pmax} approaches the combustion TDC at the most retarded point of SA = 30˚ BTDC for sufficiently slow burning cycles, as shown in Fig. 5.25. This occurs when the rate of increase in the cylinder pressure due to combustion decreases considerably so that it is offset by the pressure reduction due to the volume increase during expansion. Eventually for extremely slow and late burning, θ_{pmax} may approach TDC, similar to the in-cylinder pressure for motored engine.

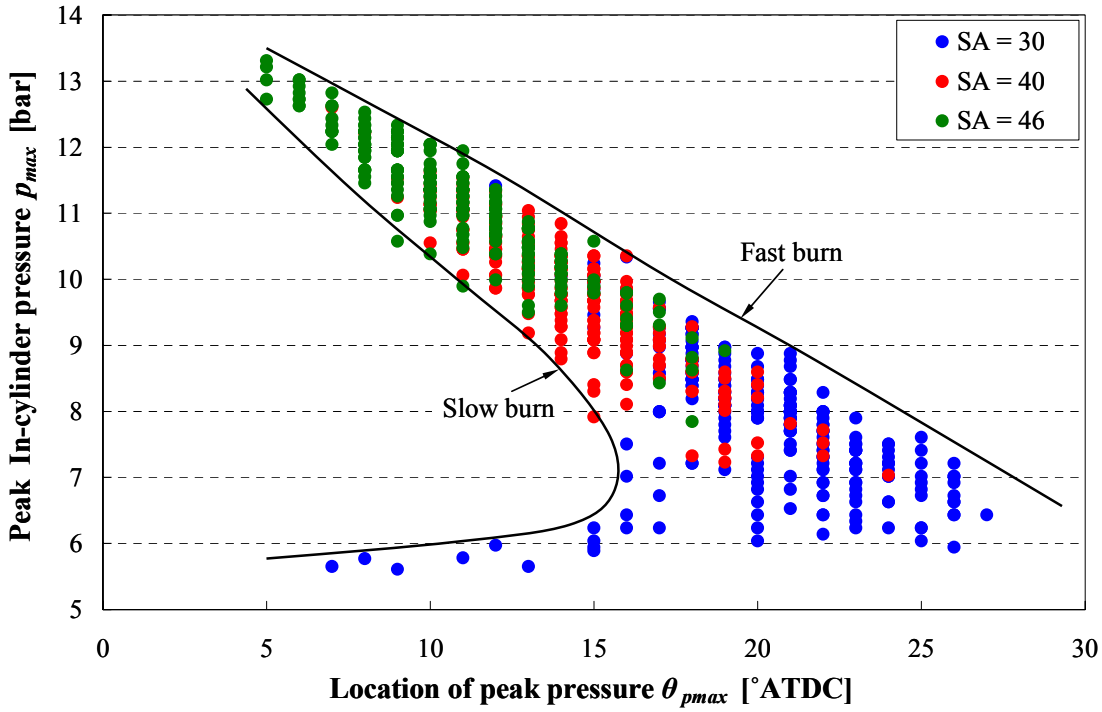

Figure 5.25. Variation of peak in-cylinder (#1) pressure p_{max} vs. the corresponding location θ_{pmax} at IP without EGR, fully open runner.

5.5 Pumping loss

Figure 5.26 compares the in-cylinder *p-V* diagrams for pumping loop at three EGR ratios (0, 11%, and maximum EGR) of MBT with (a) fully open vs. tumble, (b) fully open vs. swirl, and (c) fully open vs. swumble. For all configurations, the pressure during the intake stroke increases with EGR due to more recycled burned gas, consistent with the intake runner pressures of Fig. 5.17. Compared to fully open case at a given dilution level, the blockage reduces the mean pressure during the induction period without much deviation in the exhaust stroke, resulting in more pumping losses. The mean pressure for intake stroke appears comparable for blocked runners at a specific EGR.

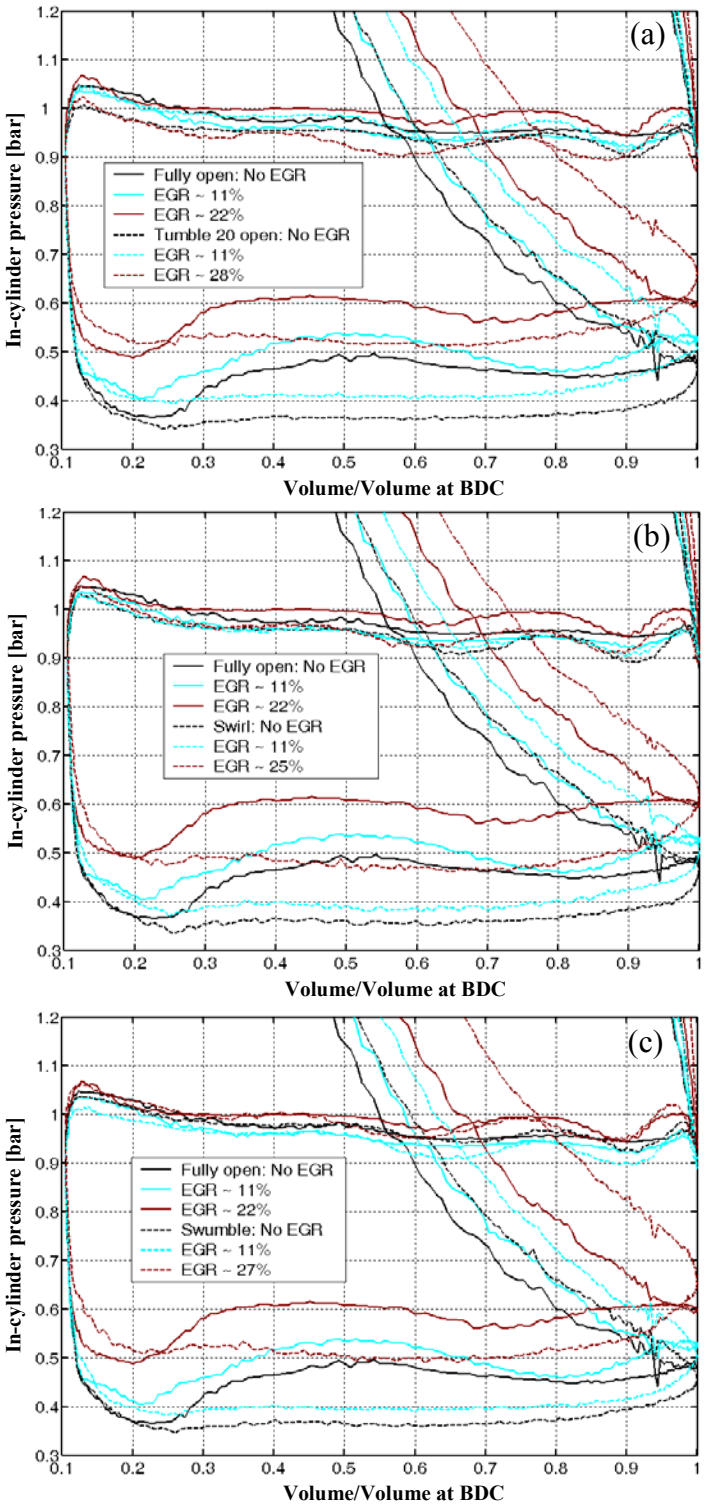

Figure 5.26. In-cylinder pressure vs. volume under WP, at MBT, cylinder 1.

Figures 5.27(a) – 5.27(d) exhibit PMEP variation as a function of spark advance for fully open runner, tumble, swirl, and swumble, respectively. PMEP decreases with EGR dilution for all configurations while the rate of reduction increases with increasing EGR rates, particularly for swirl and swumble. Pumping loss is observed to increase with increasing runner restriction, as illustrated in Fig. 5.27(b) for tumble 60%, 40%, and 20%-open runners without dilution, leading to increased BSFC as illustrated in Fig. 5.6(b). Fig. 5.28 compares PMEP as a function of EGR at MBT; these values along with their ratio to IMEP (PMEP/IMEP) are listed in Table 5.2. PMEP as well as PMEP/IMEP at MBT decrease gradually with EGR due to increased cylinder pressure during the intake process (Fig. 5.26), leading to improved η_f. At a given dilution level shown in Fig. 5.28, charge motion has increased PMEP because of higher flow losses through the blockage. This effect correlates well with the BSFC trend shown in Fig. 5.11. Pumping losses are comparable for blocked runners at most EGR levels, as illustrated in both Fig. 5.28 and Table 5.2, due to similar mean cylinder pressures during the intake and exhaust strokes (recall Fig. 5.26).

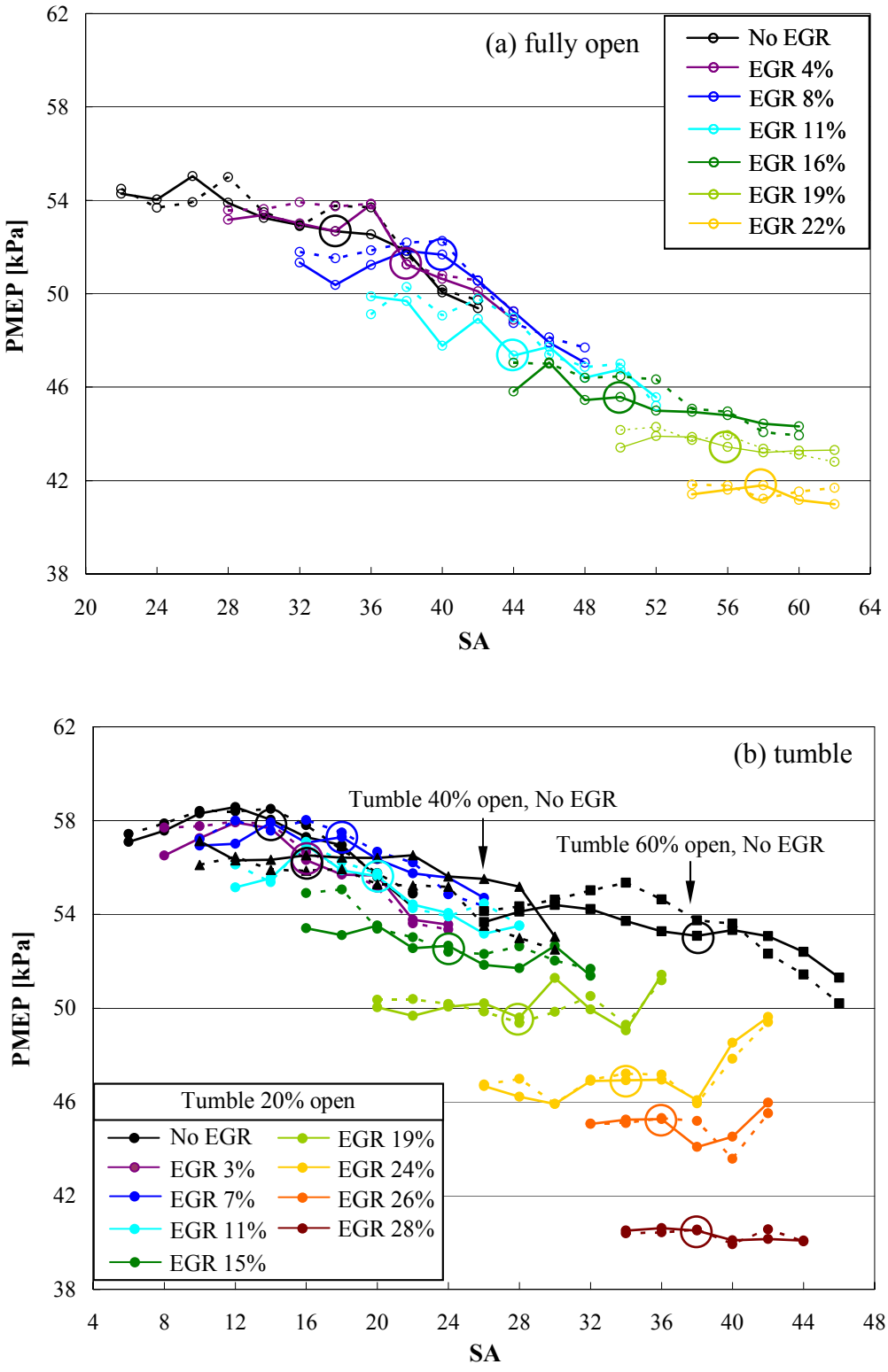

Figure 5.27. Effect of blockages on PMEP at WP, cylinder 1. (Continued)

Figure 5.27: Continued.

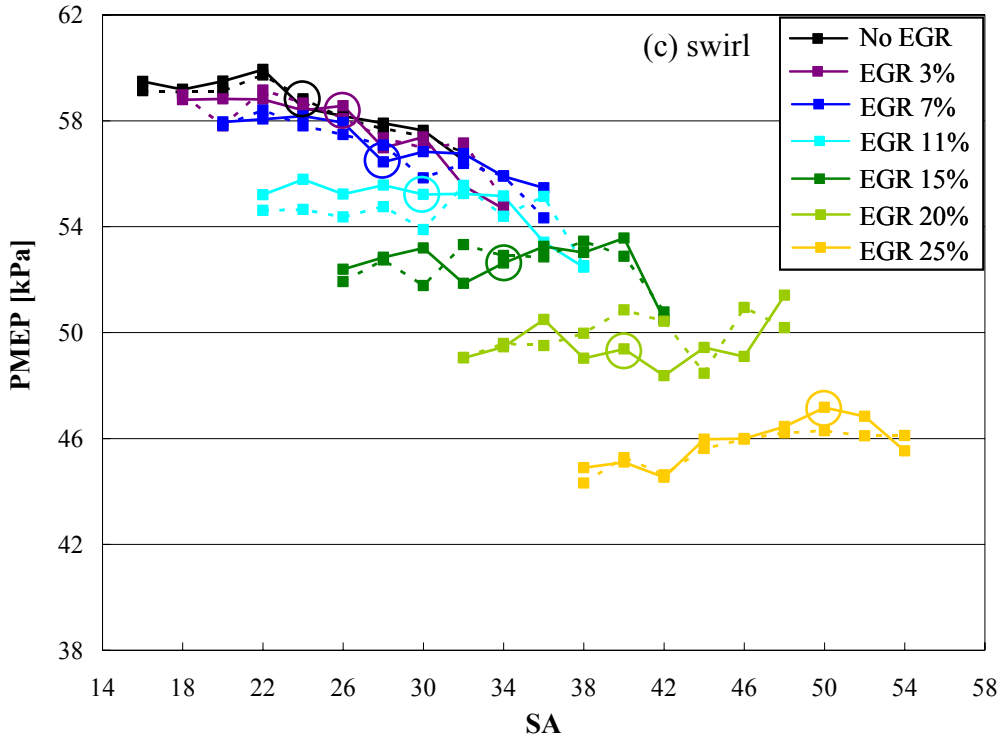

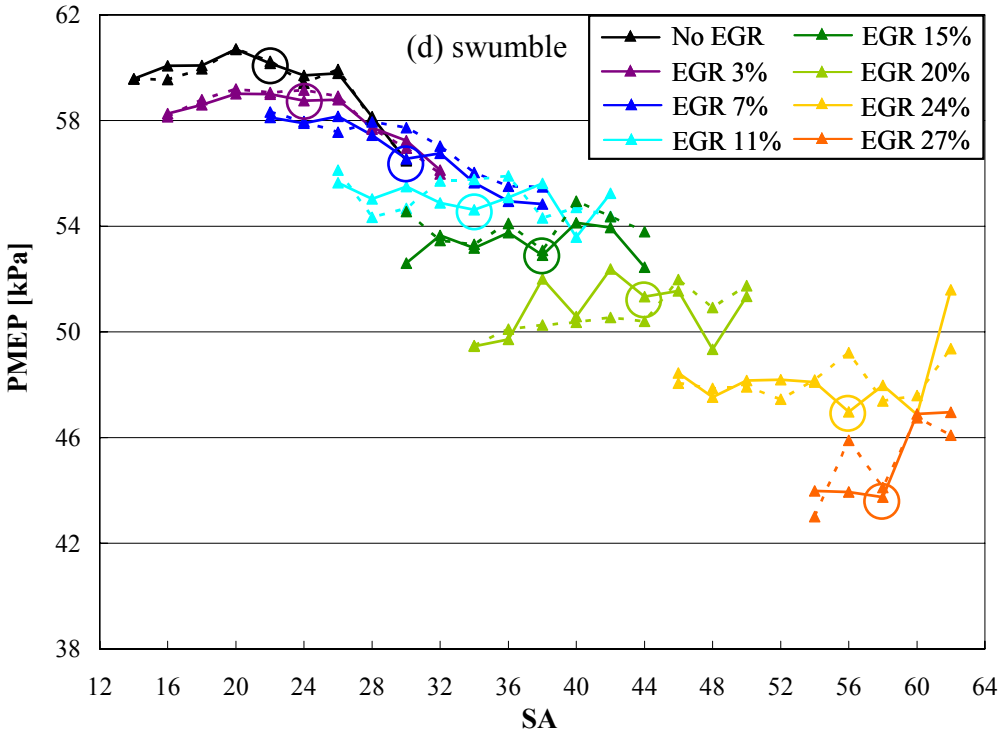

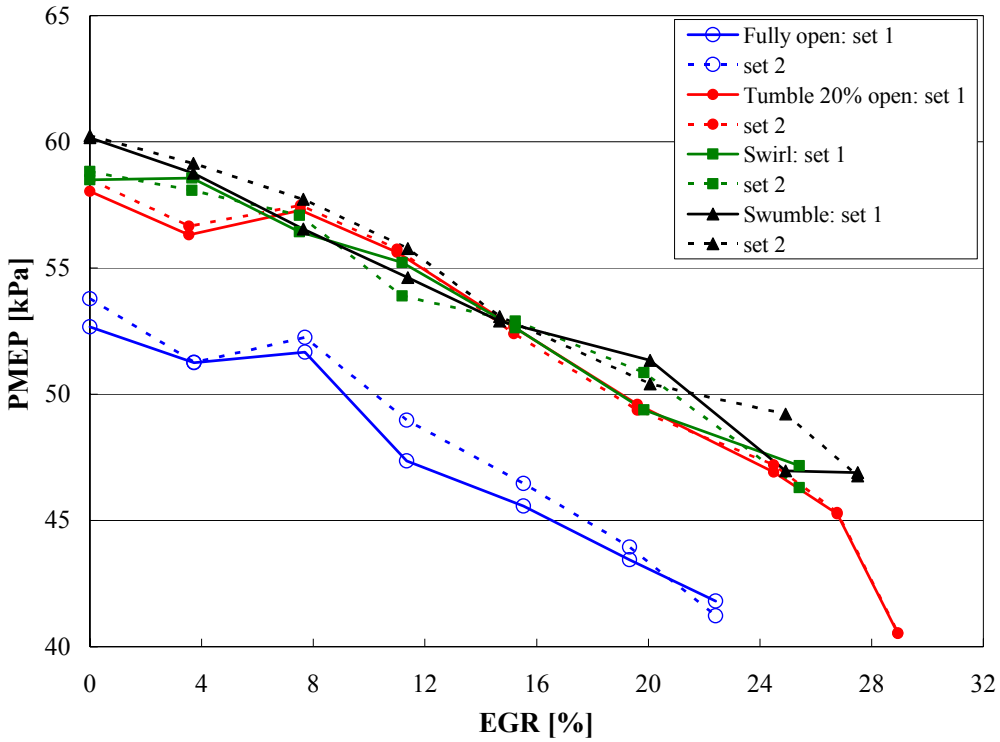

Figure 5.28. PMEP comparison with EGR under WP, at MBT, cylinder 1.

WP (2.41 bar BMEP @1600 rpm)							
IR fully open				IR 20% open - Tumble			
Estimated EGR	MBT (˚BTDC)	PMEP [kPa]	PMEP/ IMEP	Estimated EGR	MBT (˚BTDC)	PMEP [kPa]	PMEP/ IMEP
0	34	52.67	0.1730	0	14	58.04	0.1808
4%	38	51.25	0.1692	3%	16	56.31	0.1751
8%	40	51.67	0.1669	7%	18	57.30	0.1755
11%	44	47.35	0.1602	11%	20	55.63	0.1749
16%	50	45.57	0.1549	15%	24	52.65	0.1712
19%	56	43.44	0.1509	19%	28	49.59	0.1685
22%	58	41.80	0.1435	24%	34	46.91	0.1644
				26%	36	45.26	0.1584
				28%	38	40.51	0.1327

Table 5.2. Comparison of PMEP and its ratio to IMEP at MBT, cylinder 1. (Continued)

Table 5.2: Continued.

WP (2.41 bar BMEP @1600 rpm)							
IR 20% open - Swirl				IR 20% open - Swumble			
Estimated EGR	MBT (˚BTDC)	PMEP [kPa]	PMEP/ IMEP	Estimated EGR	MBT (˚BTDC)	PMEP [kPa]	PMEP/ IMEP
0	24	58.49	0.1811	0	22	60.16	0.1832
3%	26	58.56	0.1834	3%	24	58.75	0.1810
7%	28	56.44	0.1789	7%	30	56.55	0.1799
11%	30	55.22	0.1766	11%	34	54.62	0.1792
15%	34	52.63	0.1715	15%	38	52.90	0.1759
20%	40	49.38	0.1668	20%	44	51.34	0.1755
25%	50	47.17	0.1540	25%	56	46.97	0.1647
				27%	58	46.89	0.1645

The variation of the corresponding MAP is shown in Fig. 5.29 as function of spark advance, followed by a comparison of MAPs for different blockages at MBT in Fig. 5.30. As expected in light of Fig. 5.17, MAP increases with dilution. At a given dilution level shown in Fig. 5.29, MAP exhibits somewhat higher value at the most advanced spark timing than the most retarded point over 0 to moderate EGR. MAP does not significantly change with spark at the highest EGR rates. As Fig. 5.30 illustrates, charge motion is associated with higher MAP compared to the unrestricted runner at a specific EGR. This is mainly due to the larger throttle opening for restricted case to counter the decreasing engine breathing capacity which will be elaborated in Chapter 6.

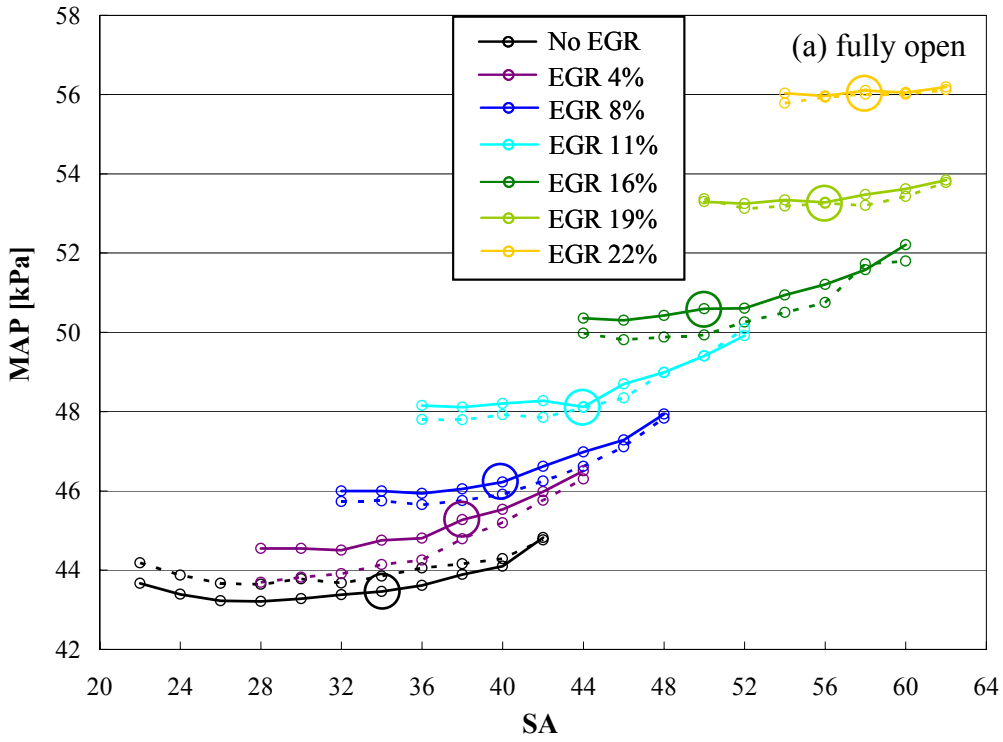

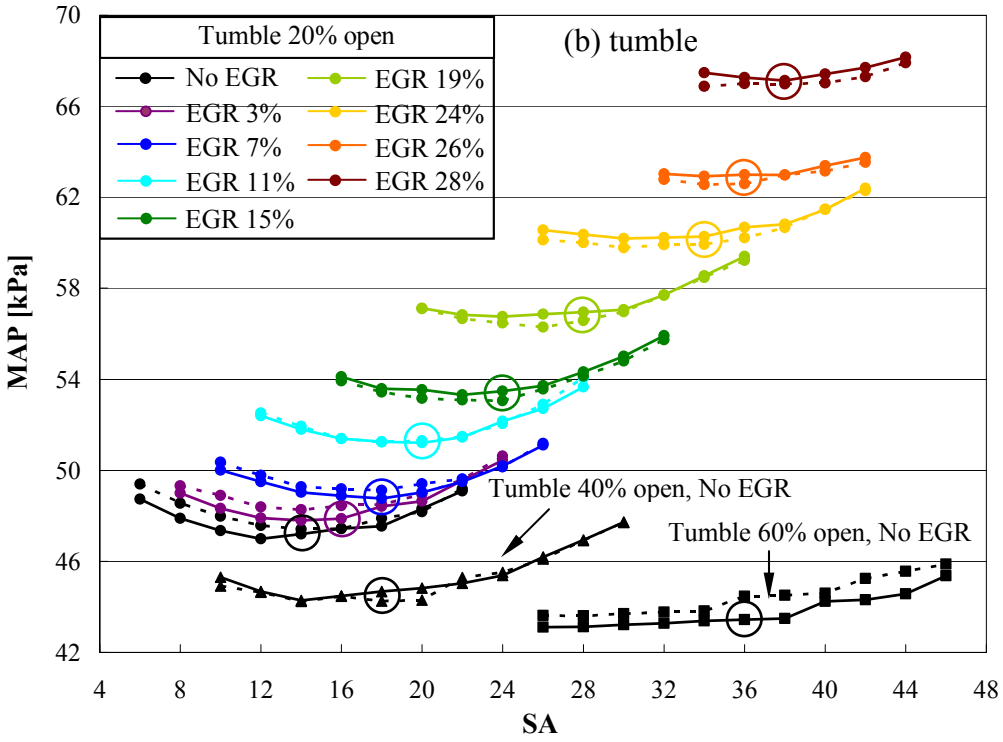

Figure 5.29. Effect of blockages on MAP at WP. (Continued)

Figure 5.29: Continued.

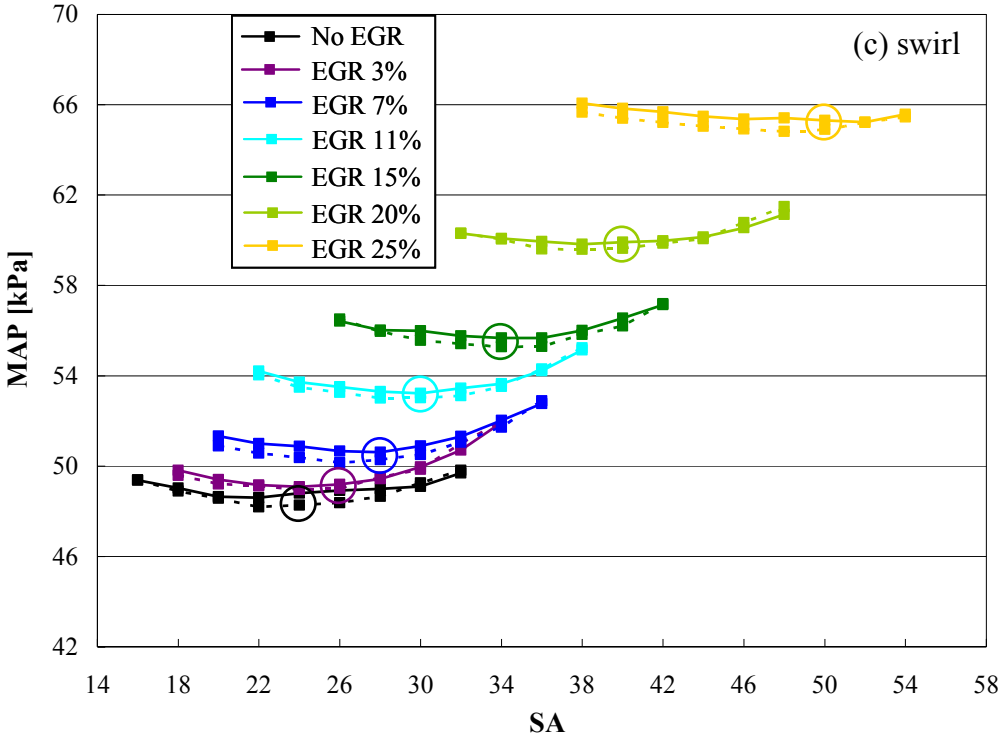

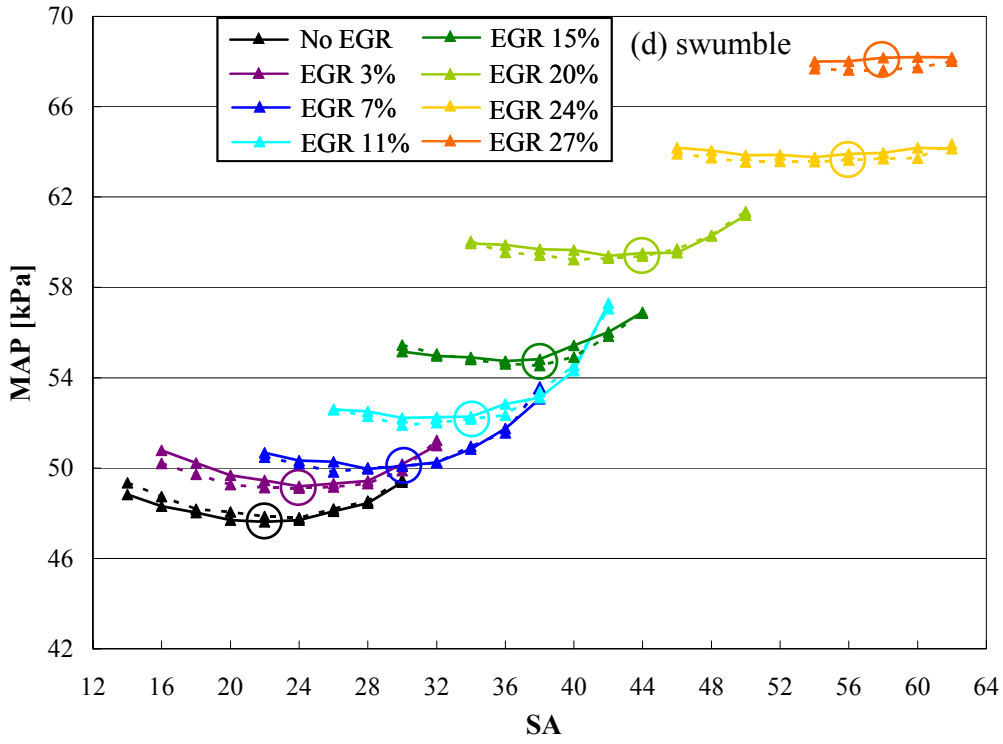

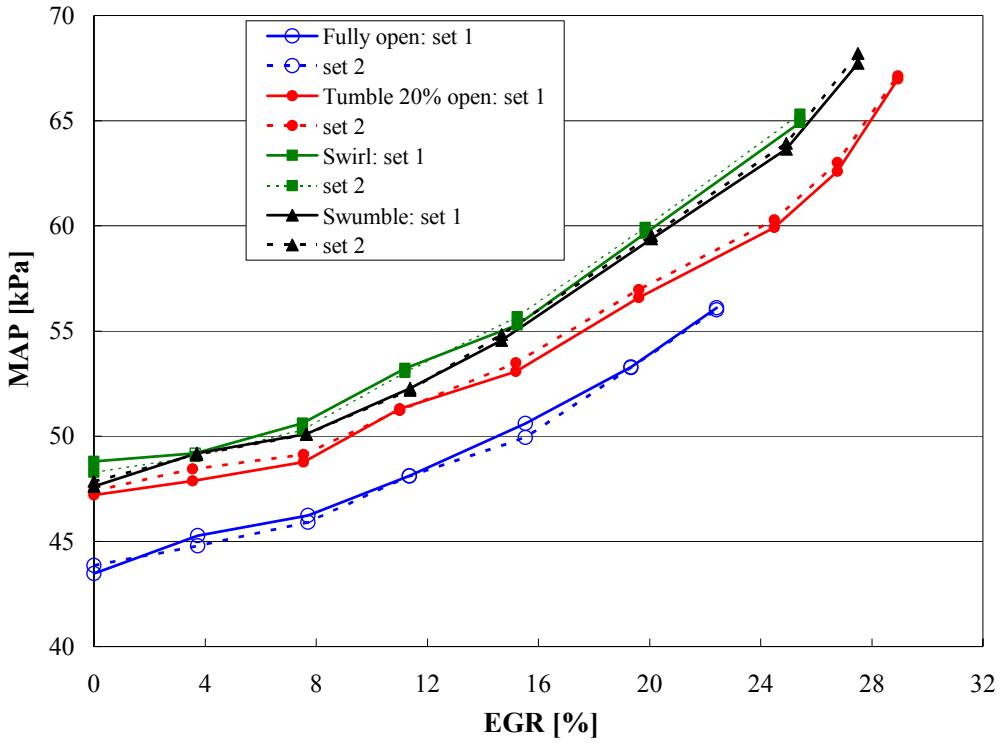

Figure 5.30. MAP comparison with EGR under WP, at MBT.

5.6 Combustion characteristics

In-cylinder charge motion has a strong influence on the combustion characteristics, particularly on the combustion duration. The variation of 0-100% burn duration (abbreviated as θ_{0-100}) with spark advance is depicted in Figs. 5.31(a) – 5.31(d) for fully open, tumble, swirl, and swumble, respectively, which is calculated by a modified combustion pressure rise method (recall Section 4.5). At MBT, θ_{0-100} increases with EGR for all configurations because of reduced flame speed and burn rate, particularly at high dilution level. At a specific EGR, θ_{0-100} decreases first as spark is advanced from the most retarded timing until the point corresponding to the lowest θ_{0-100} [for example, the most retarded spark timing and the one for the minimum θ_{0-100} are 16˚

and 28° BTDC, respectively, for tumble at 15% EGR; Fig. 5.31(b), dark green curve]. Advancing spark from the most retarded timing results in earlier burn of the fuel during compression with higher peak in-cylinder pressure (recall Fig. 5.15) and temperature, which may lead to shorter burn duration. θ_{0-100} starts increasing as the spark is further advanced beyond the ignition point corresponding to the minimum burn duration [for example, above 28° for tumble at 15% EGR; Fig. 5.31(b), dark green curve]. Figure 5.32 compares θ_{0-100} between unblocked and blocked runners as a function of EGR at MBT timing. 0 – 100% burn duration increases with EGR dilution, similar to the experimental findings of Goldwitz and Heywood (2005). Compared to the fully open runner, the dramatic reduction in θ_{0-100} with tumble blockage is clear at all EGRs. A longer θ_{0-100}, however, is observed for swirl and swumble at low dilution levels indicating a reduced burn rate. For EGR levels above 12%, swumble appears to reduce θ_{0-100} moderately compared with the unblocked case, while swirl remains comparable to the fully open runner.

The 0-10% and 10-90% burn durations (θ_{0-10} and θ_{10-90}) vs. spark advance are shown at various EGR rates in Figs. 5.33 and 5.34, respectively, followed by a comparison of burn delay and flame propagation periods for different blockages as a function of EGR at MBT timing in Figs. 5.35 and 5.36. The magnitudes of the burn delay, flame propagation, and total burn duration angles are given in Table 5.3 at MBT. At a given dilution level, Fig. 5.33 illustrates that θ_{0-10} is insensitive to spark, particularly at moderate EGR rates. On the other hand, θ_{10-90} decreases significantly as the spark is advanced from the most retarded point, as shown in Fig. 5.34.

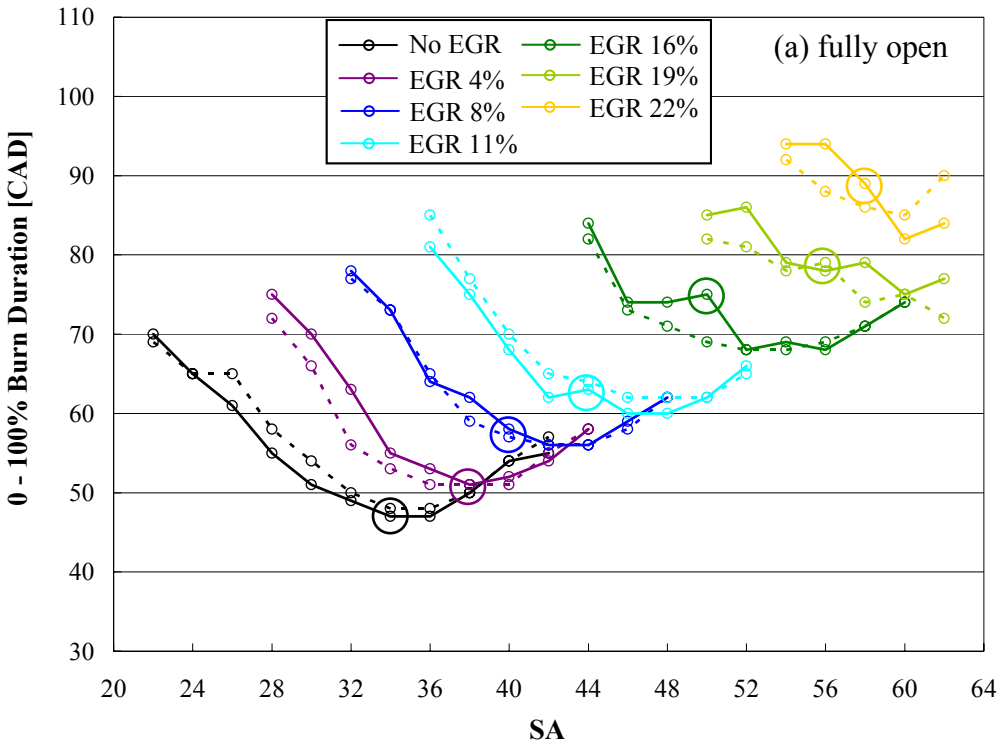

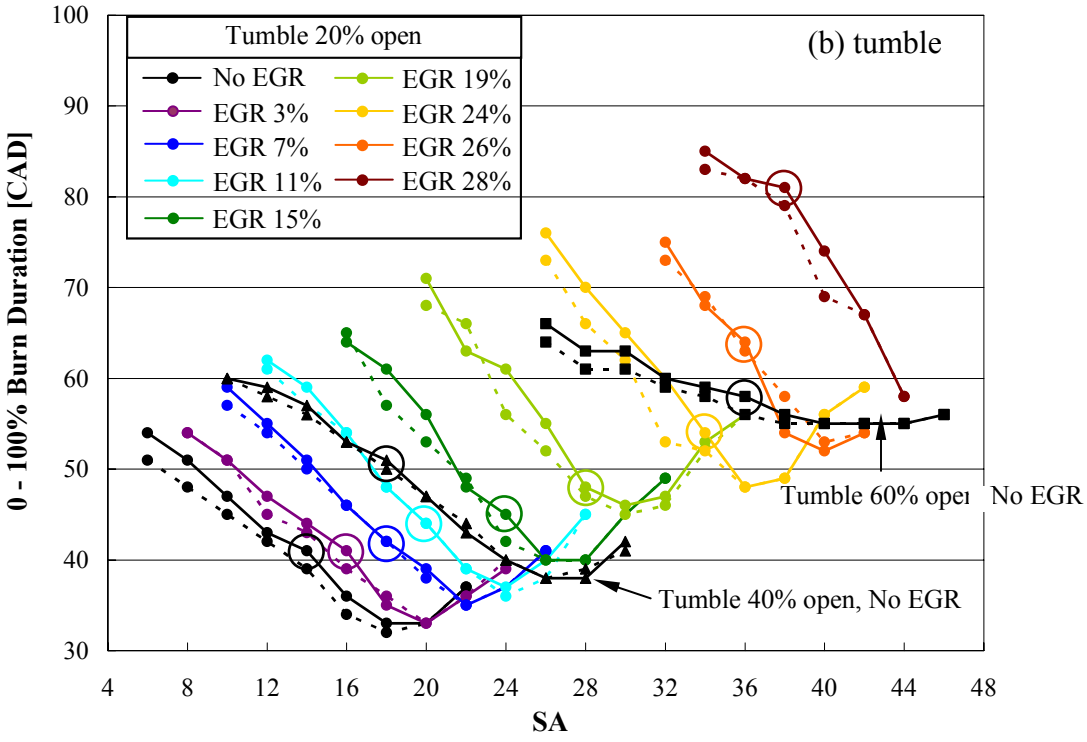

Figure 5.31. Effect of blockages on 0-100% burn duration at WP, cylinder 1. (Continued)

Figure 5.31: Continued.

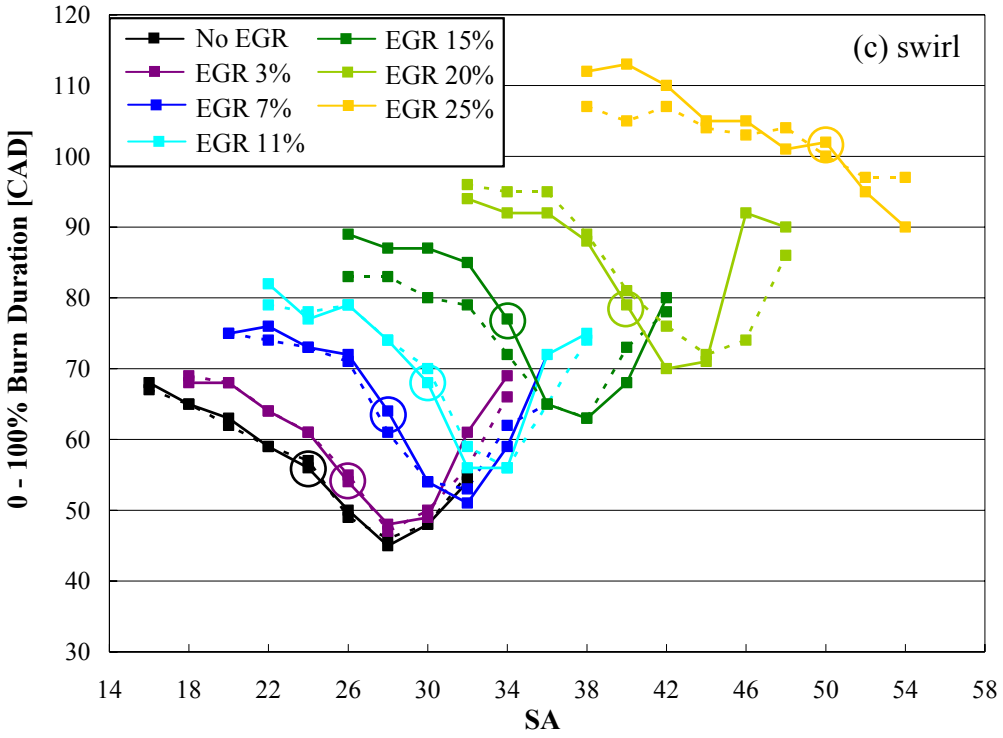

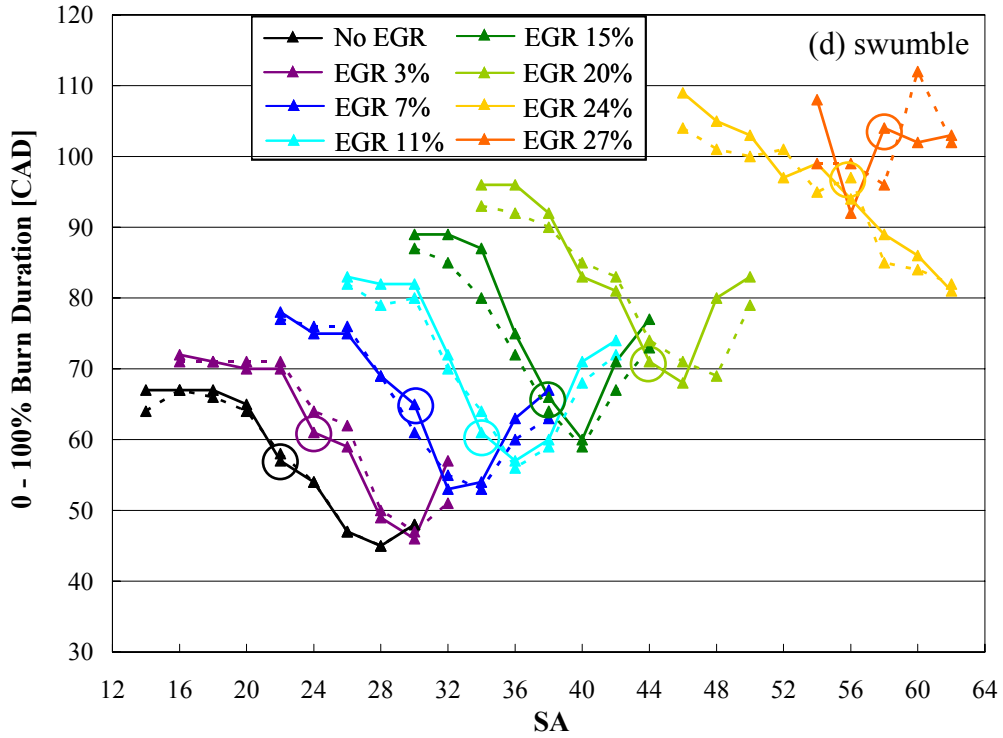

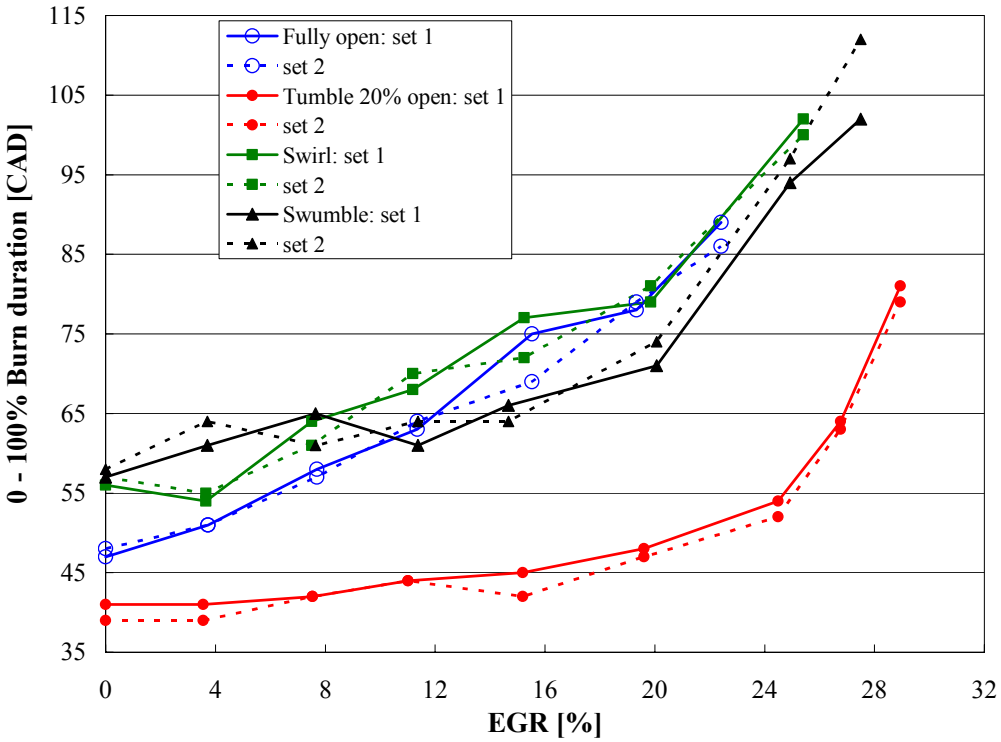

Figure 5.32. 0-100% burn duration comparison with EGR under WP, at MBT, cylinder 1.

As the in-cylinder mixture approaches the optimum EGR, θ_{10-90} is observed to increase significantly for swirl and swumble. Figure 5.35 clearly shows that the introduction of EGR increases the burn delay period at MBT, consistent with the experimental findings of Ivanic *et al.*, 2005. Blockage brings about considerable reduction in θ_{0-10} compared to the unrestricted runner, with tumble being the most effective compared to swirl and swumble. For fully open runner and swirl, θ_{10-90} increases with EGR as illustrated in Fig. 5.36. For swumble and tumble, θ_{10-90} is less sensitive to EGR ratios below 16%, particularly for tumble, suggesting that the impact of dilution for tumble is mainly on lengthening the burn delay. At maximum EGR, θ_{10-90} is significantly lengthened for blocked runners due to substantially deteriorated combustion. Although tumble continues

to accelerate the burn rate during flame propagation period (θ_{10-90}), both swirl and swumble exhibit longer θ_{10-90} in comparison with the unblocked runner, possibly due to the structure of the in-cylinder fluid motion. As indicated earlier, swirl behaves like a solid body rotation and usually persists through compression and combustion (Heywood, 1988 and Hill and Zhang, 1994). During the flame propagation period, less turbulence is generated from the conserved swirl motion compared to the unblocked case, thereby leading to the reduction in flame speed and then the burn rate. The combustion characteristics of swumble are similar to swirl displayed in Figs. 5.35 and 5.36, suggesting that swirl and swumble may result in a similar structure of the in-cylinder fluid motion. Tumble, on the other hand, starts breaking up rapidly near TDC, leading to substantially high turbulence intensity during ignition and then the increased combustion rate (Tabaczynski, 1976 and Arcoumanis *et al.*, 1992). The enhanced turbulence results in strong reduction of the burn delay. As the breakdown of the tumble vortex continues through the combustion, the tumble-generated turbulence may still be enhanced and hence the burn rate during the flame propagation period seems to increase as well.

The corresponding location of 50% mass fraction burned $\left(\theta_{50}\right)$ is compared in Figs. 5.37 and 5.38 as a function of spark advance and EGR rate, respectively. At a specific dilution level, θ_{50} is advanced as the spark is advanced from the most retarded point for all configurations shown in Fig. 5.37, mainly due to the early combustion during compression. The introduction of blockage results in retarded θ_{50}, particularly below 16% EGR at MBT, compared to fully open runner, mainly due to the retarded spark timing for charge motion (recall Table 5.1).

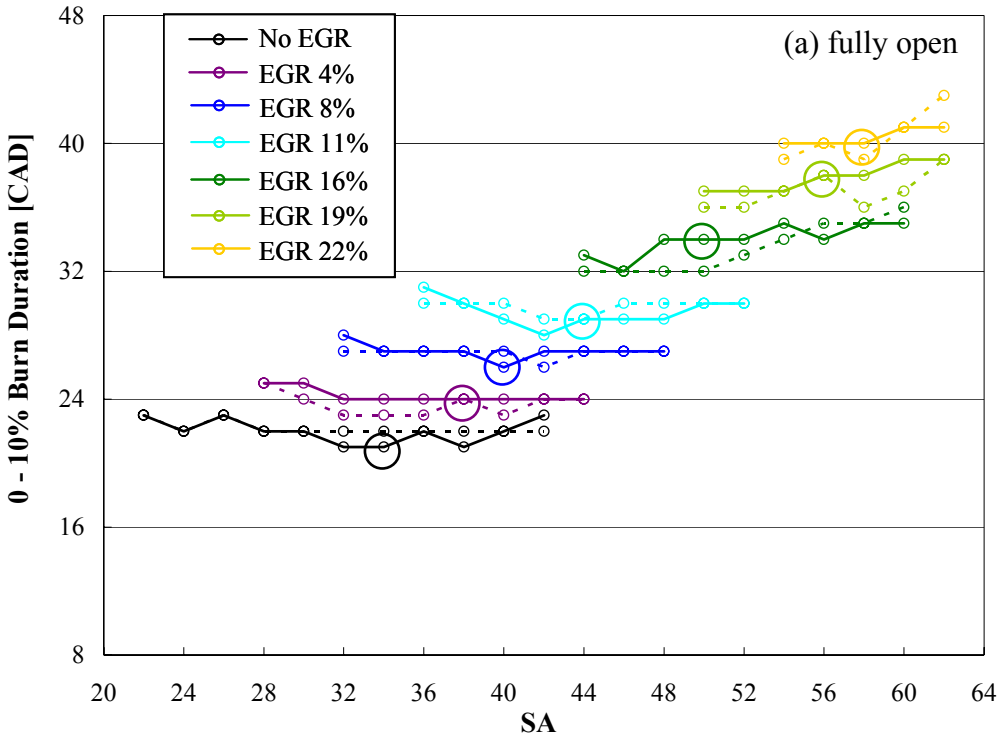

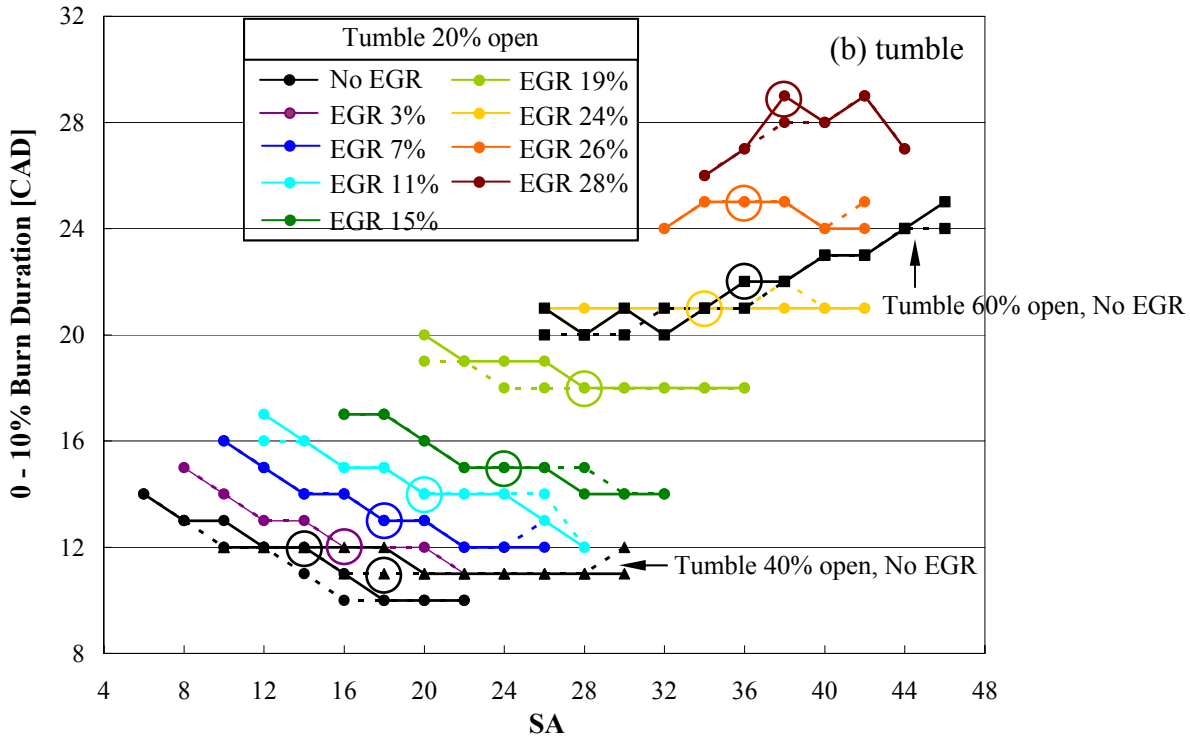

Figure 5.33. Effect of blockages on 0-10% burn duration at WP, cylinder 1. (Continued)

Figure 5.33: Continued.

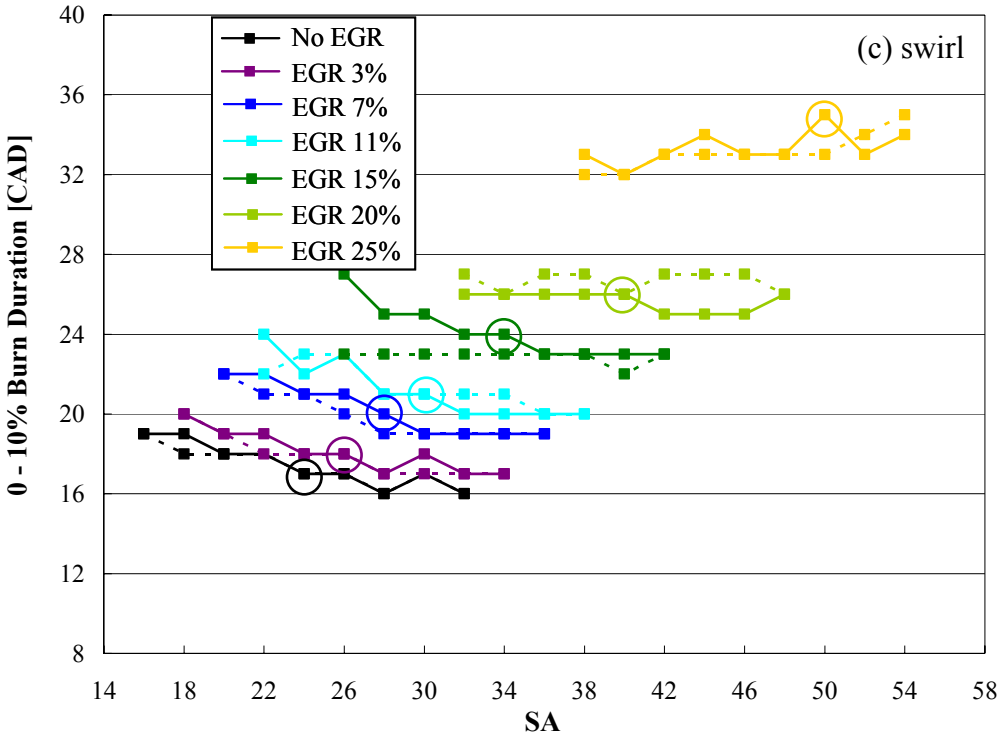

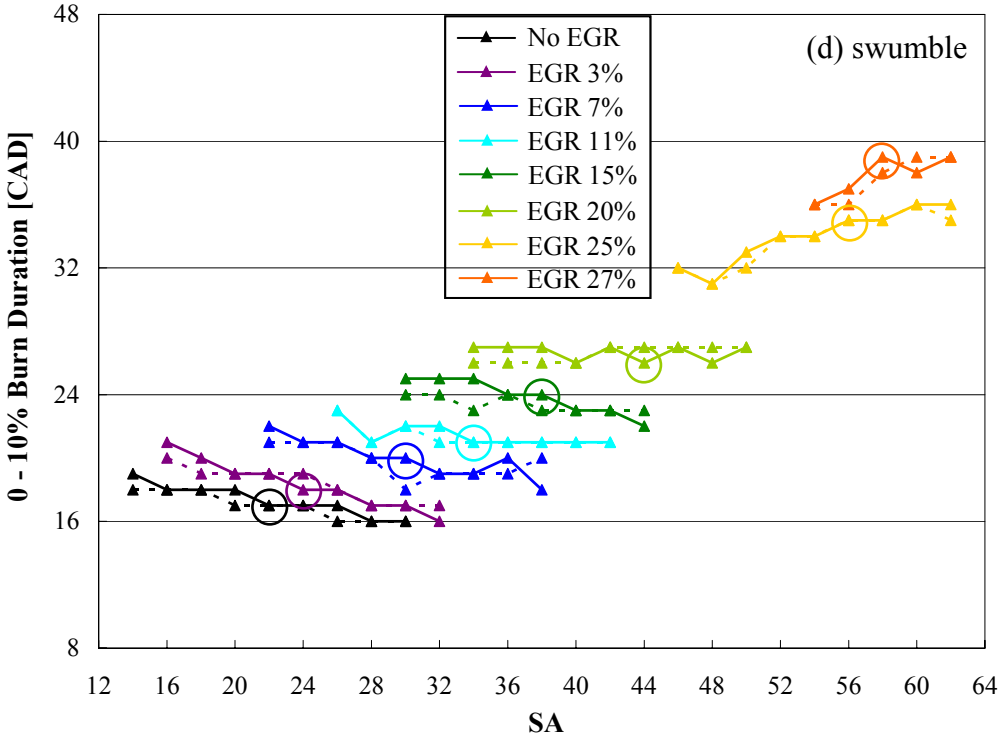

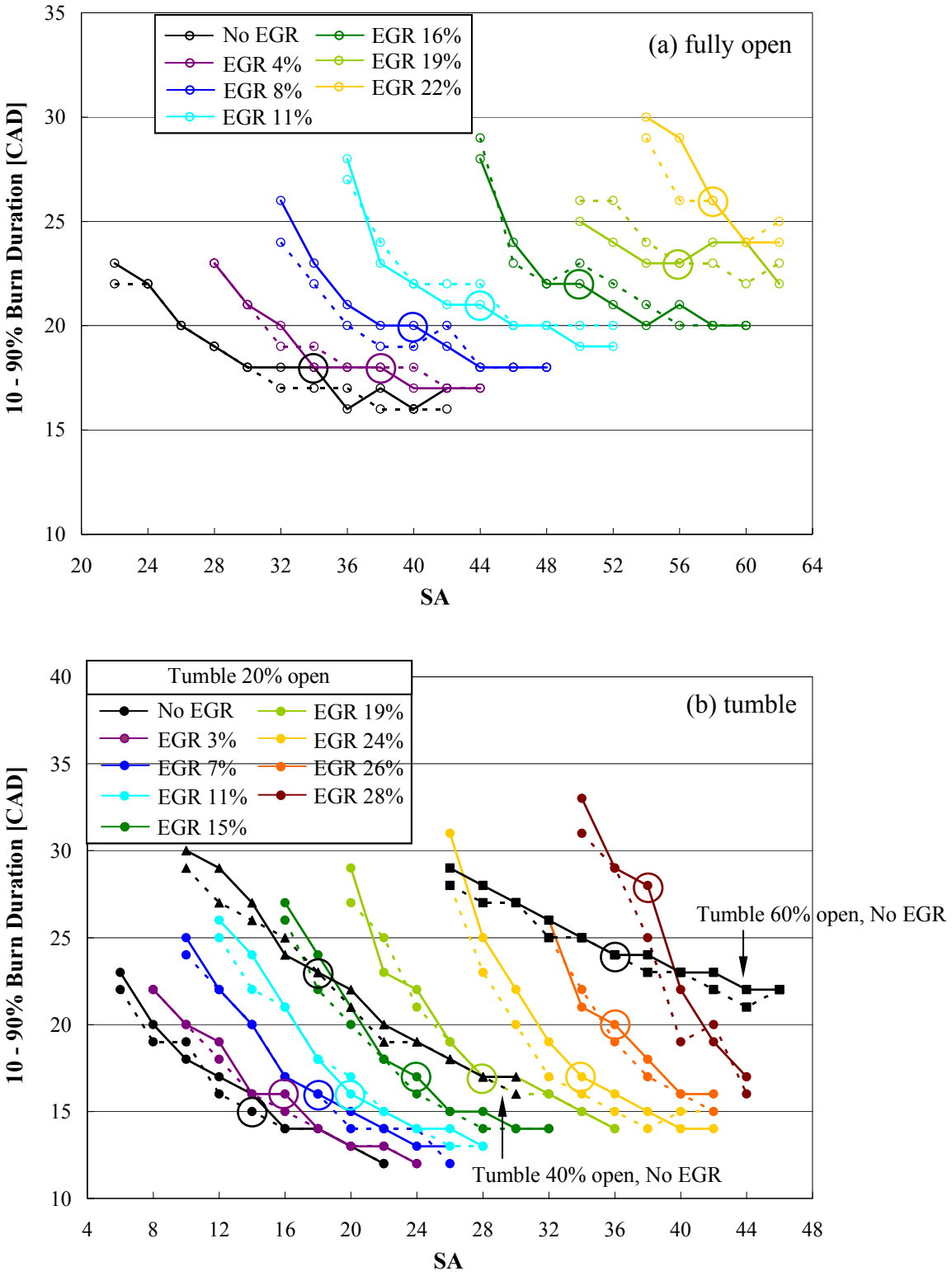

Figure 5.34. Effect of blockages on 10-90% burn duration at WP, cylinder 1.

(Continued)

Figure 5.34: Continued.

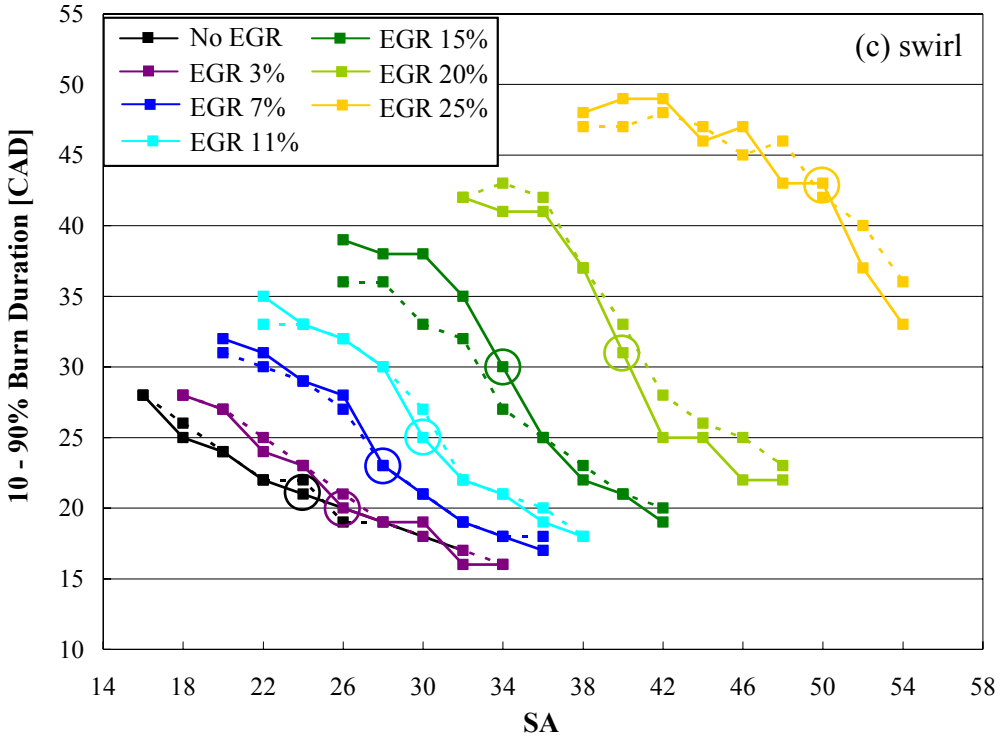

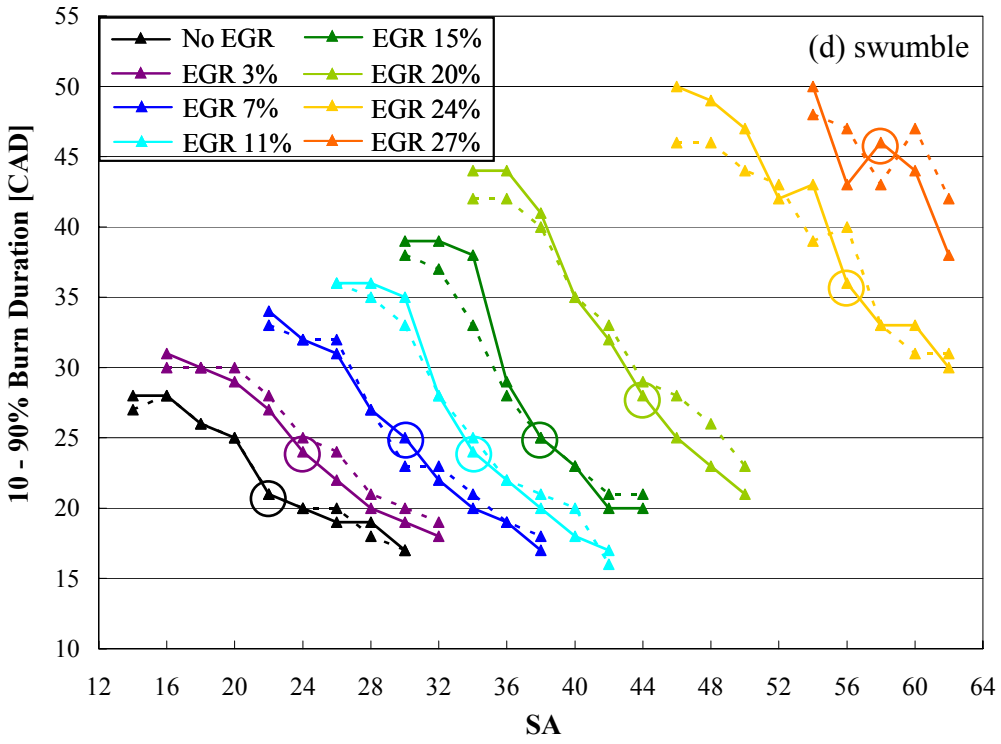

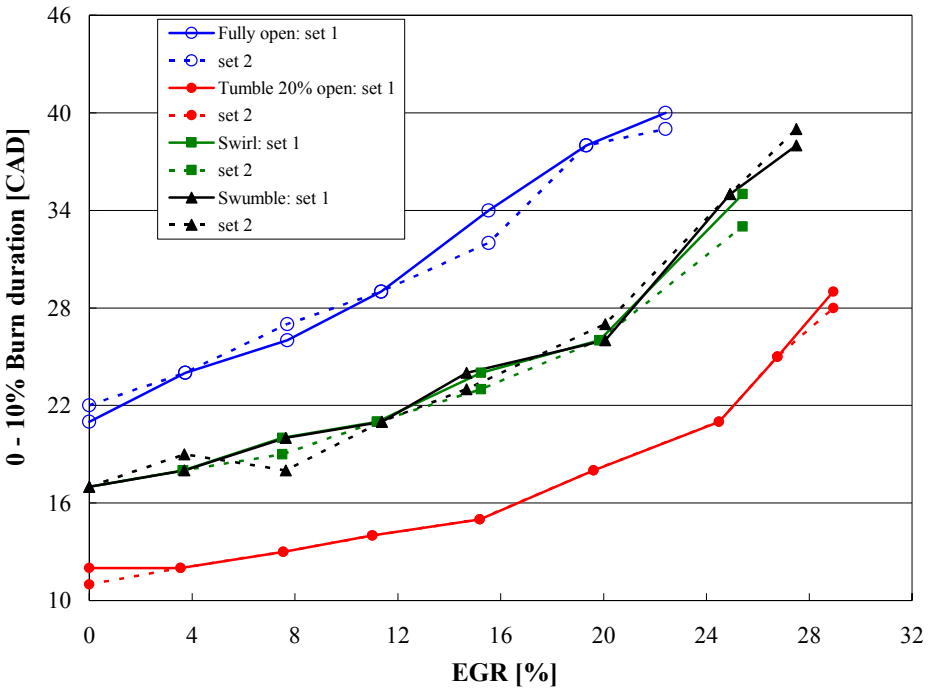

Figure 5.35. 0-10% burn duration comparison with EGR under WP, at MBT, cylinder 1.

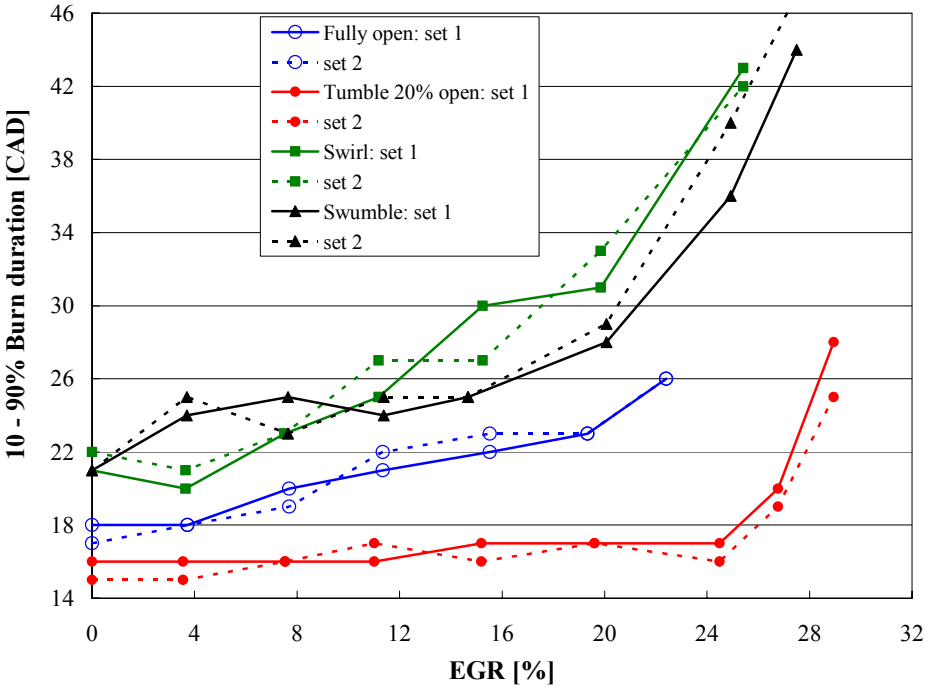

Figure 5.36. 10-90% burn duration comparison with EGR under WP, at MBT, cylinder 1.

WP (2.41 bar BMEP @1600 rpm), MBT timing							
IR fully open				IR 20% open - Tumble			
Estimated EGR	0 - 10% [CAD]	10 - 90% [CAD]	0 - 100% [CAD]	Estimated EGR	0 - 10% [CAD]	10 - 90% [CAD]	0 - 100% [CAD]
0	21	18	47	0	12	16	41
4%	24	18	51	3%	12	16	41
8%	26	20	58	7%	13	16	42
11%	29	21	63	11%	14	16	44
16%	34	22	75	15%	15	17	45
19%	38	23	78	19%	18	17	48
22%	40	26	89	24%	21	17	54
				26%	25	20	64
				28%	29	28	81

WP (2.41 bar BMEP @1600 rpm), MBT timing							
IR 20% open - Swirl				IR 20% open - Swumble			
Estimated EGR	0 - 10% [CAD]	10 - 90% [CAD]	0 - 100% [CAD]	Estimated EGR	0 - 10% [CAD]	10 - 90% [CAD]	0 - 100% [CAD]
0	17	21	56	0	17	21	57
3%	18	20	54	3%	18	24	61
7%	20	23	64	7%	20	25	65
11%	21	25	68	11%	21	24	61
15%	24	30	77	15%	24	25	66
20%	26	31	79	20%	26	28	71
25%	35	43	102	25%	35	36	94
				27%	38	44	102

Table 5.3. Comparison of burn delay (θ_{0-10}), flame propagation (θ_{10-90}), and total burn duration (θ_{0-100}).

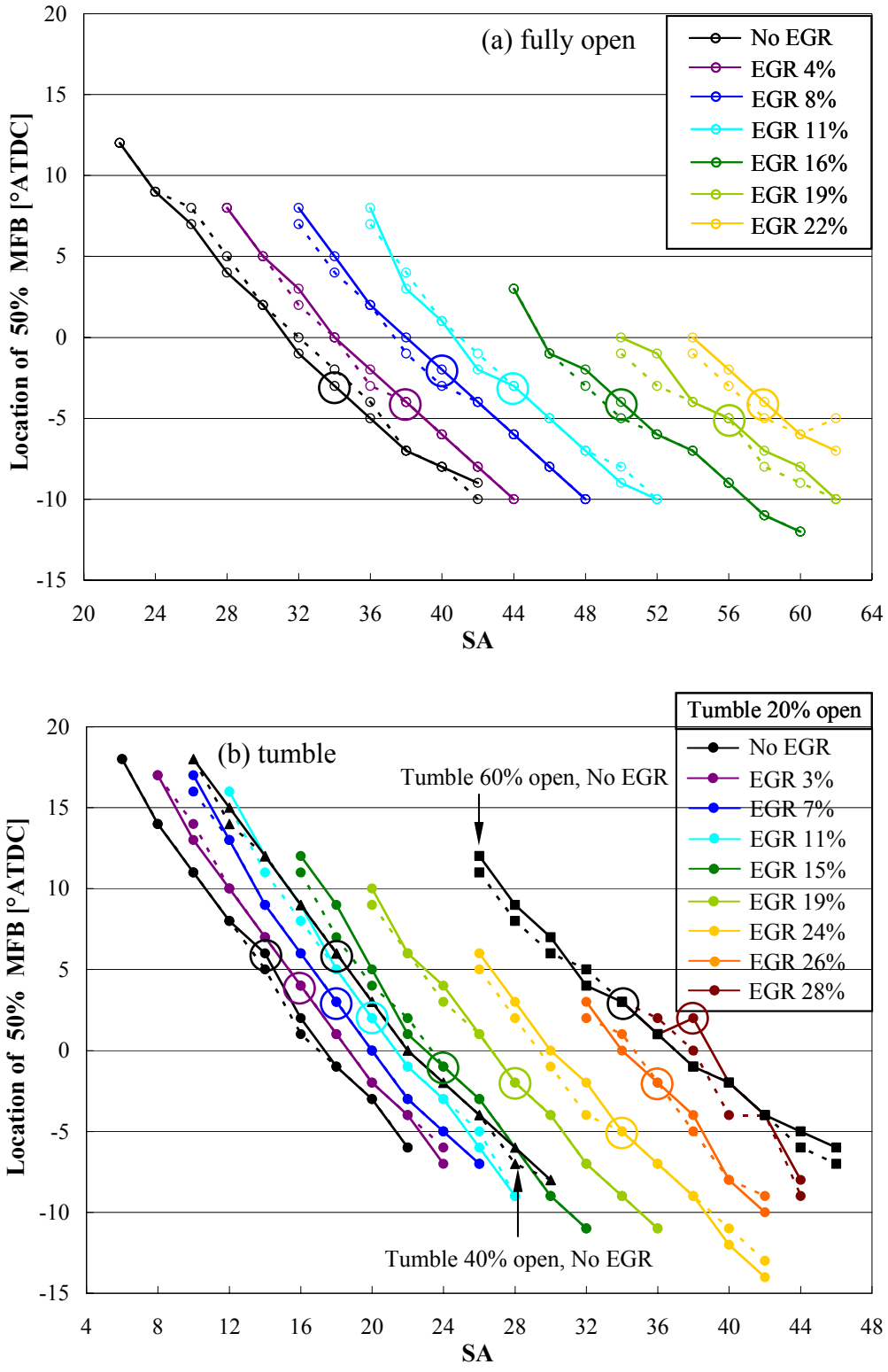

Figure 5.37. Effect of blockages on CA50 at WP, cylinder 1. (Continued)

Figure 5.37: Continued.

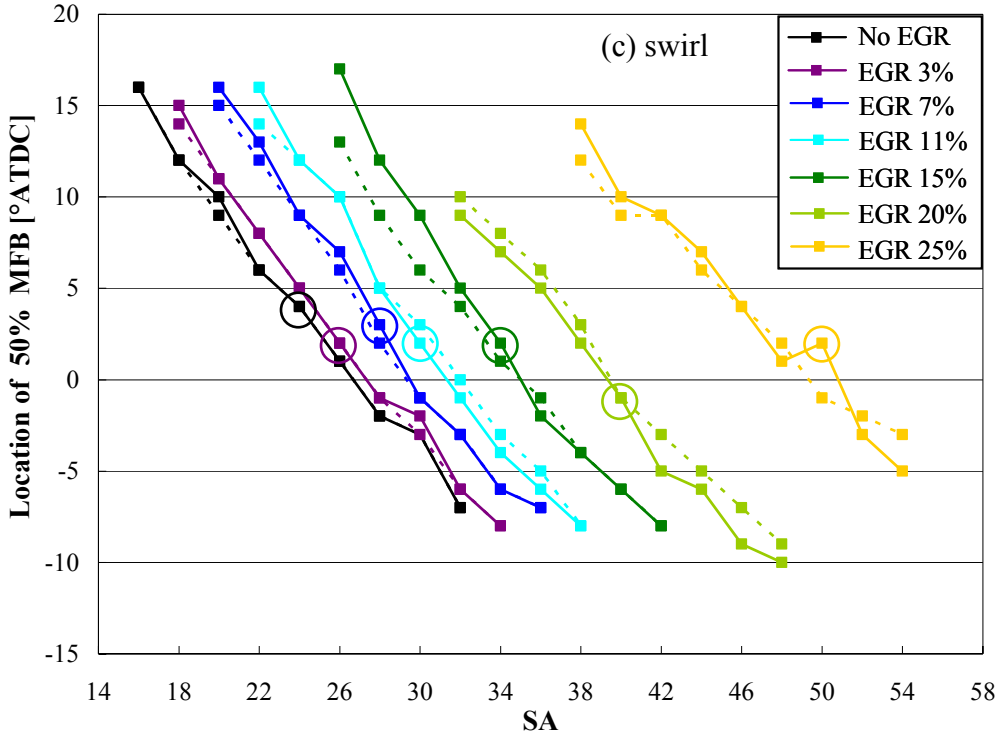

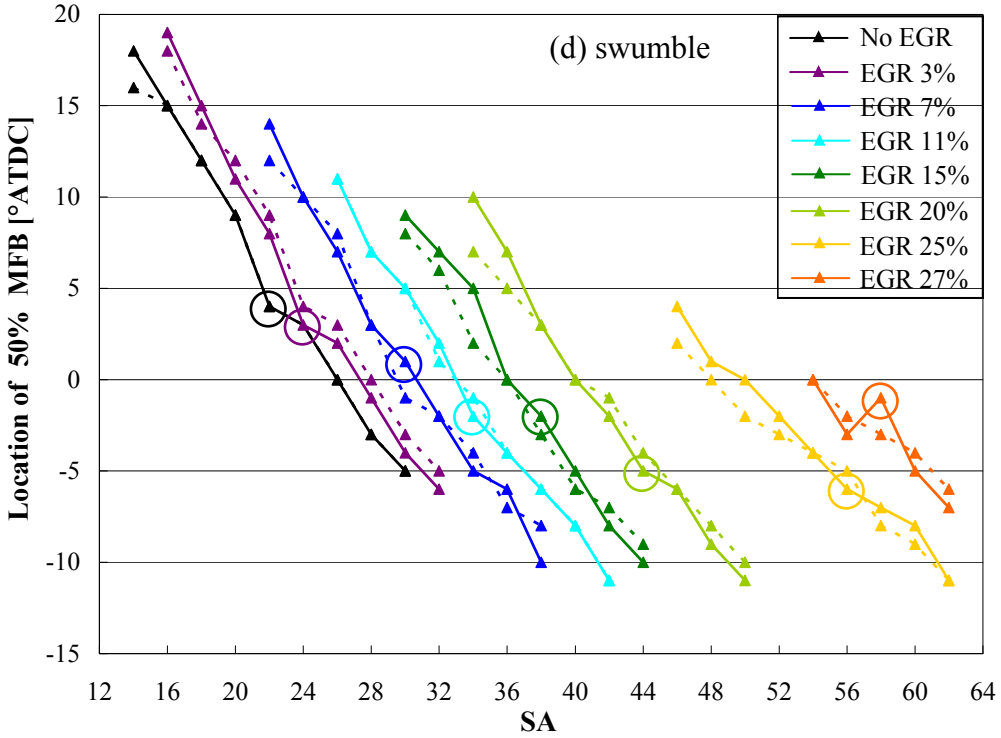

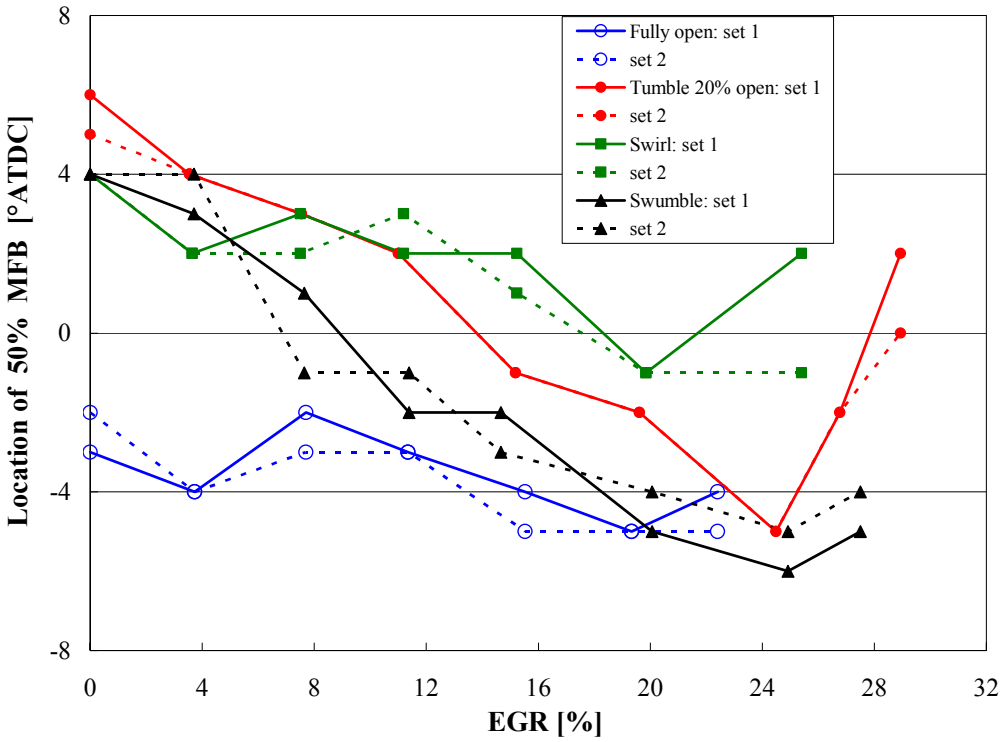

Figure 5.38. θ_{50} comparison with EGR under WP, at MBT, cylinder 1.

MFB variations with EGR dilution are compared at MBT in Fig. 5.39 for (a) fully open runner vs. tumble, (b) fully open runner vs. swirl, and (c) fully open runner vs. swumble with the origin for time chosen as the ignition point for all configurations. The introduction of blockage exhibits shorter θ_{0-10} and θ_{0-90} relative to unblocked runner at a given EGR, with tumble showing the largest effect. For the total burn duration θ_{0-100} at a given dilution level, tumble continues to display a reduction compared to fully open case, as illustrated in Fig. 5.39(a). On the other hand at some dilution levels, swirl and swumble show a somewhat comparable θ_{0-100} to the unblocked runner as shown in Fig. 5.32, suggesting a reduced burn rate for the flame termination phase (or, increased 90 – 100% burn duration, θ_{90-100}).

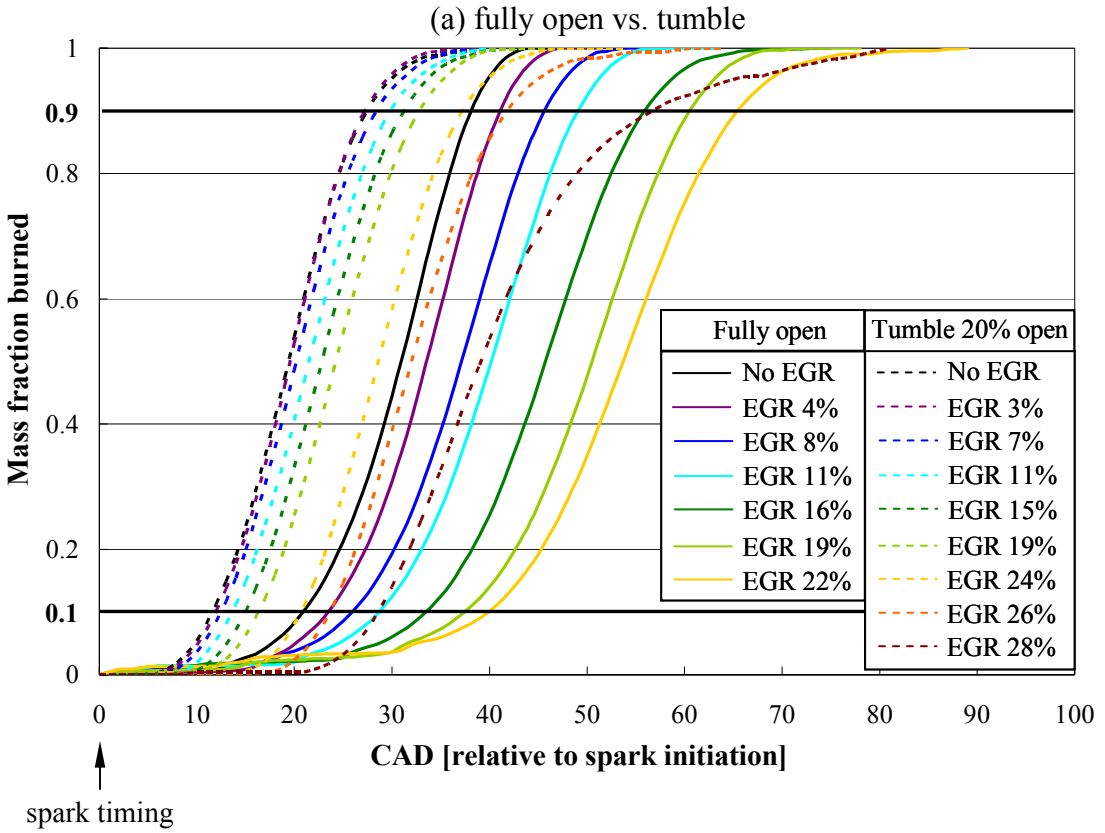

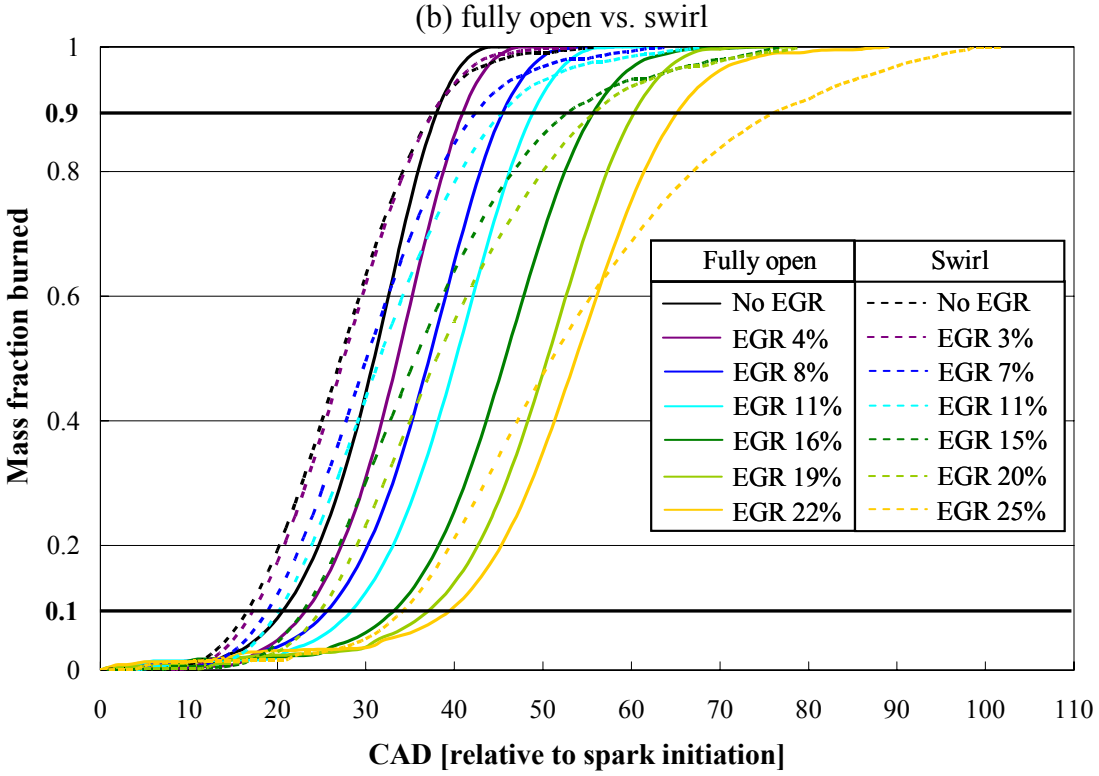

Figure 5.39. Effect of blockages on MFB under WP, at MBT, cylinder 1. (Continued)

Figure 5.39: Continued.

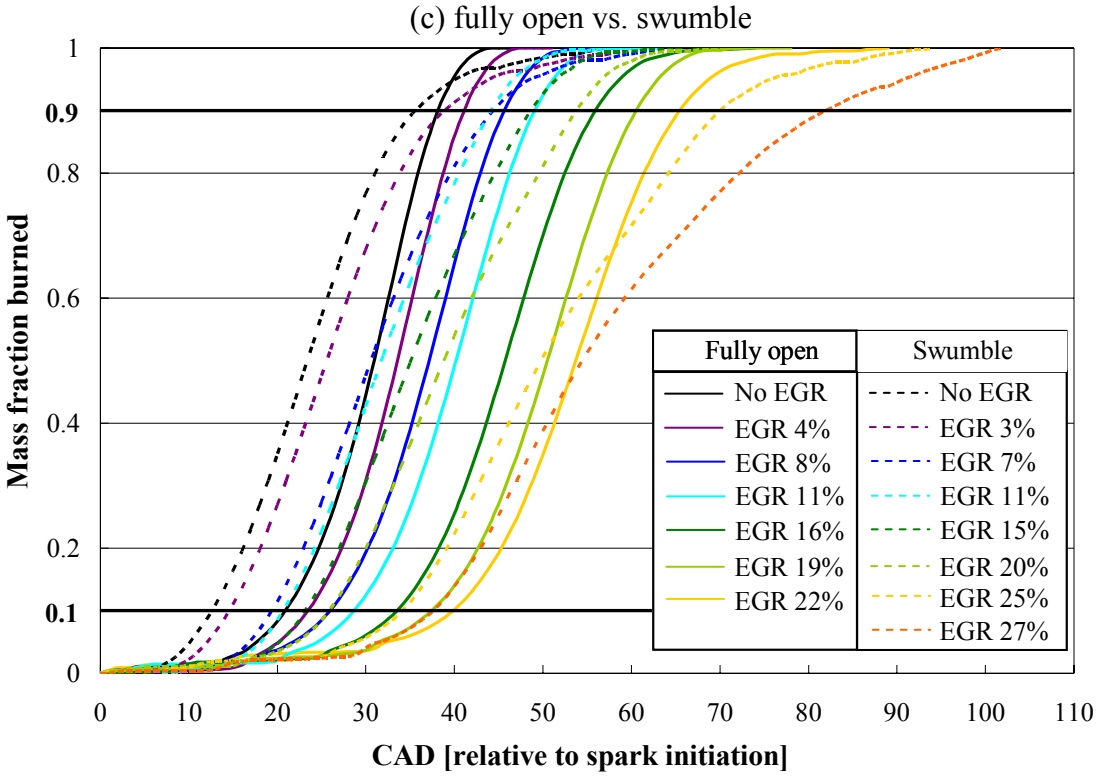

5.7 In-cylinder heat release

In-cylinder heat release is usually analyzed in terms of crank-angle-resolved cylinder pressure to determine the heat transfer to combustion chamber walls in SI engines. In this section, heat release is analyzed during the valve closed period (IVC – EVO) from the in-cylinder pressure and mass fraction burned. For all configurations, the present study applies a single-zone model (recall Section 4.6) to investigate the apparent heat release Q_{app}, in-cylinder heat transfer Q_{ht}, and the heat loss due to crevice effect Q_{cr} at different dilution levels.

For illustrative purposes, the results of the cumulative heat release for the unblocked runner are shown in Fig. 5.40 at MBT without EGR dilution, where the crank angle range is chosen as ±90° around combustion TDC, including the entire combustion

period. The lowest curve is the cumulative Q_{app} [calculated by Eq. (4.39)] and the next curve up reflects the effect of adding in-cylinder heat transfer Q_{ht} [$Q_{app} + Q_{ht}$, calculated by Eqs. (4.46) and (4.52)]. The top curve represents the chemical energy release Q_{hr} [calculated by Eq. (4.52)] which combines the effects of Q_{app}, Q_{ht}, and Q_{cr}. The crevice heat loss Q_{cr} after EOC (difference between red and dark blue curves in Fig. 5.40) appears not significant compared to Q_{ht} (difference between two blue curves) which is almost 30% the heat release Q_{hr} at EOC, as shown in Fig. 5.40.

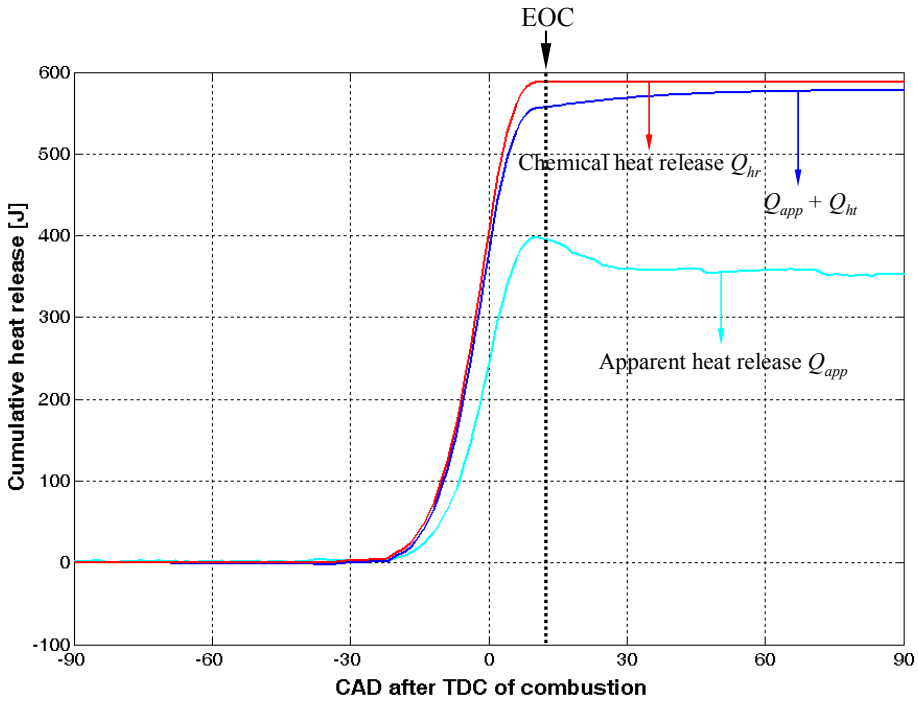

Figure 5.40. Cumulative heat release analysis for fully open runner without EGR under WP, at MBT, cylinder 1.

Figures 5.41(a) and 5.41(b) depict the cumulative heat release at three (0, 11%, and 22% for fully open runner) and four (0, 11%, 19%, and 28% for tumble) EGR rates of MBT timing, respectively. The behavior of swirl and swumble is similar to the tumble and deferred to Fig. C1. In Fig. 5.41, dash lines represent Q_{hr} which is reduced with EGR after combustion due to improved fuel economy (EOC of 13˚, 19˚, and 31˚ ATDC at 0,

11%, and 22% EGR for unblocked runner, while 27˚, 24˚, 20˚, and 43˚ ATDC at 0, 11%, 19%, and 28% EGR for tumble). The apparent heat release Q_{app} after combustion is comparable at three EGRs for unblocked runner. Tumble, however, displays a gradual reduction of Q_{app} from 0 to 19% EGR and then a substantial increase at the maximum dilution level.

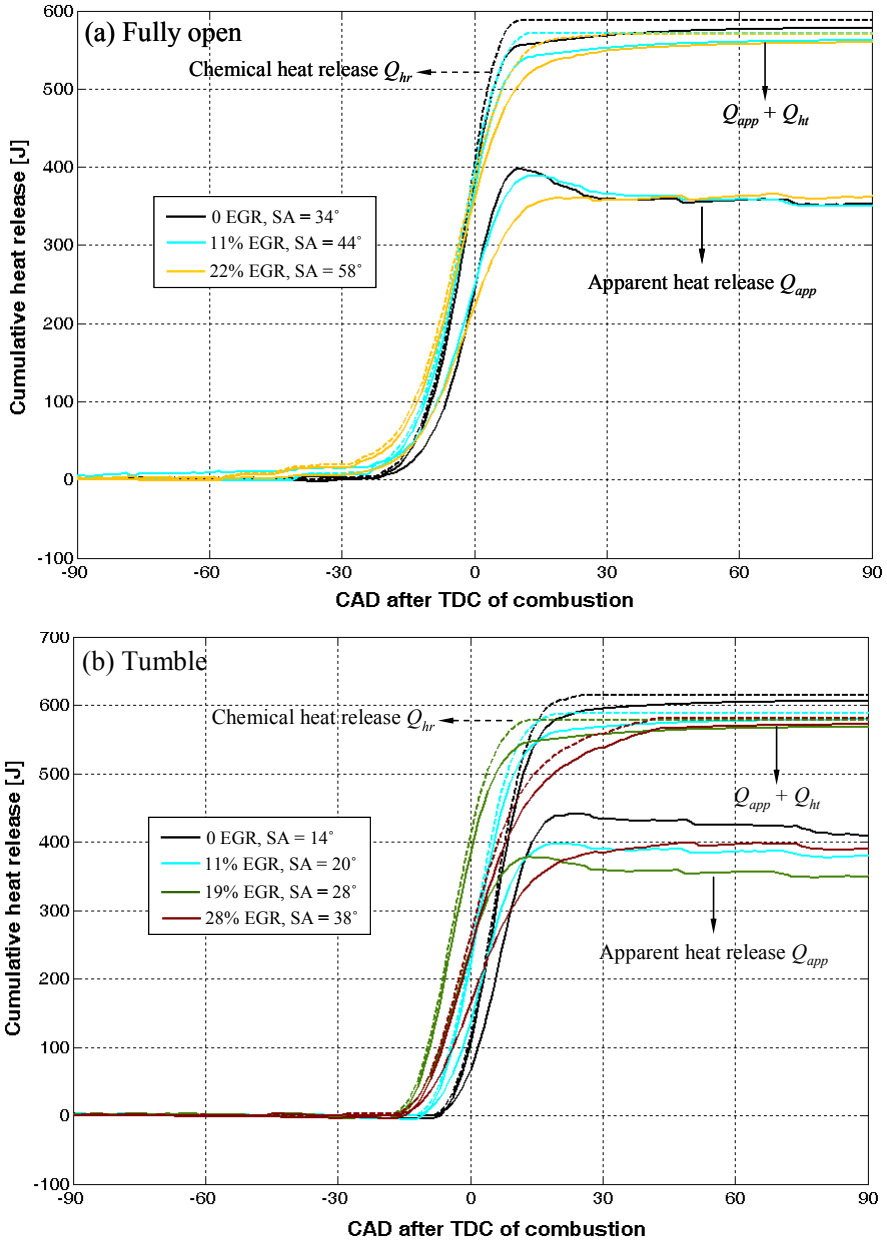

Figure 5.41. Cumulative in-cylinder heat release (#1) under WP, at MBT.

Figures 5.42(a) and 5.42(b) compare the corresponding instantaneous apparent heat release Q_{app} and in-cylinder heat transfer Q_{ht} for fully open and tumble, respectively, with dash lines representing Q_{ht}. Similarly, the comparison for swirl and swumble is deferred to Fig. C2. The peak Q_{app} decreases with EGR for both configurations, while tumble displaying a higher value at a comparable dilution level. For fully open case, the peak Q_{app} is located at about 2° BTDC for all EGR rates, as shown in Fig. 5.42(a). Tumble, on the other hand, has advanced the peak Q_{app} from 0 to 19% EGR followed by a retardation at the highest EGR, as illustrated in Fig. 5.42(b). Similar to the peak Q_{app}, the maximum Q_{ht} continues to decrease with EGR for fully open runner mainly due to the decreasing peak in-cylinder temperature. Whereas, tumble exhibits moderate increase of peak Q_{ht} from 0 to 19% EGR followed by a considerable reduction at 28% EGR, suggesting that a number of other factors play an important role on in-cylinder heat transfer such as turbulence intensity, mixing rate, tumbling flow structure, and spark timing. In addition, the trend of the location of the peak Q_{ht} with EGR is similar to that of the location of the peak Q_{app} for both configurations.

The cumulative in-cylinder heat transfer Q_{ht} is depicted in Figs. 5.43(a) and 5.43(b) for fully open and tumble, respectively, with a comparison of swirl and swumble being deferred to Fig. C3. At a given crank angle close to EVO (128° ATDC) such as 90° ATDC, the heat transfer is reduced with EGR rates for fully open runner because of decreasing flame temperature. Consistent with the instantaneous peak Q_{ht} illustrated in Fig. 5.42(b), tumble shows an opposite trend again suggesting that a number of other factors may influence the in-cylinder heat transfer for blocked cases.

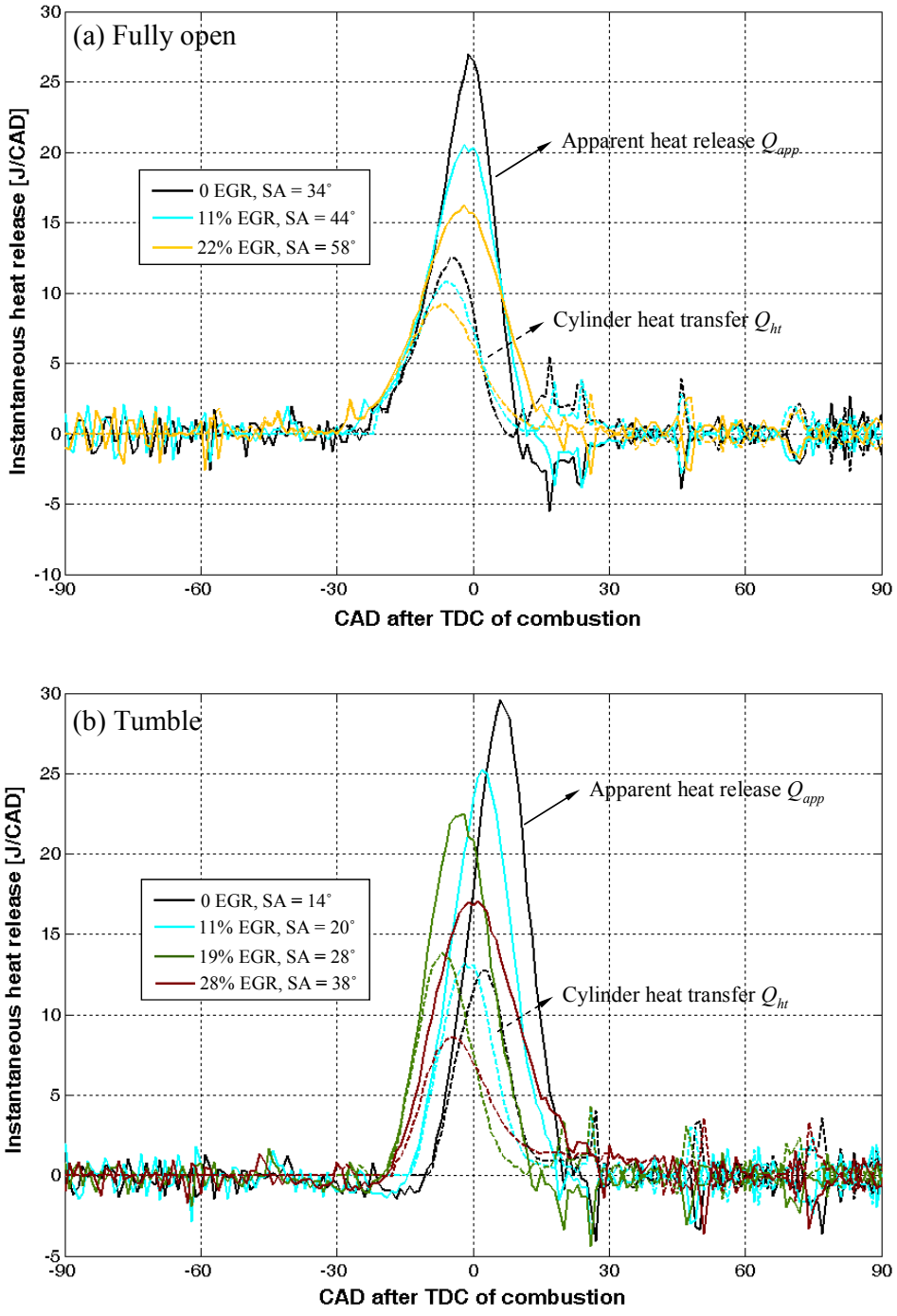

Figure 5.42. Instantaneous in-cylinder heat release (#1) under WP, at MBT.

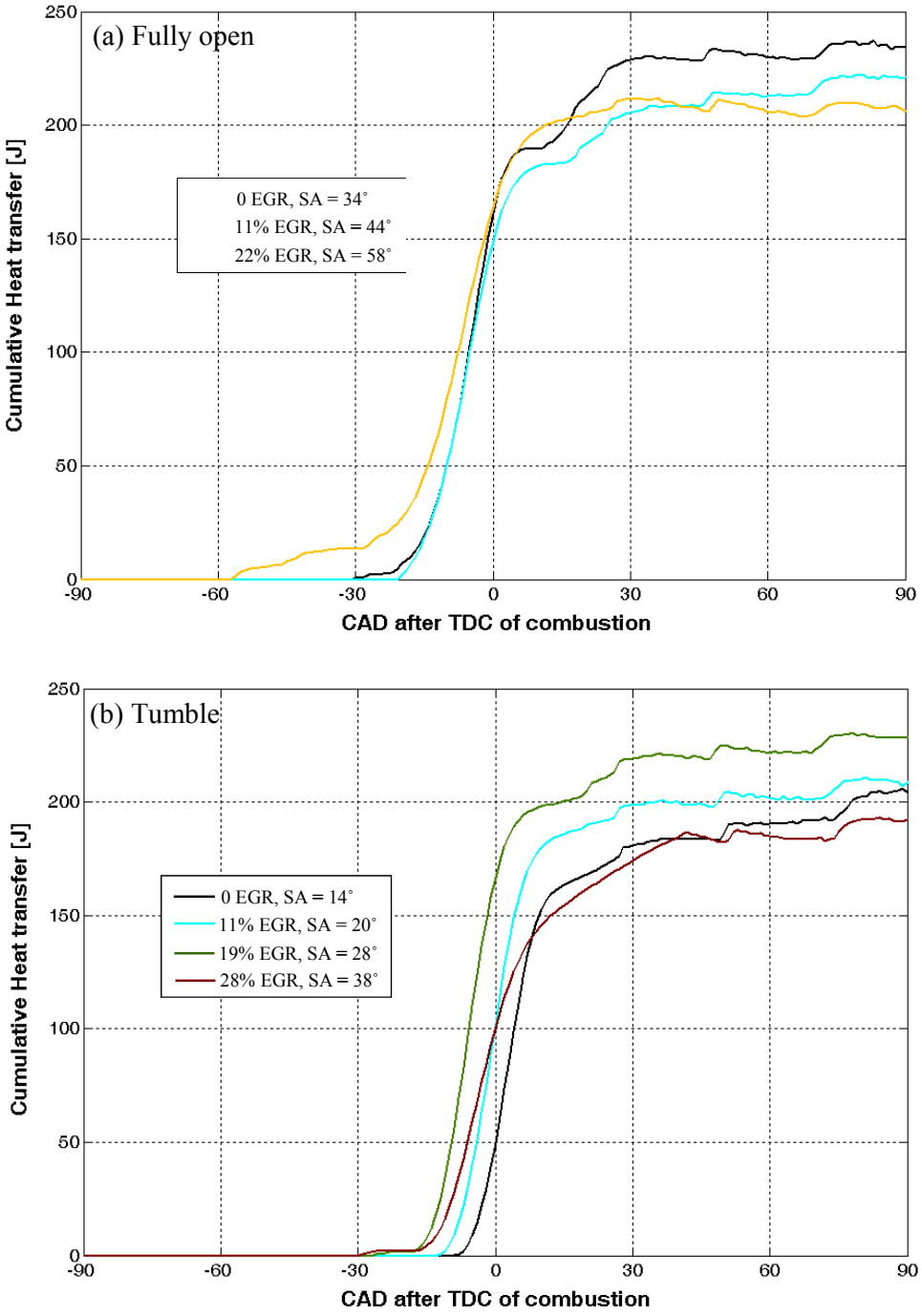

Figure 5.43. Cumulative in-cylinder heat transfer (#1) under WP, at MBT.

The overall apparent heat release Q_{app}, heat loss due to crevice effect Q_{cr}, and cylinder heat transfer Q_{ht} at EVO are compared in Figs. 5.44, 5.45, and 5.46, respectively, between fully open and tumble cases as a function of spark at different EGR, while the corresponding values listed in Table 5.4 at MBT. At a given EGR, Q_{app} decreases from the most retarded ignition point for both configurations, as shown in Fig. 5.44. From 0 to 19% EGR, Q_{app} is comparable for fully open runner at MBT, while tumble displays a gradual decrease with EGR dilution until 24%. The crevice loss Q_{cr} exhibits a nearly U-shape at a specific dilution level from 0 to moderate EGR ratio with the highest loss at the most advanced spark, as illustrated in Fig. 5.45, possibly due to the highest peak in-cylinder pressures (recall Fig. 5.15) and increased cylinder trapped mass. Q_{cr} for tumble is observed to moderately increase with EGR dilution at MBT, while this trend does not hold for the unblocked runner. At a specific dilution level as shown in Fig. 5.46, Q_{ht} is increased from the most retarded ignition with tumble exhibiting a higher rate of increase. Advanced spark results in higher peak in-cylinder pressures (recall Fig. 5.15) and presumably higher peak in-cylinder temperatures, leading to increased heat transfer. The fully open runner decreases Q_{ht} with EGR at MBT (see Table 5.4). This trend is not repeated for tumble.

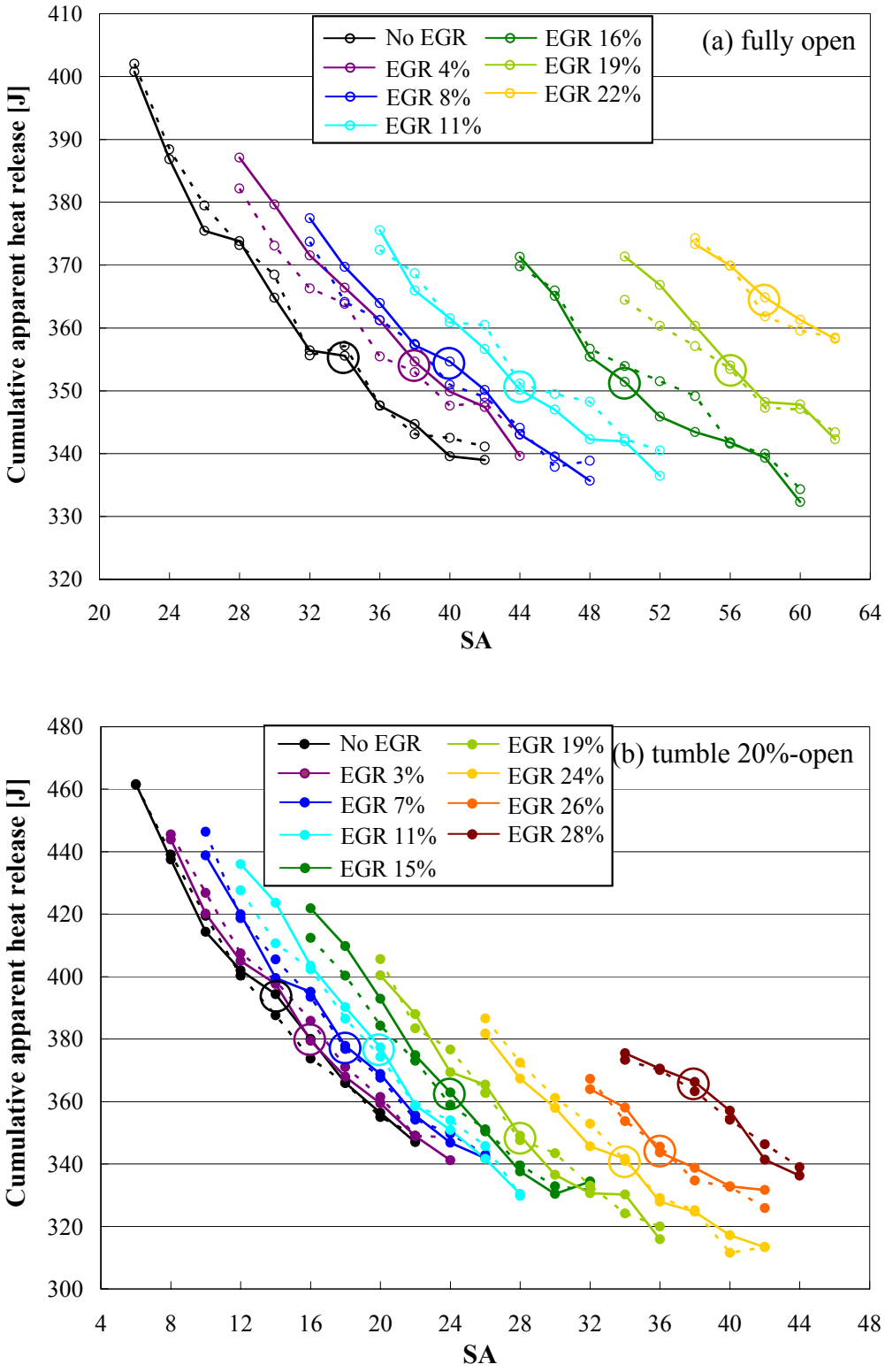

Figure 5.44. Cumulative apparent heat release Q_{app} at EVO at WP, cylinder 1.

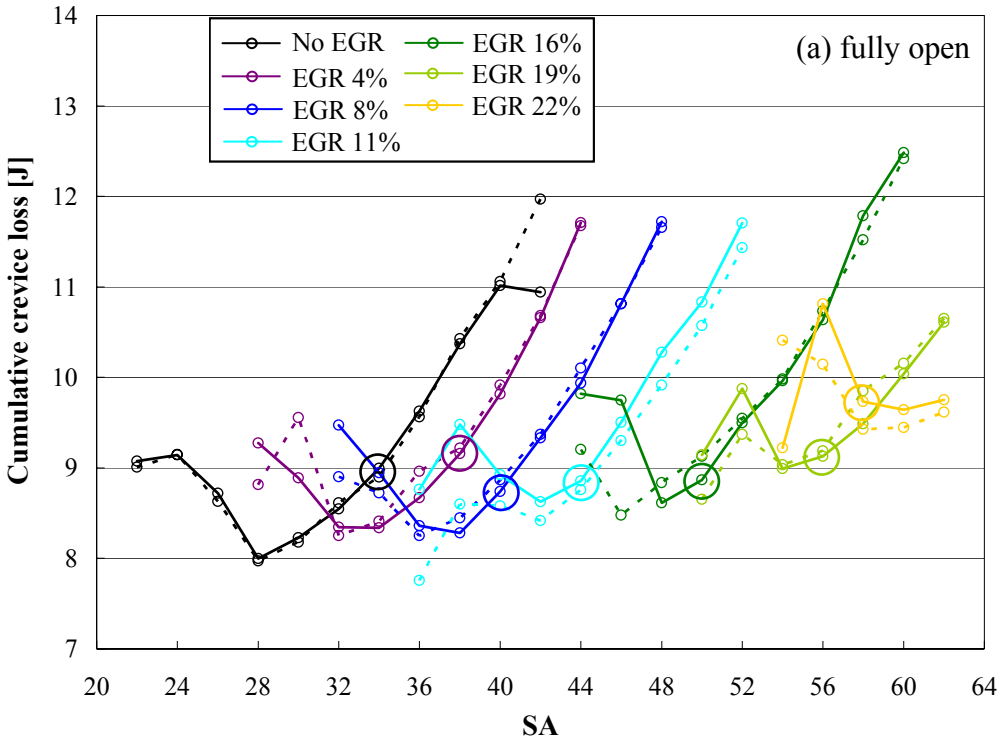

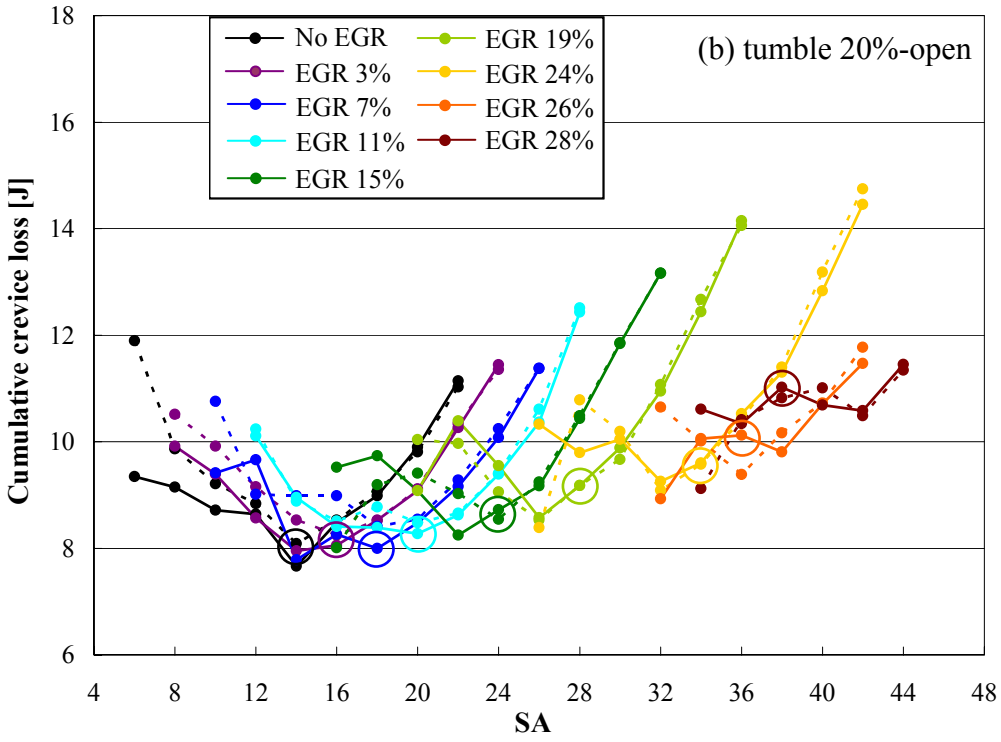

Figure 5.45. Cumulative crevice loss Q_{cr} at EVO at WP, cylinder 1.

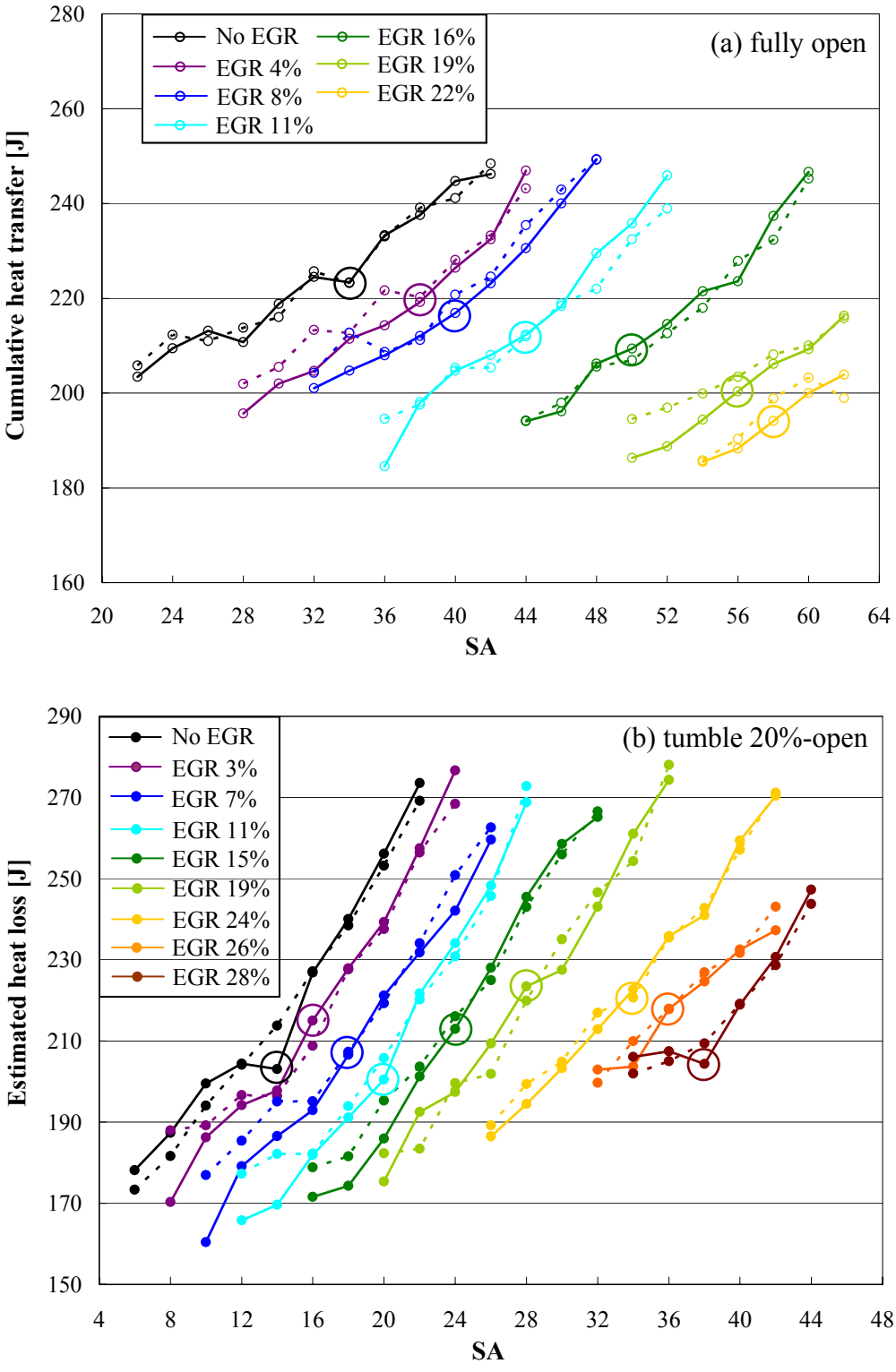

Figure 5.46. Cumulative cylinder heat transfer at EVO at WP, cylinder 1.

WP (2.41 bar BMEP @1600 rpm), MBT timing							
Intake runner fully open				Intake runner 20% open - Tumble			
Operating condition	Q_{app} [J]	$Q_{crevice}$ [J]	Q_{ht} [J]	Operating condition	Q_{app} [J]	$Q_{crevice}$ [J]	Q_{ht} [J]
No EGR	355.56	8.99	223.34	No EGR	394.39	7.66	203.07
EGR 4%	354.67	9.16	219.20	EGR 3%	379.45	8.06	214.99
EGR 8%	354.67	8.74	216.90	EGR 7%	376.78	8.00	206.59
EGR 11%	350.20	8.86	212.34	EGR 11%	377.31	8.48	200.46
EGR 16%	351.41	8.87	209.38	EGR 15%	362.89	8.54	212.91
EGR 19%	354.01	9.13	200.33	EGR 19%	347.58	9.18	223.46
EGR 22%	364.84	9.73	194.10	EGR 24%	341.02	9.58	222.69
				EGR 26%	345.52	9.38	217.81
				EGR 28%	366.27	10.82	204.34

Table 5.4. Comparison of apparent heat release Q_{app}, crevice loss Q_{cr}, and in-cylinder heat transfer Q_{ht} at EVO under WP, at MBT, cylinder 1.

5.8 Exhaust gas temperature (EGT) and engine-out emissions

Figure 5.47 depicts the variation of EGT with spark advance at different EGR for both unblocked and blocked cases under WP. Figure 5.48 compares EGT among 4 configurations at MBT timing only. Retarded ignition results in higher EGT due to late combustion and heat release (Fig. 5.47). EGT for swirl and swumble at a given spark timing is comparable to fully open runner from 0 to moderate EGR rates. With increasing dilution, EGT continues to decrease at MBT as shown in Fig. 5.48 due to reduced burned gas temperature. At the highest EGR, the EGT levels off, primarily due to the significant lengthening of the burn duration, as observed in Table 5.3. Compared to the unblocked case, EGT at MBT increases with swumble at all EGR rates and swirl exhibits an increase of EGT at EGR ratios approximately above 8%, shown in Fig. 5.48. Tumble, on the other hand, decreases EGT at all dilution levels.

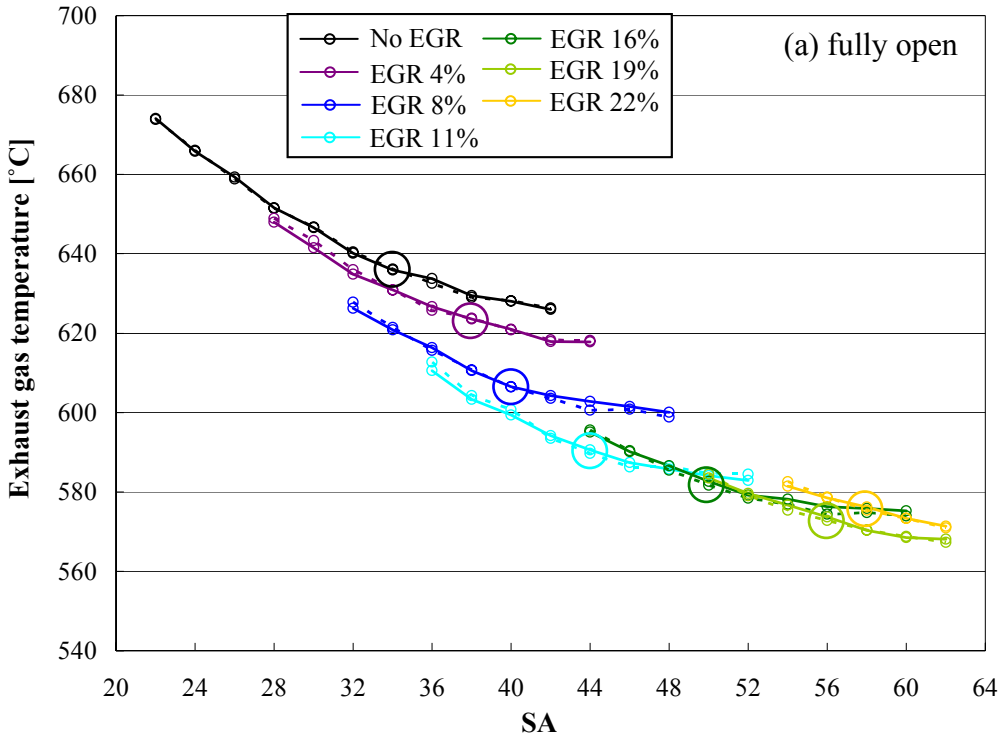

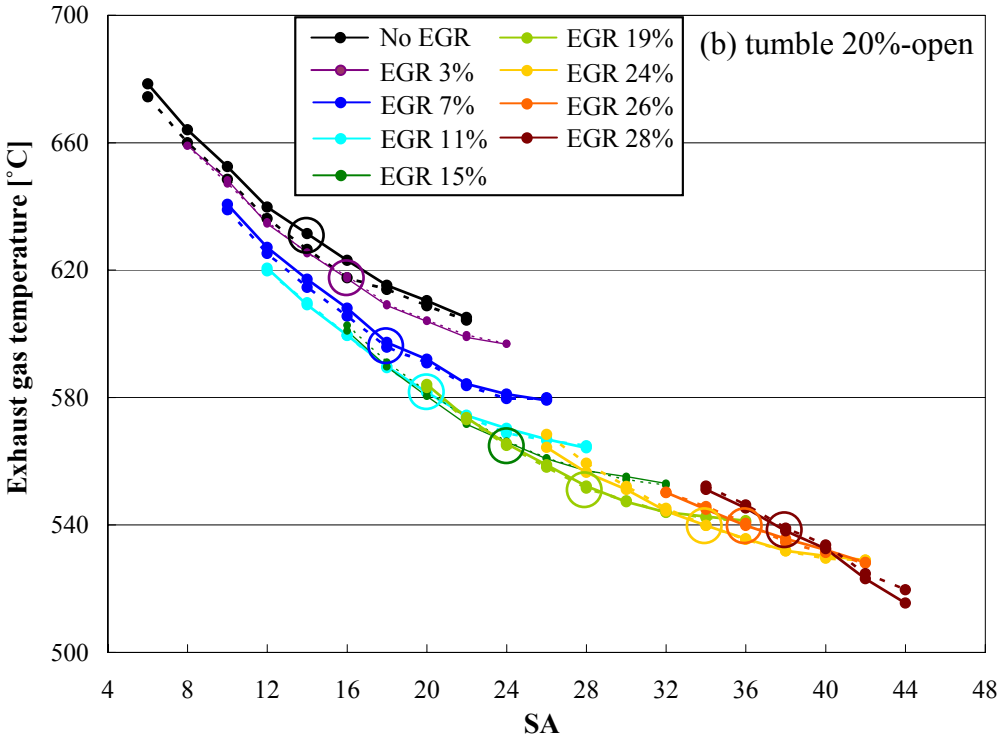

Figure 5.47. Effect of blockages on exhaust gas temperature at WP, runner 1. (Continued)

Figure 5.47: Continued.

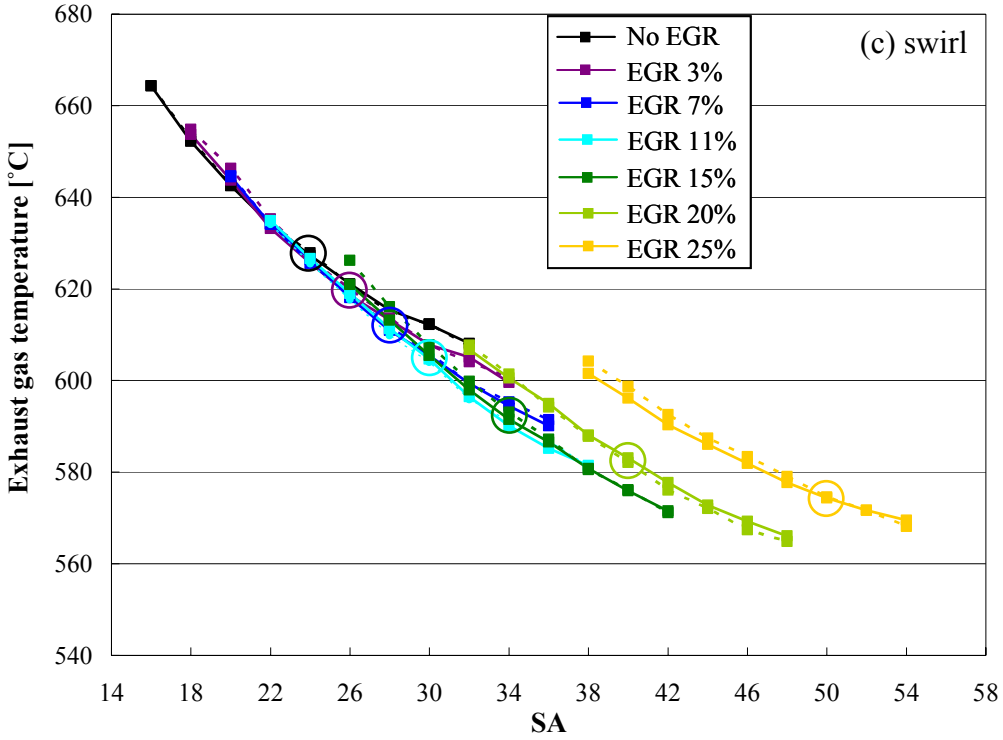

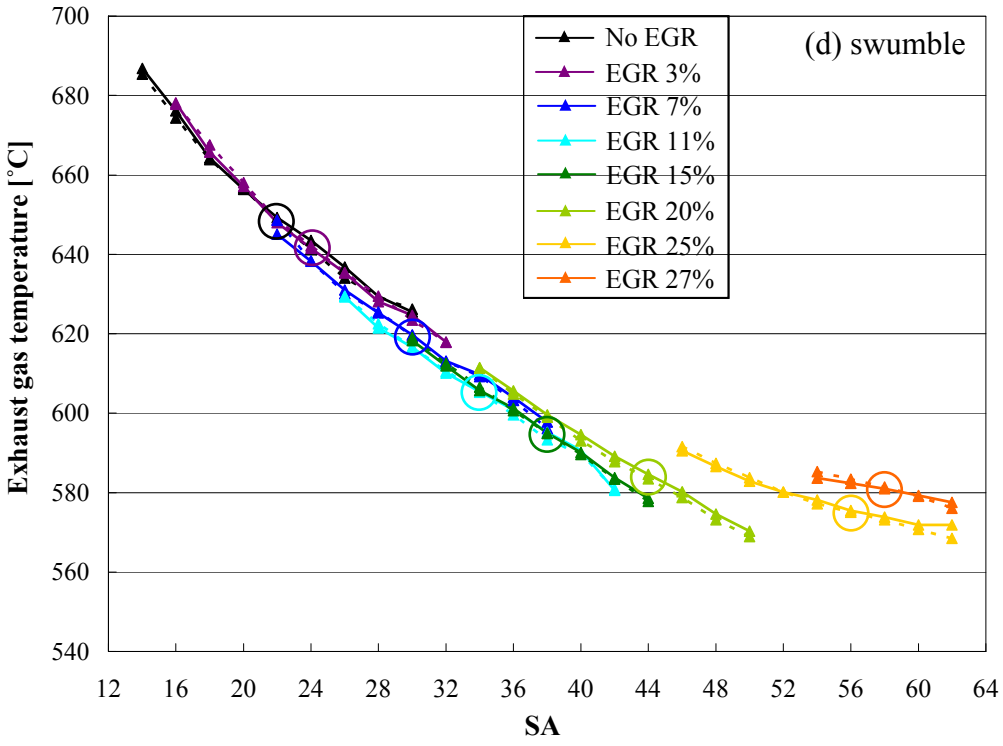

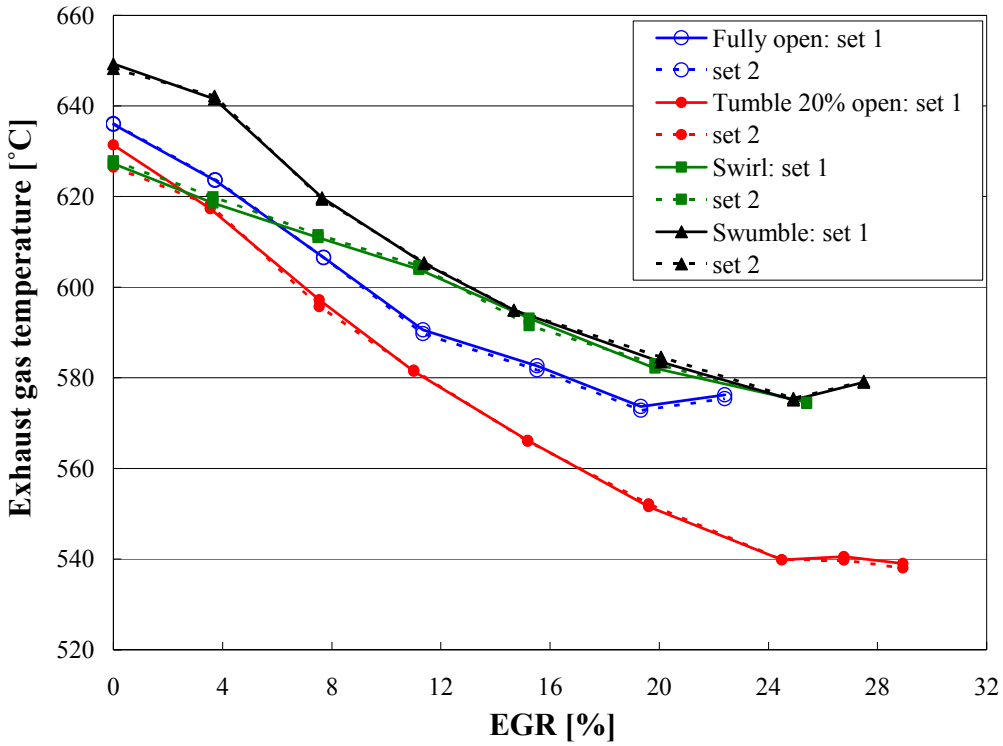

Figure 5.48. Exhaust gas temperature comparison with EGR under WP, at MBT, runner 1.

Figure 5.49 illustrates the variation of brake specific emissions of NO_x vs. spark advance at different dilution levels, while Fig. 5.50 shows NO_x emissions as a function of EGR at MBT timing for different blockages. The NO_x reduction (Fig. 5.49) with spark retard correlates well with the peak in-cylinder temperature due to the strong temperature dependency in the Zeldovich mechanism. Since NO_x formation rates increase exponentially with in-cylinder temperature, the approach that achieves low temperature combustion results in a reduction of NO_x emissions. The recirculated exhaust gases act as diluents in the unburned mixture leading to lowered flame temperature. Therefore, increasing burned gas fraction decreases NO_x emission levels, as shown in Figs. 5.49 and 5.50. For example, NO_x emissions are reduced by 91%, 83%, 80%, and 76% at the optimum EGR with MBT timing for tumble, swumble, swirl, and fully open,

respectively. The specific NO_x emissions are somewhat comparable between blocked and unblocked runners at MBT (Fig. 5.50), particularly at EGR ratios above 8%.

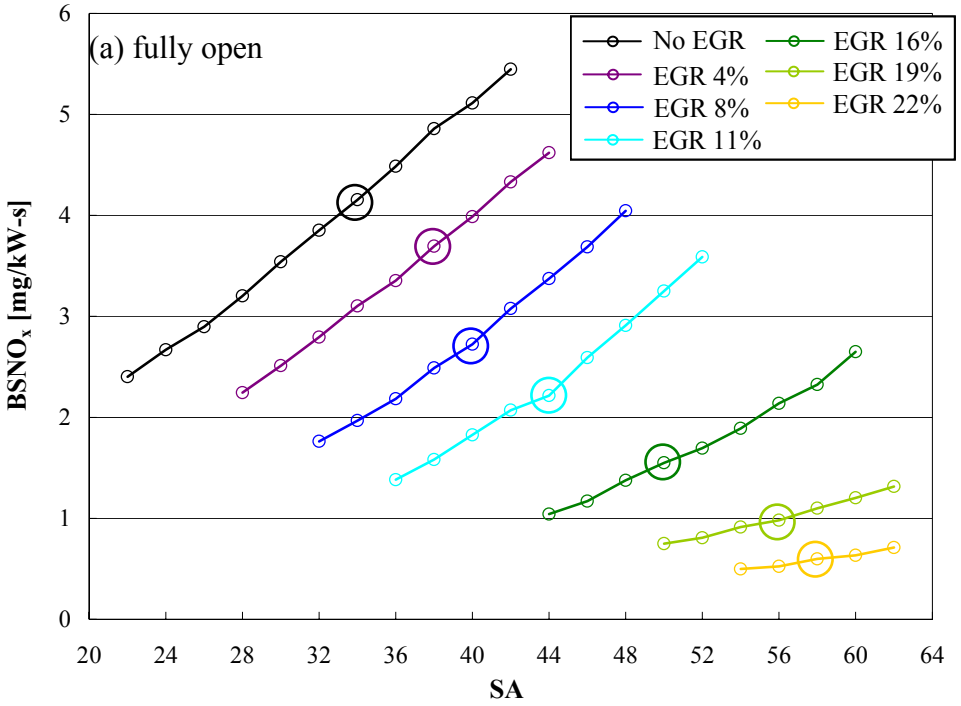

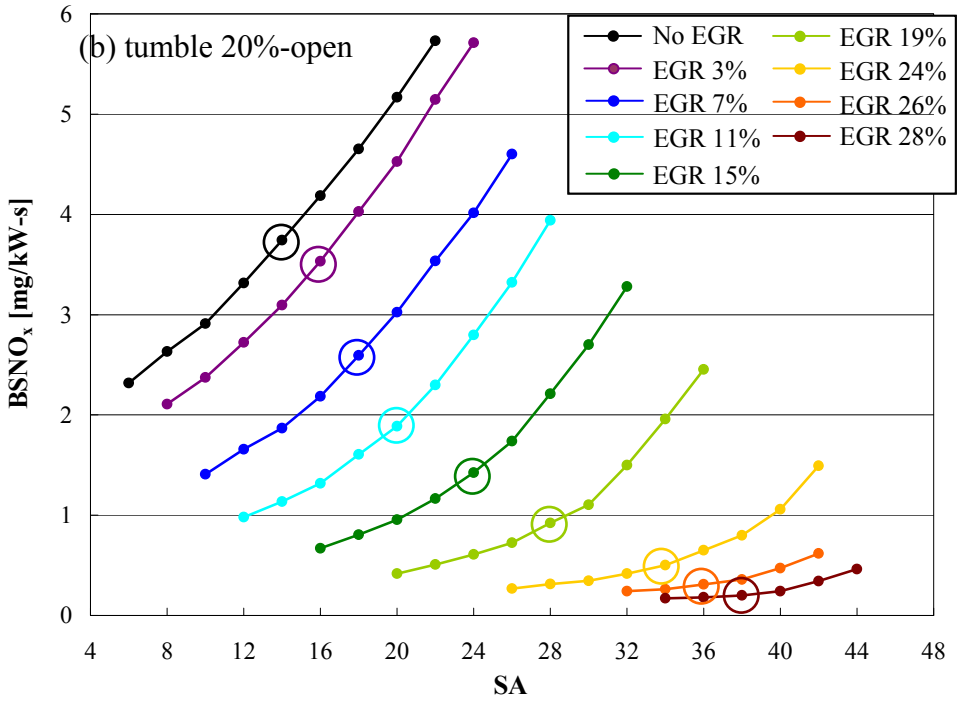

Figure 5.49. Effect of blockages on NO_x emissions at WP. (Continued)

Figure 5.49: Continued.

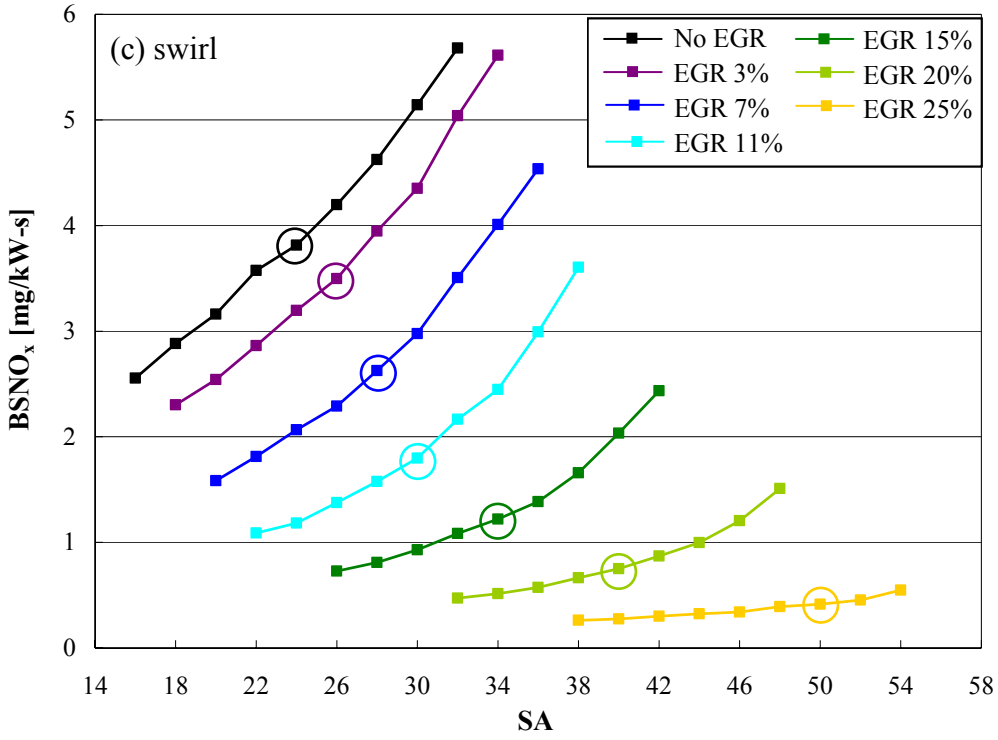

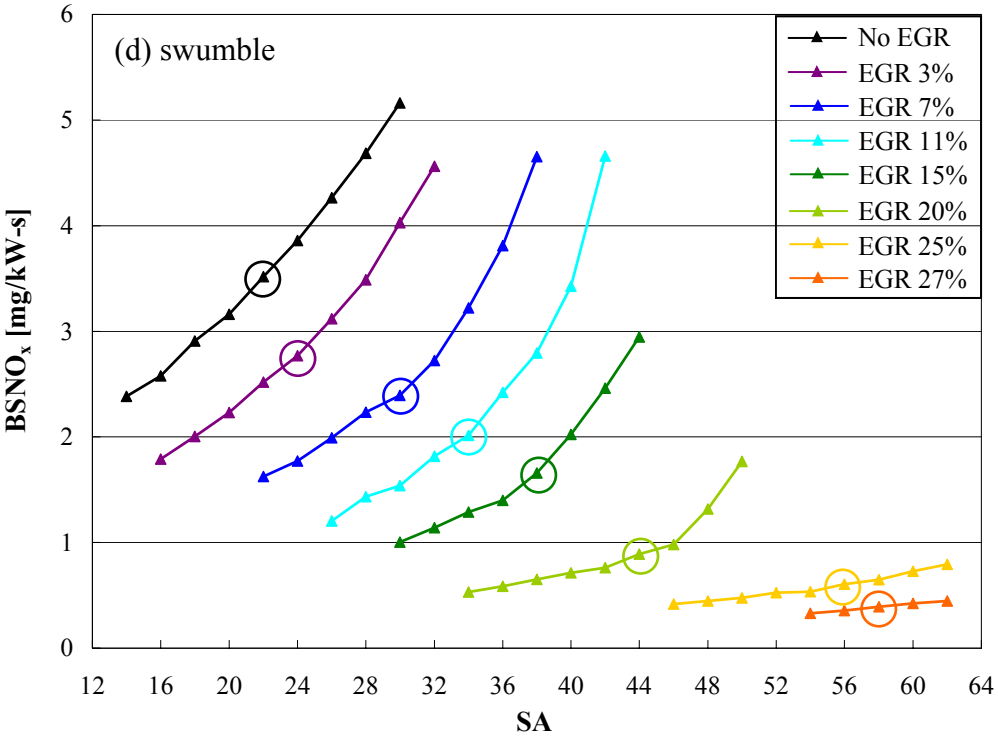

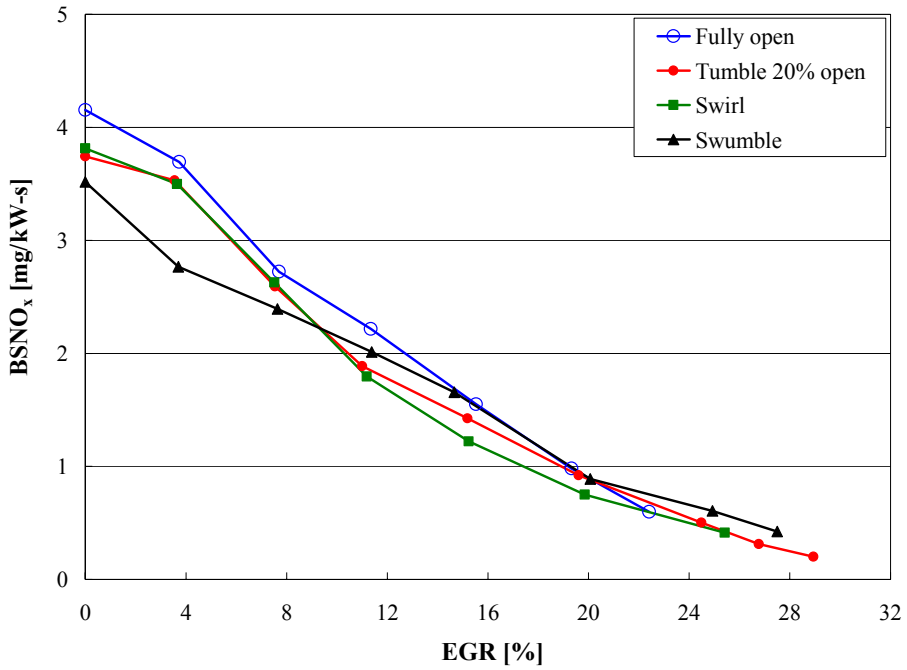

Figure 5.50. Comparison of NO_x emissions with EGR under WP, at MBT.

Similarly, the comparison of HC emissions between unblocked and blocked runners is given in Figs. 5.51 and 5.52. With no EGR dilution, the reduction of HC emissions in Fig. 5.51 with spark retard may be linked to varying peak in-cylinder pressure and EGT. The lower in-cylinder pressure may inhibit the unburned hydrocarbon storage in crevices before combustion. During exhaust stroke, the higher in-cylinder and exhaust gas temperatures may enhance the port oxidation, hence lowering the HC emissions. As the in-cylinder mixture becomes more diluted, the burn duration increases and combustion deteriorates with an increase of slow burn cycles. Eventually, partial burn and misfire occur in the cylinder. The elevated COV due to increasing number of slow burn, partial burn, and misfiring cycles (recall Figs. 5.21 and 5.23) leads to higher HC emissions, with substantial increase at the maximum EGR for blocked runners, as depicted in Figs. 5.51 and 5.52. At MBT timing, tumble displays lower HC emissions

(Fig. 5.52) than swirl and swumble, possibly due to the significantly increased burn rate and spark retardation.

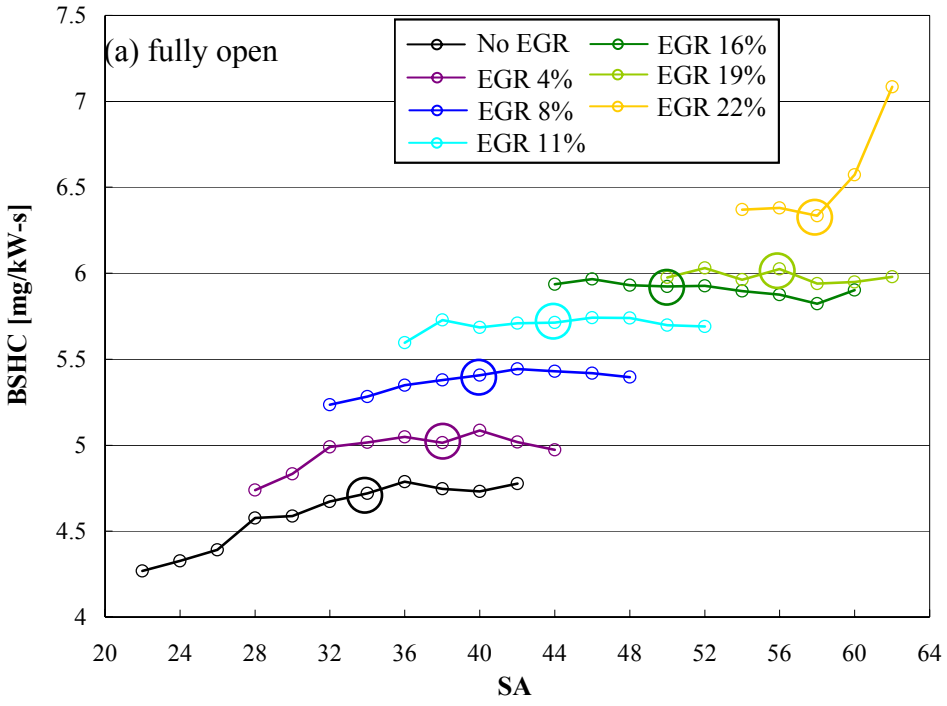

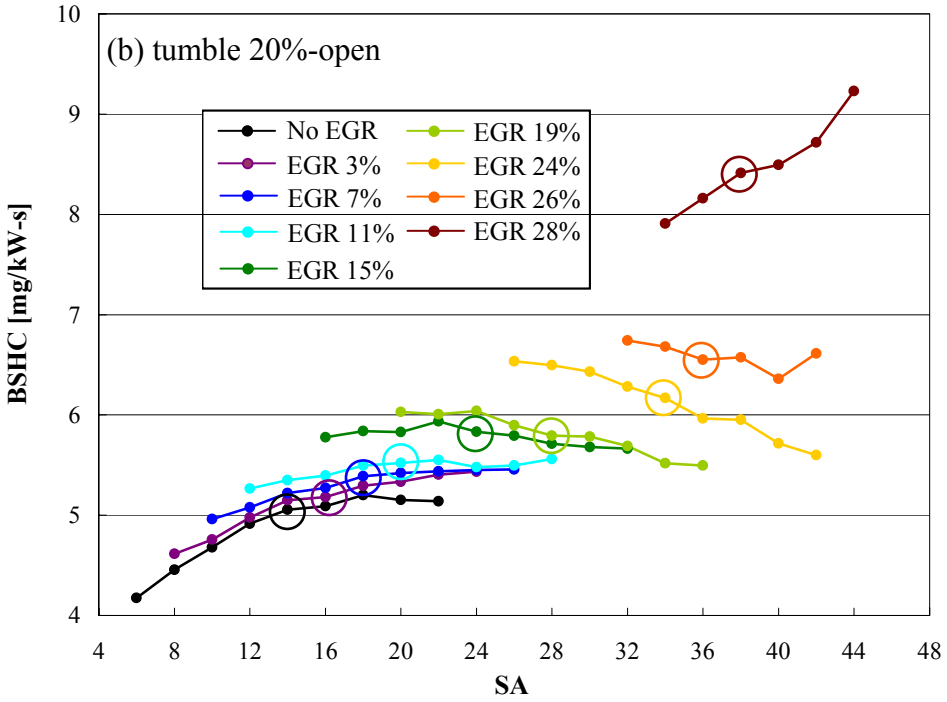

Figure 5.51. Effect of blockages on HC emissions at WP. (Continued)

Figure 5.51: Continued.

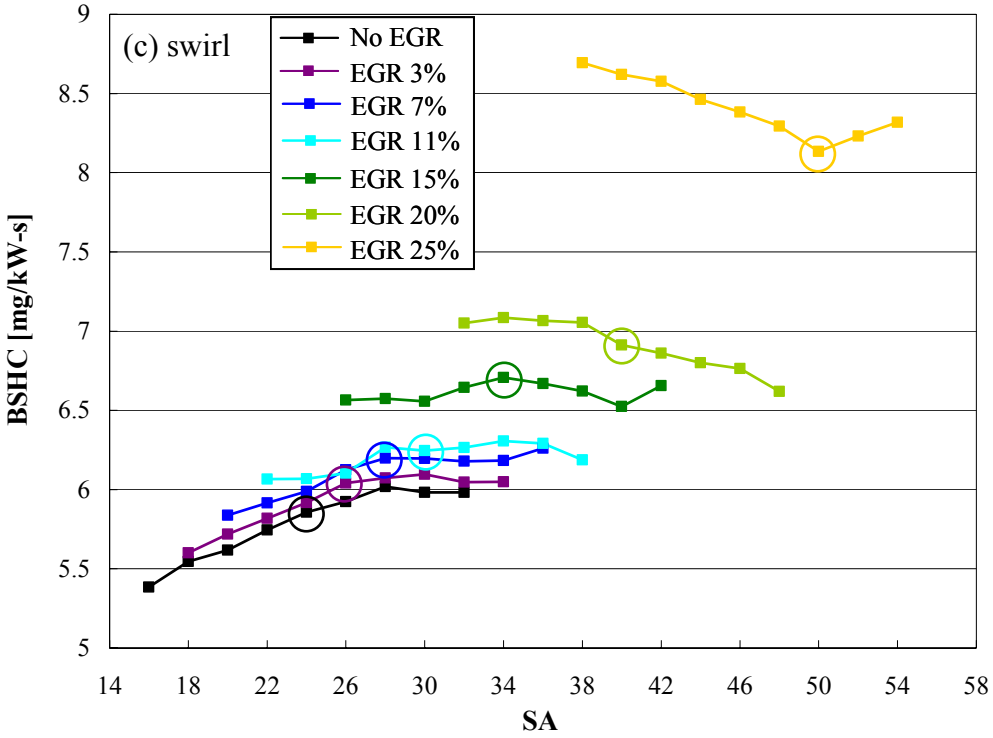

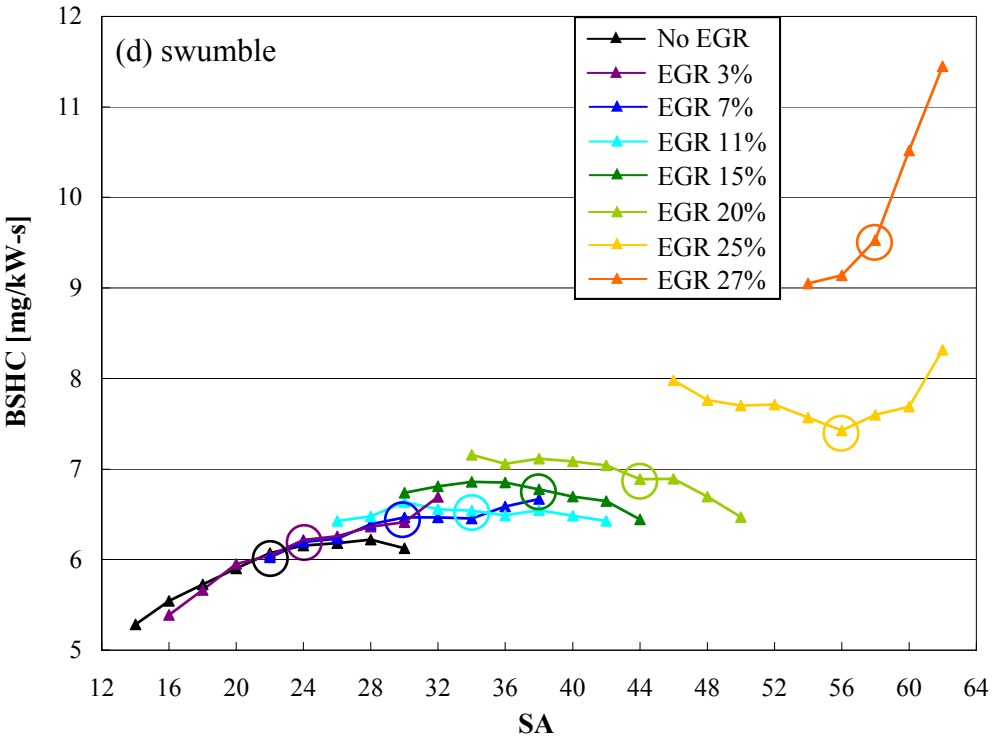

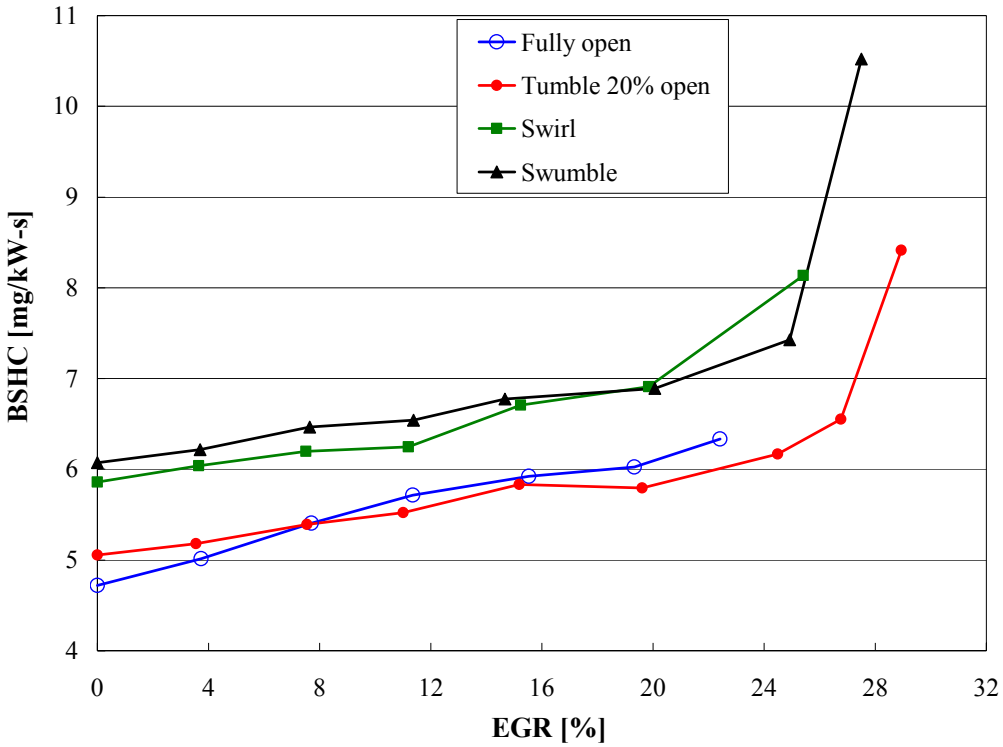

Figure 5.52. Comparison of HC emissions with EGR under WP, at MBT.

Figures 5.53 and 5.54 depict the specific emissions of CO for different blockages as a function of spark advance and EGR ratio, respectively. In Fig. 5.53(a), fully open runner displays reduction in CO emissions with EGR until the optimum dilution level, suggesting that the introduction of burned gas decreases the local fuel-rich zones where CO formation is assumed to take place. Tumble exhibits a similar trend with somewhat lower emissions, as shown in Fig. 5.53(b), possibly due to its impact on mixing. The trend, however, does not hold for swirl and swumble [Figs. 5.53(c) and 5.53(d)] which yield at MBT higher CO emissions than unblocked case as illustrated in Fig. 5.54. The emission comparisons here are based on the samples collected from the exhaust manifold right before the catalyst (Location 13 in Fig. 3.1). While this approach provides a relative assessment of the blockages, the absolute values of certain species (particularly HC and

CO reacting in ports and runners, unlike frozen NO_x) are expected to vary with location, for example, from runners to manifold.

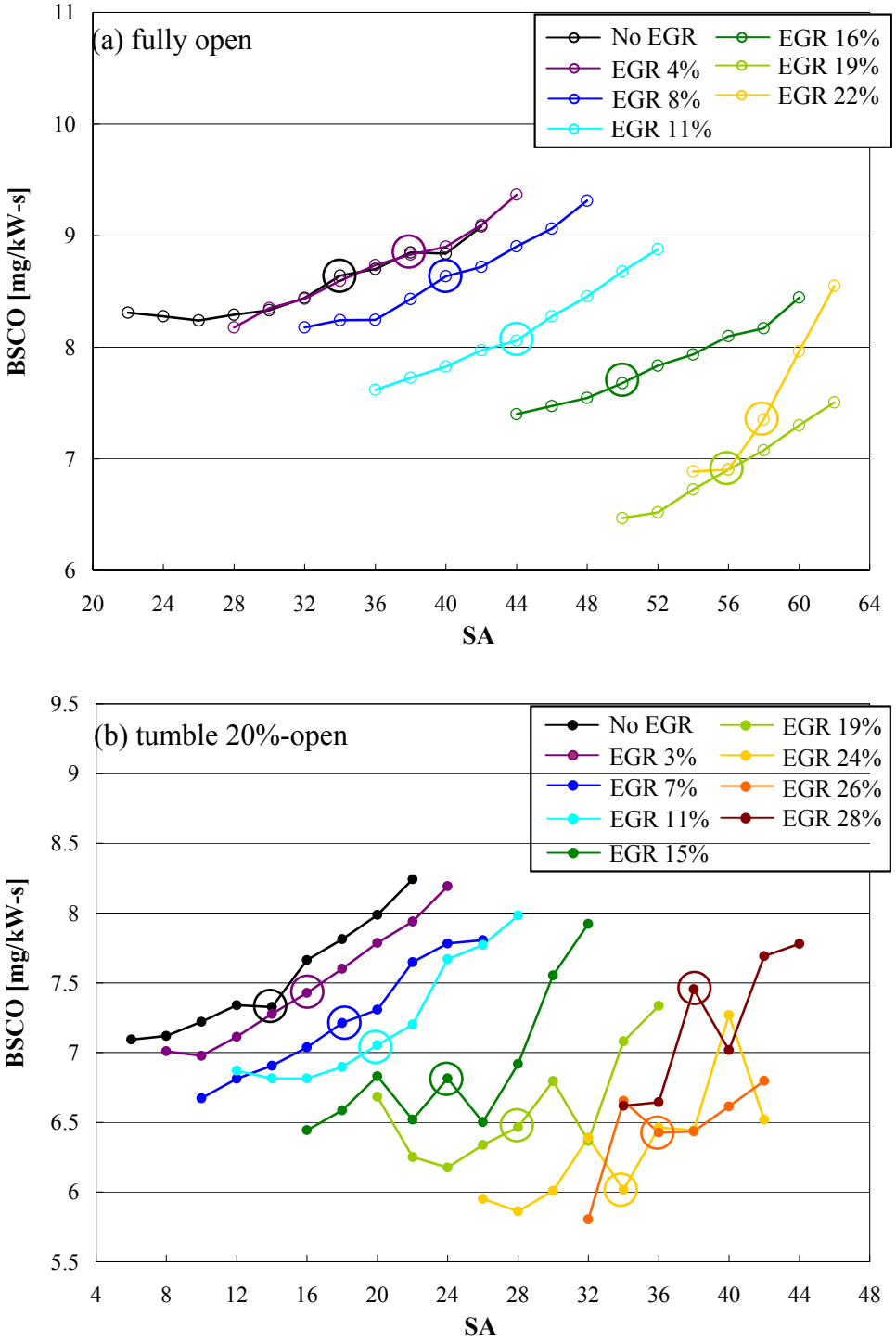

Figure 5.53. Effect of blockages on CO emissions at WP. (Continued)

Figure 5.53: Continued.

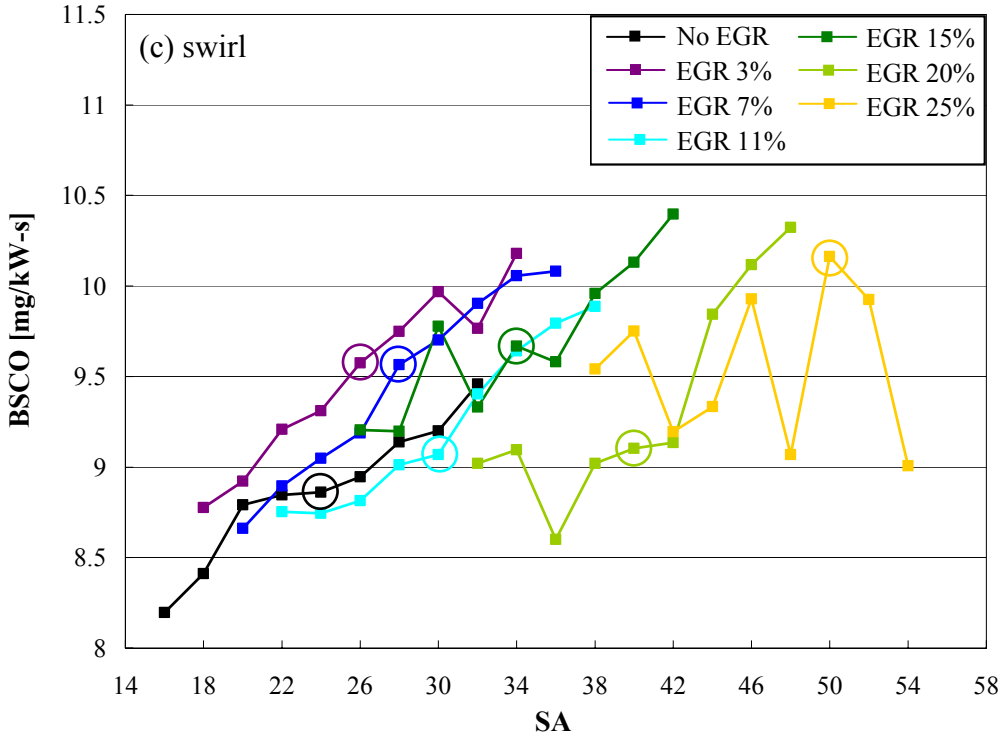

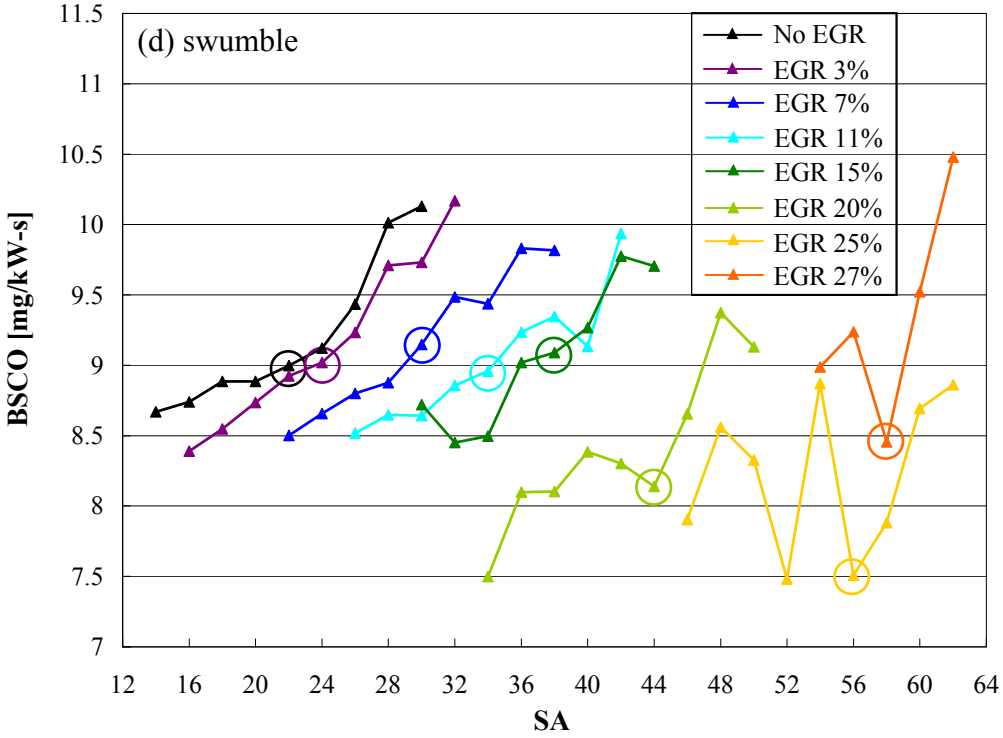

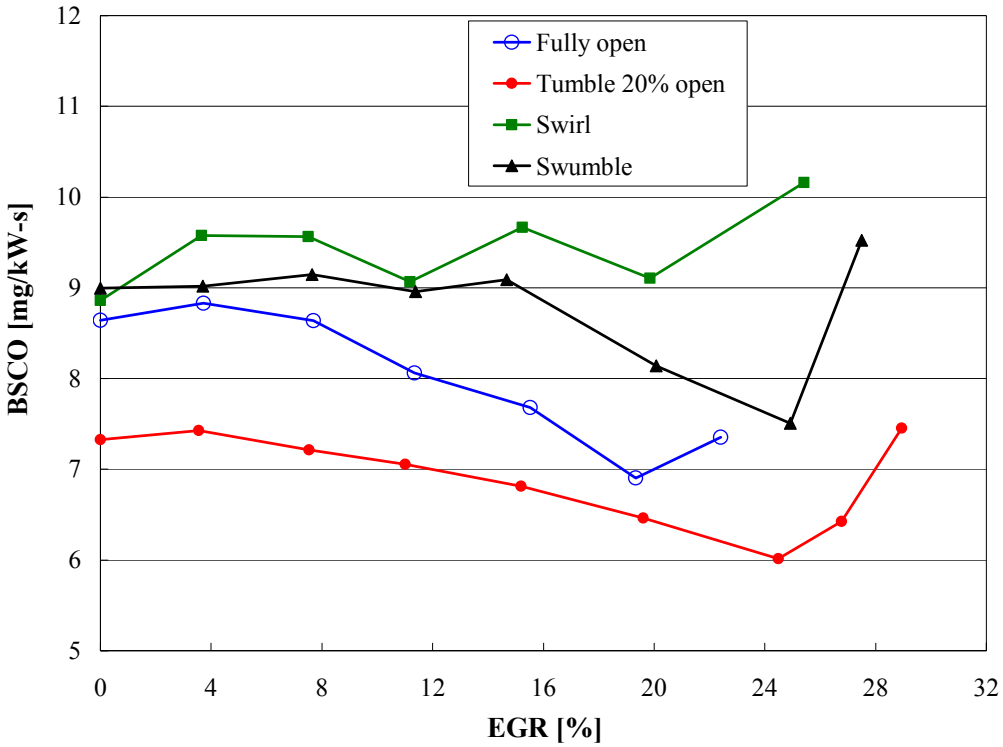

Figure 5.54. Comparison of CO emissions with EGR under WP, at MBT.

CHAPTER 6

FLOW EXPERIMENTAL RESULTS and DISCUSSION

Steady state flow experiments have been performed at varying intake valve lifts, by using the same cylinder head, intake manifold, and tumble blockages from the engine experiments. Experimental results are provided for 20%, 40%, and 60%-open tumble blockages (recall Section 3.1.1). Fully open runner is also included as the baseline for comparison with blocked runners. The flow characteristics under two engine operating conditions, WP and IP, are simulated in the flow experiments. For each blockage-load combination, the maximum air mass flow rate $\dot{m}_{air,\max,e}$ in engine experiment is matched at the peak intake valve lift ($L_{v,\max}$ = 0.325") in the flow laboratory, rather than imposing a constant bore pressure drop $\Delta P_{\infty 3}$ for all configurations. The details of the experimental procedure have already been described in Section 4.9.1, and the test matrix is given in Table 6.1. For each experiment, two sets of data have been included to illustrate the repeatability. In-cylinder tumble motion is quantified by a refined underhead tumblemeter, as introduced in Section 3.2. This chapter will first compare the flow laboratory results between unblocked and blocked runners. A correlation will then be

sought between engine and flow experiments to help quantify the impact of tumble motion on combustion duration and cyclic variation.

Operating condition	Blockage	Bore pressure drop $\Delta P_{\infty 3}$ ["H_2O]
WP (2.41 bar BMEP @ 1600 rpm)	Fully open	1.5
	Tumble - 60% open	3
	Tumble - 40% open	8
	Tumble - 20% open	32
IP (0.78 bar BMEP @ 1200 rpm)	Fully open	0.35
	Tumble - 60% open	1
	Tumble - 40% open	2.25
	Tumble - 20% open	9

Table 6.1. Test matrix for flow experiments.

6.1 Air mass flow rate

Figure 6.1 illustrates the upstream and downstream intake pressures in runner 4 for all configurations from engine experiments under WP and IP at MBT timing. Because of excellent repeatability, only one set of the data is presented here. For the unblocked runner, variation between upstream and downstream pressures is nearly negligible, as expected. The introduction of blockage has changed the pressures (particularly downstream) during the induction process, with 20%-open runner displaying the largest variation, hence the highest flow losses across the blockage. This effect is clear under both operating conditions, while more obvious at WP because of larger flow rates. The corresponding air mass flow rate $\dot{m}_{air,e}$ in the intake runner 4 is shown in Fig. 6.2 as estimated by Eq. (4.57). For both conditions, the peak $\dot{m}_{air,e}$ occurs between 40˚ and 60˚ ATDC, similar to the experimental results by Justham *et al.*, 2006. The maximum air mass flow rate $\dot{m}_{air,\max,e}$ for a given blockage-load combination is then matched in flow experiment at the peak valve lift ($L_{v,\max}$ = 0.325") with the corresponding $\Delta P_{\infty 3}$ being recorded.

Table 6.2 compares the calculated $m_{air,e}$ and $m_{air,e,P}$ (recall Section 4.9.3) under WP and IP, respectively, along with $\dot{m}_{air,\max,e}$ and measured $\Delta P_{\infty 3}$. The air mass flow exhibits only a small deviation between $m_{air,e}$ and $m_{air,e,P}$, with the maximum relative error being 7.21% and 2.46% for WP and IP, respectively. In the present work, $\dot{m}_{fuel}$ is measured for the engine, hence simply dividing $\dot{m}_{fuel}$ by N_c to get an average value for one cylinder (see Eq. 4.60) may account for part of the foregoing deviations because of cylinder-to-cylinder variation.

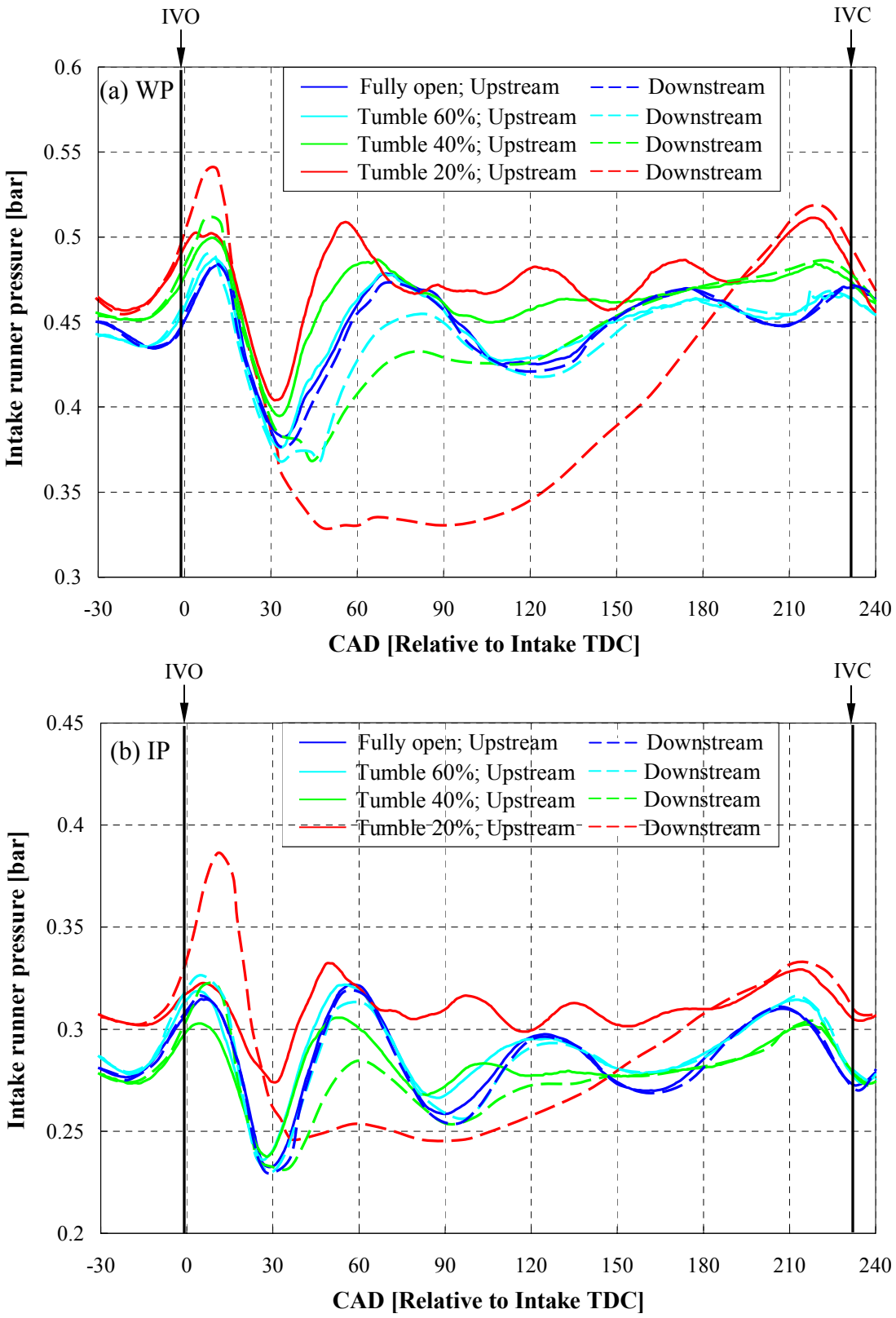

Figure 6.1. Upstream and downstream intake runner pressures under WP and IP, runner 4, MBT.

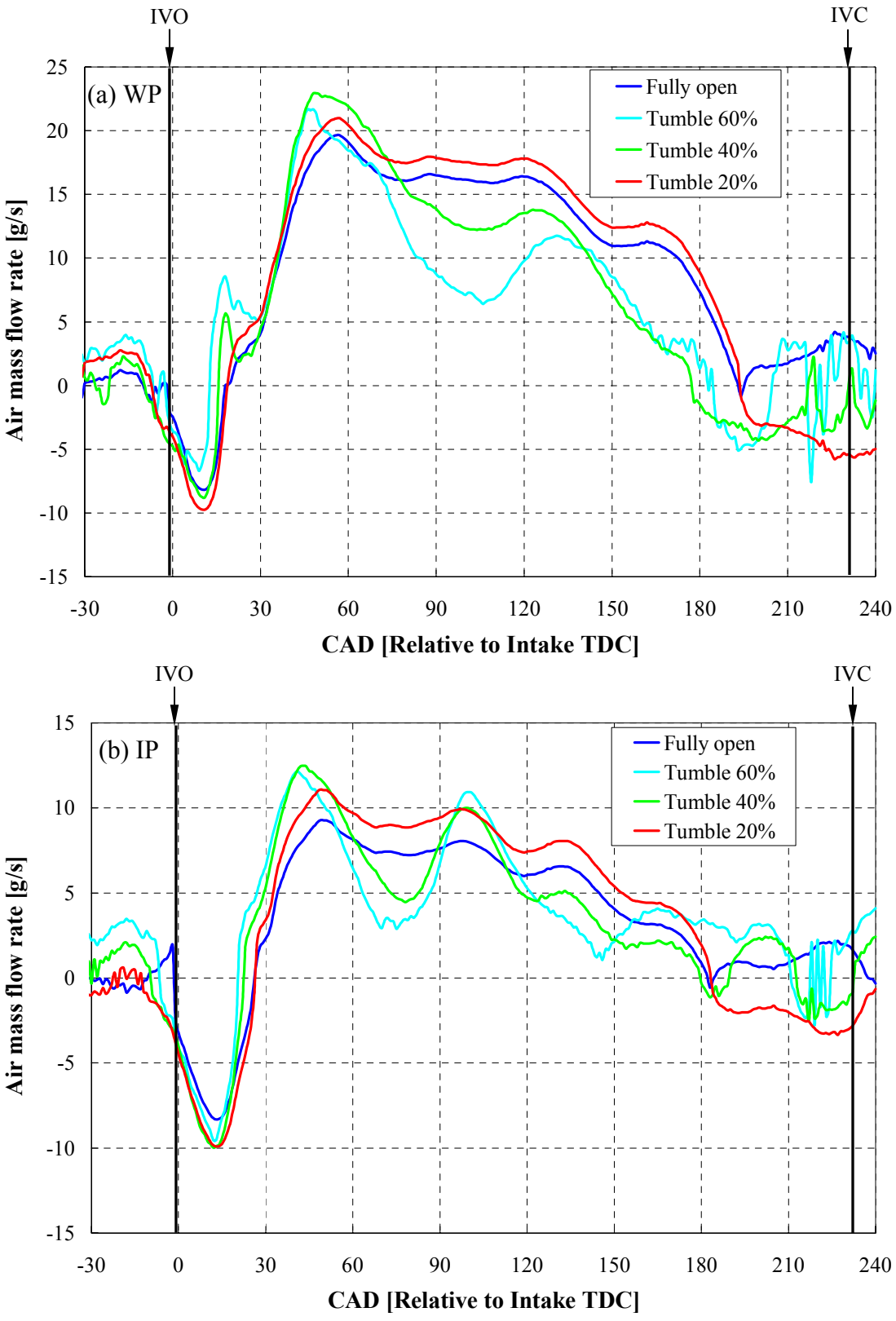

Figure 6.2. Calculated air mass flow rate in intake runner 4 under WP and IP.

Parameters	WP				IP			
	100%	60%	40%	20%	100%	60%	40%	20%
Engine speed [rpm]	1600				1200			
Average air mass flow per cycle ($m_{air,e}$) [g]	0.194	0.196	0.199	0.204	0.118	0.122	0.120	0.120
Average air mass flow per cycle (IVO – IVC) ($m_{air,e,P}$) [g]	0.208	0.210	0.211	0.217	0.116	0.119	0.120	0.120
Max. air mass flow rate $\dot{m}_{air,\max,e}$ [g/s]	19.66	21.68	22.93	20.98	9.28	12.15	12.48	11.08
Bore pressure drop $\Delta P_{\infty 3}$ ['' H_2O]	1.5	3	8	32	0.35	1	2.25	9

Table 6.2. Comparison of $m_{air,e}$, $m_{air,e,P}$, $\dot{m}_{air,\max,e}$, and $\Delta P_{\infty 3}$ under WP and IP.

Figure 6.3 compares the air mass flow rate $\dot{m}_{air,f}$ from flow experiments for each blockage-load combination under the corresponding $\Delta P_{\infty 3}$ (see Table 6.2). For both operating conditions, the $\dot{m}_{air,f}$ increases with valve lift for unblocked and 60%-open runners, as expected. The 40% and 20%-open cases also exhibit increase of $\dot{m}_{air,f}$ in the range of L_v = 0 – 0.1". However, further increase of valve lift (to 0.1" - 0.325") results in a limited increase in $\dot{m}_{air,f}$ for 40%-open blockage and a nearly negligible variation for 20%-open runner. This is due to the fact that flow losses are dominated by blockage at high valve lifts, which will be elaborated next. Both WP and IP exhibit the same trend, while the former leading to higher $\dot{m}_{air,f}$ because of larger $\Delta P_{\infty 3}$, as expected. Note that $\dot{m}_{air,f}$ at $L_{v,max}$ = 0.325" (listed in Table 6.3) shows an average deviation of 2.6% relative to $\dot{m}_{air,\max,e}$ of Table 6.2.

6.2 Flow loss coefficient and discharge coefficient

The flow loss coefficient for each blockage is determined from Eq. (4.56) as a function of intake valve lift. Figure 6.4 shows $K_{12,f}$ and $K_{13,f}$ for 20%-open blockage for $\Delta P_{\infty 3}$ = 14" and 25" H_2O in flow experiments, while the results of $K_{12,f}$ for 40% and 60%-open blockages are deferred to Fig. D1. Similar to $K_{12,f}$, the flow loss coefficient across the blockage and intake valves $K_{13,f}$ is also calculated from Eq. (4.56) by replacing $P_{2,f}$ with $P_{3,f}$. At valve lifts above L_v = 0.1", $K_{13,f}$ is nearly constant and independent of pressure drop, which suggests the dominance of blockage as the restriction. At lower lifts, losses through intake valves control the variation of $K_{12,f}$ and $K_{13,f}$. Hence, in the current

analysis, an average $K_{12,f}$ over L_v = 0.1" - 0.325" is used for $K_{12,f}$ to estimate $\dot{m}_{air,e}$ from Eq. (4.57).

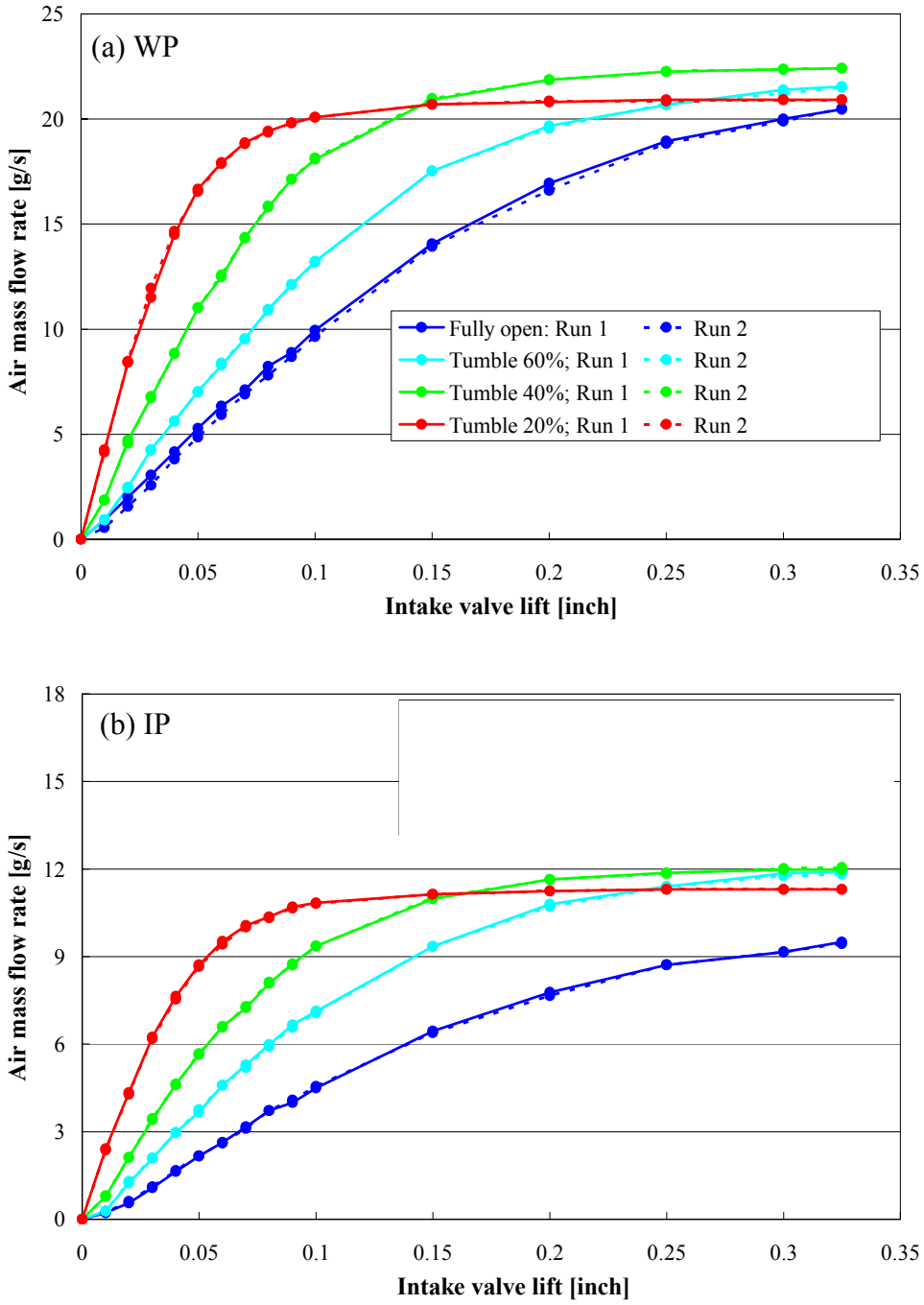

Figure 6.3. Effect of blockages on air mass flow rate.

Mass flow rate [g/s]	WP		IP	
	Engine ($\dot{m}_{air,\max,e}$)	Flow ($\dot{m}_{air,f}$ at $L_{v,\max}$ = 0.325")	Engine ($\dot{m}_{air,\max,e}$)	Flow ($\dot{m}_{air,f}$ at $L_{v,\max}$ = 0.325")
Fully open	19.66	20.45	9.28	9.44
Tumble 60%	21.68	21.55	12.15	11.91
Tumble 40%	22.93	22.42	12.48	12.05
Tumble 20%	20.98	20.92	11.08	11.29

Table 6.3. Maximum mass flow rate comparison.

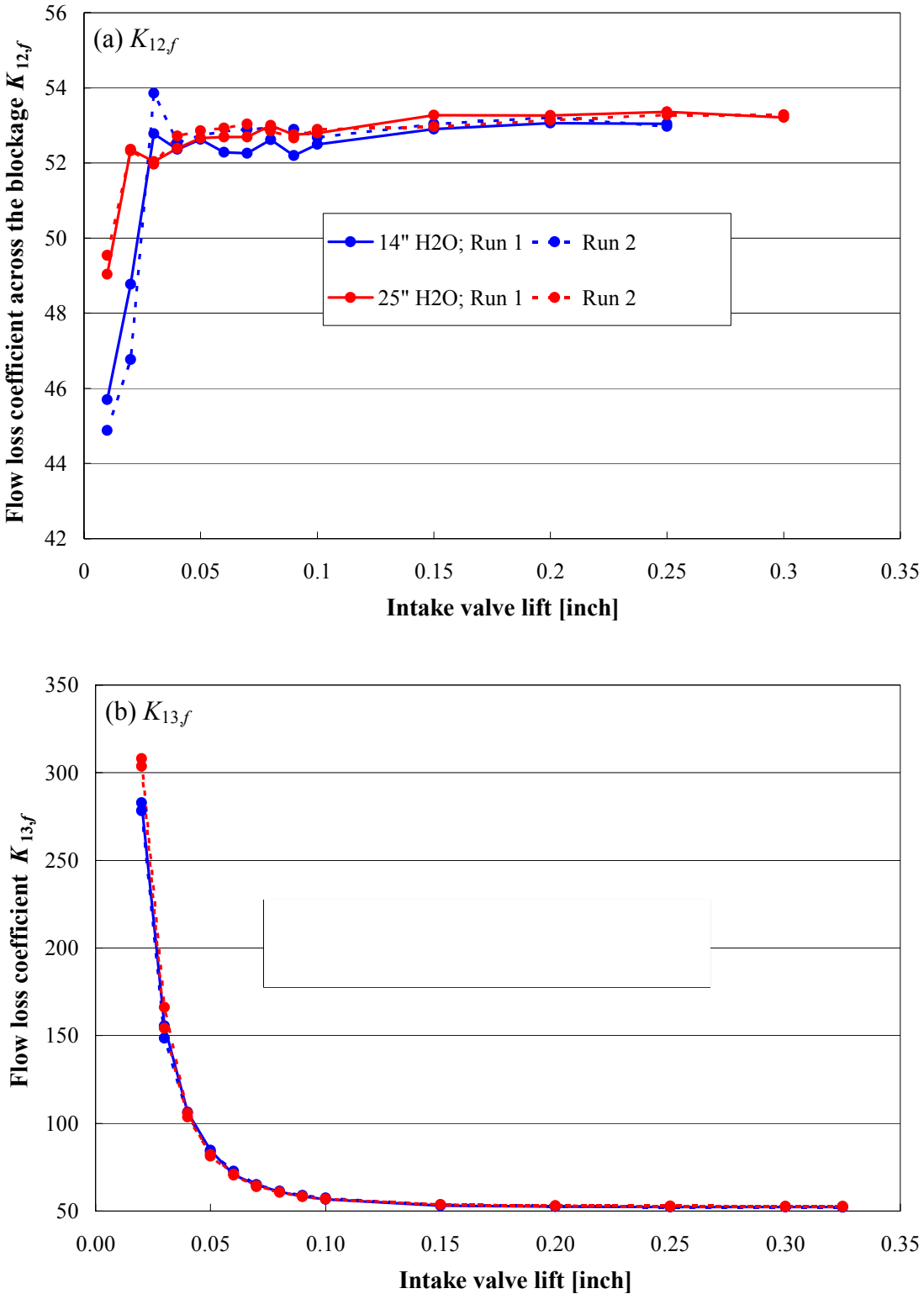

Figure 6.4. Flow loss coefficient $K_{12,f}$ and $K_{13,f}$ for 20%-open blockage.

Figure 6.5 depicts $K_{12,f}$ for different blockages under both operating conditions. The flow loss coefficient for a given blockage is comparable under different operating conditions, particularly above 0.1" valve lift, demonstrating that flow resistance across a component depends on its geometrical details only. With more runner restriction, $K_{12,f}$ continues to increase due to higher flow losses across the blockage ($K_{12,f}$ of 3.6, 11, and 53 for 60%, 40%, and 20%-open blockages, respectively). It is interesting at this point to contrast these results with conventional sharp-edged orifice losses illustrated in Appendix E by Miller, 1996. The calculation of flow loss coefficient by Eq. (E4) is a well established empirical fit to the experimental results. The empirical estimates of K from Eq. (E4) are next compared in Fig. 6.6 with the flow results here under WP. To calculate K from flow experiments, the air velocity at the blockage $V_{b,f}$ is now used in Eq. (4.56) to replace $V_{1,f}$ for consistency with the loss coefficient of Appendix E. Figure 6.6 shows now a gradual increase in K with increasing runner restriction. Two calculations for a given blockage display a small deviation primarily due to different pressure tap locations (orifice fits are based on pressure taps placed at 1 D upstream and $1/2$ D downstream of the orifice, whereas in the present work, pressure transducers are located 0.375" upstream and downstream of the blockage, about one-fourth the runner hydraulic diameter). Yet, it is impressive to observe that available empirical relationships for orifices can be used for a first order estimate of blockage behavior.

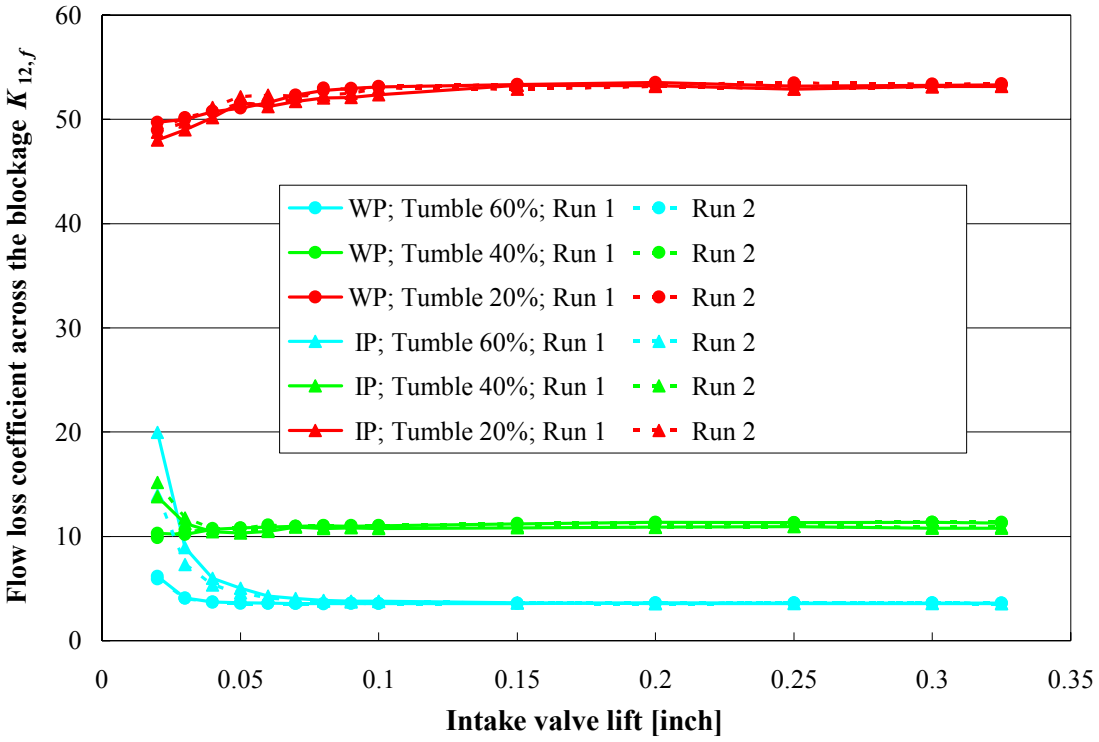

Figure 6.5. Effect of blockages on flow loss coefficient $K_{12,f}$.

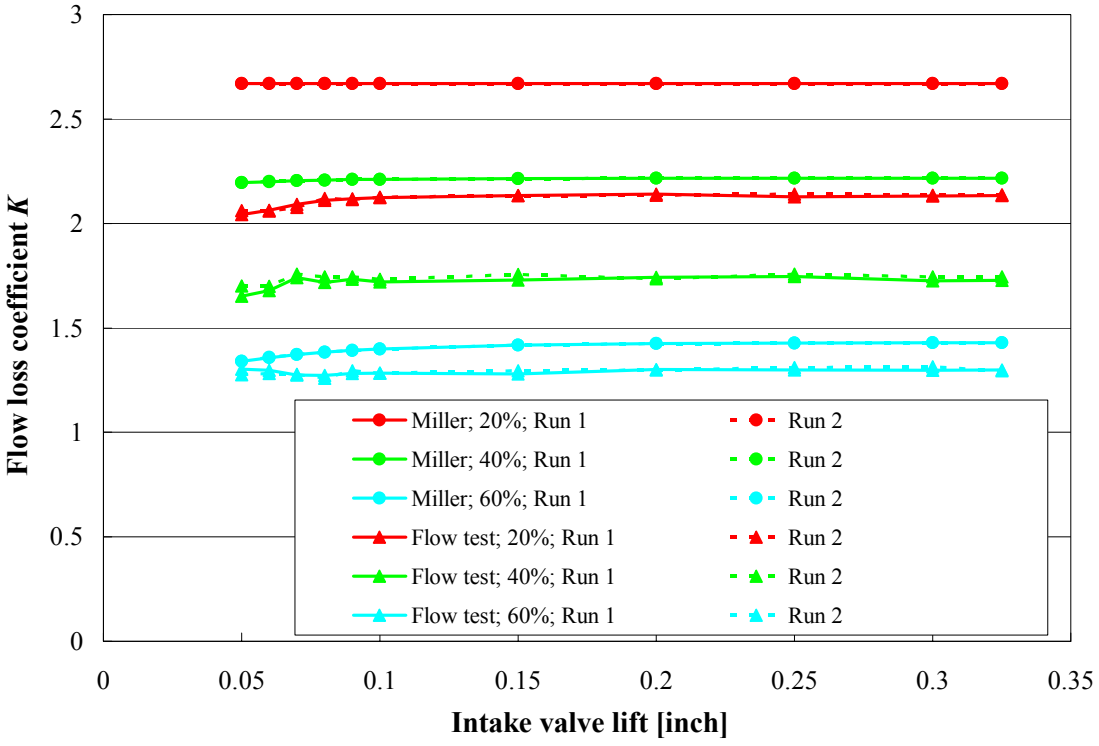

Figure 6.6. Comparison of flow loss coefficient for blockages under WP.

The discharge coefficient C_D, calculated from Eq. (4.59), is presented in Fig. 6.7 for all configurations under two operating conditions. Increasing runner restriction is associated, in general, with reduced C_D hence lowered engine breathing capacity, consistent with the increased $K_{12,f}$ of Fig. 6.5. For unblocked and 60%-open cases, C_D continues to increase with L_v, though at slower rates at high L_v's. For 40% and 20%-open blockages, C_D gradually increases in L_v = 0 – 0.1" range, but remains essentially unchanged at higher valve lifts, suggesting that the blockage plays a dominant role in flow losses at high L_v, as demonstrated in Fig. 6.4 for the 20%-open runner. The behavior of C_D is consistent between WP and IP, as expected.

6.3 Tumble number and tumble ratio

Three vertical loads measured by the underhead tumblemeter (recall Figs. 3.6 and 3.8) are compared in Fig. 6.8 for 20%-open blockage under $\Delta P_{\infty 3}$ of 32" and 9" H_2O corresponding to WP and IP, respectively. The results for unblocked, 60%, and 40%-open cases are deferred to Figs. D2 – D4, respectively. In flow experiments, entering air forms a large scale tumble vortex in the cylinder at high L_v (Floch *et al.*, 1995). The flow acts on the screen and exerts vertical forces measured by the load cells. Two loads on the exhaust side (Locations 2 and 3 in Fig. 3.8) are higher than the one on the intake side (Location 1), as expected. Furthermore, the readings differ between Locations 2 and 3 for both WP and IP. This is due to the port geometry, orienting flow more towards Location 3, resulting in a larger load on the screen at this position. Both operating conditions exhibit a similar trend for three loads, while WP yields a value three times larger than IP at peak valve lift.

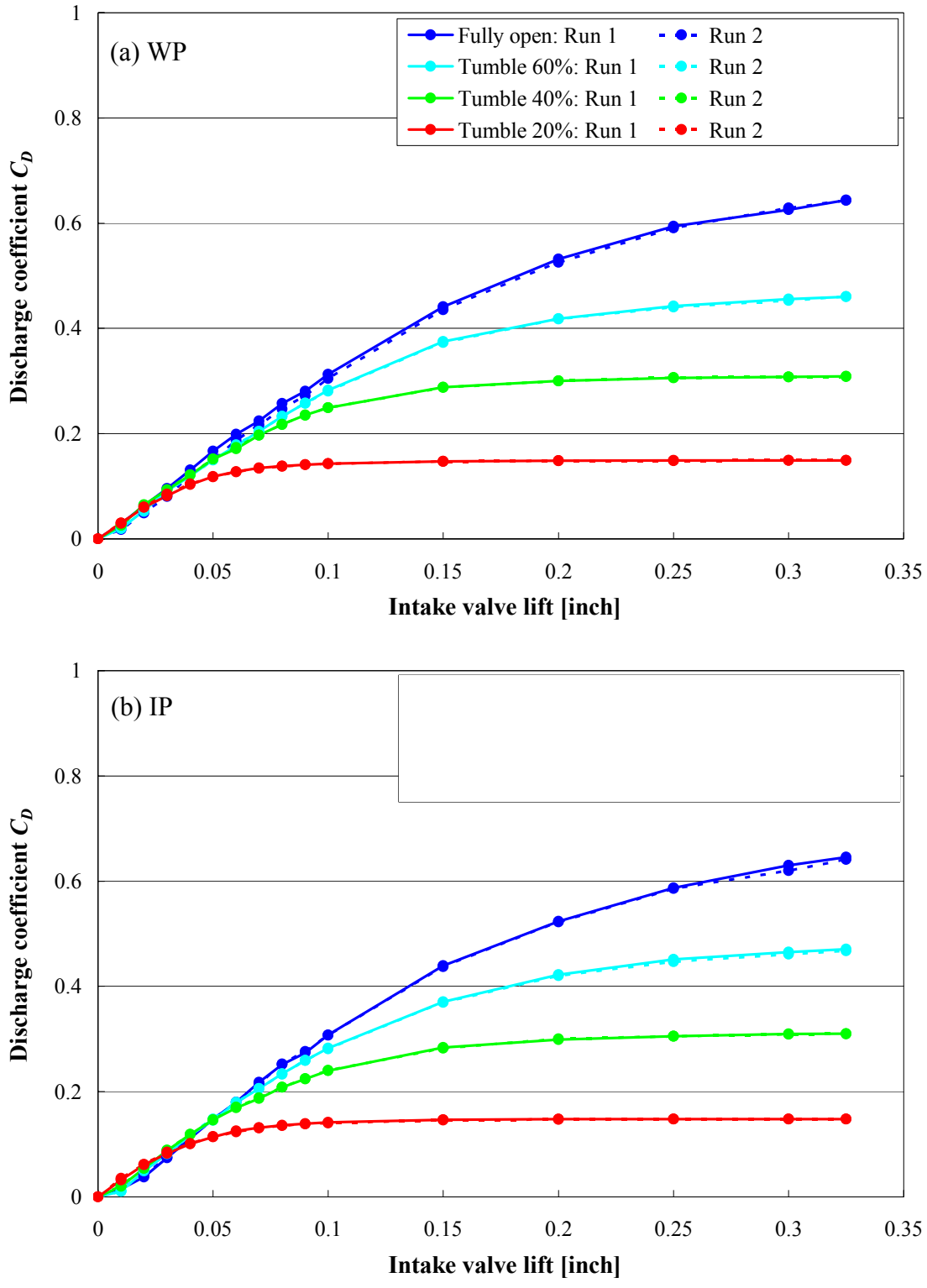

Figure 6.7. Effect of blockages on discharge coefficient.

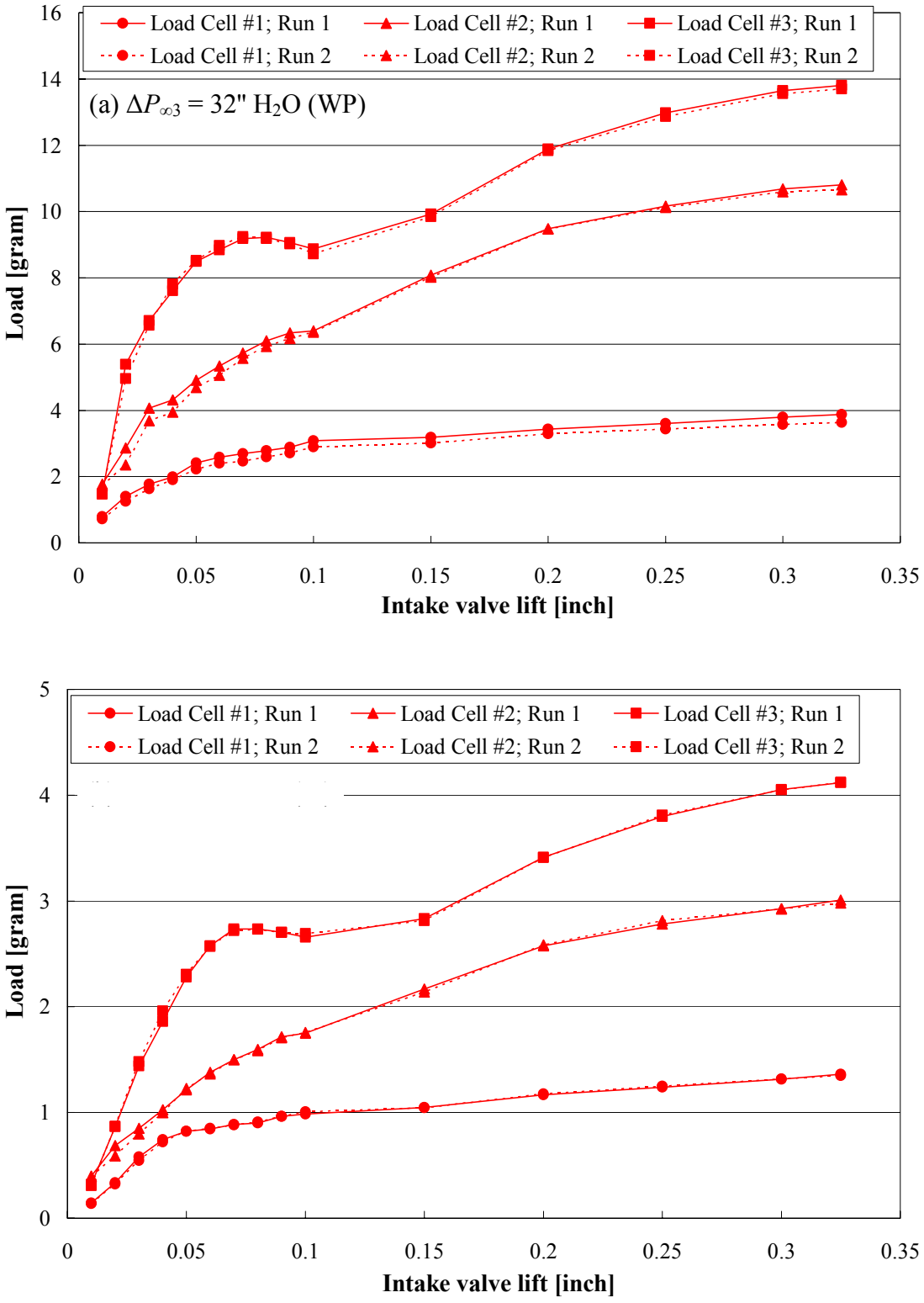

Figure 6.8. Vertical loads on the screen for 20%-open blockage.

The tumble number, calculated by Eq. (4.69), is compared in Fig. 6.9 for all configurations under WP and IP. At the low L_v range of about 0 - 0.1", TN decreases markedly for both conditions. At low L_v, however, the large scale tumbling flow has not yet formed in the cylinder, thus TN cannot truly reflect the tumble characteristics (Floch *et al.*, 1995). The tumble vortex strength is observed to increase with L_v = 0.1" – 0.325" range and exhibit higher TN for 20%-open blockage, consistent with the experimental results by Arcoumanis *et al.*, 1992, indicating a strong tumble motion. The 40%-open blockage exhibits only a small increase in TN, while TN for the 60%-open runner remains essentially the same over L_v = 0.15" – 0.325". The unblocked runner, on the other hand, displays a gradual reduction of TN, particularly for WP. TN at L_v = 0.325" increases with increasing runner restriction for both conditions, with IP showing the lower value. For WP, TN = 1.97, 1.13, 0.56, and 0.27 for 20%, 40%, 60%, and fully open runners, respectively, while the corresponding values for IP are 1.62, 0.96, 0.39, and 0.08. It is worth noting in Fig. 6.10 the linear relationship between $K_{12,f}$ (on a log scale) and TN at L_v = 0.325" under both operating conditions, indicating that strong tumble motion leads to a linearly increased flow losses.

Tumble ratio, as determined from Eq. (4.79), is depicted in Fig. 6.11. TR increases with increasing runner restriction under both conditions while WP gives rise to higher values than IP for a given blockage, similar to the trend of TN at the peak L_v. For example, TR = 0.433, 0.341, 0.217, and 0.197 for 20%, 40%, 60%, and fully open runners at WP (Run 1 in Fig. 6.11), respectively, with the corresponding values at IP being 0.333, 0.291, 0.195, and 0.052. The relationship between TN and TR is presented

in Fig. 6.12. As observed in Fig. 6.9, TN at L_v = 0.325" increases with increasing restriction hence TR for both WP and IP.

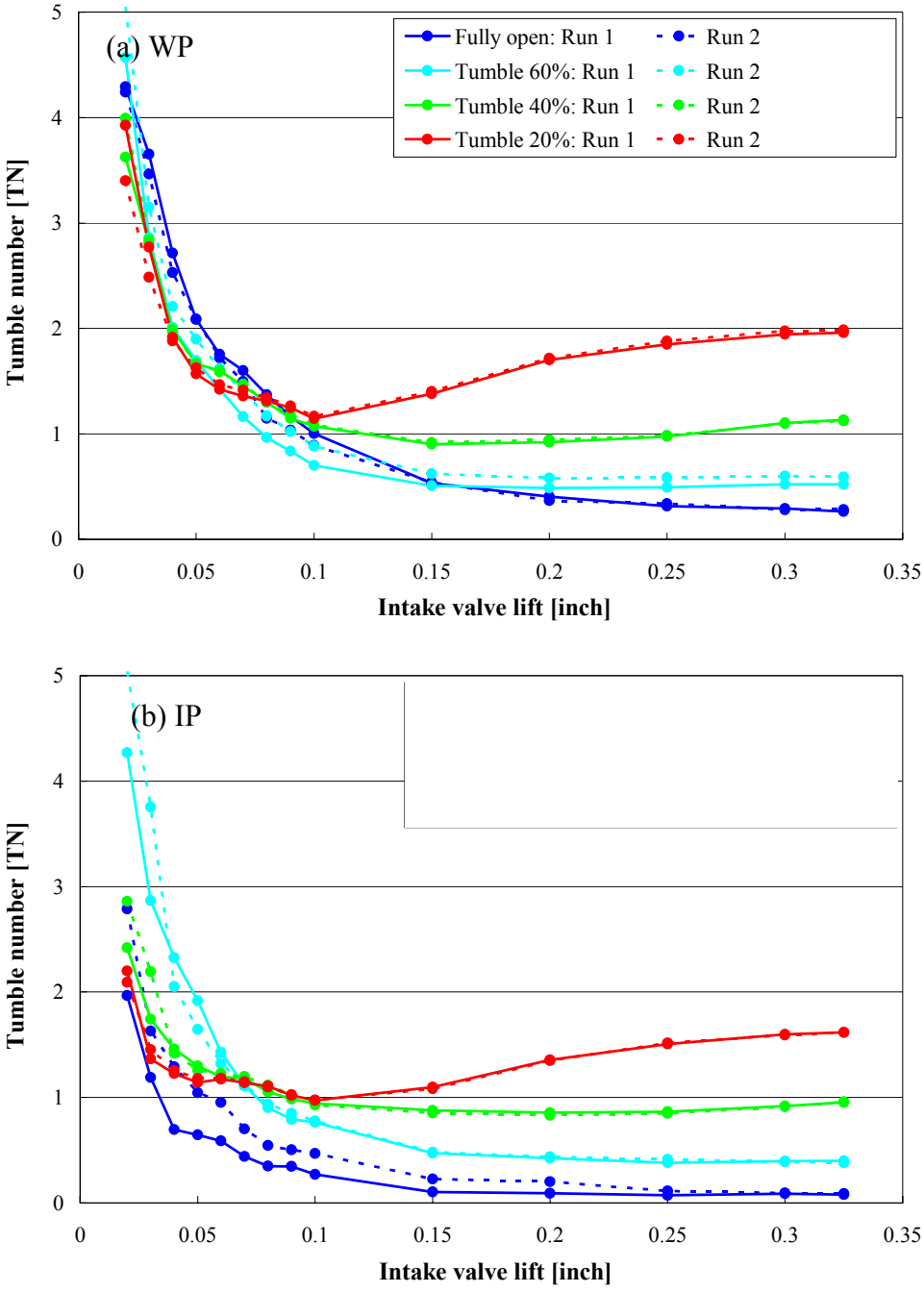

Figure 6.9. Effect of blockages on tumble number.

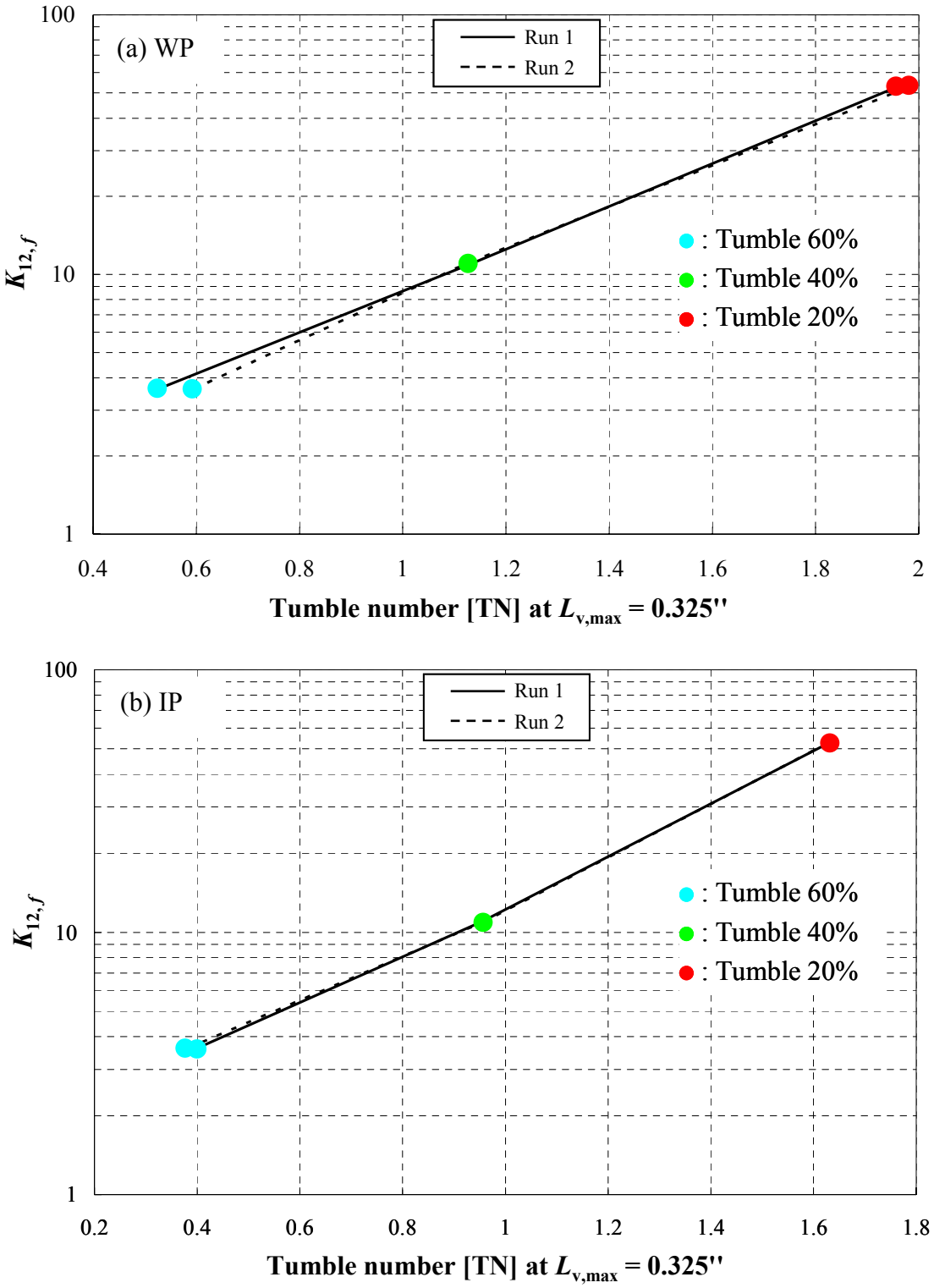

Figure 6.10. Comparison of $K_{12,f}$ vs. TN at $L_{v,max}$ = 0.325" for blockages.

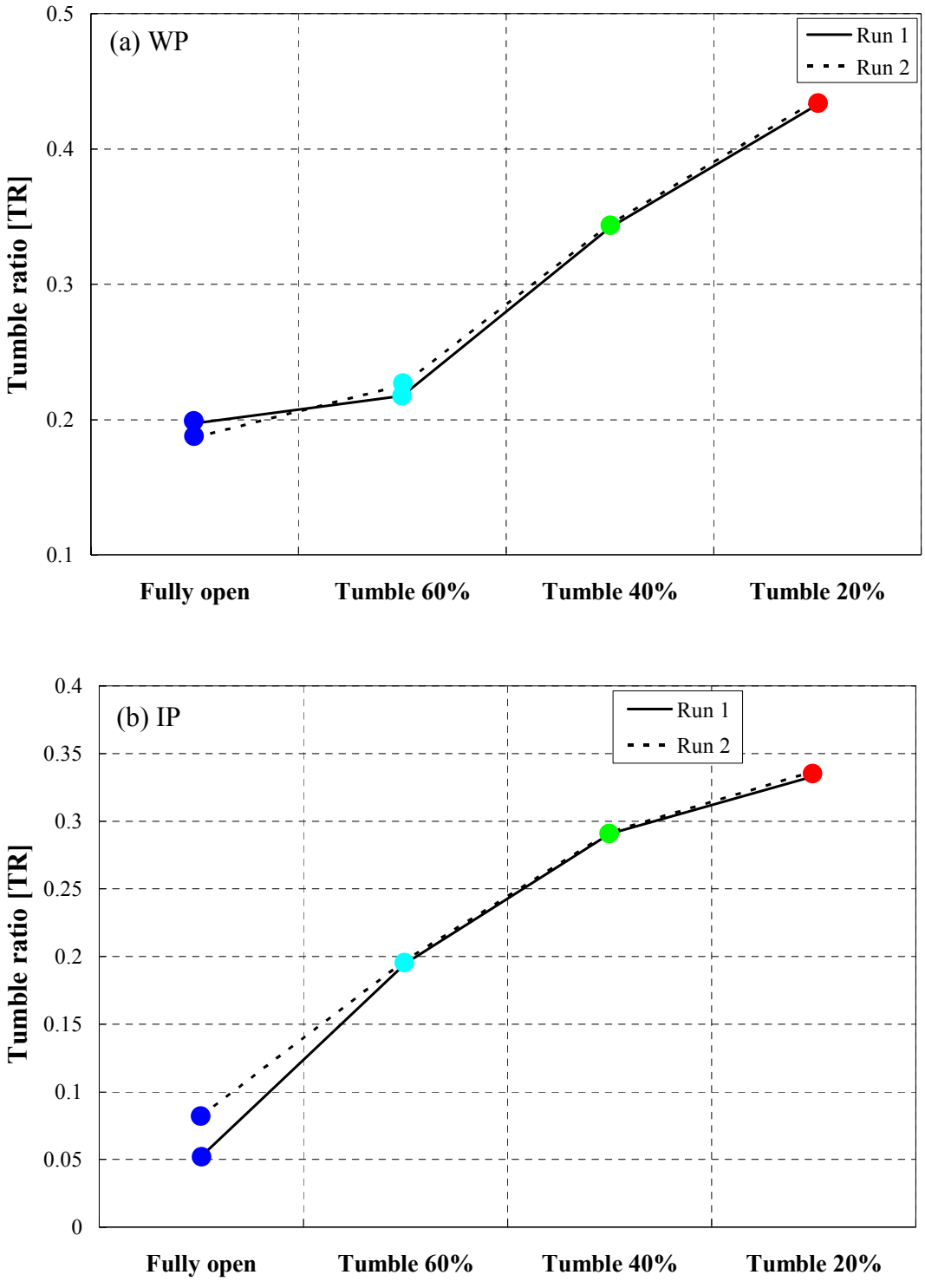

Figure 6.11. Effect of blockages on tumble ratio.

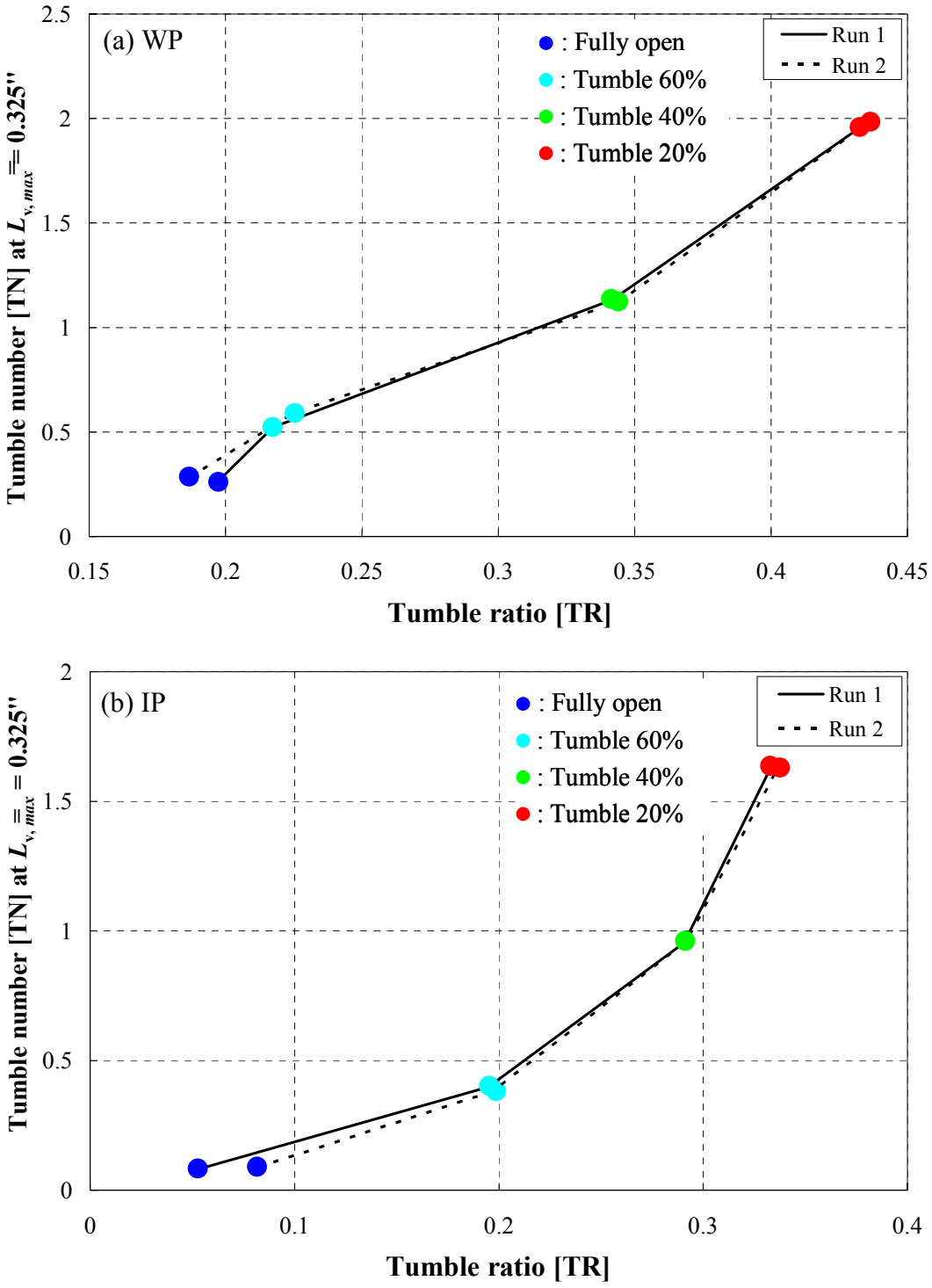

Figure 6.12. Tumble number at peak valve lift vs. tumble ratio.

6.4 Correlation between flow and engine experiments

0 – 10% and 10 – 90% burn durations (θ_{0-10} and θ_{10-90}) have been determined by applying Eq. (4.27) to in-cylinder pressure from the engine experiments with an improved combustion pressure rise method. Figure 6.13 depicts θ_{0-10} for all configurations as a function of TR under both operating conditions. Here, TR is used to correlate with the engine results, while the corresponding correlation based on TN at $L_{v,max}$ = 0.325" is shown in Fig. D5 which exhibits a similar behavior. Fully open runner is associated with the longest θ_{0-10} of 27° and 39° for WP and IP (Run 1 in Fig. 6.13), respectively, primarily because the in-cylinder gas motion generates the lowest TR, leading to insignificant increase of u' and S_T, hence the slow burning. The introduction of 60%-open blockage increases TR to about 0.2 for both conditions as shown in Figs. 6.13, but θ_{0-10} does not appear to significantly decrease, suggesting that the low level of tumble motion cannot help accelerate the flame propagation during the early stage of combustion. The tumble ratio increases to 0.341 and 0.291 at WP and IP, respectively, for 40%-open blockage, with a reduction in θ_{0-10} of 11° at WP and 15° at IP as compared to the unblocked runner. Further runner restriction with 20%-open blockage continues to increase TR and the reduction in θ_{0-10} reaches 14° and 19° for WP and IP, respectively, suggesting a strong tumble motion and the associated fast combustion. Figure 6.14 gives a correlation between θ_{10-90} and TR, with a similar comparison in terms of TN deferred to Fig. D6. The trend displayed in Fig. 6.14 is somewhat similar to Fig. 6.13, indicating that highly intensified tumble vortex does shorten the θ_{0-10} and θ_{10-90} while the tumble motion with low TR does not influence the burn duration. The blocked runner has more impact in

reducing θ_{10-90} at IP than WP. As illustrated in Fig. 6.14, θ_{10-90} is reduced only by 1° and 2° for 40% and 20%-open blockages at WP compared to the unblocked case, whereas the corresponding reduction at IP is 10° and 13°.

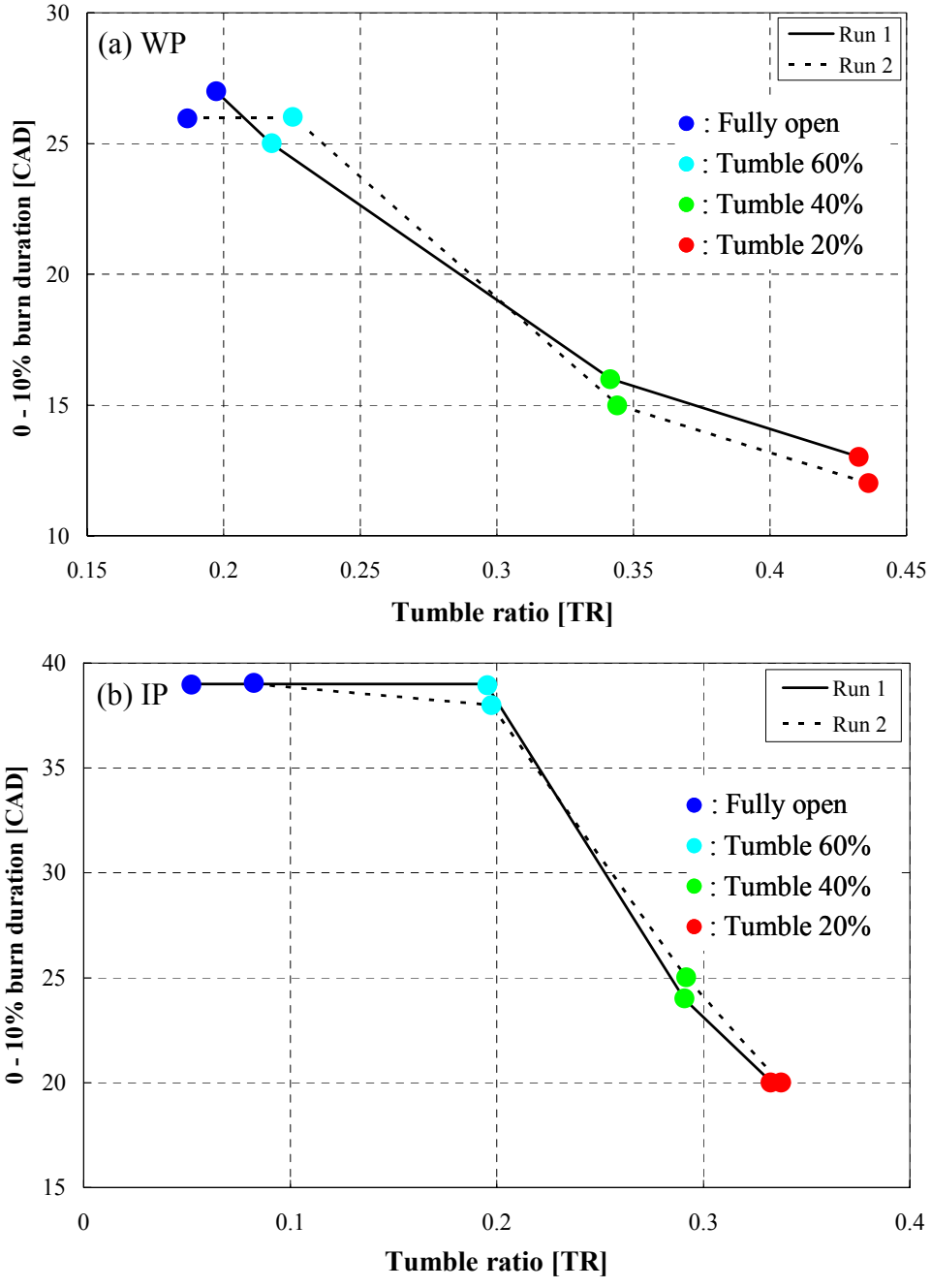

Figure 6.13. 0 – 10% burn duration vs. tumble ratio.

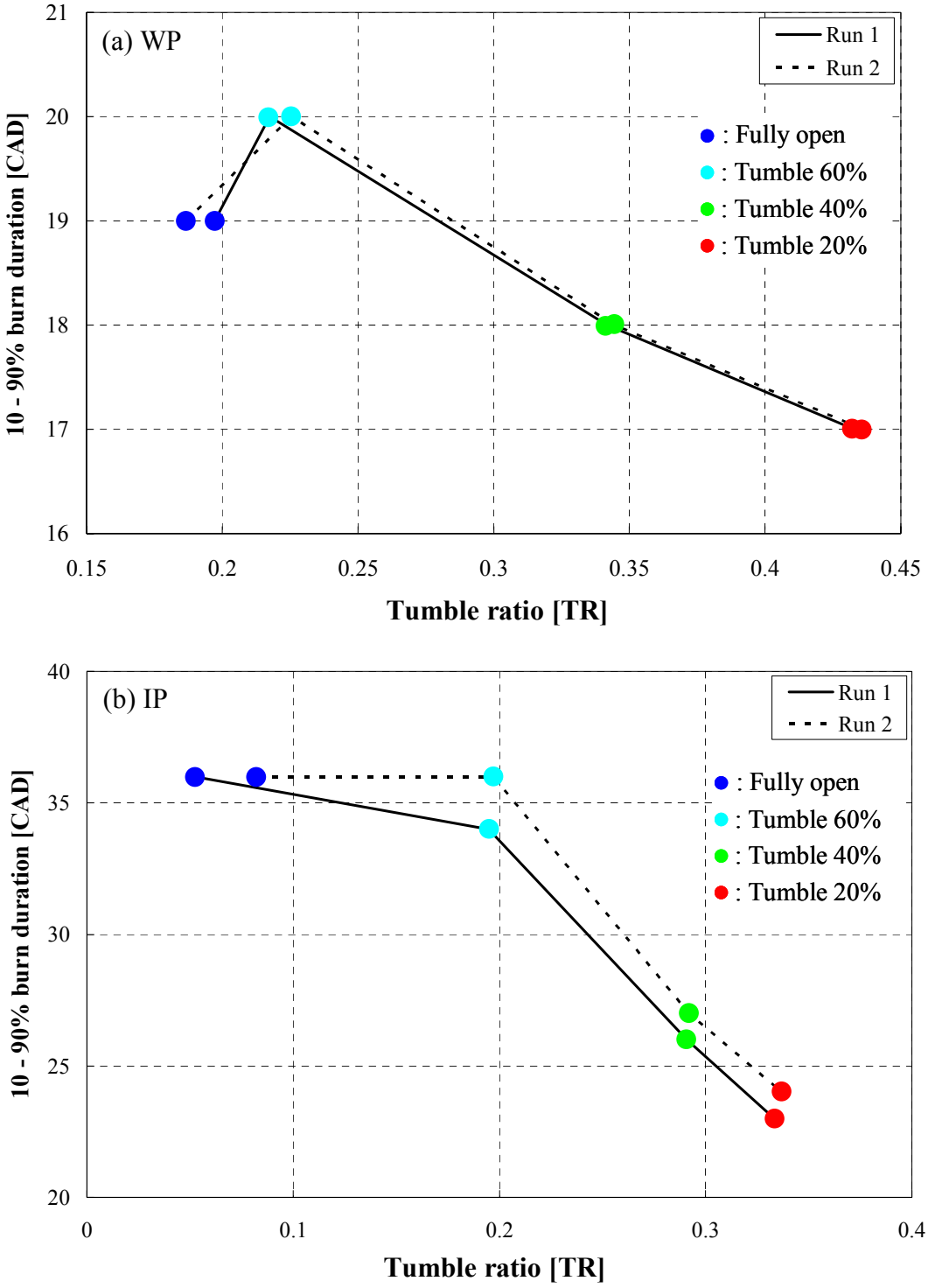

Figure 6.14. 10 – 90% burn duration vs. tumble ratio.

To investigate the effect of tumble intensity on cyclic combustion variation (recall Section 4.3), COV vs. TR and LNV vs. TR are shown in Figs. 6.15 and 6.16, respectively, with the corresponding illustration based on TN being deferred to Figs. D7 and D8. The 60%-open runner does not help stabilize the combustion noticeably compared to the unblocked case. On the other hand, COV is reduced to 0.72% and 0.55% for 40% and 20%-open blockages at WP (TR = 0.341 and 0.433, respectively), compared to 1.39% for fully open runner (TR = 0.197). The corresponding values at IP are 3.45%, 2.38%, and 1.67% for unblocked, 40%, and 20%-open runners, with TR = 0.052, 0.291, and 0.333. Figure 6.16 illustrates the increase in LNV to 97.7% and 98.7% for 40% and 20%-open blockages at WP, in contrast to 96.1% for the unblocked runner, whereas the values at IP are 84%, 92.2%, and 95.8% for unrestricted, 40%, and 20%-open cases. Hence, the combustion stability can be improved with increased tumble intensity under part-load operating conditions, similar to the observations by Omori *et al.*, 1991.

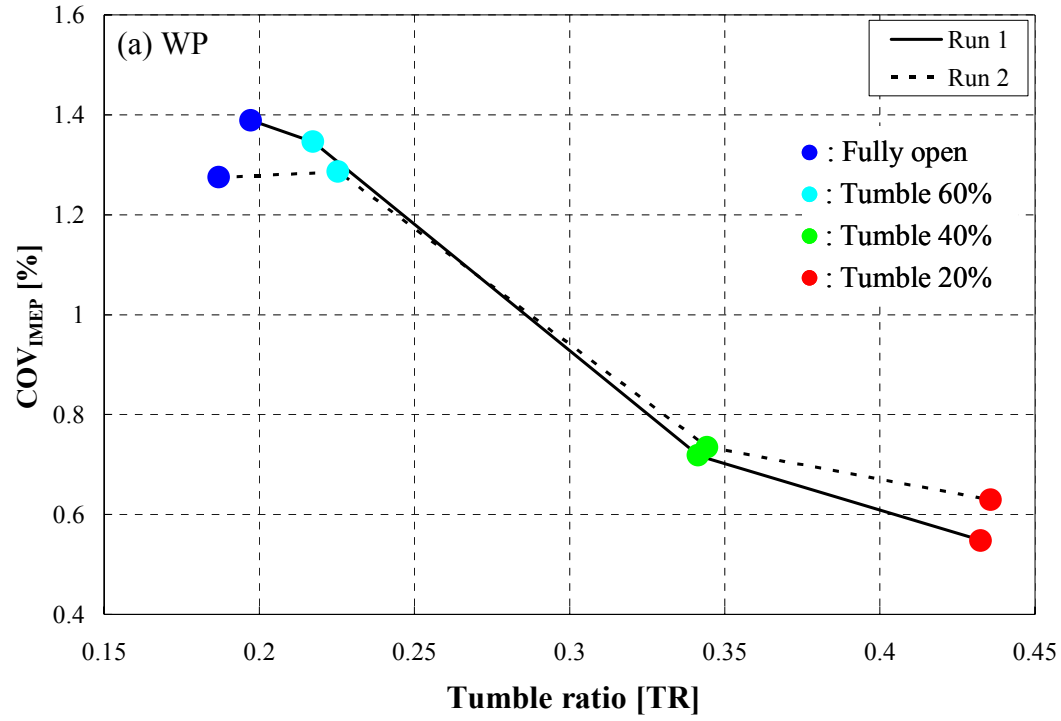

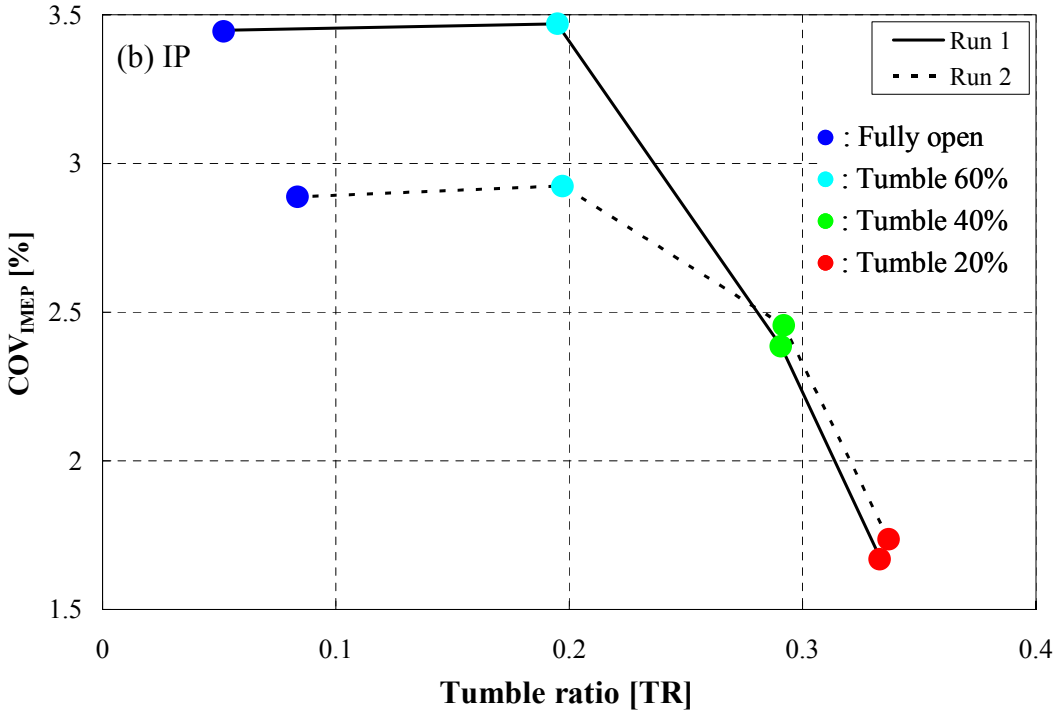

Figure 6.15. COV in IMEP vs. tumble ratio.

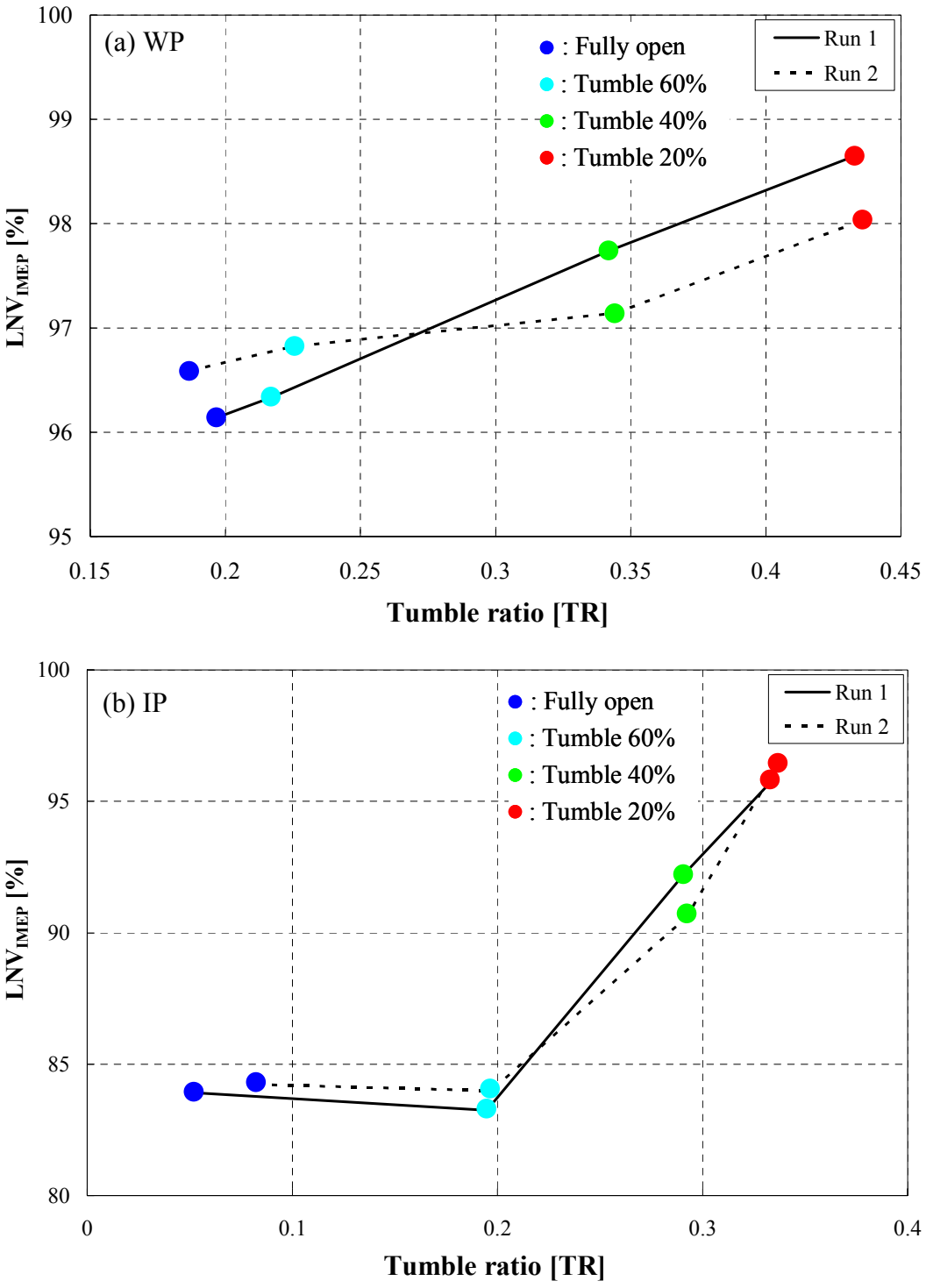

Figure 6.16. LNV in IMEP vs. tumble ratio.

CHAPTER 7

CONCLUSIONS

The present study has performed a comprehensive experimental investigation of the impact of intake runner blockages on a Chrysler 2.4L 4-valve I4 spark ignition engine under part-load operating conditions in dynamometer and flow laboratories. Different types of charge motion (tumble, swirl, and swumble) have been generated by runner blockages in engine experiments, leading to significant changes in the combustion characteristics, in-cylinder heat release, and exhaust emissions with stoichiometric and EGR-diluted mixtures at various spark timings. A modified combustion pressure rise method and one-zone model are developed to characterize combustion and in-cylinder heat release, respectively.

Steady-state flow-bench experiments have also been conducted to quantify the blockage-generated tumble vortex by using the same hardware, including cylinder head, intake manifold, and blockages from the engine experiment. For this setup, a tumblemeter has been designed and mounted under the cylinder head with a new methodology developed to accurately quantify the in-cylinder tumble motion of different magnitudes. A correlation has been observed between the engine and flow lab

experiments under the operating conditions WP and IP, which helps assess the impact of tumble blockages on combustion and cyclic variability.

Engine experiments have been conducted under five part-load operating conditions for unblocked and blocked runners with stoichiometric and EGR-diluted mixtures. The results are summarized as follows:

- The optimum EGR ratio has been extended to 26%, 20%, and 25% with the tumble, swirl, and swumble blockages, from 19% of the unblocked runner, under the operating condition WP.
- COV increases with EGR while LNV showing an expected opposite trend, indicating more cyclic combustion variability with increased dilution mainly due to increasing slow burn, partial burn, and misfiring cycles. Charge motion is observed to significantly reduce the instability with tumble showing a better improvement than swirl and swumble at a specific EGR level.
- Pumping losses decrease with dilution mainly due to more recycled burned gas leading to increased MAP and in-cylinder pressure during intake process. The blocked runner brings about flow separation and backflow downstream of the blockage leading to increased flow losses and considerable change of the intake runner pressures at various dilution levels. The blockage flow losses are responsible for higher pumping losses with charge motion.
- The introduction of EGR increases θ_{0-10} for all configurations at MBT timing. EGR dilution increases θ_{10-90} for fully open and swirl cases, whereas, for tumble and swumble, θ_{10-90} remains mostly insensitive to dilution at EGR

ratios below 16%, particularly for tumble. Compared to unblocked runner, both θ_{0-10} and θ_{10-90} are significantly shortened by tumble motion. Swirl and swumble reduce θ_{0-10} in contrast to fully open runner, however, θ_{10-90} increases mainly due to reduced turbulence generation from the conserved solid body rotation.

- Exhaust gas temperature decreases with EGR due to reduced burned gas temperature until the optimum dilution level. Compared to unblocked runner at MBT, swumble has raised EGT at all dilution levels and swirl has also increased EGT at EGR ratios above 8%. Tumble, on the other hand, decreases EGT due possibly to the variation of peak combustion temperature and in-cylinder heat transfer.
- With increasing dilution, NO_x emissions are reduced continuously due to the significance of temperature in the Zeldovich mechanism. For example, NO_x emissions are reduced by 91%, 83%, 80%, and 76% at the optimum EGR with MBT timing for tumble, swumble, swirl, and fully open, respectively. The specific NO_x emissions are relatively comparable for both unblocked and blocked runners at MBT, particularly at EGR ratios above 8%.
- HC emissions at MBT increase as the in-cylinder mixture becomes more diluted due to substantial cyclic variation and deteriorated combustion. Compared to the unrestricted runner at MBT, tumble displays similar HC emissions while higher HC emissions are observed for swirl and swumble.
- CO emissions at MBT decrease with dilution until the optimum EGR for fully

open runner. Tumble shows a similar trend with even lower emissions. This trend, however, does not hold for swirl and stumble, which yield higher CO emissions than unblocked runner at MBT.

In addition, steady flow bench experiments have been performed to quantify the engine breathing capacity and the blockage-generated in-cylinder tumble motion for different configurations. Two engine operating conditions WP and IP are simulated in the flow laboratory. A correlation is obtained between the flow and engine experiments to help quantify the impact of tumble vortex on engine combustion characteristics. Some key results from this investigation are summarized as follows:

- The maximum air mass flow rate $\dot{m}_{air,\max,e}$ is matched in flow experiments at $L_{v,max}$ = 0.325" for each blockage-load combination rather than a constant bore pressure drop $\Delta P_{\infty 3}$ for all configurations. This approach allows for a more realistic comparison of the flow characteristics between flow and engine experiments, hence leading to desirable correlations between the two facilities.
- The flow loss coefficient $K_{12,f}$ increases and discharge coefficient C_D decreases with increasing runner restriction, as expected. For 20% and 40%-open runners, the flow at valve lifts above 0.15" is dictated by the blockage only.
- Tumble number at $L_{v,max}$ = 0.325" increases with increasing runner restriction for both operating conditions, with WP giving rise to higher values than IP due to higher flow rates. Displaying a similar trend to TN at the peak valve

lift, tumble ratio, hence the impact of in-cylinder tumble motion increases with increasing runner restriction, consistent with the observations of Floch *et al.*, 1995. $K_{12,f}$ in log-scale increases nearly linearly with TN at L_v = 0.325" under both WP and IP.

- A good correlation is observed between the flow and engine experiments. Under both operating conditions, enhanced tumble with higher tumble ratio significantly decreases θ_{0-10} for the 20% and 40%-open blockages, while low level of tumble produced, for example, by 60%-open blockage does not increase θ_{10-90}. Tumble is more effective in decreasing θ_{10-90} at IP than WP, particularly for 20% and 40%-open runners. Combustion stability has been improved with increasing tumble ratio under both operating conditions.

The suggestions for future work include: (a) performing air-lean engine experiments with the current blockages to examine the impact on fuel consumption, engine combustion, dilution limit, and emissions; (b) searching for alternative blockage designs to reduce flow losses associated with these components; (c) investigating the effect of charge motion in stabilizing the combustion with aggressive ignition retard to improve the cold-start catalyst light-off; and (d) using computational tools such as CFD to further understand the in-cylinder flow characteristics, determine the turbulence intensity during compression and combustion, predict the engine breathing capacity and intensity of flow motion, and then correlate with the current experimental findings.

APPENDIX A

NOMENCLATURE

ACB	Air cleaner box
ADC	Analog to digital converter
AEOC	Approximate end of combustion
AFR	Air fuel ratio
ATDC	After top dead center
A_{runner}	Intake runner cross-sectional area
a	Crank radius = $S/2$
B	Cylinder bore
BTDC	Before top dead center
BDC	Bottom dead center
BMEP	Brake mean effective pressure
BSFC	Brake specific fuel consumption
CAD	Crank angle degree
CO	Carbon monoxide
CO_2	Carbon dioxide
COV	Coefficient of variation
C_D	Discharge coefficient
c_v	Specific heat at constant volume
D	Hydraulic diameter
DOHC	Double overhead cam
dt	Differential time for every crank angle degree
ECU	Engine control unit
EGR	Exhaust gas recirculation
EGT	Exhaust gas temperature
EOC	End of combustion
EVC	Exhaust valve closing
EVO	Exhaust valve opening
F	Force exerted on the screen
G	Angular momentum
h	Enthalpy

HC	Hydrocarbon
HP	Engine condition of 500 kPa BMEP at 2000 rpm
I	Moment of inertia
IBDC	Intake bottom dead center
IMEP	Indicated mean effective pressure
IP	Engine condition of 78 kPa BMEP at 1200 rpm
IR	Intake runner
ISFC	Indicated specific fuel consumption
IVC	Intake valve closing
IVO	Intake valve opening
IVOP	Intake valve open period
K_{12}	Flow loss coefficient across the blockage
$K_{\infty 1}$	Flow loss coefficient based on entrance to the engine inlet port and upstream of the blockage
L	Connecting rod length
L_V	Intake valve lift
LML	Lean misfire limit
LNV	Lowest normalized value
m_{air}	Air mass flow per engine cycle
m_c	Mass of cylinder contents
m_{crevice}	Mass in the crevice volume
$\dot{m}_{air}$	Air mass flow rate
$\dot{m}_{air,\max}$	Maximum air mass flow rate
$\dot{m}_{fuel}$	Engine fuel mass flow rate
MAP	Manifold absolute pressure
MBT	Maximum brake torque
MFB	Mass fraction burned
N	Measurement points in flow experiment from 0 to peak intake valve lift
N_c	Number of cylinders
N_{eng}	Engine speed

NO_x	Nitric oxides
n	Polytropic coefficient
n_c	Polytropic coefficient for compression
n_e	Polytropic coefficient for expansion
O_2	Oxygen
P_1	Intake runner pressure, upstream of the blockage
P_2	Intake runner pressure, downstream of the blockage
P_3	Bore pressure
P_∞	Barometric pressure
ΔP_{12}	Pressure drop across the blockage, $P_1 - P_2$
$\Delta P_{\infty 3}$	Bore pressure drop, $P_\infty - P_3$
PMEP	Pumping mean effective pressure
p	In-cylinder pressure
p_{max}	Maximum in-cylinder pressure
p_{int}	Mean in-cylinder pressure during intake stroke
p_{exh}	Mean in-cylinder pressure during exhaust stroke
Δp	Pressure rise due to combustion
P_b	Brake power
P_i	Indicated power
Q_{app}	Apparent heat release
Q_{LHV}	Lower heating value of the fuel, 44 MJ/kg
Q_{hr}	Heat release from the combustion
Q_{ht}	In-cylinder heat transfer to the combustion chamber walls
Q_{cr}	Heat loss due to flow of the in-cylinder mass into and out of the crevice volume
$\dot{Q}$	Volumetric flow rate
$\dot{Q}_{hr}$	Rate of in-cylinder heat release from the combustion
$\dot{Q}_{ht}$	Rate of in-cylinder heat transfer to the combustion chamber walls
r_c	Compression ratio

R	Gas constant for air, $287\ \mathrm{J/kg \cdot K}$
RPR	Rate of combustion pressure rise
rpm	Revolution per minute
Re	Reynolds number
S	Piston stroke
$\overline{S}_p$	Mean piston speed
SA	Spark advance, crank angle degree BTDC or °BTDC
sfc	Specific fuel consumption
SI	Spark ignition
S_L	Laminar flame speed
S_T	Turbulent flame speed
T	Rate of the angular momentum of the tumble vortex, or torque
TDC	Top dead center
T_e	Time period of engine cycle
T_{wall}	Combustion chamber wall temperature
T_0	Ambient temperature
TI	Turbulence intensity
TN	Tumble number
TR	Tumble ratio
U_S	Sensible internal energy of the cylinder contents
u'	Turbulence intensity
V	In-cylinder volume
V_1	Air velocity in the intake runner, upstream of the blockage
V_b	Volume of the burned zone in combustion chamber
$V_{blockage}$	Air velocity at the blockage
V_c	Engine clearance volume
V_{cr}	Crevice volume
V_d	Displacement volume
V_u	Volume of the unburned zone in combustion chamber
V_0	Isentropic velocity

V_1	Air velocity, upstream of the blockage in intake runner 4
WOT	Wide open throttle
WP	Engine condition of 241 kPa BMEP at 1600 rpm
WP_GM	Engine condition of 295 kPa BMEP at 1300 rpm
WP_FEV	Engine condition of 200 kPa BMEP at 2000 rpm
W_i	Indicated work done on the piston
x_b	Fraction of mass burned
y	Mole fraction
γ	Specific heat ratio
η_f	Fuel conversion efficiency
η_v	Volumetric efficiency
θ_{0-10}	0 – 10% burn duration
θ_{0-90}	0 – 90% burn duration
θ_{0-100}	0 – 100% burn duration
θ_{10-90}	10 – 90% burn duration
θ_{50}	Location of 50% mass fraction burned
θ_1	Crank angle at IVO
θ_2	Crank angle at IVC
θ_{pmax}	Crank angle for maximum in-cylinder pressure
μ	Dynamic viscosity
ν	Kinematic viscosity
ρ	Air density
σ	Standard deviation
ω	Angular velocity

Subscript

∞	Ambient conditions
0	Stagnation condition
1	Conditions upstream of the blockage

2	Conditions downstream of the blockage
3	Conditions in bore from flow experiment
b	Burned zone in combustion chamber
e	Parameters from engine experiment
f	Parameters from flow experiment
s	Swirl
t	Tumble
u	Unburned zone in combustion chamber

Superscript

'	Conditions in crevice volume

APPENDIX B

ENGINE EXPERIMENTAL RESULTS AT WP_GM AND WP_FEV

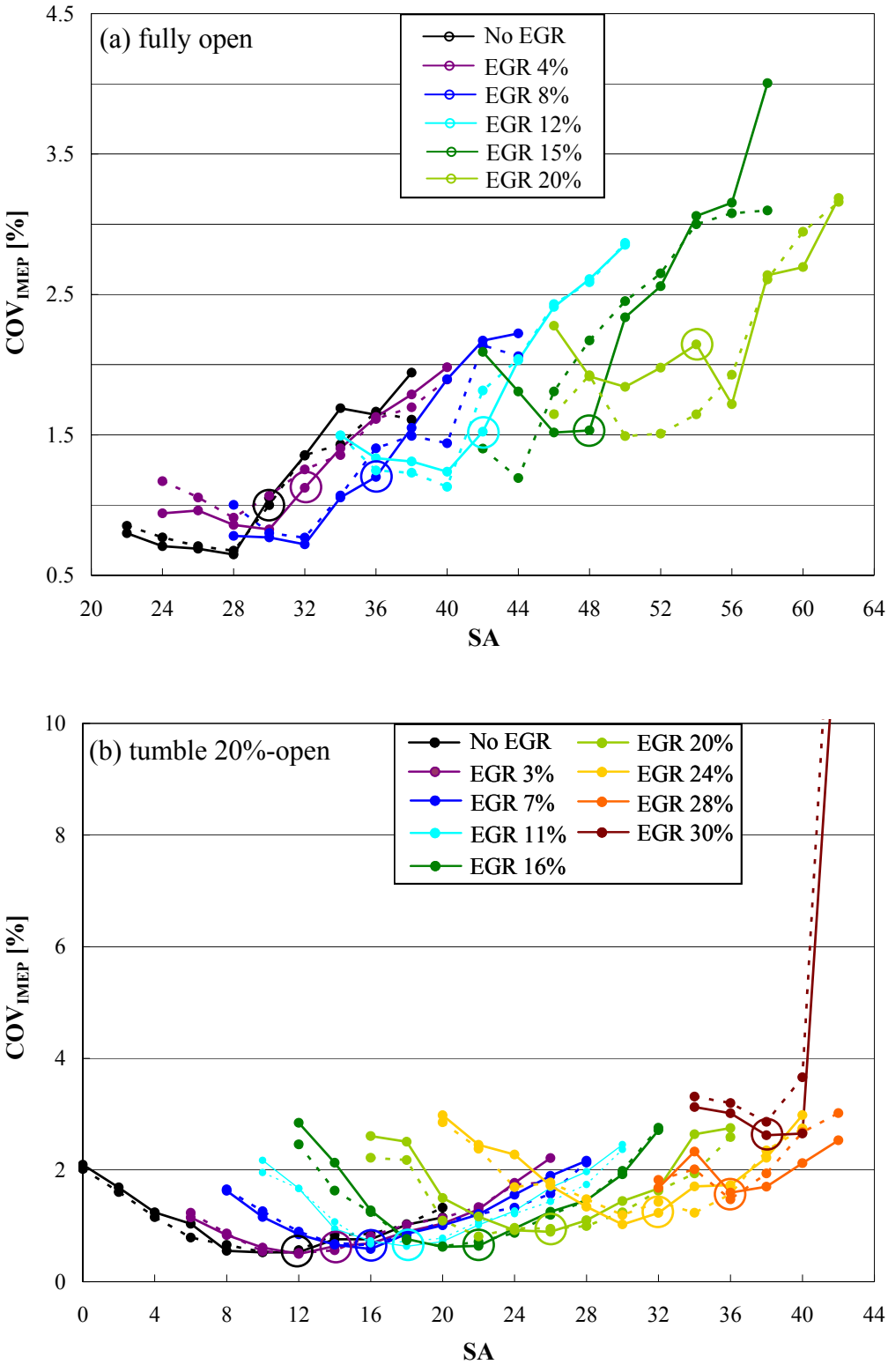

Figure B.1. Effect of blockage on COV in IMEP (#1) at WP_GM.

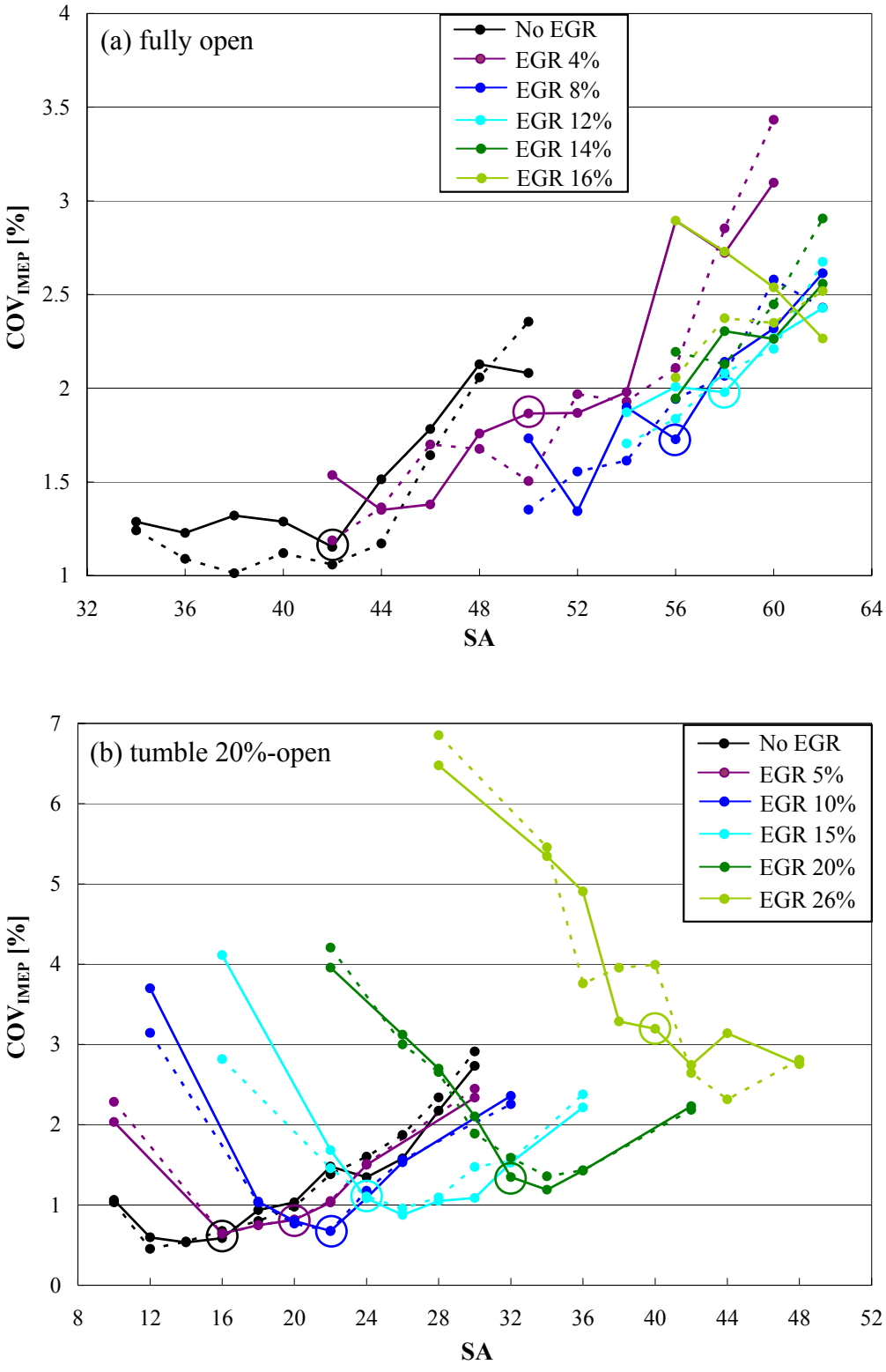

Figure B.2. Effect of blockage on COV in IMEP (#1) at WP_FEV.

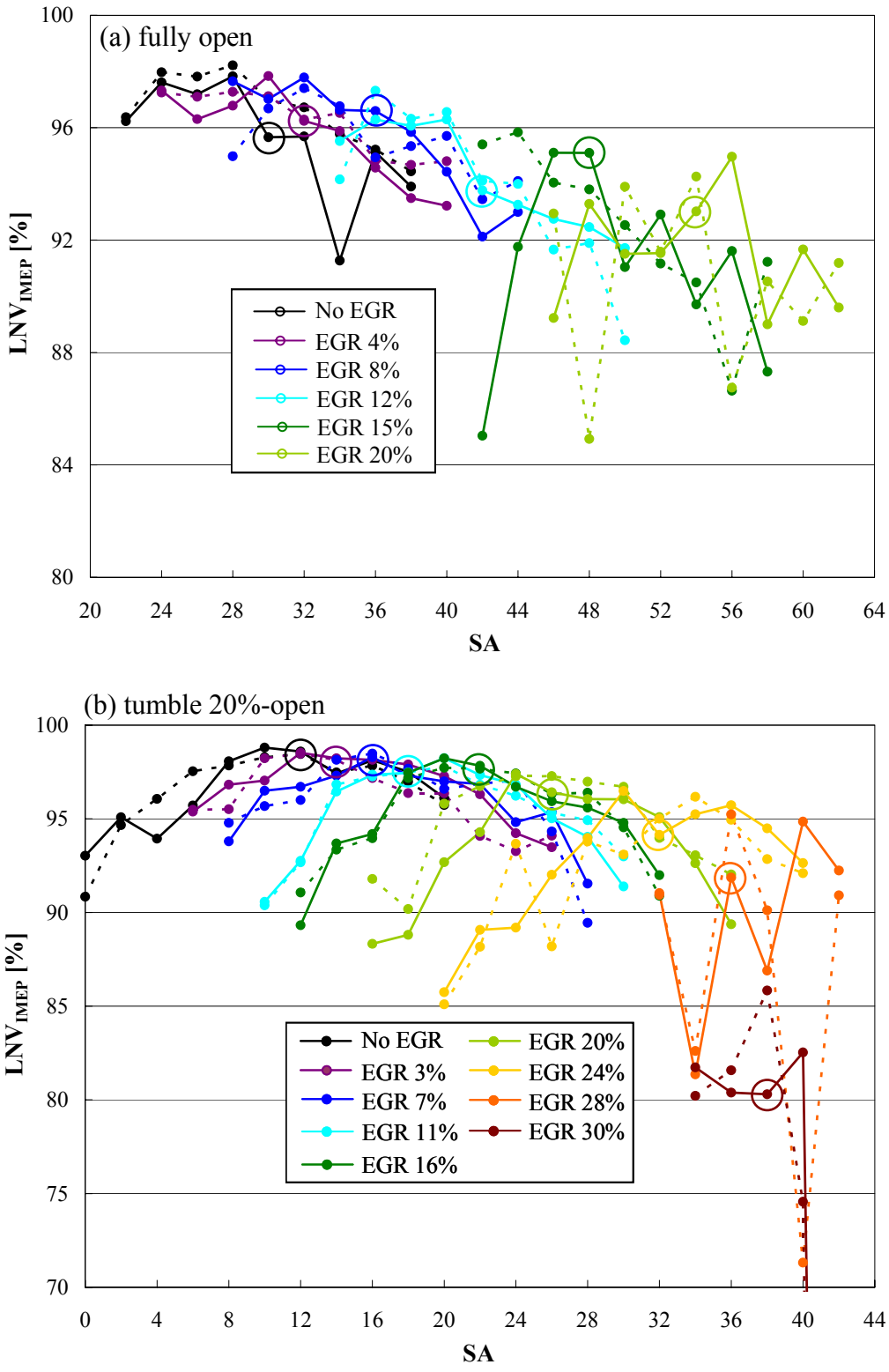

Figure B.3. Effect of blockage on LNV in IMEP (#1) at WP_GM.

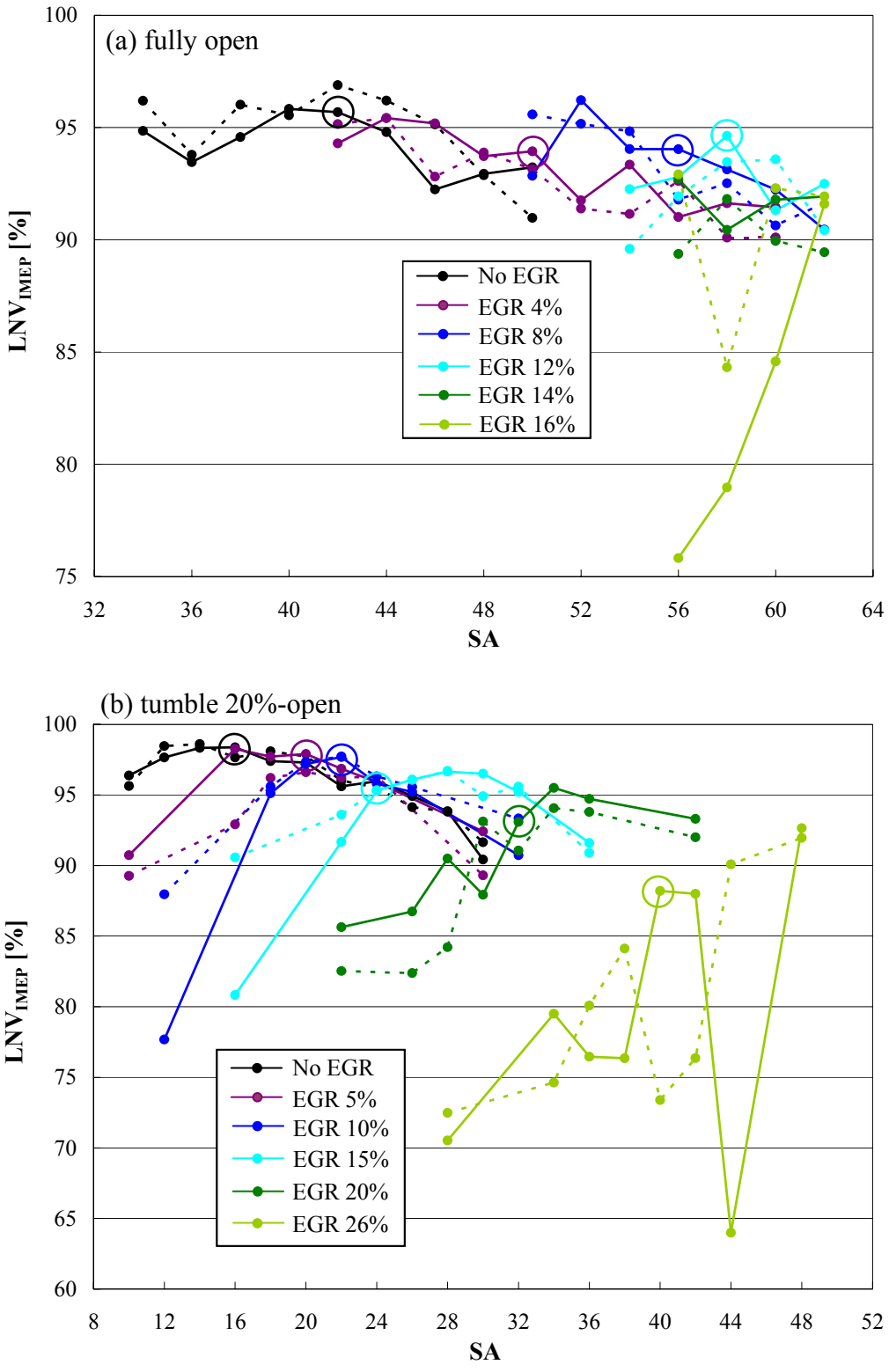

Figure B.4. Effect of blockage on LNV in IMEP (#1) at WP_FEV.

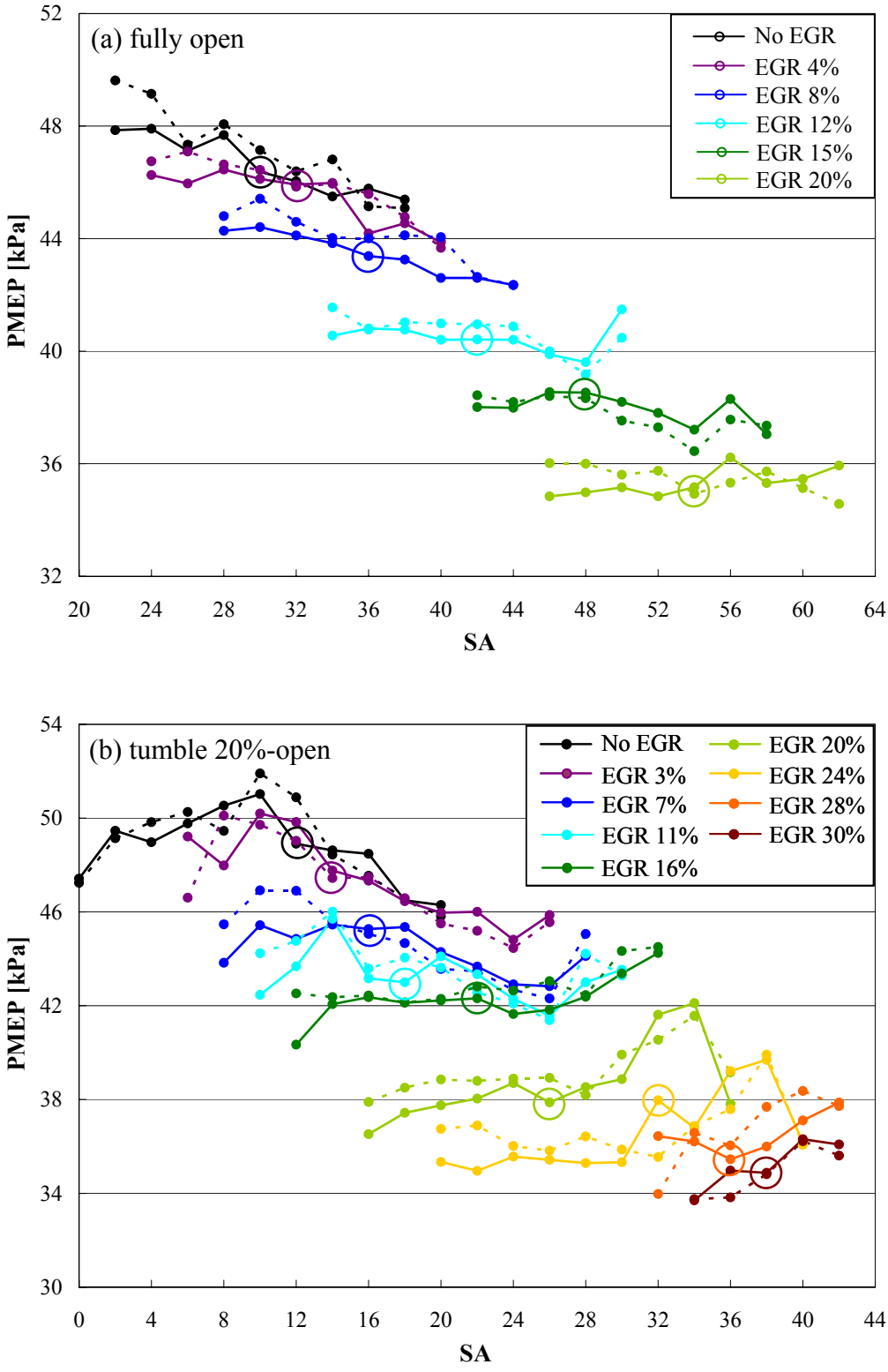

Figure B.5. Effect of blockage on PMEP (#1) at WP_GM.

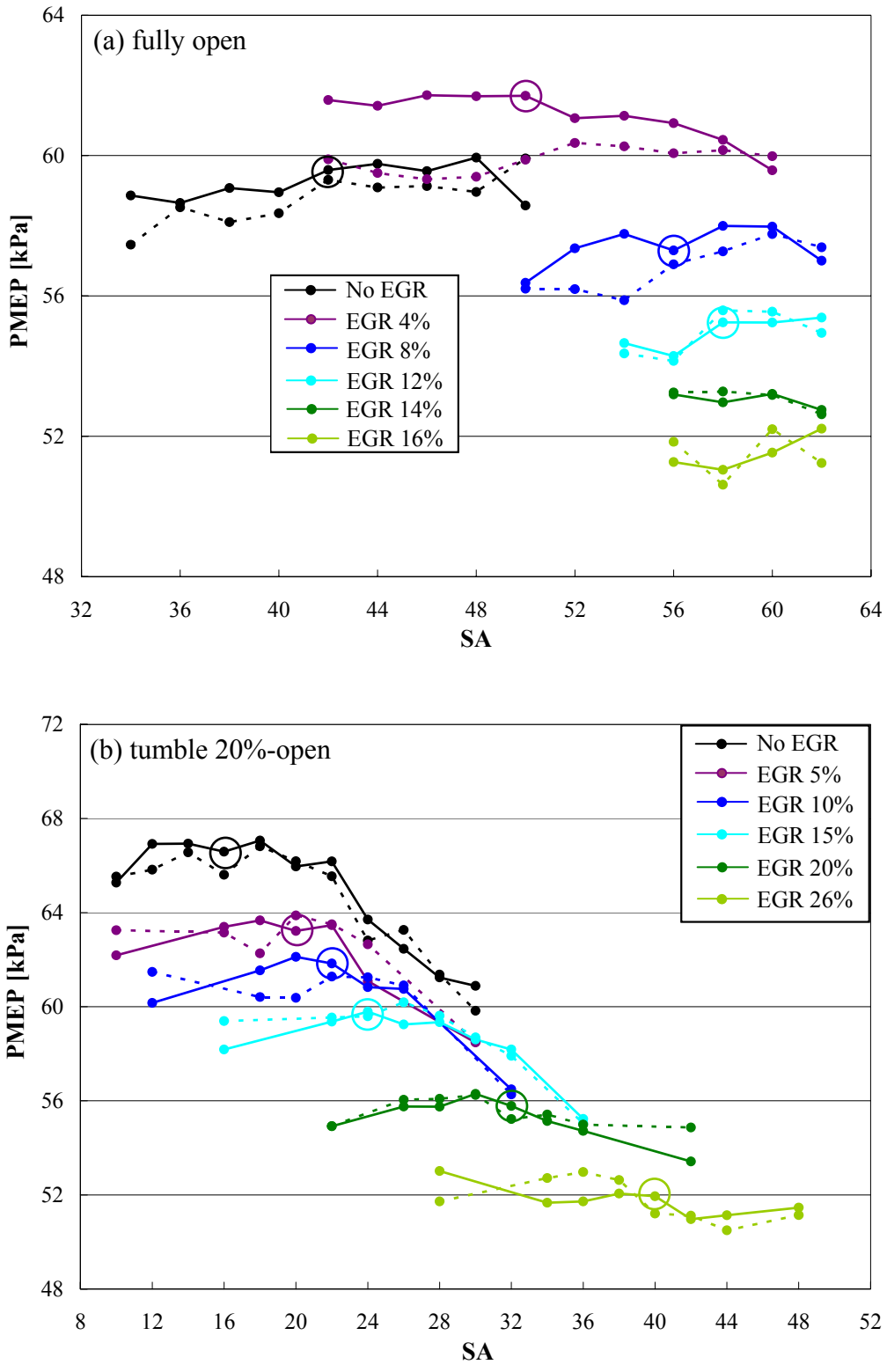

Figure B.6. Effect of blockage on PMEP (#1) at WP_FEV.

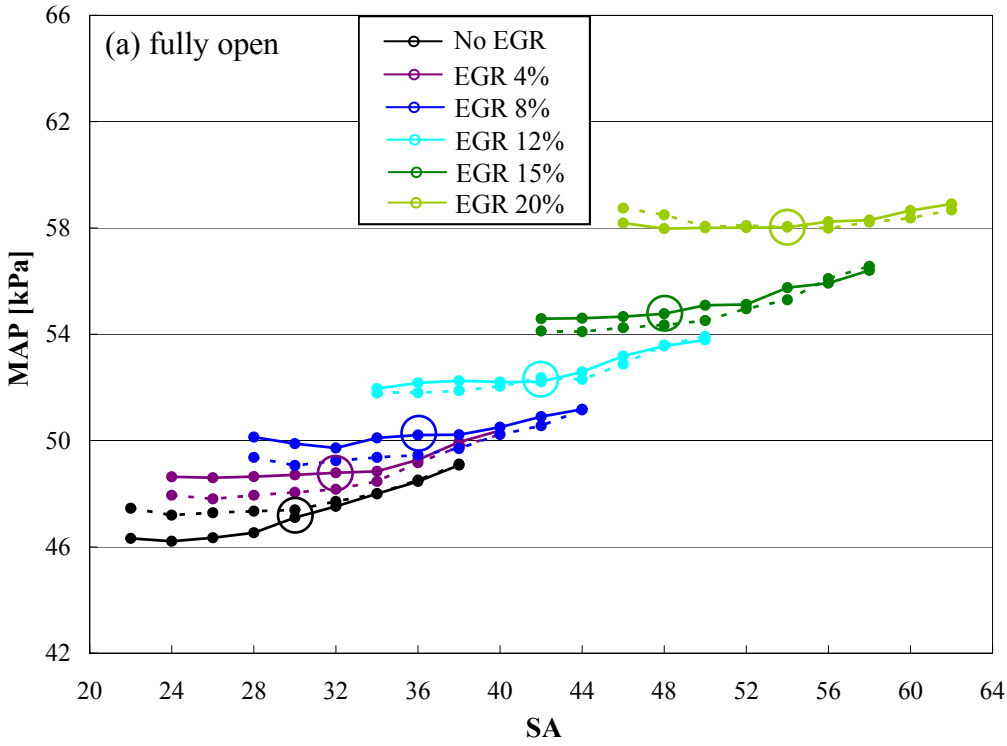

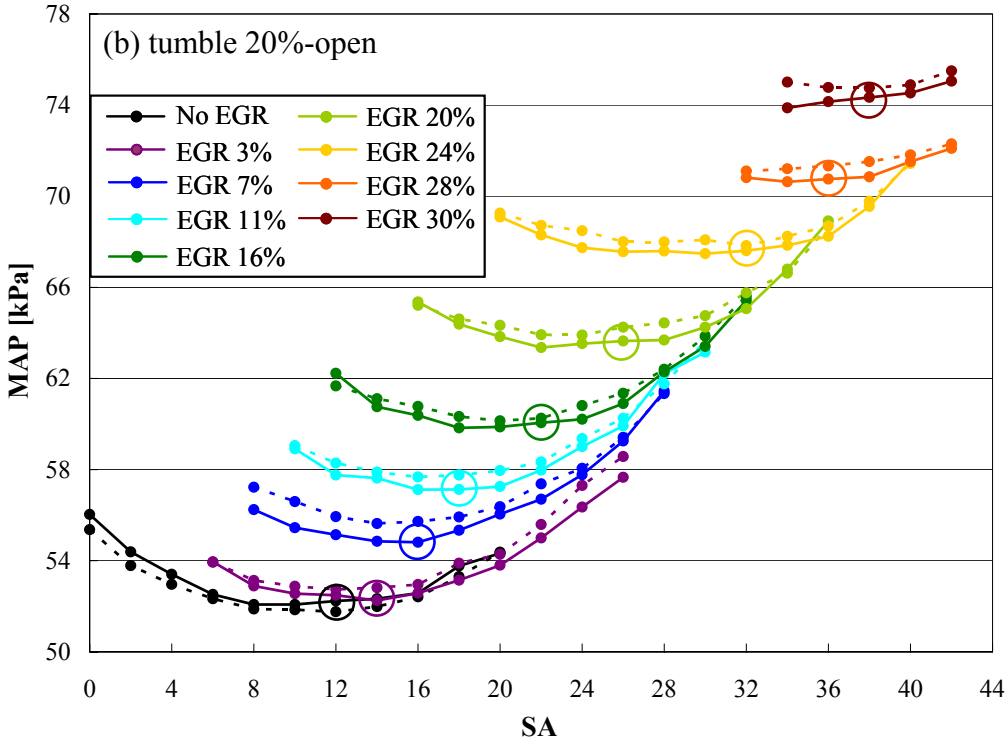

Figure B.7. Effect of blockage on MAP at WP_GM.

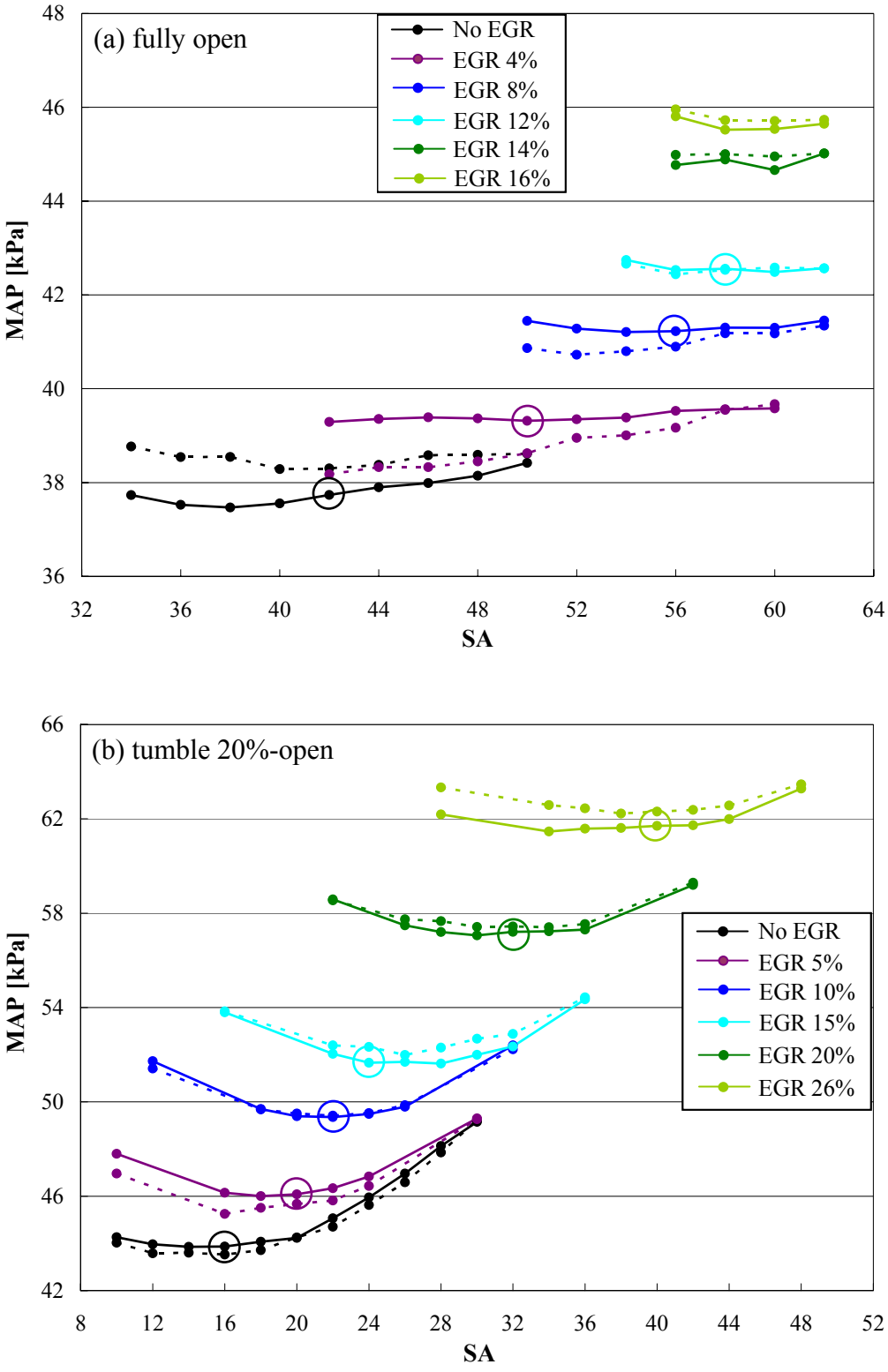

Figure B.8. Effect of blockage on MAP at WP_FEV.

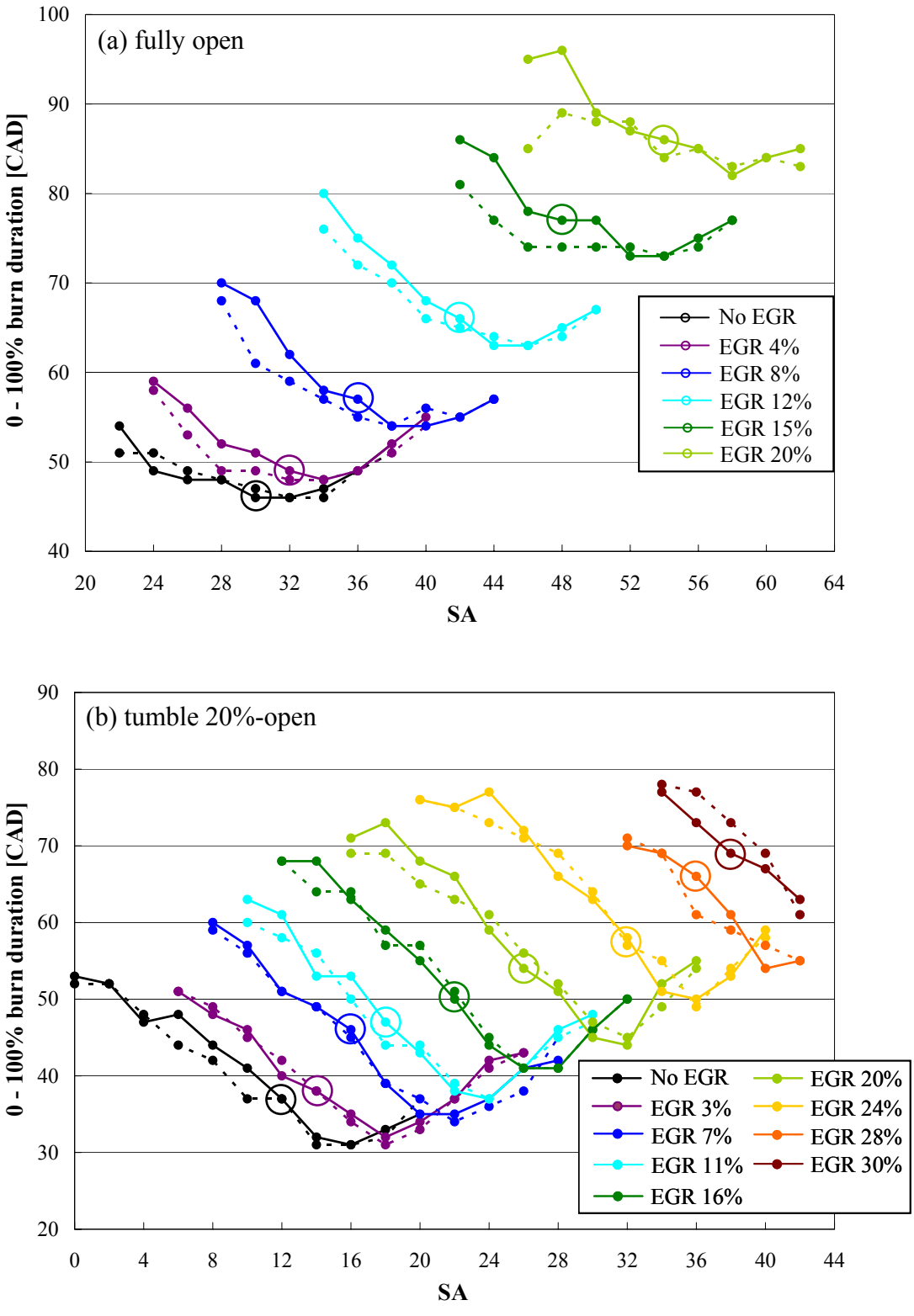

Figure B.9. Effect of blockage on 0 – 100% burn duration (#1) at WP_GM.

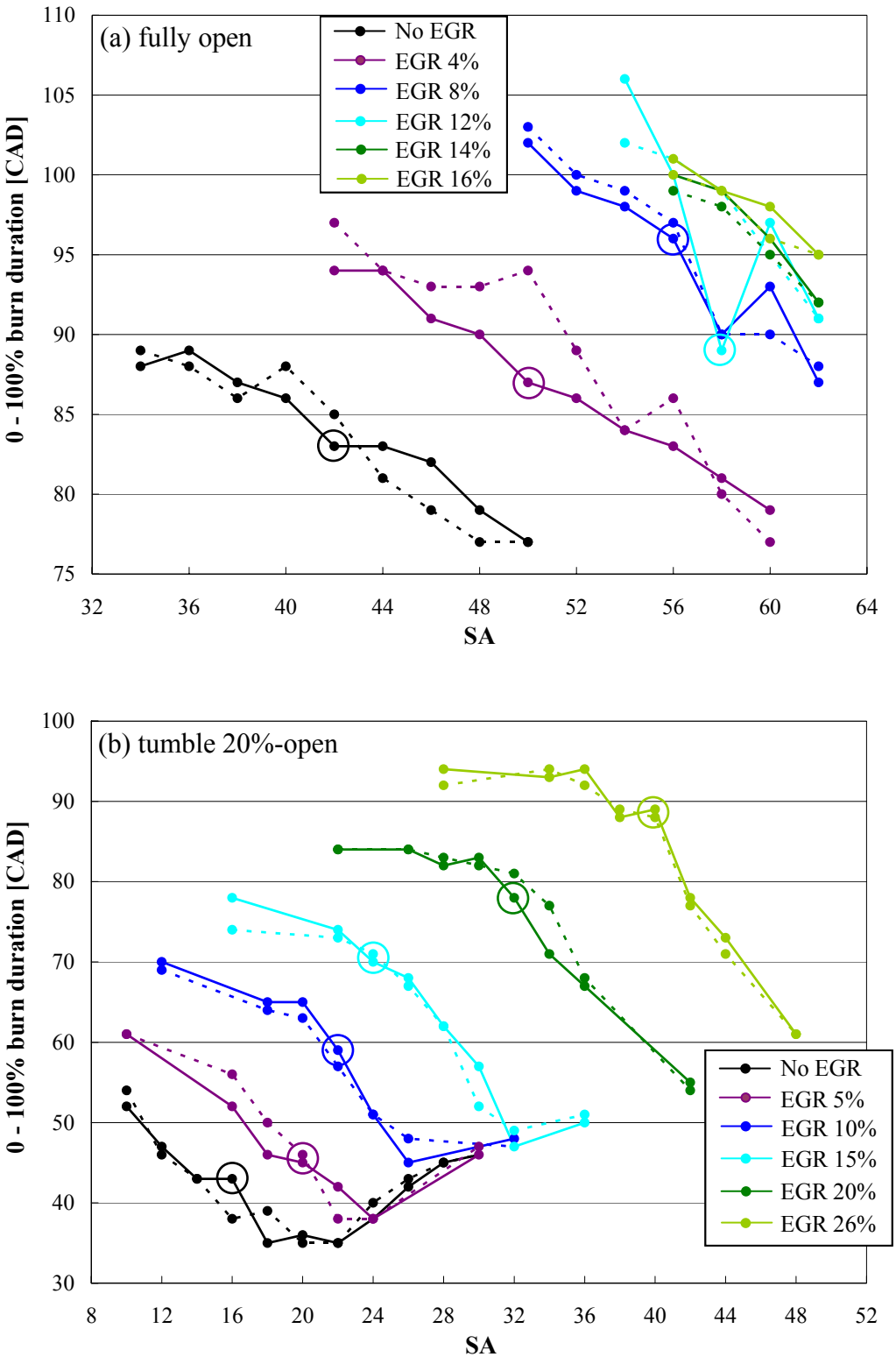

Figure B.10. Effect of blockage on 0 – 100% burn duration (#1) at WP_FEV.

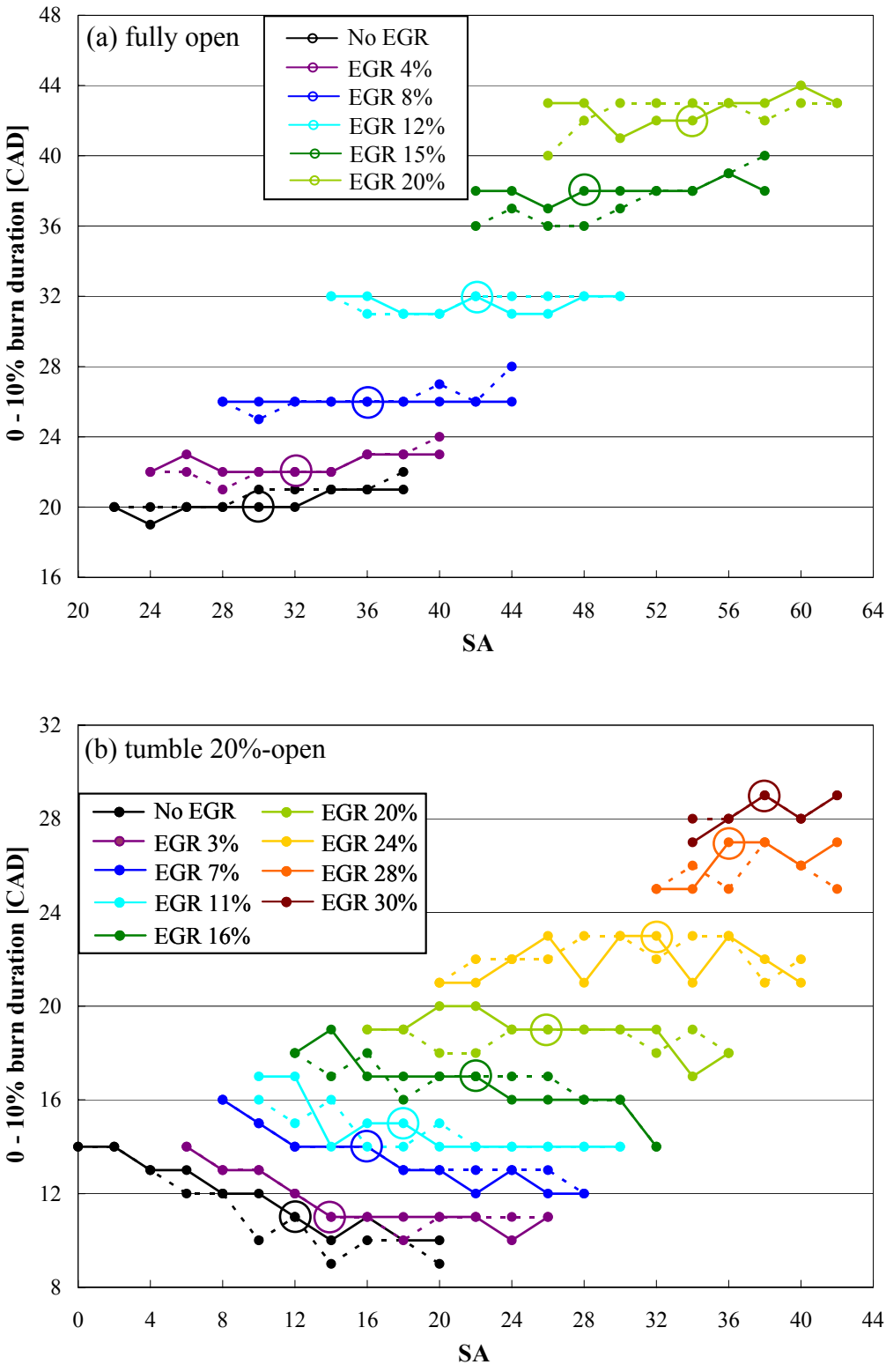

Figure B.11. Effect of blockage on 0 – 10% burn duration (#1) at WP_GM.

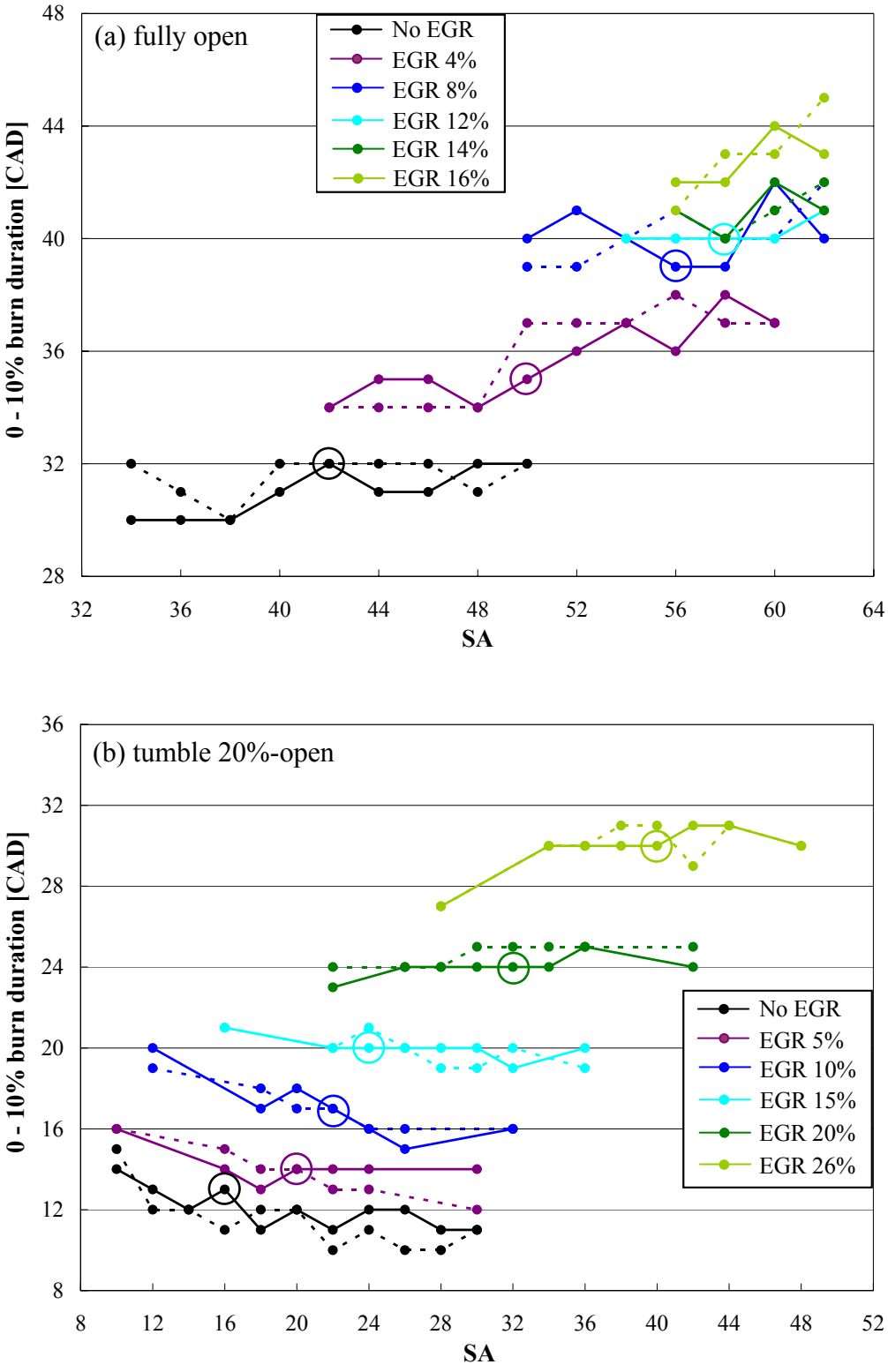

Figure B.12. Effect of blockage on 0 – 10% burn duration (#1) at WP_FEV.

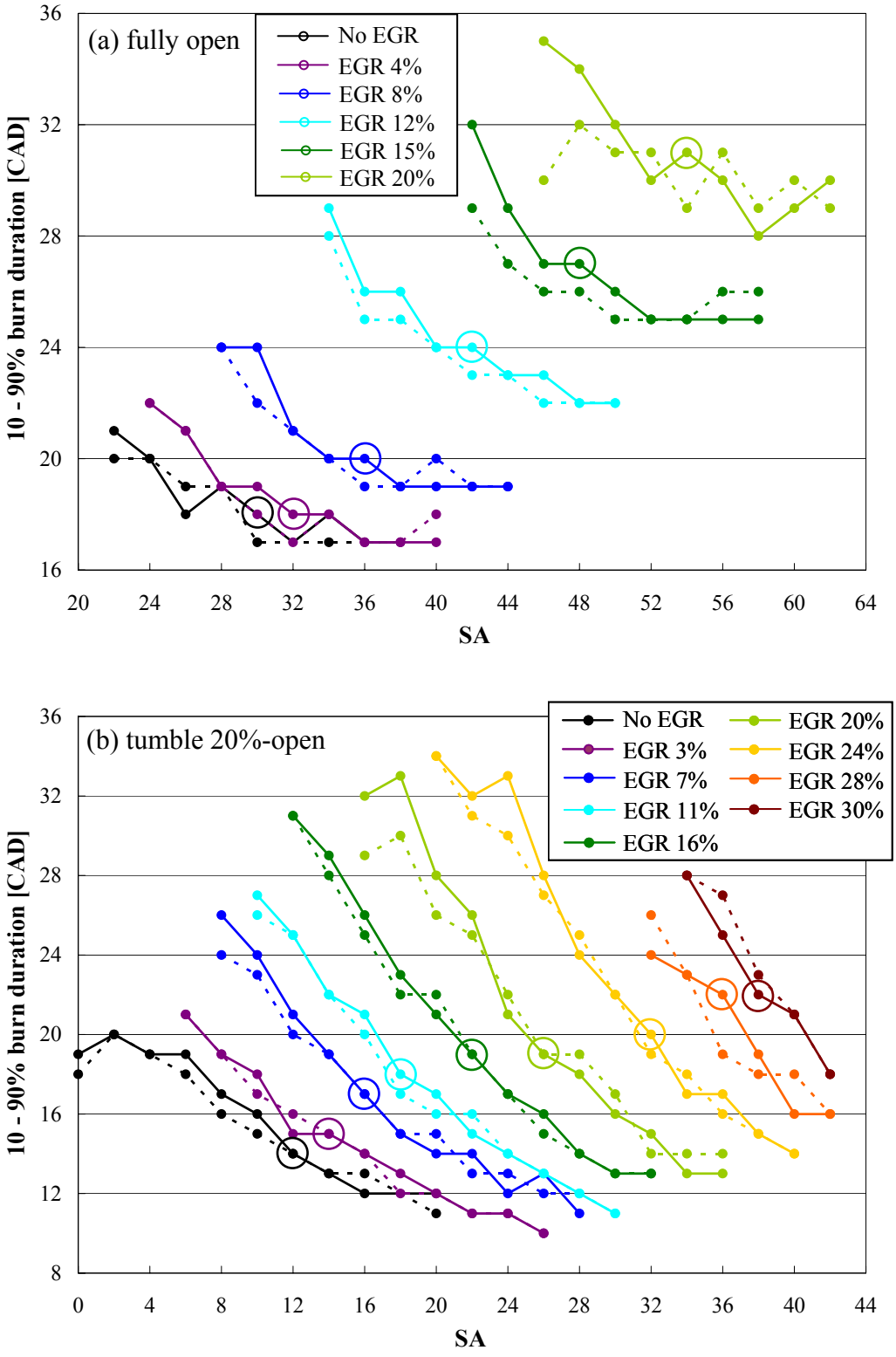

Figure B.13. Effect of blockage on 10 – 90% burn duration (#1) at WP_GM.

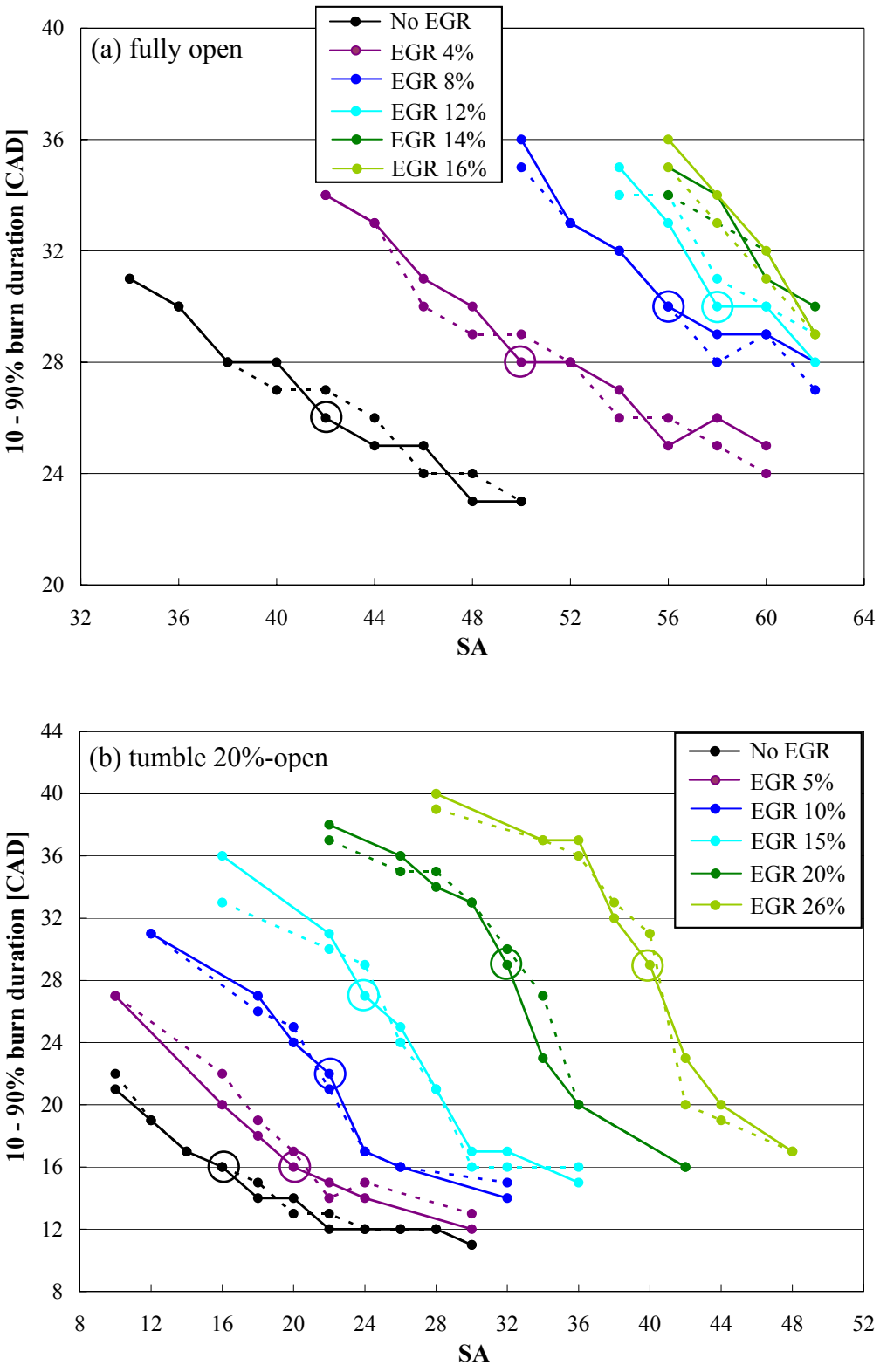

Figure B.14. Effect of blockage on 10 – 90% burn duration (#1) at WP_FEV.

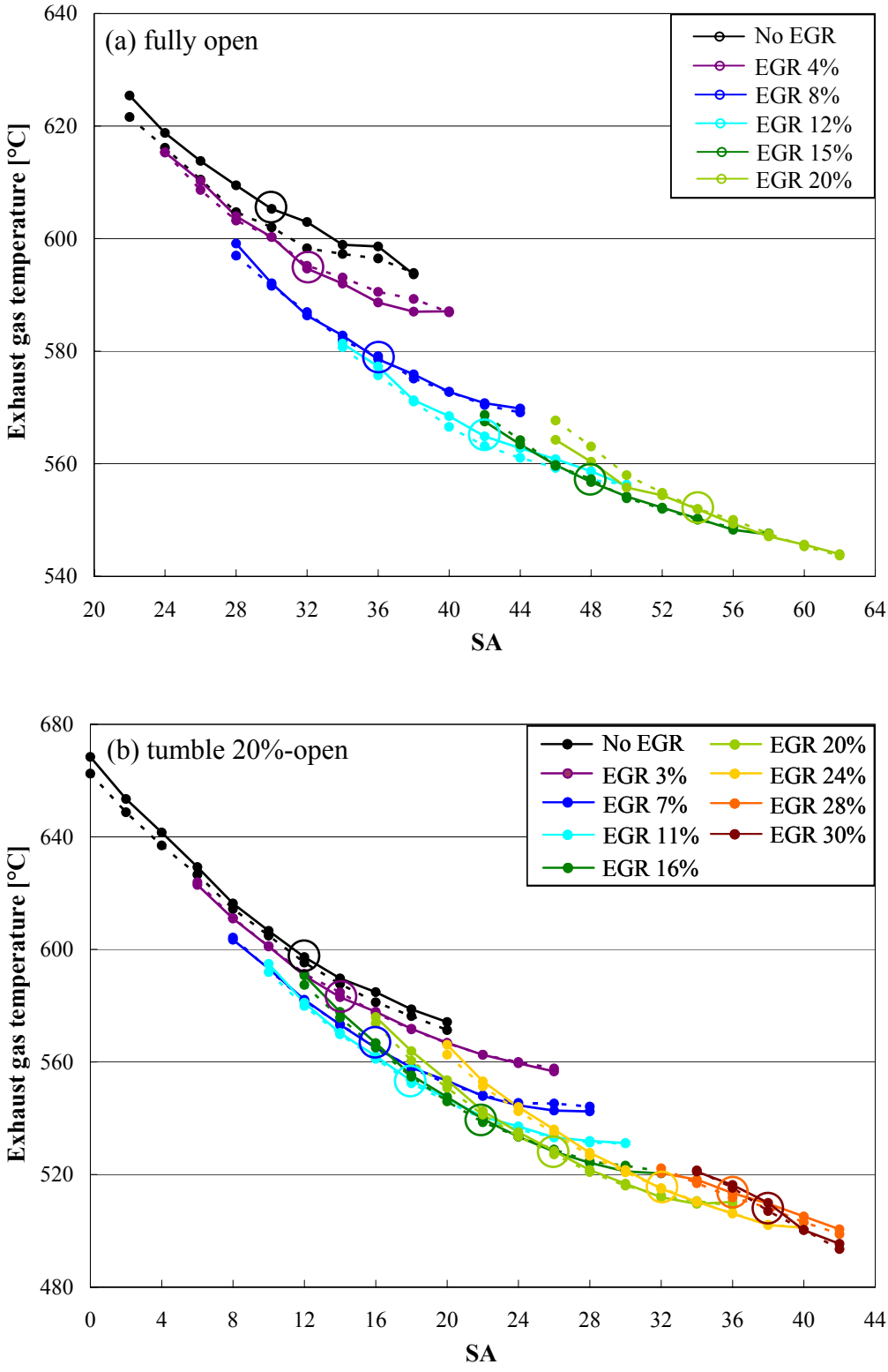

Figure B.15. Effect of blockage on EGT (#1) at WP_GM.

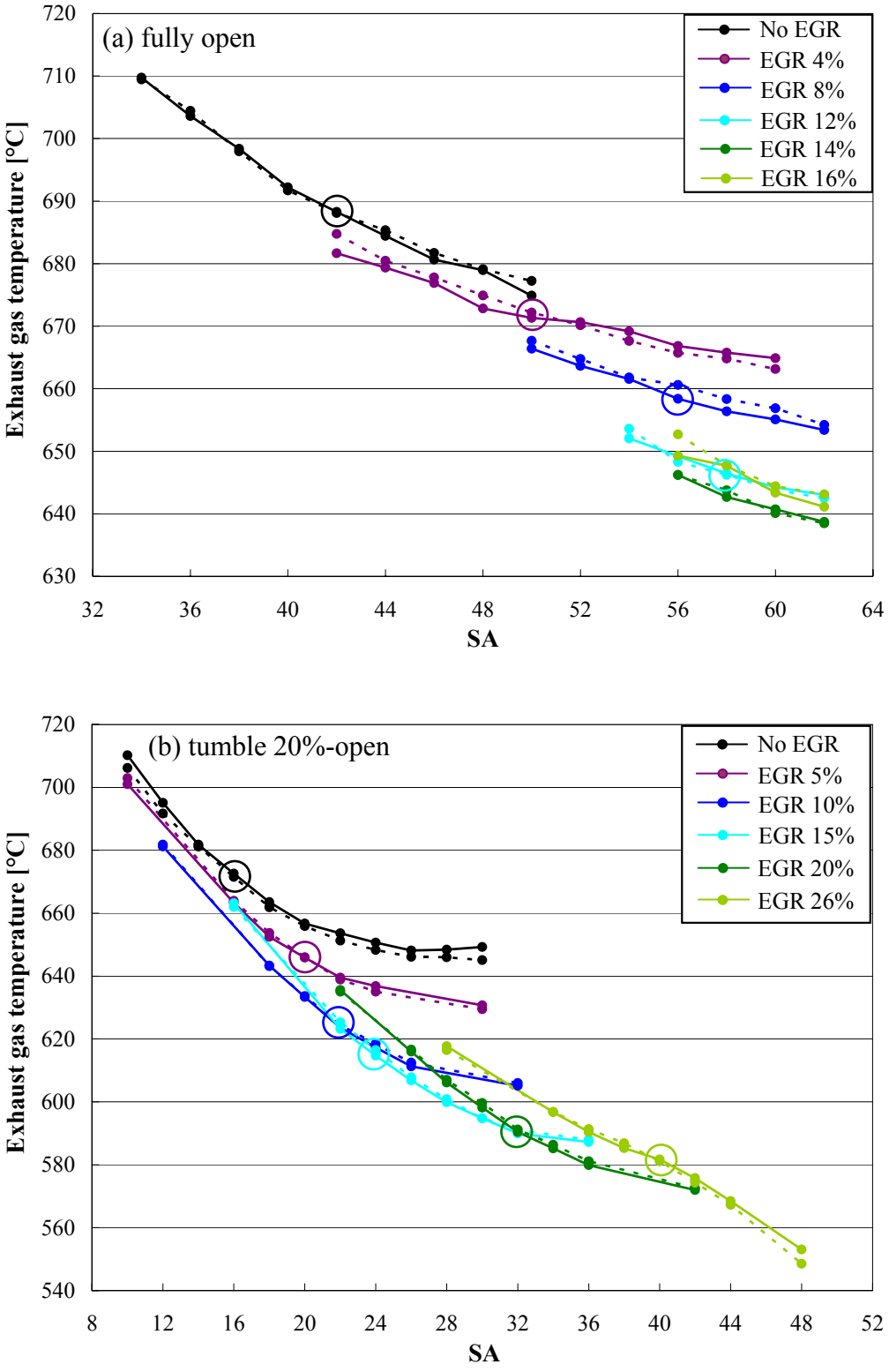

Figure B.16. Effect of blockage on EGT (#1) at WP_FEV.

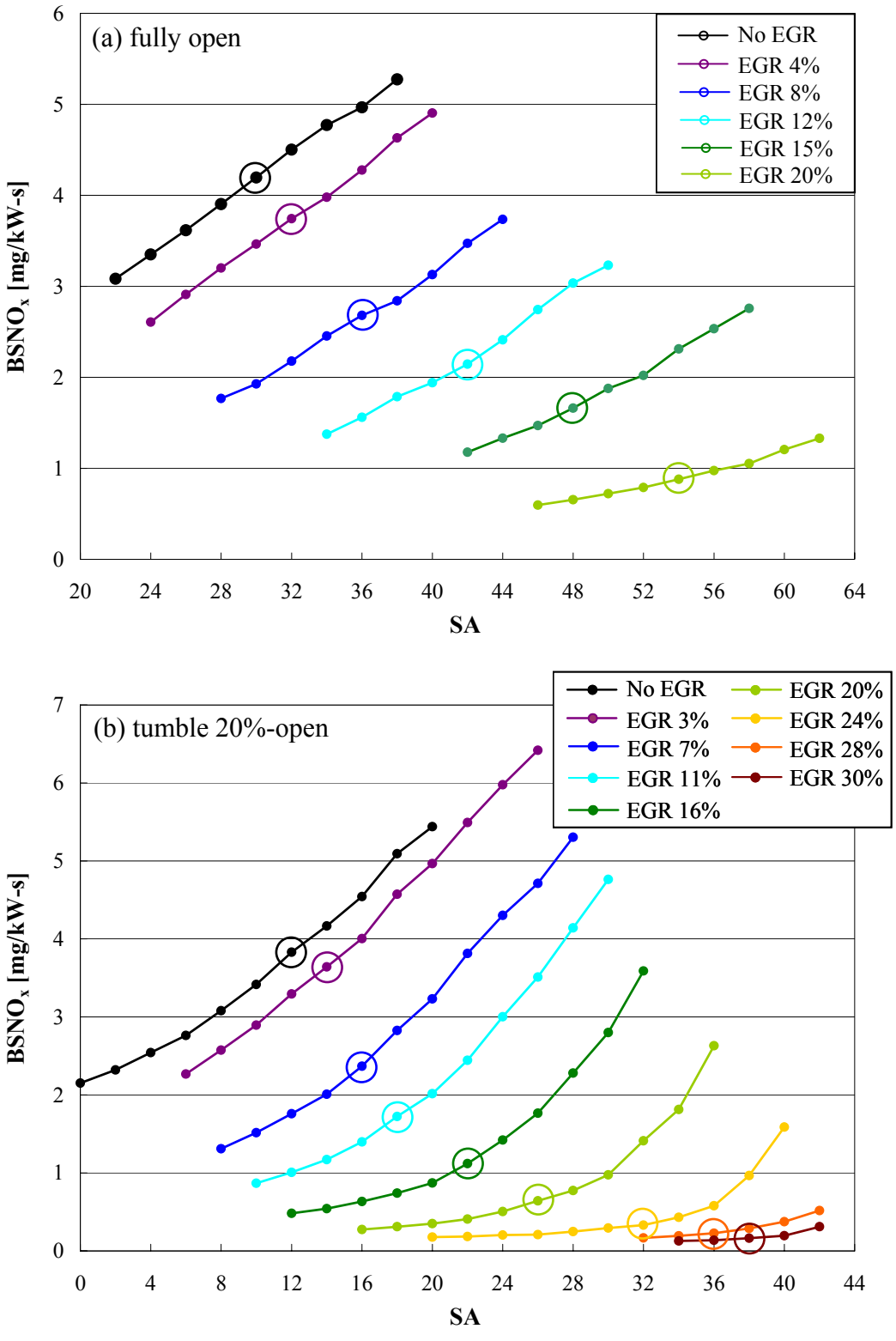

Figure B.17. Effect of blockage on NO_x emissions at WP_GM.

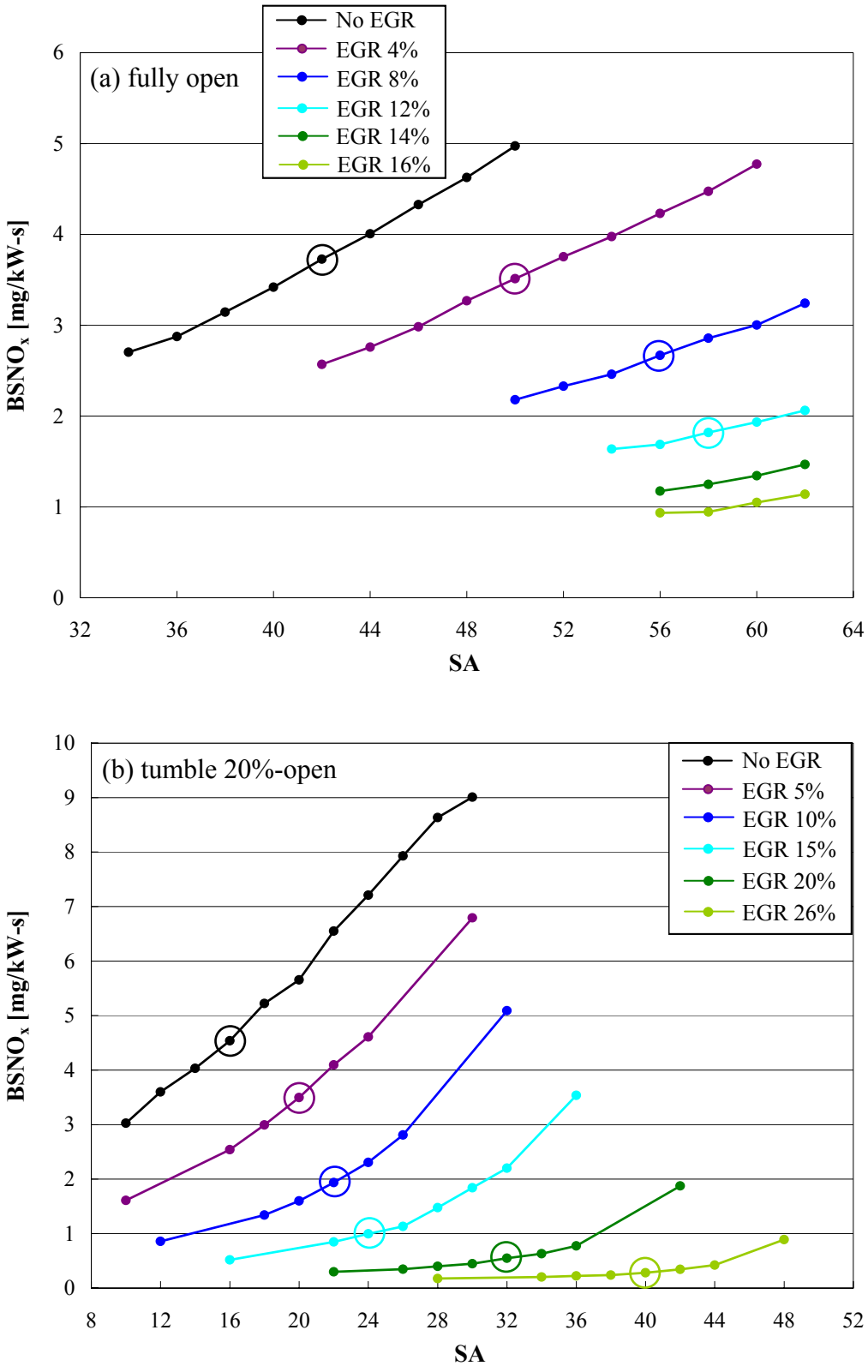

Figure B.18. Effect of blockage on NO_x emissions at WP_FEV.

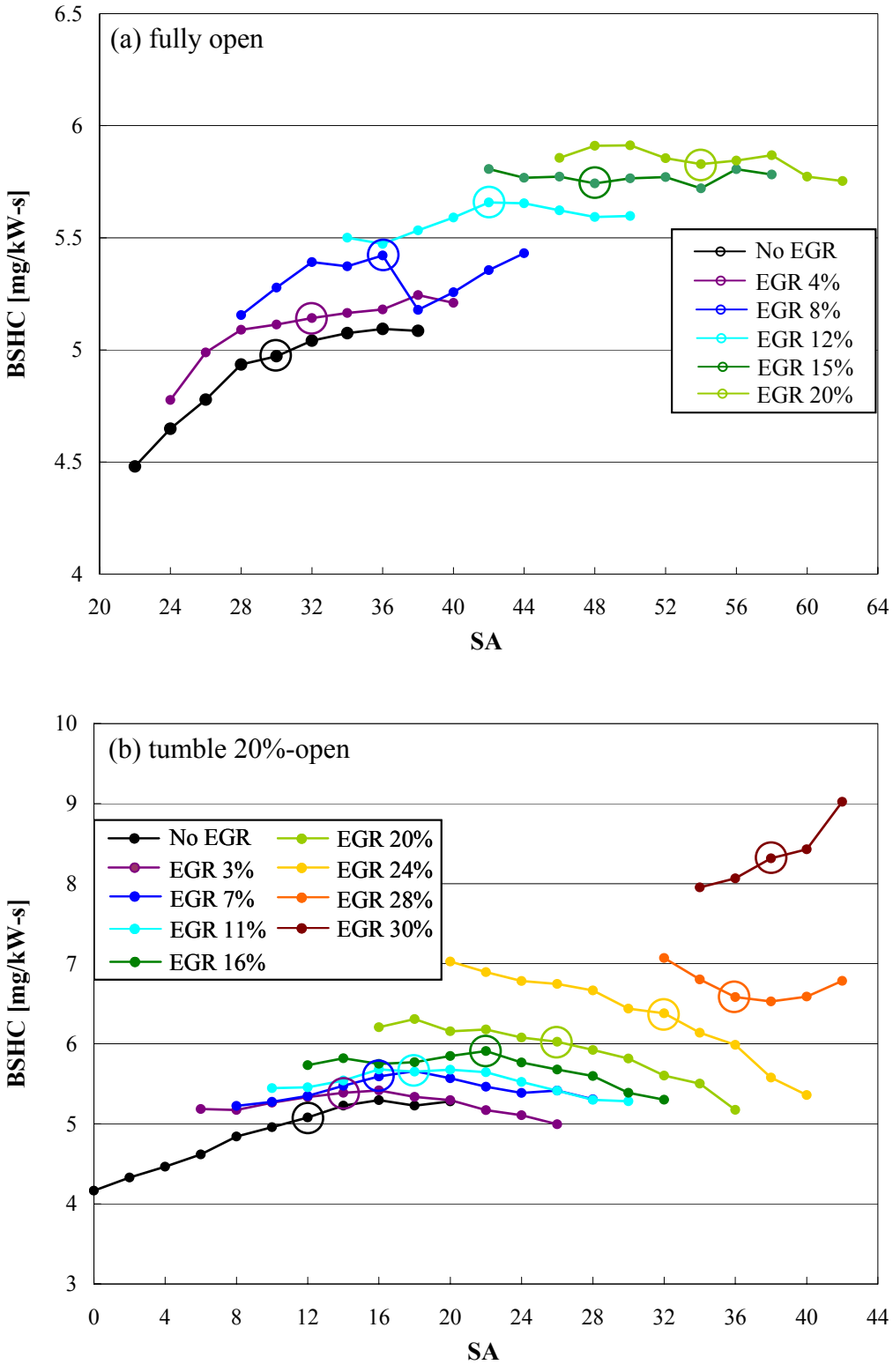

Figure B.19. Effect of blockage on HC emissions at WP_GM.

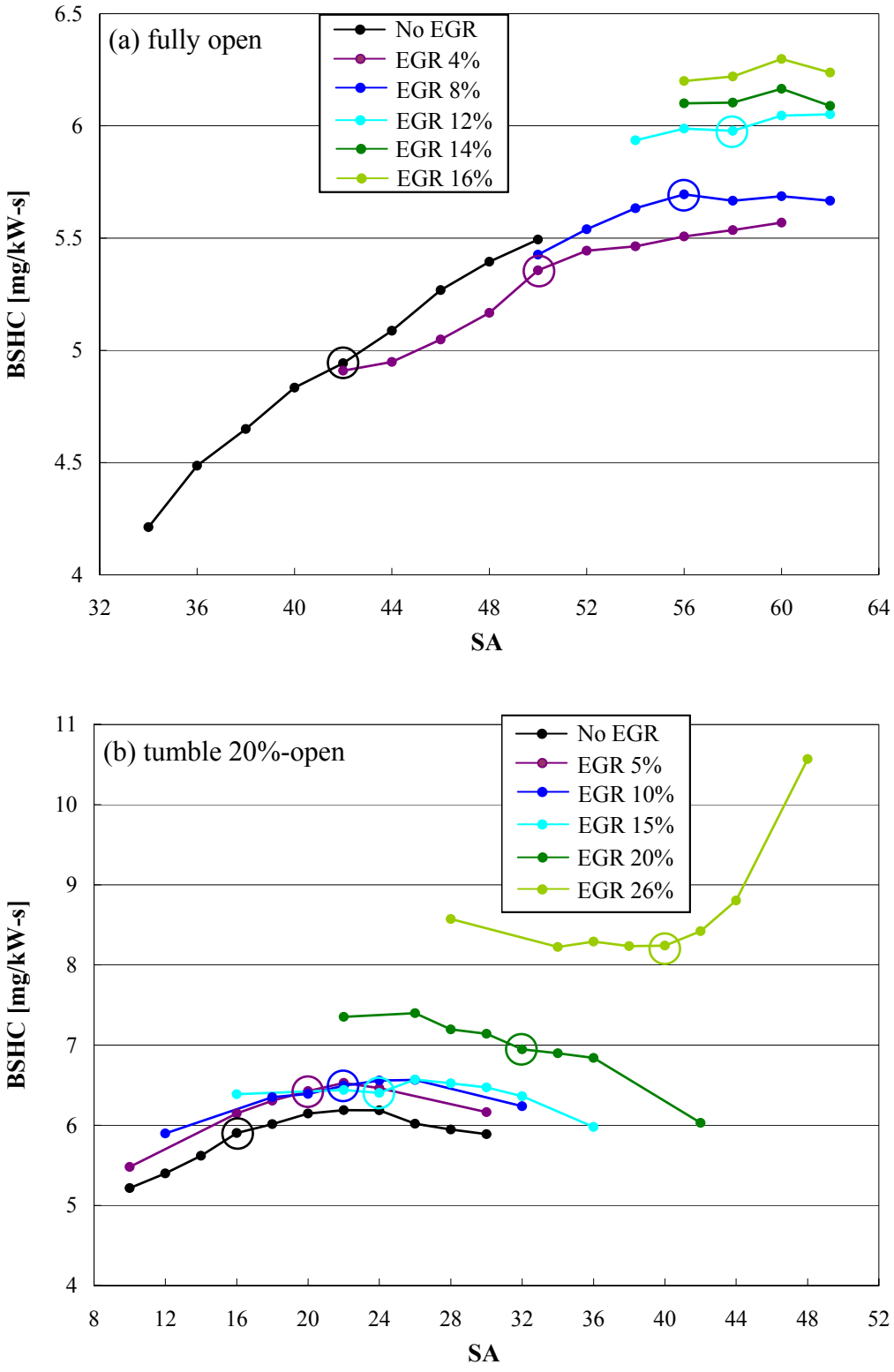

Figure B.20. Effect of blockage on HC emissions at WP_FEV.

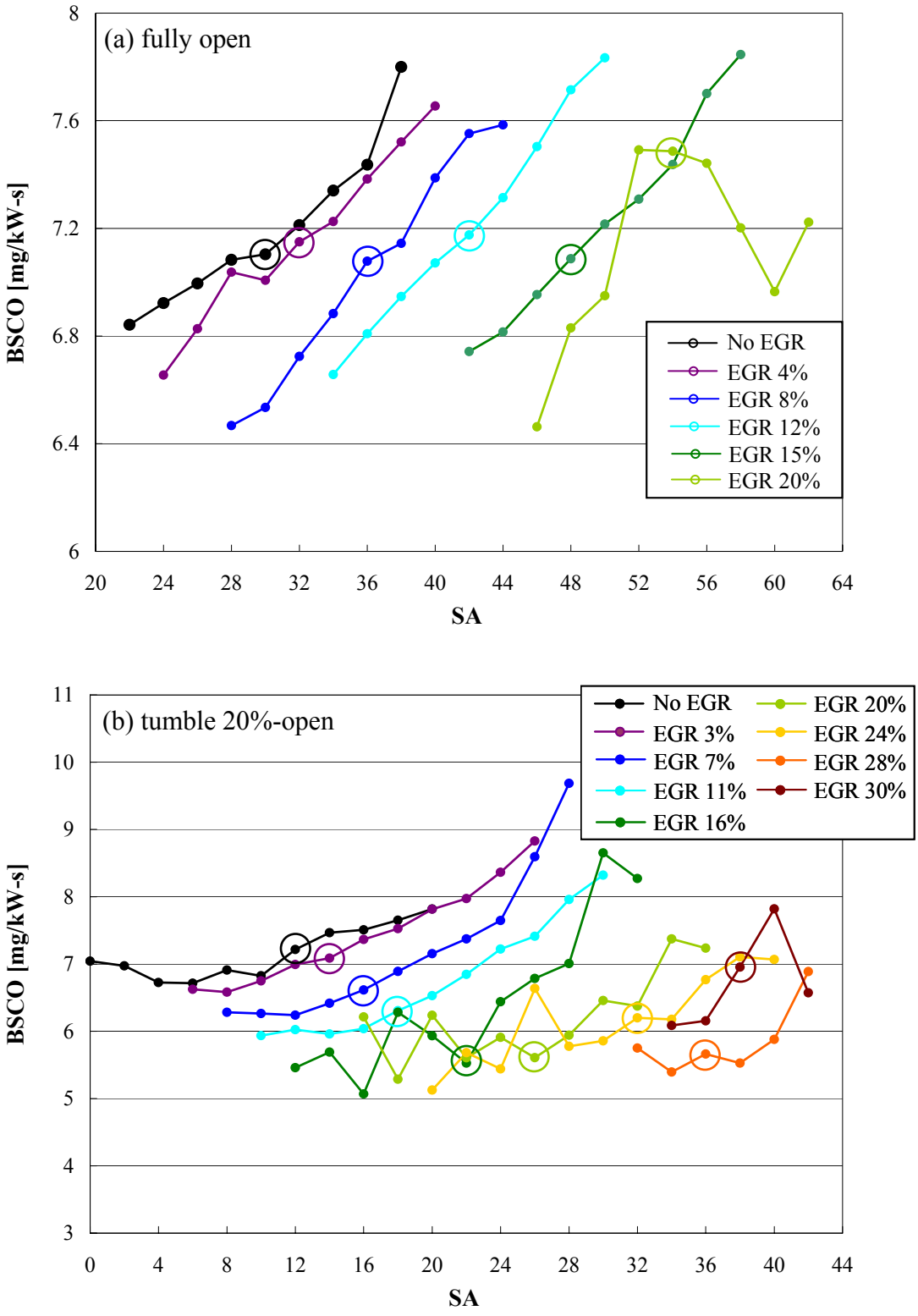

Figure B.21. Effect of blockage on CO emissions at WP_GM.

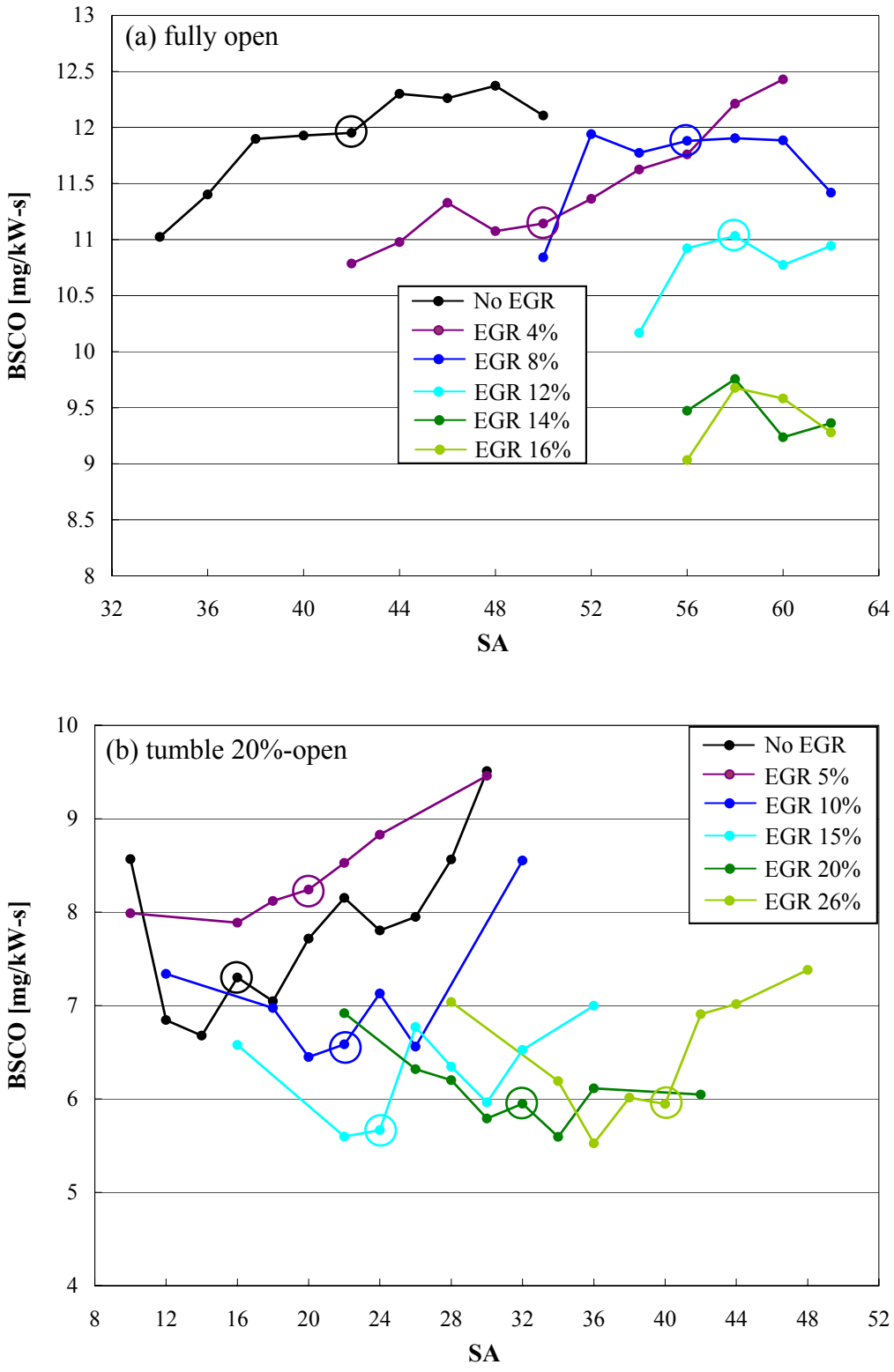

Figure B.22. Effect of blockage on CO emissions at WP_FEV.

APPENDIX C

HEAT RELEASE ANALYSIS RESULTS FOR SWIRL AND SWUMBLE UNDER WP

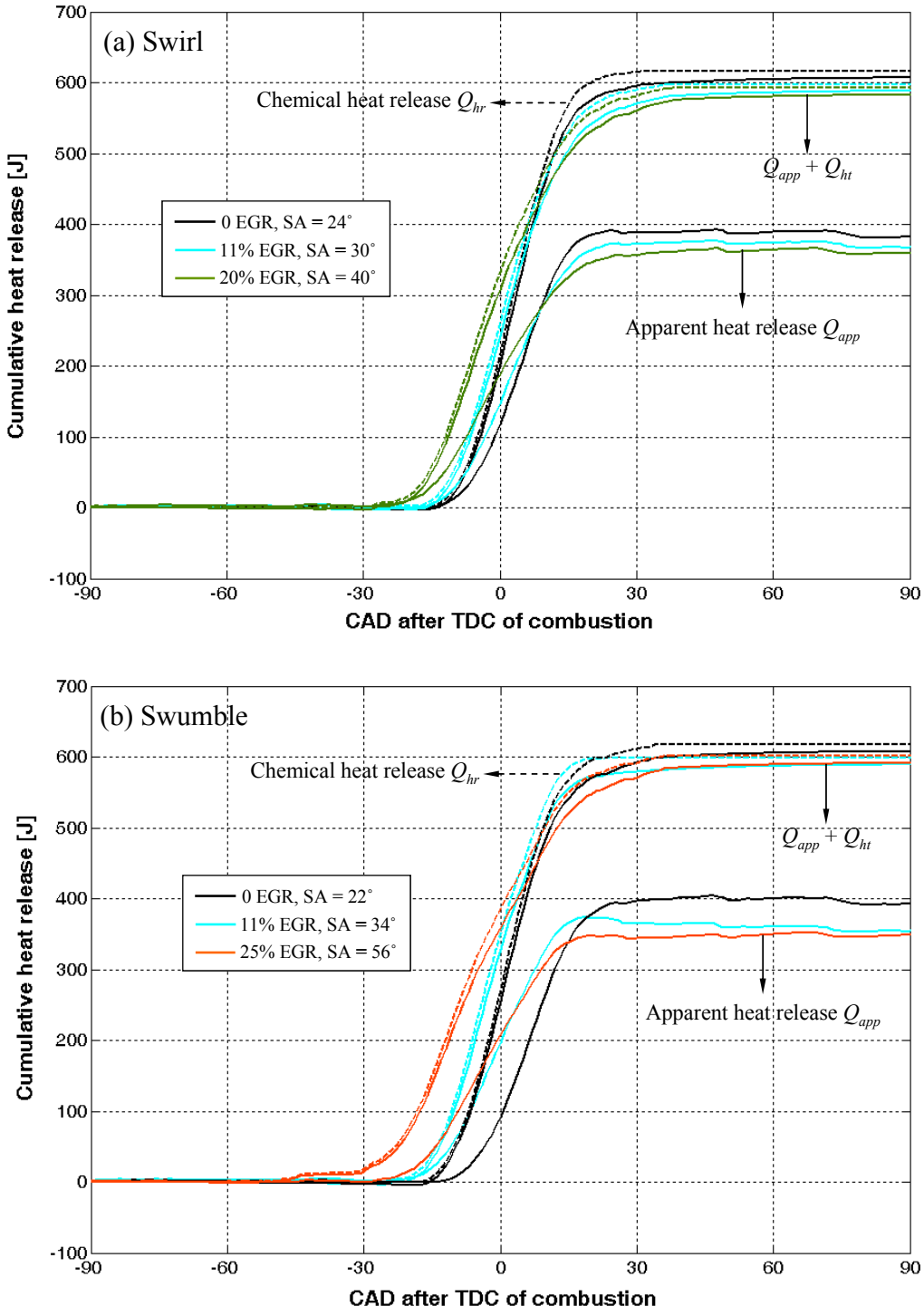

Figure C.1. Cumulative in-cylinder heat release (#1) under WP, at MBT.

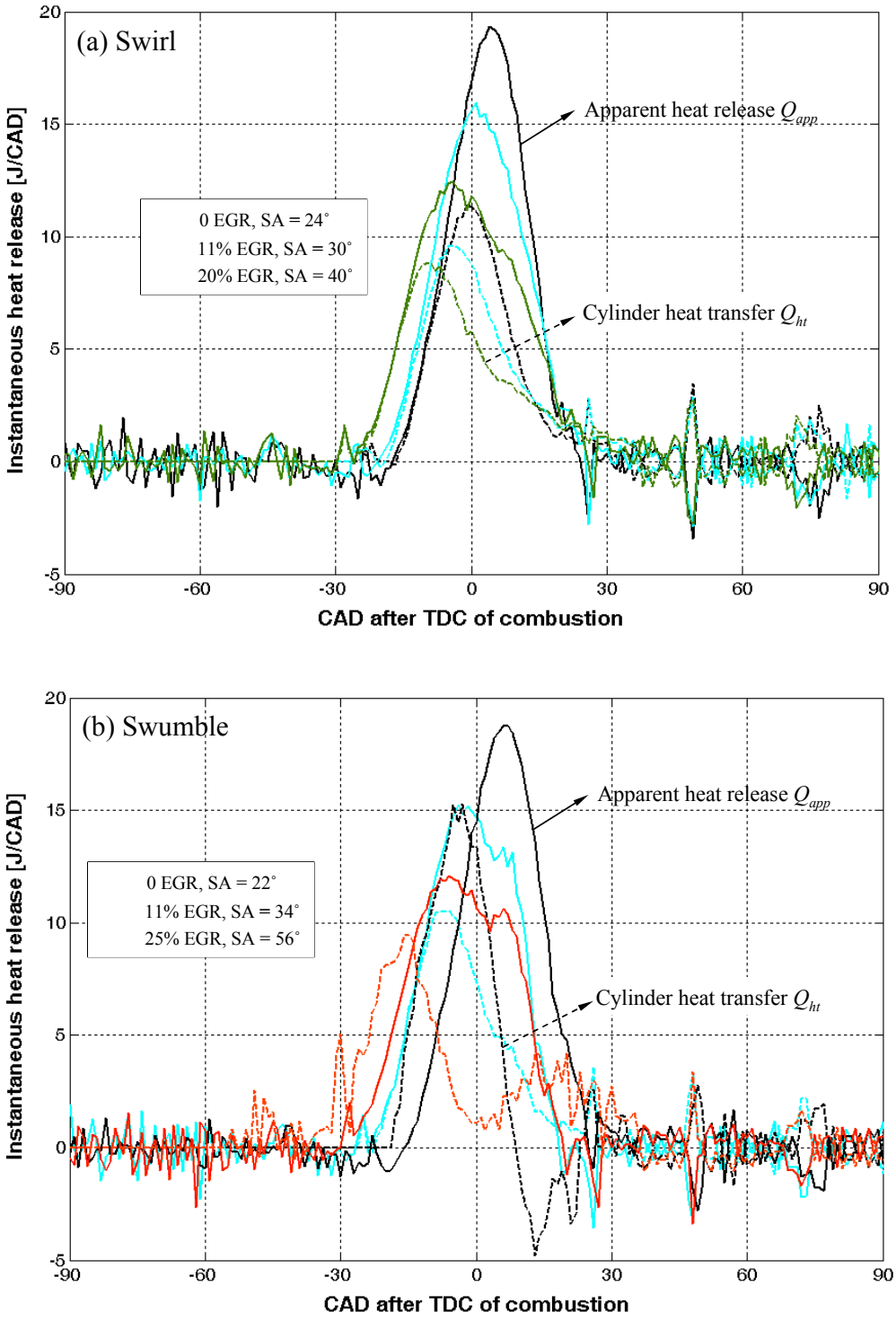

Figure C.2. Instantaneous in-cylinder heat release (#1) under WP, at MBT.

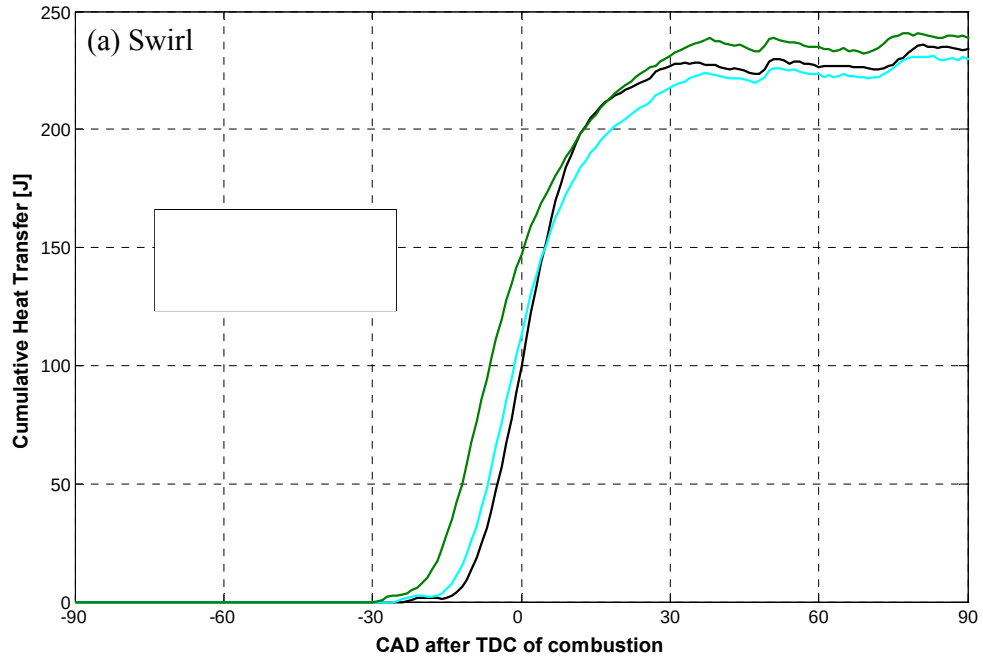

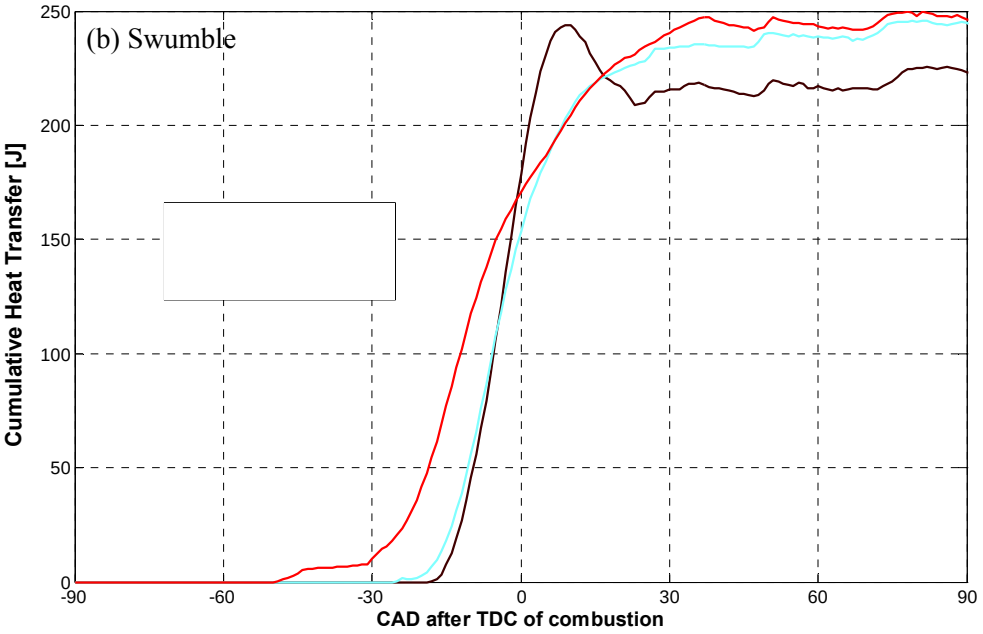

Figure C.3. Cumulative in-cylinder heat transfer (#1) under WP, at MBT.

APPENDIX D

FLOW EXPERIMENTAL RESULTS

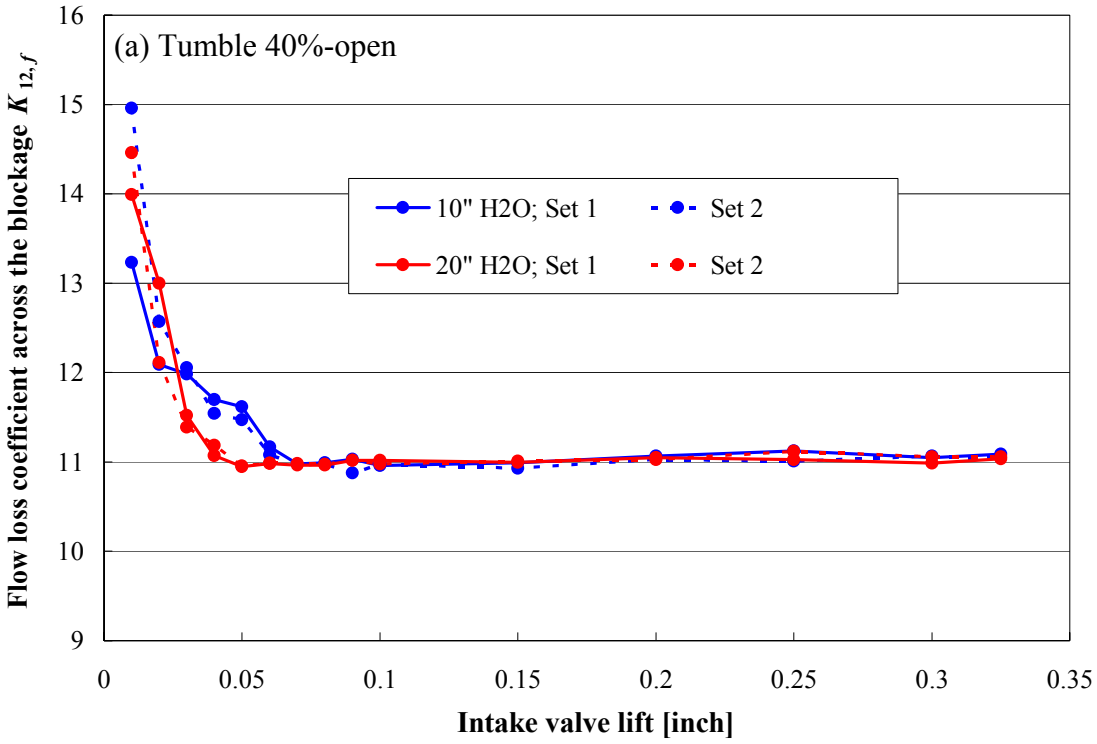

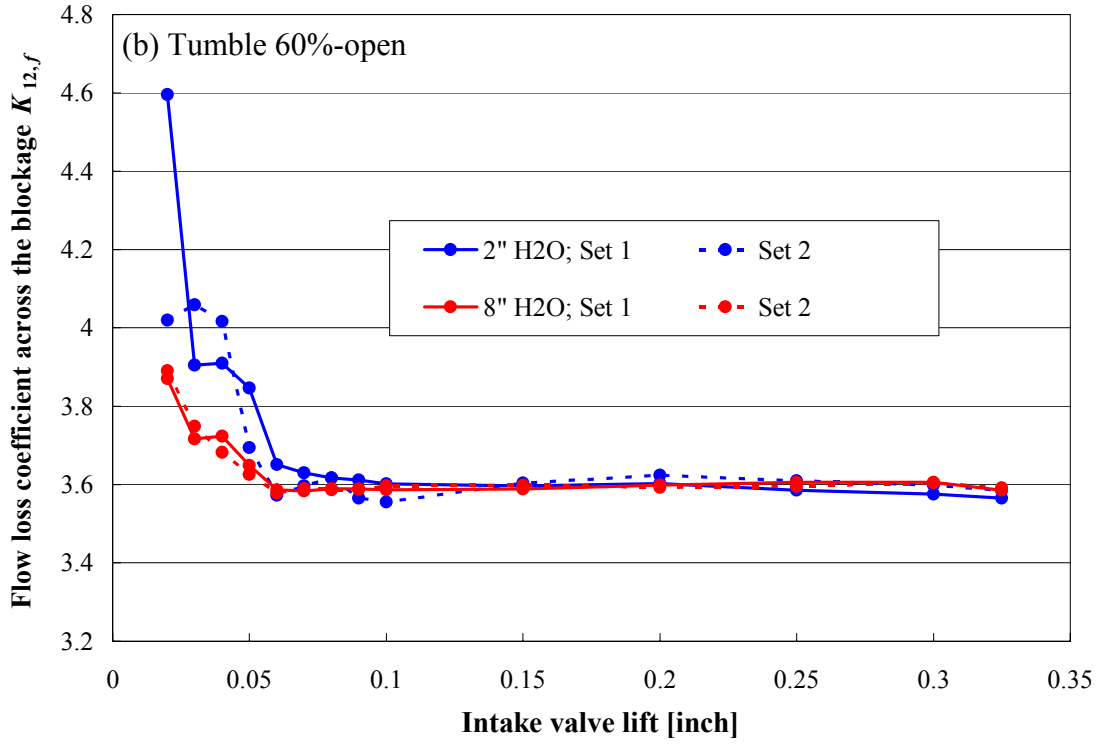

Figure D.1. Flow loss coefficient $K_{12,f}$ across 40% and 60%-open tumble blockages.

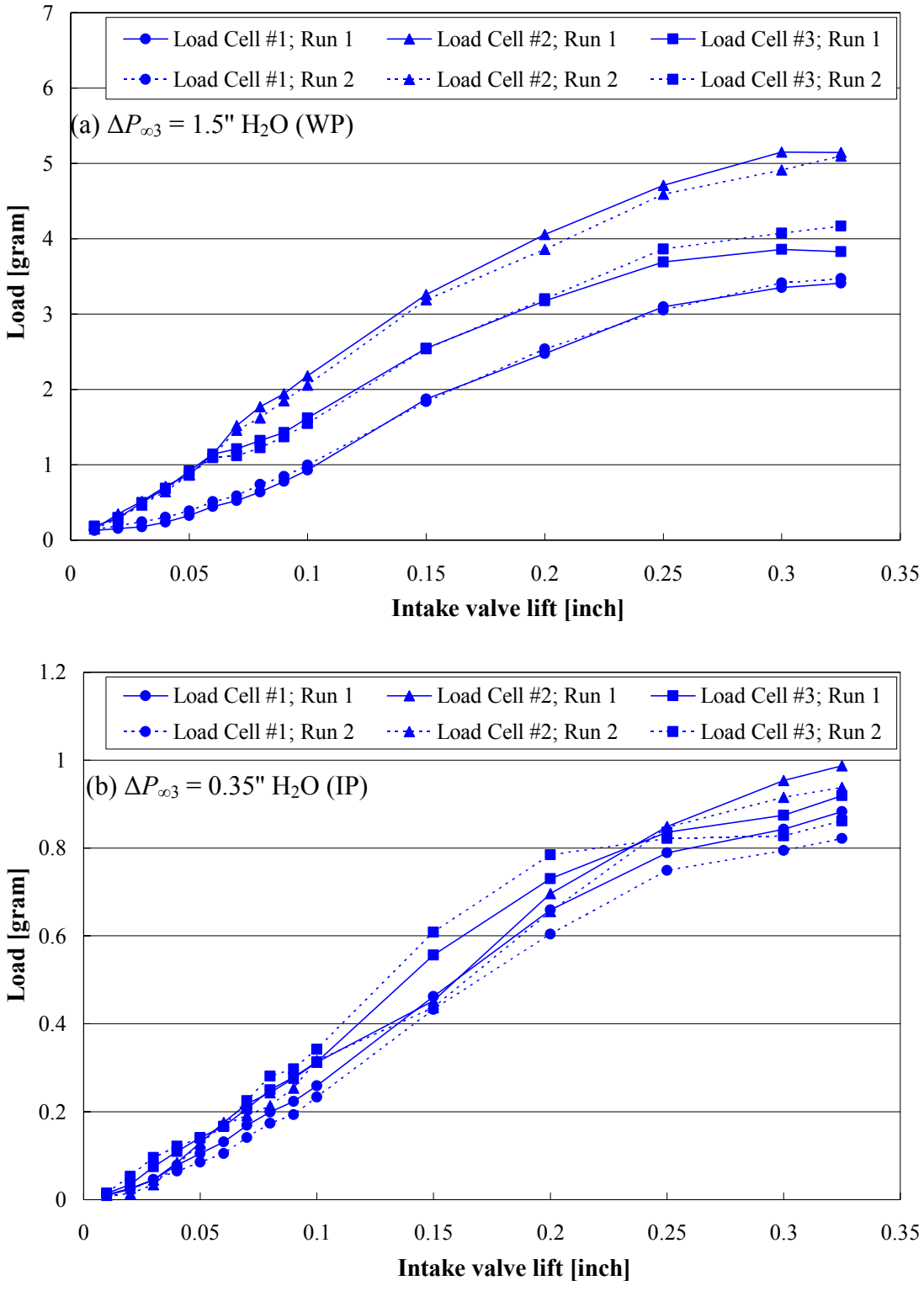

Figure D.2. Vertical loads on the screen for fully open runner.

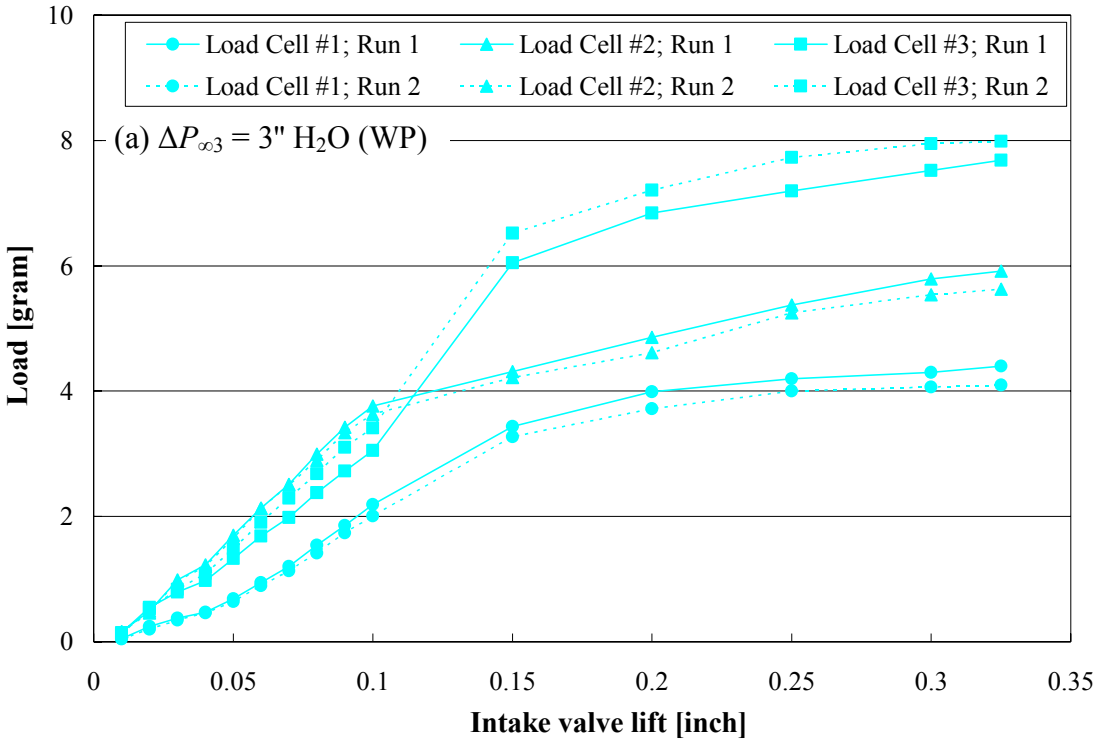

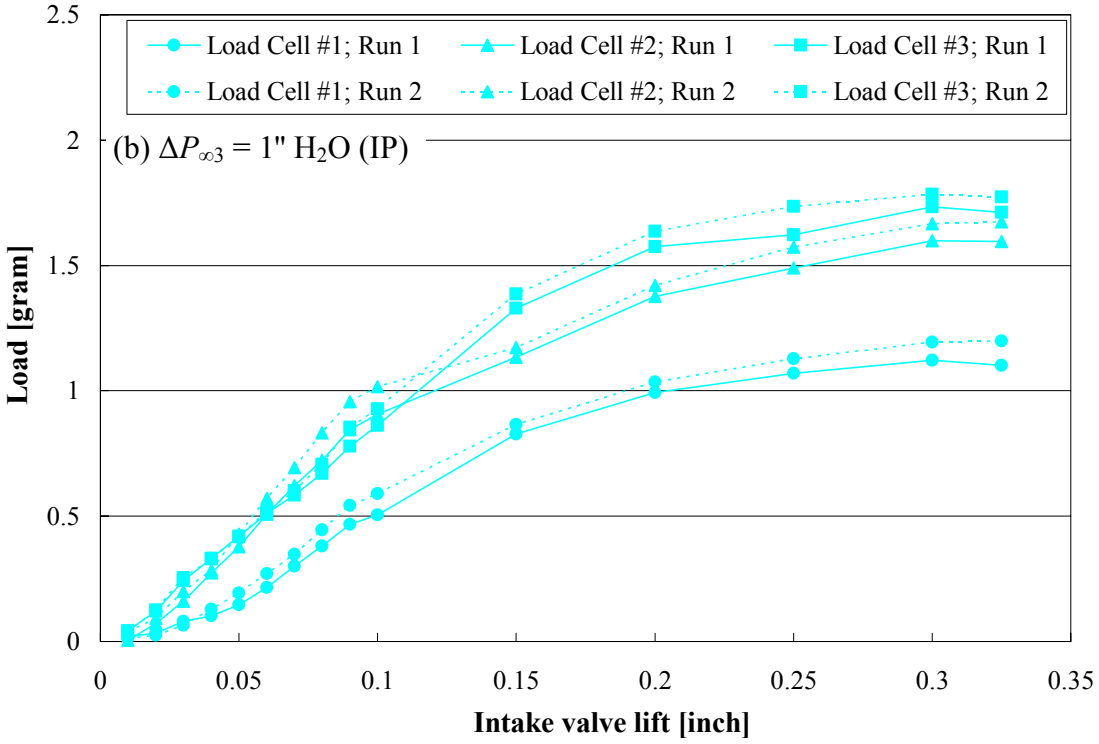

Figure D.3. Vertical loads on the screen for 60%-open blockage.

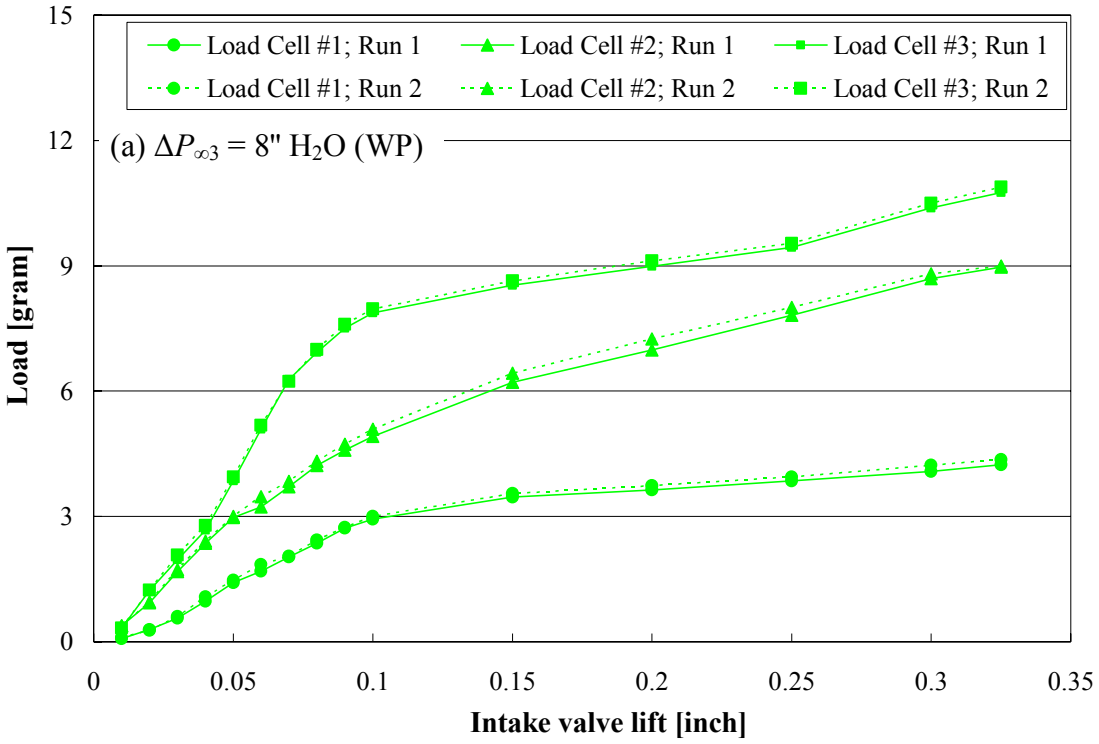

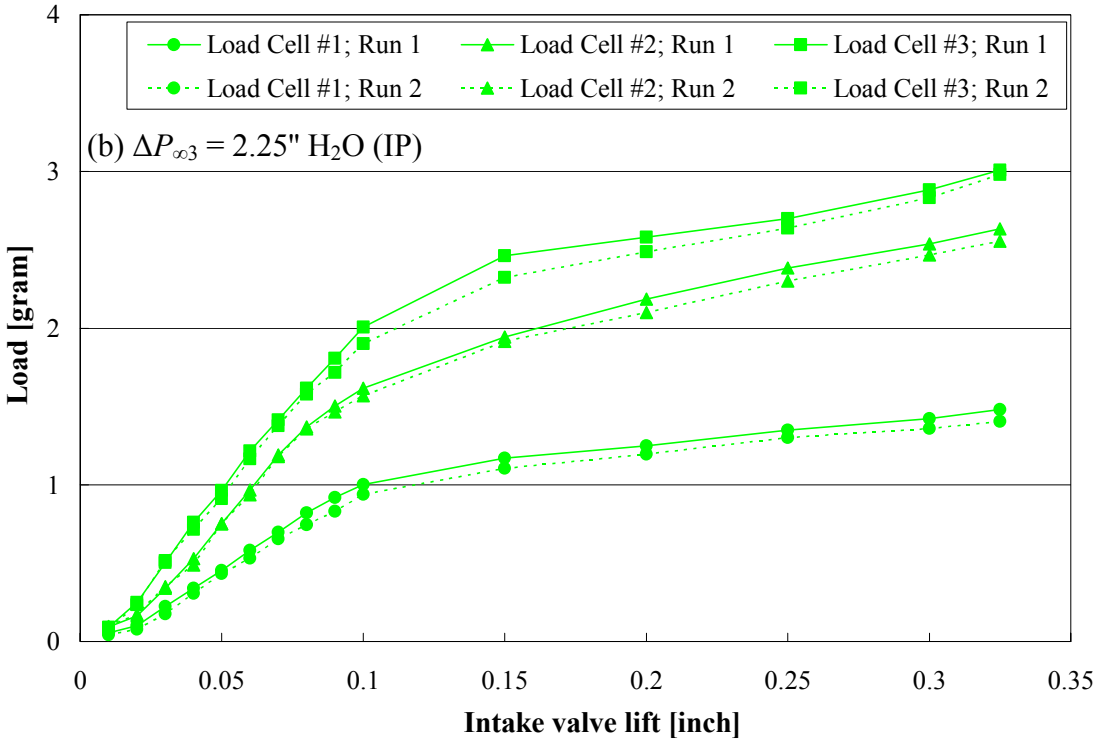

Figure D.4. Vertical loads on the screen for 40%-open blockage.

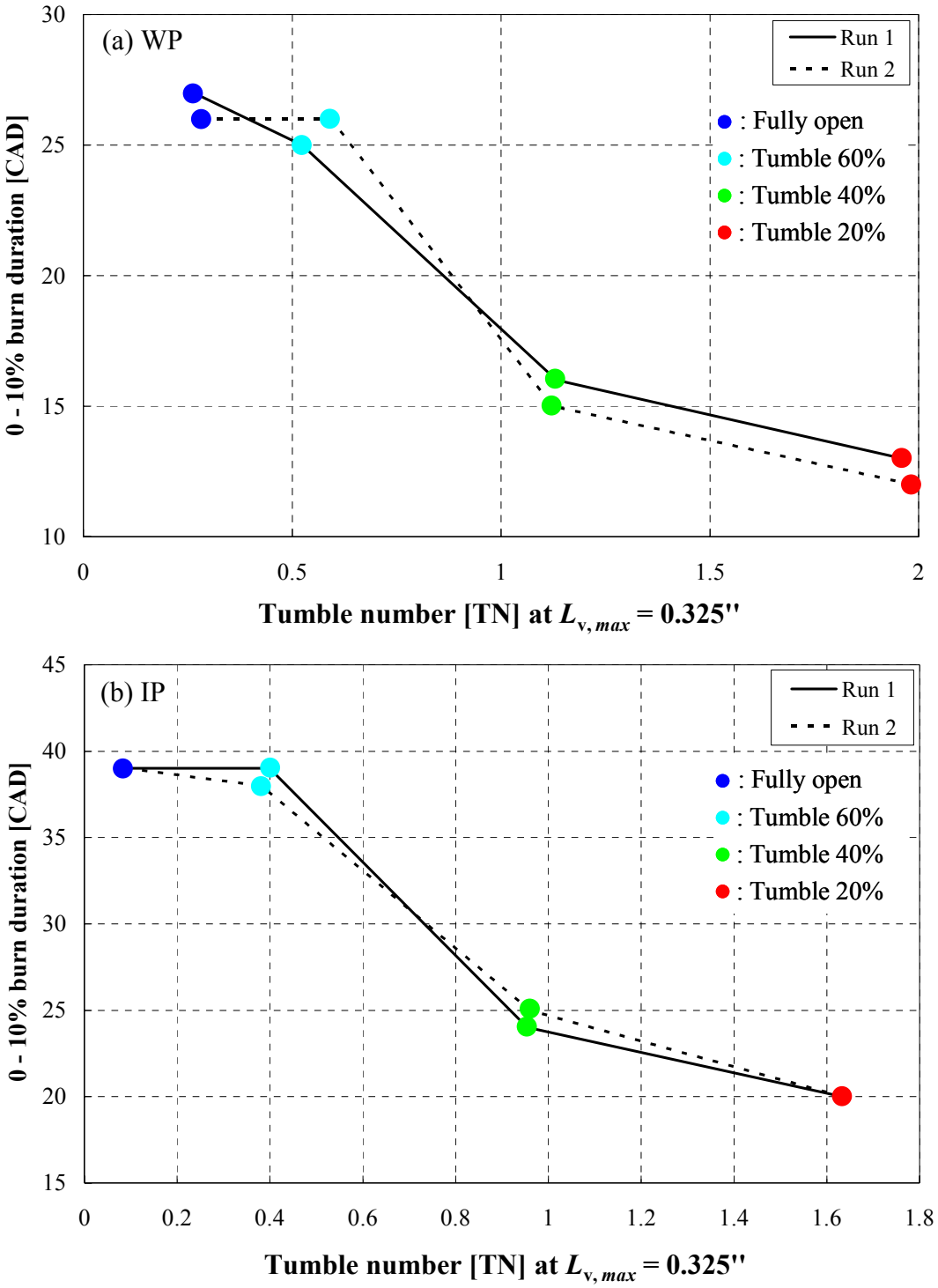

Figure D.5. 0 – 10% burn duration vs. tumble number at peak valve lift.

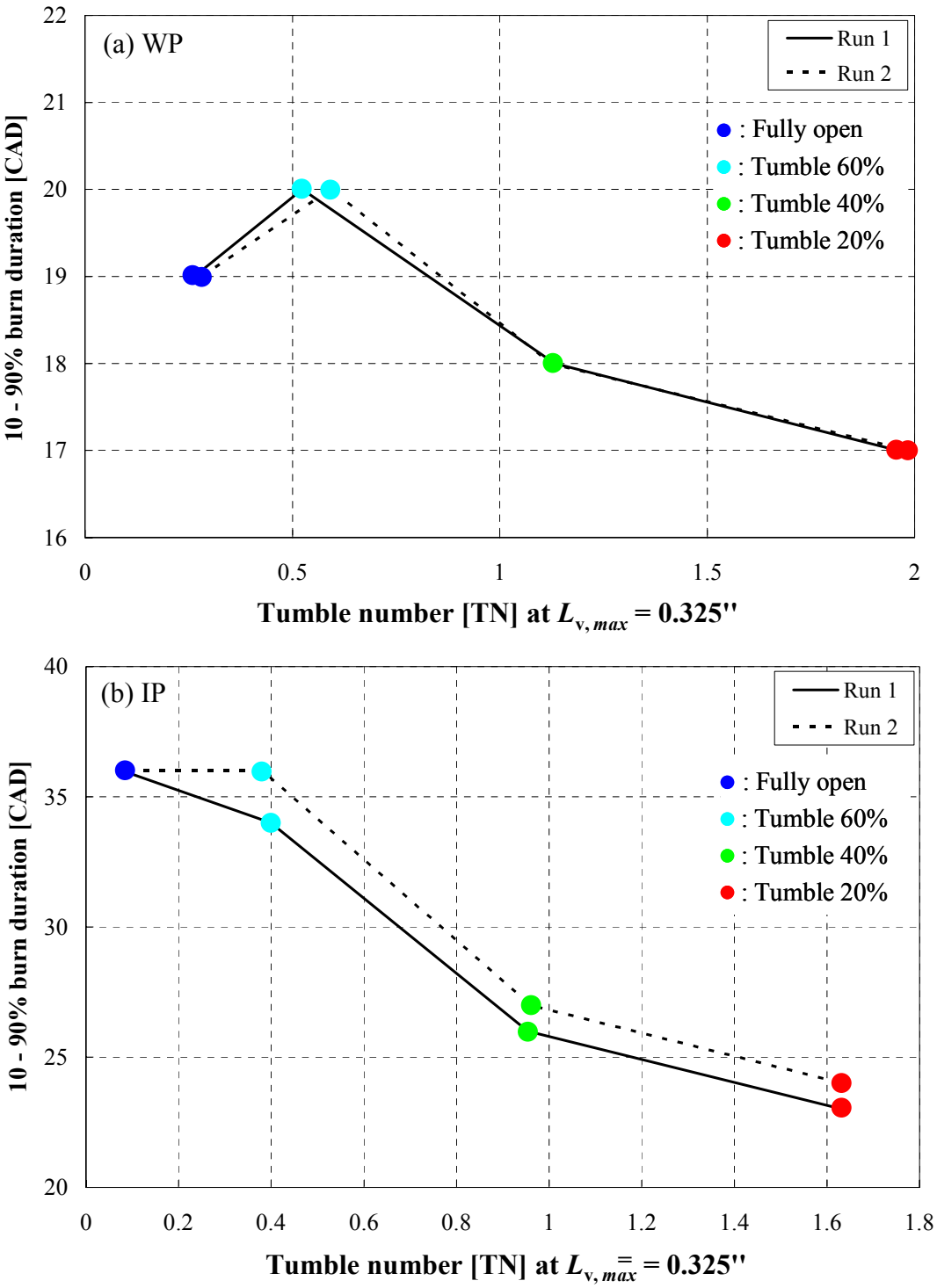

Figure D.6. 10 – 90% burn duration vs. tumble number at peak valve lift.

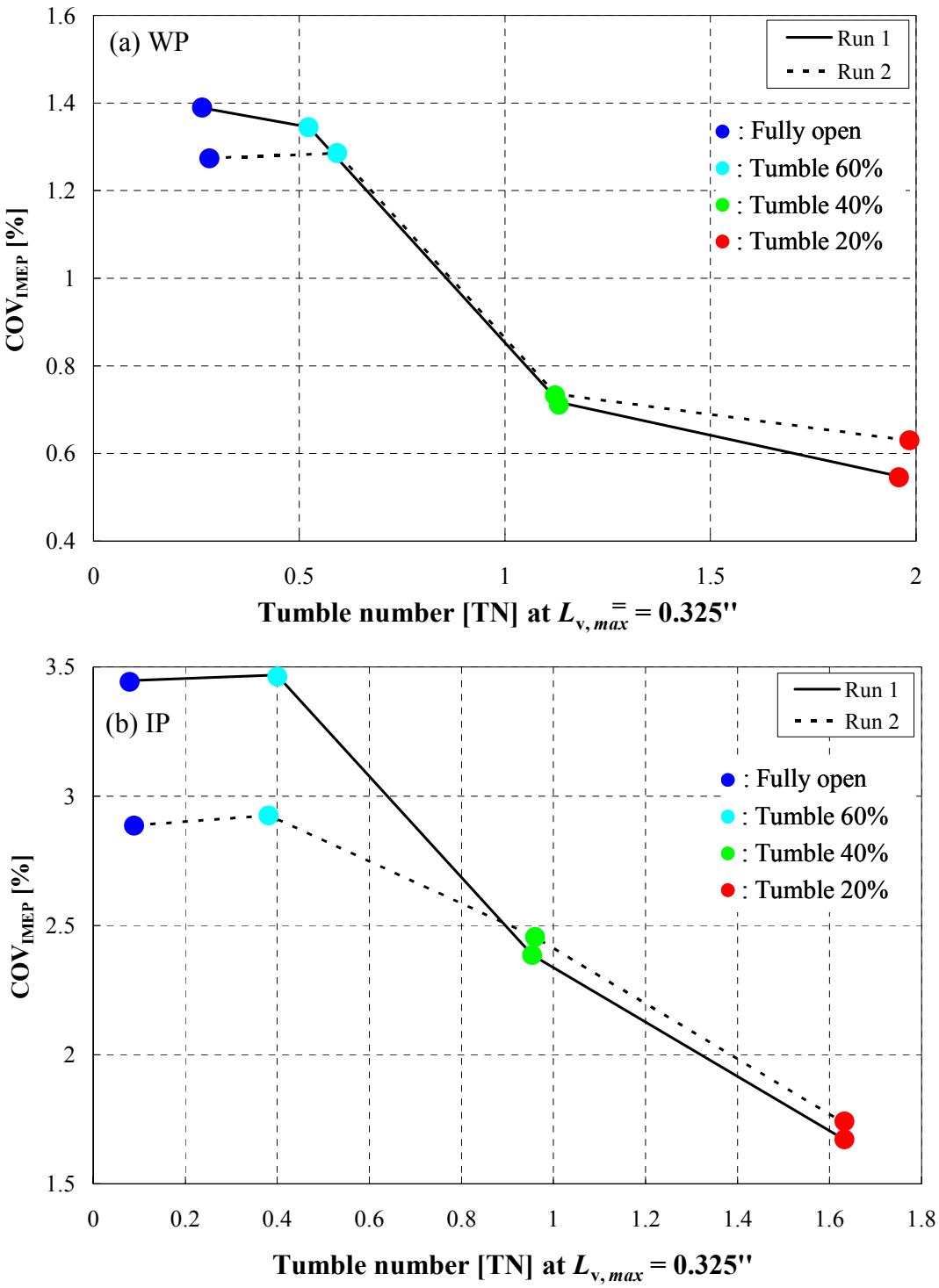

Figure D.7. COV in IMEP vs. tumble number at peak valve lift.

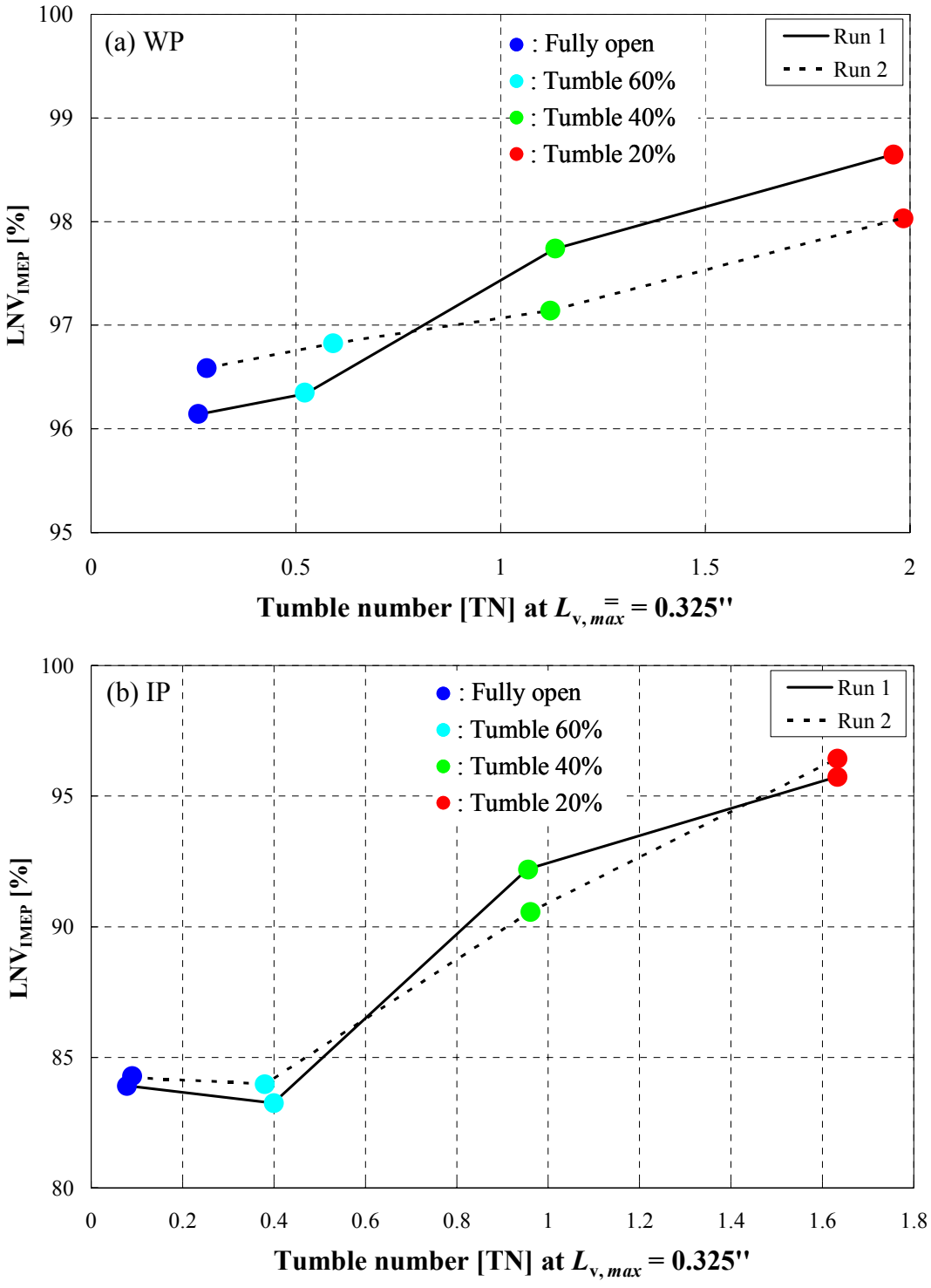

Figure D.8. LNV in IMEP vs. tumble number at peak valve lift.

APPENDIX E

EMPIRICAL CORRELATIONS FOR DISCHARGE COEFFICIENT AND FLOW LOSS COEFFICIENT OF SHARP-EDGED PIPE ORIFICES

Following Miller, 1996, this Appendix briefly describes the empirical relations for the discharge and flow loss coefficients of sharp-edged pipe orifices. Traditional orifice flow measurements are made with one pressure tap located one pipe diameter (D) upstream of the orifice, and the other $\frac{1}{2}D$ downstream (Fig. E1). An empirical expression is then given for the discharge coefficient as

$$C_D = 0.5959 + 0.0312\beta^{2.1} - 0.184\beta^8 + 0.039\frac{\beta^4}{1-\beta^4} - 0.0158\beta^3 + 91.71\frac{\beta^{2.5}}{\mathrm{Re}_D^{0.75}}, \qquad \text{(E1)}$$

where

$$\beta = \frac{d}{D}, \qquad \text{(E2)}$$

and d is the orifice throat diameter. The Reynolds number is calculated by

$$\mathrm{Re}_D = \frac{V_1 D}{\nu}, \qquad \text{(E3)}$$

where V_1 and ν are the velocity upstream of the orifice and kinematic viscosity, respectively. The flow loss coefficient based on the velocity head at the orifice throat diameter may be developed as

$$K = \frac{1-\beta^4}{C_D^2} - 2\beta^2\left(\frac{1}{C_c} - \beta^2\right), \qquad \text{(E4)}$$

where

$$C_c = 0.61375 + 0.13318\beta^2 - 0.26095\beta^4 + 0.51146\beta^6$$

is the contraction coefficient ($C_c = A_3/A_2$).

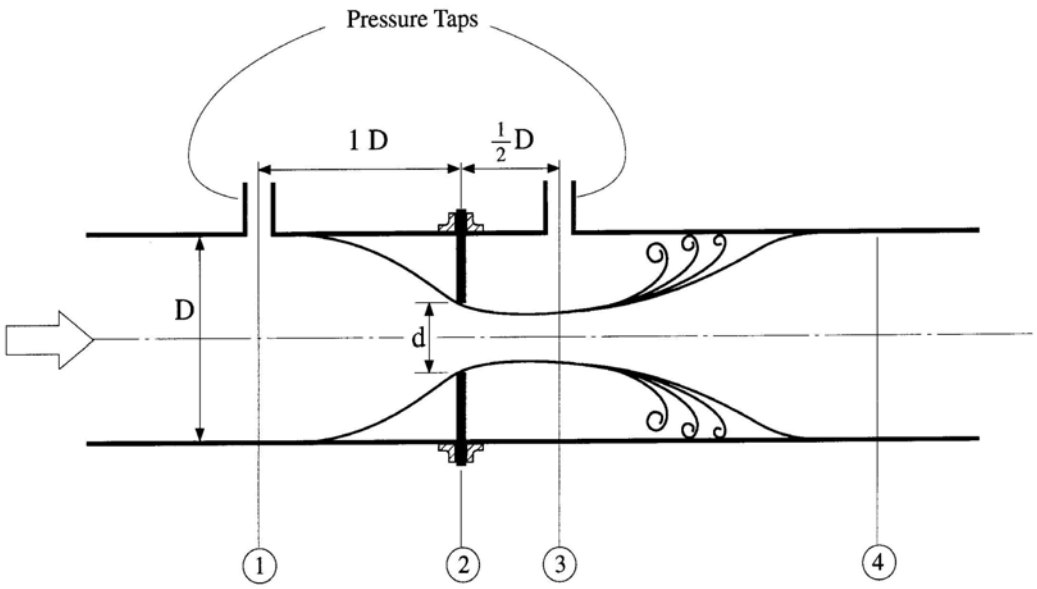

Figure E1. $1D-\frac{1}{2}D$ tap pipe orifice.

REFERENCES

Abd-Alla, G.H. (2002). Using exhaust gas recirculation in internal combustion engines: a review, *Energy Conversion & Management*, **43**: 1027-1042.

Aita, S., Tabbal, A., Munck, G., Fujiwara, K., Hongoh, H., Tamura, E., and Obana, S. (1990). Numerical simulation of port-valve-cylinder flow in reciprocating engines, SAE Paper 900820.

Al-Alousi, Y. H. and Karim, G. A. (1984). Some considerations of cyclic variations in spark ignition engines fuelled with gaseous fuels, SAE Paper 840232.

Alkidas, A. C., Puzinauskas, P. V., and Peterson, R. C. (1990). Combustion and heat transfer studies in a spark-ignited multivalve optical engine, SAE Paper 900353.

Ancimer, R., Jaaskelainen, H., and Wallace, J. (1999). Experiments into the flame kernel development in high swirl production spark ignition engines, SAE Paper 1999-01-3544.

Anderson, W. J., Lestz, S. S., and Meyer, W. E. (1973). The effect of charge dilution on cycle-by-cycle variations and exhaust emissions of an SI engine, SAE Paper 730152.

Arcoumanis, C., Bicen, A. F., and Whitelaw, J. H. (1981). Measurements in a motored four-stroke reciprocating model engine, *Fluid Mech. of Combustion System, presented at the Fluids Eng. Conf.,* ASME, Boulder, Colorado, June 22-23.

Arcoumanis, C., Hadjiapostolous, A., and Whitelaw, J. H. (1987). Swirl center precession in engine flows, SAE Paper 870370.

Arcoumanis, C. and Whitelaw, J. H. (1987). Fluid mechanics of internal. combustion engines - a review, *Proc. Instn. Mech. Engrs*, **201**: 57-74.

Arcoumanis, C. and Tanabe, S. (1989). Swirl generation by helical ports, SAE Paper 890790.

Arcoumanis, C., Hu, Z., Vafidis, C., and Whitelaw, J. H. (1990). Tumbling motion - A mechanism for turbulence enhancement in spark-ignition engines, SAE Paper 900060.

Arcoumanis, C., Hu, Z., and Whitelaw, J. H. (1992). Steady flow characterization of tumble generating four valve cylinder heads, *Proc. Instn. Mech. Engrs*., **207**: 203-210.

Arcoumanis, C., Nouri, J., Xu, H. M., and Stone, R. (1997). Analysis of the steady flow characteristics of tumble-generating four-valve cylinder heads, *Optical Diagnostics in Engineering*, **2**(2): 71-83.

Arcoumanis, C., Godwin, S.N., and Kim, J.W. (1998). Effect of tumble strength on exhaust emissions in a single cylinder 4-valve S.I engine, SAE Paper 981044.

Baker, P., Benjamin, S. F., Girgis, N. S., Newman, A. W., and Seeley, W. A. (1995). Characterization of barrel swirl motion under steady flow conditions, SAE Paper 950729.

Baritaud, T. A. (1989). Combustion and fluid dynamic measurements in a spark-ignition engine - Effects of thermochemistry and velocity field; turbulent flame speeds, SAE Paper 892098.

Baruah, P. C., Benson, R. S., and Balouch, S. K. (1978). Performance and emission predictions of a multi-cylinder spark ignition engine with exhaust gas recirculation, SAE Paper 780663.

Bates, S. C. (1989). Flame imaging studies of cycle-by-cycle combustion variation in a SI four-stroke engine, SAE Paper 892086.

Benson, J. D. and Stebar, R. F. (1971). Effects of charge dilution on nitric oxide emission from a single-cylinder engine, SAE Paper 710008.

Bianchi, G. M., Cantore, G., Parmeggiani, P., and Michelassi, V. (2002). On application of nonlinear k-ε models for internal combustion engine flows, *Journal of Engineering for Gas Turbines and Power, ASME*, **124**: 668-677.

Blair, G. P. and Drouin, F. M. M. (1996). Relationship between discharge coefficients and accuracy of engine simulation, SAE Paper 962527.

Brunt, M. F. J. and Emtage, A. L. (1997). Evaluation of burn rate routines and analysis errors, SAE Paper 970037.

Brunt, M. F. J., Rai, H., and Emtage, A. L. (1998). The calculation of heat release energy from engine cylinder pressure data, SAE Paper 981052.

Cains, T., Richardson, D., and Wallace, S. (1997). High dilution combustion through axial and barrel swirl, SAE Paper 974131.

Catania, A. E. (1982). 3-D swirling flow in an open chamber automotive diesel engine with different induction systems, *ASME Symposium on Flows in Internal Combustion Engines*, November.

Catania, A. E., Misul, D., Mittica, A., and Spessa, E. (2001). A refined two-zone heat release model for combustion analysis in SI engines, *The Fifth International Symposium on Diagnostics and Modeling of Combustion in Internal Combustion Engines* (COMODIA 2001), Nagoya, July 1-4, 2001.

Challen, B. and Baranescu, R. (1999). Diesel engine reference book, SAE, 2nd edition.

Choi, K. H., Park, J. H., Lee, N. H., Yu, C. H., and Noh, S. H. (1999). A research on fuel spray and air flow fields for spark-ignited direct injection using laser measurement technology, SAE Paper 1999-01-0503.

Chun, K. M. and Heywood, J. B. (1987). Estimating heat release and mass of mixture burned from SI engine pressure data, *Combust. Sci. Tech.*, **54**: 133-143.

Church, W. and Farrell, P. V. (1998). Effects of intake port geometry on large scale in-cylinder flows, SAE Paper 980484.

Das, S. and Dent, J. D. (1995). Simulation of the mean flow in the cylinder of a motored 4- valved spark ignition engine, SAE Paper 952384.

Davis, G. C. and Borgnakke, C. (1982). The effect of in-cylinder flow processes (swirl, squish and turbulence intensity) on engine efficiency - model predictions, SAE Paper 820045.

Desantes, J. M., Arregle, J., and Molina, S. (2000). Influence of the EGR rate, oxygen concentration and equivalent fuel/air ratio on the combustion behavior and pollutant emissions of a heavy-duty diesel engine, SAE Paper 2000-01-1813.

Dyer, T. M. (1979). Characterization of one- and two-dimensional homogeneous combustion phenomena in a constant volume bomb, SAE Paper 790353.

Fan, L. and Reitz, R.D. (1999). Intake flow simulation and comparison with PTV measurements, SAE Paper 1999-01-0176.

Fansler, T. D. (1985). Laser velocimetry measurements of swirl and squish flows in an engine with a cylindrical piston bowl, SAE Paper 850124.

Floch, A., Frank, J.V., and Ahmed, A. (1995). Comparison of effects of intake-generated swirl and tumble on turbulence characteristics in a 4-valve engine, SAE Paper 952457.

Fons, M., Muller, M., Chevalier, A., Vigild, C., Hendricks, E., and Sorenson, C. (1999). Mean value engine modeling of an SI engine with EGR, SAE Paper 1999-01-0909.

Gale, N. F. (1990). Diesel engine cylinder head design - The compromises and the techniques, SAE Paper 900133.

Gatowski, J. A., Balles, E. N., Chun, K. M., Nelson, F. E., Ekchian, J. A., and Heywood, J. B. (1984). Heat release analysis of engine pressure data, SAE Paper 841359.

Geiger, J., Grigo, M., Lang, O., Wolters, P., and Hupperich, P. (1999). Direct injection gasoline engines - Combustion and design, SAE Paper 1999-01-0170.

Gillespie, L., Lawes, M., Sheppard, C. G. W., and Wooley, R. (2000). Aspects of laminar and turbulent burning velocity relevant to SI engines, SAE Paper 2000-01-0192.

Glass, W., Russell, F. R., Wade, D. T., and Hollabaugh, D. M. (1970). Evaluation of exhaust recirculation for control of nitrogen oxides emissions, SAE Paper 700146.

Glover, A. R., Handleby, G. E., and Hadded, O. (1988). The development of scanning LDA for the measurement of turbulence in engines, SAE Paper 880378.

Goldwitz, J. A. and Heywood, J. B. (2005). Combustion Optimization in a Hydrogen-Enhanced Lean Burn SI Engine, SAE Paper 2005-01-0251.

Gosman, A. D., Tsui, Y. Y., and Vafidis, C. (1985). Flow in a model engine with a shrouded valve - a combined experimental and computational study, SAE Paper 850498.

Gouldin F C. (1989). An application of fractals to modeling premixed turbulent flames. *Combustion and Flame*, **77**(4): 241-259.

Grimm, B. M. and Johnson, R. T. (1990). Review of simple heat release computations, SAE Paper 900445.

Guelder, O. L. (1990). Turbulent premixed combustion modeling using fractal geometry, *23rd Symposium on combustion*, the Combustion Institute.

Gumbleton, J.J., Bolton, R.A., and Lang, H.W. (1974). Optimizing engine parameters with exhaust gas recirculation, SAE Paper 740104.

Hadded, O. and Denbratt, I. (1991). Turbulence characteristics of tumbling air motion in 4-valve SI engines and their correlation with combustion parameters, SAE Paper 910478.

Haghooie, M. and Kent, J. C. (1987). The effect of maximum valve lift on TDC flow field in a high swirl piston engine, *Proceeding of the NATO Advanced Study Institute on Instrumentation for Combustion and Flow in Engines*, Vimeira, Portugal, September 13-26.

Hall, M. J. and Bracco, F. V. (1987). A study of velocities and turbulence intensities measured in firing and motored engines, SAE Paper 870453.

Hamamoto, Y., Tomita, E., Tanaka, Y., and Katayama, T. (1985). The effect of swirl on spark ignition engine combustion, *International Symposium on Diagnostics and Modeling of Combustion in Reciprocating Engines*, Tokyo, September.

Hascher, H. G., Schock, H. J., Avanessian, O., and Novak, J. (2000). A comparison of modeled and measured 3-D in-cylinder charge motion throughout the displacement of a four-valve SI engine, SAE Paper 2000-01-2799.

Haworth, D. C., El Tahry, S. H., Huebler, M. S., and Chang, S. (1990). Multidimensional port-and-cylinder flow calculations for two-and four-valve-per-cylinder engines - Influence of intake configuration on flow structure, SAE Paper 900257.

Heywood, J. B. (1987). Fluid motion within the cylinder of internal combustion engines, *Journal of Fluids Engineering*, **109**: 3-35.

Heywood, J. B. (1988). *Internal combustion engine fundamentals*, McGraw-Hill, New York.

Hill, P. G. and Kapil A. (1989). The relationship between cyclic variations in spark ignition engines and the small structure of turbulence, *Combust. Flame*, **78**: 237-247.

Hill, P. G. and Zhang, D. (1994). The effect of swirl and tumble on combustion in spark-ignition engines. *Prog. Energy Combust. Sci.*, **20**:373-429.

Hong, C-W. and Tarng, S-D. (2001). In-cylinder tumble flow fields measurements and predictions, *Journal of Engineering for Gas Turbines and Power, ASME*, **123**: 139-145.

Hoult, D. P. and Nguyen, V. H. (1985). A turbulent burning law derived from combustion experiments, *International Symposium on Diagnostics and Modeling of Combustion in Reciprocating Engines*, Tokyo, September.

Ikegami, M., Shioji, M., Wei, D. Y., and Sugiura, M. (1985). In-cylinder measurement of turbulence by laser monodyne principle, *International Symposium on Dianostics and Modeling of Combustion in Reciprocating Engines*, Tokyo, September.

Inoue, T., Iguchi, S., and Yamada, T. (1988). In cylinder gas motion, mixture formation and combustion of 4-valve lean burn engine, *9th International Wienna Motor Symposium*, VDI **99**: 200-218.

Isshiki, Y., Shimamoto, Y., and Wakisaka, T. (1985). Numerical prediction of effect of intake port configurations on the induction swirl intensity by three-dimensional gas flow analysis, *International Symposium on Diagnosistics and Modeling of Combustion in Reciprocating Engines*, Tokyo, September.

Ivanic, Z., Ayala, F., Goldwitz, J., and Heywood, J. B. (2005). Effects of Hydrogen Enhancement on Efficiency and NOx Emissions of Lean and EGR-Diluted Mixtures in a SI Engine, SAE Paper 2005-01-0253.

Jackson, N. S., Stokes, J., Lake, T. H., Sapsford, S. M., Heikal, M., and Denbratt, I. (1996). Understanding the CCVS stratified EGR combustion system, SAE Paper 960837.

Jeon, C-H., Chang, Y-J., Cho, K-B., and Kang, K-Y. (1998). Effects of intake ports on in-cylinder flow and lean combustion in a 4-valve engine, SAE Paper 981048.

Jie, M-S., Kim, M-H., and Kim, W-T. (1993). The effect of tumble flow on engine performance and flame propagation, SAE Paper 931946.

Justham, T., Jarvis, S., Garner, C. P., Hargrave, G. K., Clarke, A, and Richardson, D. (2006). Single-Cylinder-Motored SI IC Engine Intake Runner Flow Measurement Using Time-Resolved Digital Particle Image Velocimetry, SAE Paper 2006-01-1043.

Kajiyama, K., Nishida, A., Arai, M., and Hiroyasu, H. (1984). An analysis of swirling flow in cylinder for predicting DI diesel engine performance, SAE Paper 840518.

Kang, K-Y. and Baek, J-H. (1996). Tumble flow and turbulence characteristics in a small four-valve engine, SAE Paper 960265.

Kang, K-Y., Oh, S-M., Lee, J-W., Lee, K-H., and Bae, C-S. (1997). The effects of tumble flow on lean burn characteristics in a 4-valve SI engine, SAE Paper 970791.

Kang, K-Y. and Baek, J-H. (1998). Turbulence characteristics of tumble flow in a four-valve engine, *Experimental Thermal and Fluid Science*, **18**: 231-243.

Kapus, P. E. And Poetscher, P. (2000). ULEV and fuel economy - A contradiction, SAE Paper 2000-01-1209.

Kent, J. J., Mikulec, A., Rimai, L., Adamczyk, A. A., Mueller, S. R., Stein, R. A., and Warren, C. C. (1989). Observations on the effects of intake-generated swirl and tumble on combustion duration, SAE Paper 892096.

Kawashima, J-I., Ogawa, H., and Matsui, Y. (1996). A study of variable swirl intake port on 4 valves high speed di diesel engine-development of very high swirl helical with steady state air flow test and 3-dimensional computation, SAE Paper 968451.

Kawashima, J-I., Ogawa, H., and Tsuru, Y. (1997). Research on variable swirl intake port for high-speed multivalve DI diesel engine - Effects of port configuration on flow characteristics and swirl generation capacity, SAE Paper 978223.

Kawashima, J-I., Ogawa, H., and Tsuru, Y. (1998). Research on a variable swirl intake port for 4-valve, high-speed DI diesel engines, SAE Paper 982680.

Keck, J. C. and Heywood, J. B. (1987). Early flame development and burning rates in spark ignition engines and their cyclic variability, SAE Paper 870164.

Kent, J. C., Haghgooie, M., Mikulec, A., Davis, G. C., and Tabaczynski, R. J. (1987). Effects of intake port design and valve lift on in-cylinder flow and burnrate, SAE Paper 872153.

Kent, J. C., Mikulec, A., Rimal, L., Adamczyk, A. A., Mueller, S. R., Stein, R., A., and Warren, C. C. (1989). Observations on the effects of intake-generated swirl and tumble on combustion duration, SAE Paper 892096.

Khalighi, B. (1990). Intake-generated swirl and tumble motions in a 4-valve engine with various intake configurations - flow visualization and Particle Tracking Velocimetry, SAE Paper 900059.

Khalighi, B., Tahry, S. H. E., Haworth, D. C., and Huebler, M. S. (1995). Computation and measurement of flow and combustion in a four- valve engine with intake variations, SAE Paper 950287.

Kido, H., Wakuri, Y., Ono, S., and Murase, E. (1980). Influences of Swirl and Turbulence on the Burning Velocity in an Engine Cylinder, Bulletin of the JSME, **23**(186): 2088-2095.

Kothamasu, V. (1998). Effect of intake and exhaust elements on sound attenuation and engine performance: An experimental and computational investigation, Master's Thesis, The Ohio State University.

Kyriakides, S. C. and Glover, A. R. (1988). A study of the correlation between in-cylinder air motion and combustion in gasoline engines, *Instn. Mech. Engineering*, C55/88.

Kyriakides, S. C. and Glover, A. R. (1988). A study of the correlation between in-cylinder air motion and combustion in gasoline engines, SAE Paper 884055.

Li, Y. F., Li, L. L., Xu, J. F., Gong, X. H., Liu, S. L., and Xu, S. D. (2000). Effects of combination and orientation of intake ports on swirl motion in four-valve DI diesel engines, SAE Paper 2000-01-1823.

Li, Y., Zhao, H., Peng, Z., and Ladommatos, N. (2001). Analysis of tumble and swirl motions in a four-valve SI engine, SAE Paper 2001-01-3555.

Liou, T. M. and Santavica, D. A. (1983). Cycle resolved turbulence measurements in a ported engine with and without swirl, SAE Paper 830419.

Lord, D. L., Anderson, R. W., Brehob, D. D., and Kim, Y. (1993). The effects of charge motion on early flame kernel development, SAE Paper 930463.

Lumley, J. L. (1999). *Engines – An Introduction*, pp. 134-181, Cambridge University Press.

Marc, D., Boree, J., Bazile, R., and Charnay, G. (1997). Tumbling vortex flow in a model square piston compression machine: PIV and LDV Measurements, SAE Paper 972834.

Mayo, J. (1975). The effect of engine design parameters on combustion rate in spark-ignited engines, SAE Paper 750355.

Mikulec, A., Kent, J. C., and Tabaczynski, R. J. (1988). The effect of swirl on combustion in a pancake chamber spark ignition engine: the case of constant kinetic energy, SAE Paper 880200.

Mikulec, A., Kent, J. C., Adamczyk, A. A., and Rimai, L. (1988). Effects of intake port configuration on induction-generated swirl in a piston engine: a water analog experiment using particle tracking velocimetry, *2nd International Symposium on Fluid Control, Measurement, Mechanics, and Visualization*, Sheffield University, England, September 5-9.

Miller, R. W. (1996). *Flow Measurement Engineering Handbook*, chapter 9: Differential Products Engineering Equations. McGraw-Hill, NY, third edition.

Musser, G. S., Wilson, J. A., Hyland, R. G., and Ashby, H. A. (1971). Effectiveness of exhaust gas recirculation with extended use, SAE Paper 710013.

Nagayama, I., Araki, Y., and Iloka, Y. (1977). Effects of swirl and squish on S.I. engine combustion and emission, SAE Paper 770217.

Nagao, A. and Tanaka, K. (1983). The effect of swirl control on combustion improvement of spark ignition engine, Institute of Mechanical Engineering.

Naitoh, K., Takagi, Y., Kuwahara, K., Krause, E., and Ishii, K. (1990). Computation of transition to turbulence in the compression stage of a reciprocating engine, *Fluid Dynamics Research*, **6**: 277-294.

Neuber, H. J., Endres, H., and Breuer, M. (1994). New variable intake and mixture formation system for multi- valve SI engines, SAE Paper 940449.

Neuber, H. J., Spiegel, L., and Ganser, J. (1995). Particle Tracking Velocimetry, a power tool to shape the in-cylinder flow of modern multi-valve engine concepts, SAE Paper 950102.

Nishiwaki, K. (1985). Prediction of three-dimensional fluid motions during intake process and swirl ratios in four-cycle engines, *International Symposium on Diagnosistics and Modeling of Combustion in Reciprocating Engines*, Tokyo, September.

Omori, S., Iwachido, K., Motomochi, M., and Hirako, O. (1991). Effect of intake port flow pattern on the in-cyliner tumbling air flow in mlti-valve SI engines, SAE Paper 910477.

Ozkan, M., Sandalci, T., and Ozkan, D.B. (2005). Comparison of EGR ratios determined by four different methods for electronic re-circulation gate control, *Int. J. Environment and Pollution*, **23**(2): 223-231.

Partington, G. D. (1982). Development and application of a fully machined helical inlet port for high speed DI engines, SAE Paper 824121.

Payri, F., Benajes, J., Margot, X., and Gil, A. (2004). CFD modeling of the in-cylinder flow in direct-injection Diesel engines, *Computers & Fluids*, **33**: 995-1021.

Pettiffer, H. F. (1982). Interaction of port design and injection rate for a D.I. diesel, SAE Paper 820358.

Pischinger, S. and Heywood, J. B. (1990). The effect of engine design parameters on combustion rate in spark ignited engines, SAE Paper 900021.

Przastek, J., Dabkowski, A., and Teodorczyk, A. (1999). The study of exhaust gas recirculation on efficiency and NO_x emission in spark-ignition engine, SAE Paper 1999-01-3514.

Quader, A. A. (1971). Why intake charge dilution decreases nitric oxide emission from spark ignition engines, SAE Paper 710009.

Ramadan, B. (2001). A Study of Swirl Generation in DI Engines Using KIVA-3V, *11th International Multidimensional Engine Modeling User's Group Meeting at the SAE Congress*, Detroit, Michigan, Mar. 4.

Rassweiler, G. M. and Withrow, L. (1938). Motion pictures of engine flames correlated with pressure cards, SAE Paper 800131 (reprinted version).

Rauckis, M. J. and Maclean, W. J. (1979). The effect of hydrogen addition on ignition delays and flame. Propagation in spark ignition engines, *Combust. Sci. Tech.*, **19**: 207-216.

Reeves, M., Garner, C. P., Dent, J. C., and Halliwell, N. A. (1996). Particle Image Velocimetry measurements of in-cylinder flow in a multi-valve internal combustion engine, *Proc. Instn. Mech. Engrs.*, Part D, **210**: 63-70.

Rönnbäck, M., Wang, X. L., and Linna, J. R. (1991). Study of induction tumble by Particle Tracking Velocimetry in a 4-valve engine, SAE Paper 912376.

Rouland, E., Trinité, M., Dionnet, F., Floch, A., and Ahmed, A. (1997). Particle Image Velocimetry measurements in a high tumble engine for in-cylinder flow structure analysis, SAE Paper 972831.

Rupal, S. (2003). Experimental study of the effect of intake primary runner blockages on combustion and emissions in SI engines under part-load conditions, Master's Thesis, the Ohio State University.

Santavicca, D. A., Liou, D., and North, G. L. (1990). A fractal model of turbulent flame kernel growth, SAE Paper 900024.

Saxena, V. and Rask, R. B. (1987). Influence of inlet flows on the flow field in an engine, SAE Paper 870369.
Schock, H., Shen, Y., Timm, E., Stuecken, T., Fedewa, A., and Keller, P. (2003). The measurement and control of cyclic variation of flow in a piston cylinder assembly, SAE Paper 2003-01-1357.

Selamet, A., Rupai, S., and He, Y. (2004). An experimental study on the effect of intake primary runner blockages on combustion and emissions in SI engines under part-load conditions, SAE Paper 2004-01-2973.

Shayler, P. J., Wiseman, M. W., and Ma, T. (1990). Improving the determination of mass fraction burnt, SAE Paper 900351.

Shayler, P.J., Chick, J., Darnton, N.J., and Eade, D. (1999). Generic functions for fuel consumption and engine-out emissions of HC, CO and NO_x of spark-ignition engines, *Proc. Instn. Mech. Engrs.*, Part D, **213**: 365-378.

Shayler, P.J., Winborn, L.D., Hill, M.J., and Eade, D. (2000). The influence of gas/fuel ratio on combustion stability and misfire limits of spark-ignition engines, SAE Paper 2000-01-1208.

Stephenson, P. W., Claybaker, P. J., and Rutland, C. T. (1996). Modeling the effects of intake generated turbulence and resolved flow structures on combustion in DI diesel engines, SAE Paper 960634.

Stokes, J., Lake, T. H., Christie, M. J., and Denbratt, I. (1994). Improving the NO_x/fuel economy trade-off for gasoline engines with the CCVS combustion system, SAE Paper 940482.

Stone, C. R. and Ladommatos, N. (1992). The measurement and analysis of swirl in steady flow, SAE Paper 921642.

Stone, R. (1999). *Introduction to internal combustion engines*, the Macmillan Press.

Sztenderowicz, M. L. and Heywood, J. B. (1990). Mixture nonuniformity effects on SI engine combustion variability, SAE Paper 902142.

Tabaczynski, R. J. (1976). Turbulence and turbulent combustion in spark ignition engines, *Prog. Energy Comb. & Sci.*, **2**: 143-165.

Tabata, M., Yamamoto, T., and Fukube, T. (1995). Improving NO_x and fuel economy for mixture injected SI engine with EGR, SAE Paper 950684.

Tindal, M. J., Williams, T. J., and Aldoory, M. (1982). The effect of inlet port design on cylinder gas motion in direct injection diesel engines, *Flows in Internal Combustion Engines, ASME*, pp. 101-111.

Trigui, N., Kent, J. C., Guezennec, Y. G., and Choi, W-C. (1994). Characterization of intake-generated flow fields in I.C. engines using 3-D particle tracking velocimetry (3-D PTV), SAE Paper 940279.

Udayakumar, R., Arasu, P. V., and Sriram, S. (2003). Experimental investigation on emission control in C.I. engines using shrouded inlet valve, SAE Paper 2003-01-0350.

Urushihara, T., Murayama, T., Takagi, Y., and Lee, K. H. (1995). Turbulence and cycle-by-cycle variation of mean velocity generated by swirl and tumble flow and their effects on combustion, SAE Paper 950813.

Urushihara, T., Nakada, T., Kakuhou, A., and Takagi, Y. (1996). Effects of swirl/tumble motion on in-cylinder mixture formation in a lean-burn engine, SAE Paper 961994.

Uzkan, T., Borgnakke, C., and Morel, T. (1983). Characterization of flow produced by a high-swirl inlet port, SAE Paper 830266.

Vandevoorde, M., Sierens, R., and Dick, E. (2000). Validation of a new TVD scheme against measured pressure waves in the inlet and exhaust system of a single cylinder engine, *Journal of Engineering for Gas Turbines and Power, ASME*, **122**: 533-540.

Wigley, G. and Hawkins, M. G. (1978). Three dimensional velocity measurements by laser anemometry in a diesel engine cylinder under steady state inlet flow conditions, SAE Paper 780060.

Wills, D. A., Meyer, W. E., and Birnie, C. (1966). Mapping of airflow patterns in engines with induction swirl, SAE Paper 660093.

Witze, P. O. and Vilchis, F. R. (1981). Stroboscopic laser shadowgraph study of the effect of swirl on homogeneous combustion in a spark-ignition engine, SAE Paper 810226.

Witze, P. O. (1982). The effect of spark location on combustion in a variable-swirl engine, SAE Paper 820044.

Witze, P. O., Martin, J. K., and Borgnakke, C. B. (1983). Measurements and predictions of the precombustion fluid motion and combustion rates in a spark ignition engine, SAE Paper 831697.

Witze, P. O., Hall, M. J., and Wallace, J. S. (1988). Fiber-optic instrumented spark plug for measuring early flame development in spark ignition engines, SAE Paper 881638.

Xu, H. M. (2001). Some critical technical issues on the steady flow testing of cylinder heads, SAE Paper 2001-01-1308.

Yamamoto, H. and Misumi, M. (1987). Analysis of cyclic combustion variation in a lean operating SI engine, SAE Paper 870547.

Yoo, S. C. (1994). An experimental analysis of in-cylinder flow field in a four-valve SI engine - Focus on the effect of the angular momentum, SAE Paper 943903.

Young, M. B. (1980). Cyclic dispersion – Some quantitative cause and effect relationship, SAE Paper 800459.

Young, M. B. (1981). Cyclic dispersion in the homogeneous-charge spark-ignition engine - a literature survey, SAE Paper 810020.

Yun, J-E., Lee, J-J. (2000). A study on combine effects between swirl and tumble flow of intake port system in cylinder head, SAE Paper 2000-05-0098.

Zhang, D. H. and Frankel, S. H. (1997). Optimization of natural gas engine performance by multidimensional modeling, SAE Paper 971567.

2000 Service Manual, Town & Country, Caravan and Voyager, 9-62: Engine Specifications, DaimlerChrysler Corporation.